Quantum Gas Microscopy of Frustrated Quantum Many-Body Systems

Jirayu Mongkolkiattichai
Nan, Thailand

B.S., Chiang Mai University,
Thailand, 2018

A Dissertation presented to the Graduate Faculty of
the University of Virginia in Candidacy for the Degree of
Doctor of Philosophy

Department of Physics

University of Virginia
May, 2024

Abstract

Quantum gas microscopy has played an important role in the understanding of many-particle physics in strongly correlated systems. The single-atom-resolved imaging enables the detection of microscopic properties on many-fermion systems on the single site level in the quantum regime. Relying on the unique tunability of ultracold atoms in atomic interactions via Feshbach resonances, density, and spin imbalance, a wide parameter range in the phase diagram can be explored. Some of the theoretically most challenging systems with rich phase diagrams are frustrated systems. Triangular lattices are the simplest example of geometric frustration in which three spins with antiferromagnetic interactions cannot be antiparallel, leading to a large degeneracy in the many-body ground state and could result in quantum spin liquids.

In this dissertation, I report on the development of a triangular-lattice quantum gas microscope and the study of geometrically frustrated Mott insulators. The microscope enables us to detect unprecedented details of Hubbard physics in the geometrically frustrated system through imaging of the occupation, the spin density, and spin correlation functions on the single site level. I present the first realization of a Mott insulator of ^{6}Li on a symmetric triangular lattice with a lattice spacing of 1003 nm. For the first time, we image fermionic lithium in a triangular lattice via a Raman sideband cooling technique with an imaging fidelity of 98%. In addition, we measure spin-spin correlations and observe nearest-neighbor anticorrelations consistent with short-range 120° order. We find a good agreement between the results and simulations (Determinantal Quantum Monte Carlo [DQMC] and Numerical Linked-Cluster Expansion [NLCE]). In addition, spin-resolved density is implemented in a square lattice, allowing us to obtain all information on the density in the system and direct measurement of spin-spin correlations.

By utilizing spin-resolved imaging, we explore a three-component Fermi-Hubbard model with imbalanced interactions between spin components. Our observations reveal a signature of a Mott insulator state through the variance of density and compressibility. We examine the interplay between the different spin components through pairing correlations. This study opens possibilities for simulating physics beyond condensed matter models by realizing three-component Fermi lattice gases.

Quantum gas microscope expands our understanding of exotic phenomena in materials, such as high-temperature superconductors from first principles in tunable systems. Our microscope offers a platform for exploring nuclear physics, including the formation of baryons and their superfluidity, through ultracold-atom systems. Additionally, the capabilities of the microscope in studying quantum spin liquids hold promise for the discovery of new quantum phases.

Acknowledgments

Firstly, I would like to express my sincere gratitude to my supervisor, Prof. Peter Schauss, for his continuous support of my Ph.D. study and related research, for his patience, motivation, and immense knowledge. His guidance has been invaluable from the beginning of my work until the writing of this dissertation.

In addition to my supervisor, I would like to thank the rest of my research committee: Prof. Stefan Baessler, Prof. Cass Sackett, and Prof. Xinfeng Gao for their insightful comments and encouragement, but also some questions which inspire me to explore my research from various perspectives.

I would like to thank Dr. Jin Yang for making rapid progress in setting up the experiment during the COVID-19 pandemic when graduate students were not allowed to work in the lab. I also express my thank to my colleague, Liyu Liu, for collaborating on the triangular-lattice Mott insulators and for inviting me to join fun activities. I appreciate his work on setting up the RF antenna, which allowed us to access the other spin mixtures. Additionally, I would like to thank Jae Woo Kim, who set up the MOT laser during my first year when I was busy with coursework.

I wish to express my deep appreciation to the Development and Promotion of Science and Technology Talents Project (DPST) from the Royal Thai Government for their financial support during my pursuit of a Ph.D. degree at the University of Virginia.

I am also thankful to Assist. Prof. Jirakan Nunkaew and Assist. Prof. Narupon Chattrapiban, who were my advisors in Thailand, for their support and suggestions.

I would like to thank the Thai community in Charlottesville for treating me to Thai food and making the US feel like home. A special thanks to Pimonwan Kamjan, who always invited me for great dinners. Additionally, I thank Khomphop Pramoonjago

for providing me with the best Pad Thai in Charlottesville and for sharing his experiences in life and work.

Many thanks to James Owen Whitlow and Shawn Lloyd Ritchie, who offered me fun activities and explorations in the US. This experience is awesome and will never be forgotten.

I would like to express my thanks to Narenrit Thananusak and Pitchayapak Kitisri for their feedback and support during the writing of my dissertation. Additionally, I am deeply grateful to my close friend, Sutida Arinjae, for her unwavering support and understanding throughout my Ph.D. journey.

I acknowledge the ComponentLibrary for drawing diagrams related to laser optics, including many optics but also electronic components. I express my thanks to Inkscape for graphic design, Latex for seamless typesetting especially for Pgfplots for high-quality plots, and Eagle for electronic design and generation of schematic drawings. I appreciate the assistance of ChatGPT developed by OpenAI in enhancing the clarity and appeal of my written content.

Last but not least, I extend my heartfelt gratitude to my family – my parents, my brothers, and my sisters – for supporting me spiritually throughout my research and my life in general. Their kindness propels me forward and serves as a constant reminder not to give up.

This dissertation is dedicated to my parents,
Anunt and Srisaad Mongkolkiattichai.

Contents

Abstract ii

Acknowledgements iv

1 Introduction **1**

1.1 Phase transitions and strongly correlated systems 4

1.2 Complexity of many-body calculations and quantum simulators 6

1.3 Frustrated systems 8

2 Single-Atom-Resolved Imaging **11**

2.1 From tight-binding to Fermi-Hubbard model 11

2.2 Image analysis 15

2.2.1 Detecting isolated atoms 17

2.2.2 Lattice angles and constants 17

2.2.3 Reconstruction 21

3 Triangular-Lattice Quantum Microscope Setup **22**

3.1 ^{6}Li spectroscopy 23

3.2 Zeeman slower 25

3.3 Magneto-optical trap 26

3.4 Low field and high field imaging 31

3.5 Raman sideband cooling 35

3.6 Optical dipole trap . . . 40
3.6.1 RF state preparation in ground state manifold . . . 45
3.6.2 Radio frequency sweep . . . 46
3.7 Light sheet . . . 47
3.8 Bottom beam . . . 49
3.9 Accordion lattice . . . 50
3.9.1 Frequency doubling . . . 52
3.9.2 Accordion lattice setup . . . 53
3.10 Triangular lattice . . . 58
3.10.1 Depth calibration of 1d optical lattices . . . 61
3.10.2 Depth calibration of 2d optical lattices . . . 63
3.11 Square lattice . . . 65

4 The Triangular-Lattice Fermi-Hubbard Model 69
4.1 Band structure . . . 70
4.1.1 Band structure in 1d . . . 70
4.1.2 Band structure in 2d . . . 73
4.2 Wannier functions . . . 81
4.2.1 Maximally localized states . . . 82
4.2.2 Eigenstates of the projection operator . . . 83
4.2.3 Tunneling parameter . . . 87
4.3 Fermi-Hubbard model . . . 89
4.3.1 Hubbard tunneling calibrations . . . 91
4.3.2 Hubbard interaction calibrations . . . 93
4.4 Mott insulator . . . 97
4.5 Non-interacting Fermi gas . . . 98
4.6 Observables in the quantum gas microscope . . . 100
4.6.1 Density . . . 101
4.6.2 Spin removal . . . 104
4.6.3 Doublon hiding . . . 104

4.6.4 Correlations . . . 106

5 Quantum Gas Microscopy of Fermionic Triangular-Lattice Mott Insulators 109

5.1 Introduction . . . 109
5.2 Experimental setup . . . 112
5.3 Triangular-lattice Mott insulators . . . 113
5.4 Spin-spin correlations . . . 114
5.5 Thermometry . . . 116
5.6 Conclusion and outlook . . . 118

6 Implementation of Spin-Resolved Imaging 121

7 Quantum Gas Microscopy of Three-Component Fermi-Hubbard Systems 130

7.1 Fermi-Hubbard model . . . 133
7.2 High-temperature series expansion . . . 136
7.3 Experimental setup . . . 137
7.4 Three-component Mott insulators . . . 139
7.5 Competition between pairwise components . . . 142
7.6 Conclusion and outlook . . . 147

8 Conclusion and Outlook 149

A Electronics 152

A.1 Acousto-optic modulator . . . 152
A.2 Electro-optic modulator . . . 155
A.3 Intensity stabilization . . . 156
A.4 Two-step voltage controller oscillator . . . 157
A.5 H-bridge driver . . . 157
A.6 Rotational waveplate . . . 160

B Existing Apparatus **161**

B.1 Vacuum chamber setup . . . 161
B.2 Control system . . . 166
B.3 Sequences . . . 170
B.4 Water-cooling system . . . 173
B.5 Power supplies . . . 177
B.6 Magnetic coils . . . 178
B.7 Cameras . . . 183

C Cold Atoms **185**

C.1 Dipole traps formed by Gaussian beams . . . 185
C.2 Fluorescence imaging . . . 186
C.3 Absorption imaging . . . 187
C.4 Time of flight . . . 188
C.5 Degenerate Fermi gases . . . 189
C.6 Feshbach resonances . . . 192
C.7 Kapitza-Dirac scattering . . . 194
C.8 Hyperfine Zeeman splitting . . . 195
C.9 Light shift . . . 197

D ^{6}Li Atomic Properties **200**

E Timeline of the Experiment **202**

Bibliography **222**

List of Figures

1.1 Evaporative cooling 2
1.2 Maxwell-Boltzmann distribution 4

2.1 The origin of energy bands in the tight-binding model 12
2.2 Models in triangular lattices 14
2.3 Site-resolved imaging 16
2.4 Image analysis. 18
2.5 Lattice angles and lattice constants 20

3.1 ^{6}Li spectroscopy 24
3.2 Hybrid Zeeman slower and its magnetic field configuration 27
3.3 Magneto-optical trap 28
3.4 Schematic of MOT laser setup 30
3.5 Schematic of MOT on the experimental table 32
3.6 Schematic of imaging laser 33
3.7 Spin population 34
3.8 Schematic of Raman laser systems 36
3.9 Raman beams configuration and Raman cooling process 38
3.10 Imaging fidelity 40
3.11 Schematic of the 1070 nm laser setup 42
3.12 Dipole force and crossed dipole trap 43
3.13 ODT trap frequency and Fermi gas 44
3.14 Radio frequency transfer 45

3.15 Light sheet schematic and amplitude modulation spectroscopy 48
3.16 Bottom beam spectroscopy 50
3.17 Crossing beams 51
3.18 Frequency doubling 54
3.19 Accordion lattice setup 55
3.20 Fermi gas in light sheet and accordion lattice 56
3.21 Schematic of lattice setup 59
3.22 Triangular lattice and Raman imaging beam 60
3.23 mBECs time of flight 62
3.24 1d Kapitza-Dirac scattering 63
3.25 2d Kapitza-Dirac scattering 65
3.26 Comparison to square lattices 67

4.1 Band structures and Bloch functions of a 1d lattice 73
4.2 Triangular-lattice band structure 81
4.3 Wannier functions for the lowest band of a 1d lattice 86
4.4 Wannier functions of 2d optical lattices. 87
4.5 Triangular-lattice Hubbard parameters as a function of lattice depth . 91
4.6 Lattice depth calibration 92
4.7 Band excitation spectroscopy 94
4.8 Doublon modulation spectroscopy 95
4.9 Singlon and doublon transfer 96
4.10 Mott insulators in square lattices 99
4.11 Azimuthal average of fermionic non-interacting gases 100
4.12 DQMC calculation for full density and singles density in the triangular Hubbard model 103
4.13 Atom number as a function of resonant light pulse time 105
4.14 Doublon hiding 106
4.15 Calculated spin-spin correlation in the triangular lattice 108

5.1 Triangular-lattice quantum gas microscope 111

5.2 Triangular-lattice Mott insulators . . . 116
5.3 Spin-spin correlations . . . 117
5.4 Thermometry and interaction dependence of spin-spin correlations . . . 119

6.1 Bilayer imaging using two light sheets . . . 123
6.2 Zero field measurement and oscillation of state $|3\rangle$ . . . 124
6.3 Count histogram and reconstruction of spin-resolved imaging . . . 125
6.4 Full density-resolved imaging . . . 126
6.5 Stern-Gerlach separation fidelity . . . 127
6.6 Spin-spin correlations . . . 129

7.1 Quantum gas microscopy of three-component Fermi gases . . . 132
7.2 Band excitation of a square lattice . . . 134
7.3 Hubbard interaction calibration . . . 135
7.4 Rabi oscillation of the three lowest hyperfine states . . . 138
7.5 Atom number histogram . . . 139
7.6 Three-component Mott insulators . . . 141
7.7 Flavor-selective pairing . . . 143
7.8 Attractive pairing . . . 145
7.9 Phase diagram of a three-component Fermi mixture . . . 146

A.1 Lower-power AOM driver setup . . . 154
A.2 Schematic of EOM . . . 156
A.3 Feedback diagrom of intensity stabilization . . . 156
A.4 Two-step VCO . . . 158
A.5 H-bridge driver . . . 159
A.6 Rotational waveplate with Arduino . . . 160

B.1 Vacuum chamber . . . 163
B.2 Lithium . . . 164
B.3 Baking of the vacuum system . . . 165
B.4 Experiment software . . . 169

B.5 MOT to ODT sequence . . . 170
B.6 Sequence to prepare Fermi gases . . . 171
B.7 Spin-resolved imaging sequence . . . 172
B.8 Water-cooling system . . . 174
B.9 Ambient temperature for experiments . . . 175
B.10 Interlock system . . . 176
B.11 Connections of coils . . . 178
B.12 Coils winding . . . 179
B.13 Zeeman slower coils . . . 180
B.14 MOT coils . . . 181
B.15 Feshbach coils . . . 182
B.16 Magnetic offset coils . . . 183
B.17 Magnetic field of offset coils . . . 184

C.1 Time of flight measurement . . . 189
C.2 Zeeman shifts of the two lowest hyperfine states . . . 197

D.1 Scattering length of the three lowest hyperfine states of ^{6}Li . . . 200

List of Tables

3.1 Degenerate Fermi gas of one spin component in different stages 57

B.1 Baking temperatures 166
B.2 Analog output channels of ADWIN system 167
B.3 Digital output channels of ADWIN system 168
B.4 Temperature and pressure for the water-cooling system 173
B.5 Typical operating temperatures of experimental components 176
B.6 Power supplies for coils 177
B.7 Cameras used in the experiment 184

D.1 Fundamental physical properties of ^{6}Li 201

Chapter 1

Introduction

More than a hundred years ago, we believed that every process that occurred in the universe could be understood by classical physics. Several phenomena, such as Stern-Gerlach experiment [1], photoelectric effect [2, 3], and neutrino oscillations [4], were found to contradict established theories. At the beginning of the twentieth century, the discovery and development of the theory of relativity and quantum mechanics opened a new era. Many phenomena have been predicted and confirmed experimentally with incredible precision. Groundbreaking discoveries in past years demonstrate the advances in our understanding of fundamental physics in nature like the Noble Prize awarded in 2022 for the violation of Bell inequalities, confirming the principles of quantum entanglement [5–7]. Another example is the Noble Prize awarded in 2023 for the development of new tools for exploring the world of electrons inside atoms and molecules using extremely short pulses of light [8–10].

The developments of laser cooling, atom trapping, and evaporation techniques give experimental access to novel fundamental phenomena in nature. For example, the achievement of Bose-Einstein condensates (BECs) in 1995 [11–13] demonstrated the capability of controlling the motional and internal state at the ultimate level. This condensation is a quantum phase transition driven by indistinguishability and the wave nature of particles. For fermions, the situation is completely different because

the quantum nature of this particle never allows them to share identical quantum numbers and the lack of thermalization of identical fermions prevents colder temperatures. We note that identical fermions do not thermalize at low temperatures because $s-$wave collisions are not allowed, and $p-$wave collisions are suppressed at those temperatures. However, evaporative cooling works in two-component Fermi gases, thus a degenerate Fermi gas can be obtained [14]. In the following, I discuss the concept of evaporative cooling using a simple model following ref. [15].

When atoms are confined in an optical dipole potential, discussed in later Chapter 3, they remain relatively hot, resulting in quantum fluctuations being negligible compared to thermal effects. The quantum regime is typically reached at lower temperatures, approaching the Fermi temperature scale, which represents the kinetic energy of fermionic particles at the Fermi level in a system. More details can be found in Appendix C.5. Achieving this temperature range typically requires the application of evaporative cooling. This method capitalizes on the fact that the system is hot primarily because most atoms possess higher kinetic energy compared to the system's average thermal energy. After removing the hot atoms, the system rethermalizes and the temperature reduces as illustrated in Fig. 1.1.

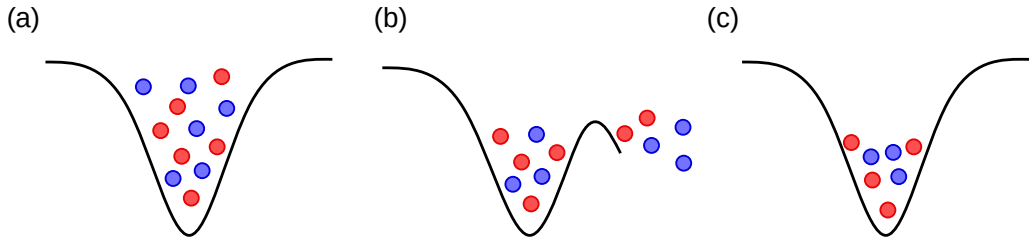

Figure 1.1: **Evaporative cooling.** (a) Initial trapped atoms. (b) Non-thermal state during evaporation. The hotter atoms are eliminated by lowering the potential in the presence of a magnetic field gradient. (c) New thermalized state. Interactions between atoms lead to rethermalization with a lower final temperature and atom number.

For a more quantitative perspective, let us assume an initial atom number and temperature of N_0 and T_0. In thermal equilibrium, non-interacting particles are

described by the Maxwell-Boltzmann distribution, which is valid for high temperatures. The number of atoms within an infinitesimal element of energy $d\epsilon$ centered on an energy ϵ is given by

$$f(\epsilon, T_0)\ d\epsilon = \frac{2N_0}{\sqrt{2(k_B T_0)^3}} \sqrt{\epsilon} e^{-\epsilon/(k_B T_0)}\ d\epsilon. \tag{1.1}$$

By removing the hot atoms with the energy greater than the cut-off energy ϵ_c, the system has remaining atoms

$$N_0' = \int_0^{\epsilon_c} f(\epsilon, T_0)\ d\epsilon. \tag{1.2}$$

Note that one can eliminate the hot atoms by lowering the trap potential in the presence of a magnetic gradient. This results in the hot atoms flying out of the trap. The remaining atoms are then in a non-equilibrium state and the system will take time to reach a new equilibrium. To expedite the rethermalization process, one can tune the interaction between atoms via Feshbach resonances. When the atoms reach equilibrium at a temperature of T_1, the total atom number remains unchanged but follows a new distribution $f(\epsilon, T_1)$ that satisfies

$$\begin{aligned} N_1 &= \int_0^{\infty} f(\epsilon, T_1)\ d\epsilon \\ &= N_0 \left[\mathrm{erf}\left(\sqrt{\frac{T_c}{T_0}} \right) - \frac{2}{\sqrt{\pi}} \sqrt{\frac{T_c}{T_0}} e^{-T_c/T_0} \right]. \end{aligned} \tag{1.3}$$

Using the fact that atom numbers before and after rethermalization are equal, leading to [15]

$$T_1 = \frac{T_0}{3} \left\{ \frac{3\sqrt{\pi}\,\mathrm{erf}\left(\sqrt{T_c/T_0}\right) - \left[6\sqrt{T_c/T_0} + 4\left(T_c/T_0\right)^{3/2}\right] e^{-T_c/T_0}}{\sqrt{\pi}\,\mathrm{erf}\left(\sqrt{T_c/T_0}\right) - 2\sqrt{T_c/T_0} e^{-T_c/T_0}} \right\}, \tag{1.4}$$

where the cut-off temperature is defined as $T_c \equiv \epsilon_c / k_B$ and erf(x) is the error function, defined by

$$\mathrm{erf}(x) = \frac{2}{\sqrt{\pi}} \int_0^x e^{-y^2}\ dy. \tag{1.5}$$

According to Eqs. 1.3 and 1.4, both expressions are consistent with the expectation that lowering the cut-off energy (removing more hot atoms) leads to a colder system

while only a few atoms remain in the system (Fig. 1.2). In practice, we perform multiple evaporative cooling steps rather than a single step because heating can occur during the transition between potentials. In addition, maximizing the atom number at lower temperatures is challenging, and multiple steps help achieve this goal. The details of multiple evaporation cooling steps can be found in Section 3.6. While this model provides a fundamental understanding of evaporative cooling, it has limitations, particularly in the transition from the classical regime to the quantum regime. In the quantum regime, the assumptions of the Boltzmann distribution no longer apply, and the statistics of Fermi-Dirac and Bose-Einstein must be considered. Despite these limitations, the model offers valuable insights into the principles of evaporative cooling.

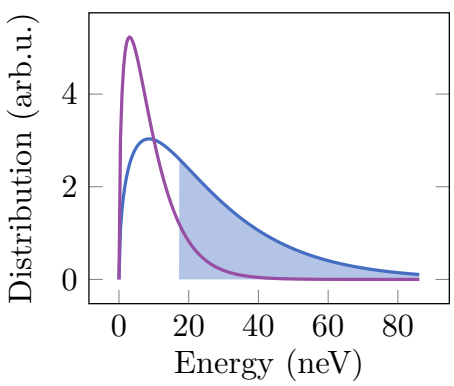

Figure 1.2: **Maxwell-Boltzmann distribution.** Trapped atoms have an average temperature of 200 µK (blue solid line). By performing evaporation, hot atoms with temperatures greater than T_c =200 µK escape (blue shading). Rethermalized atoms have an average temperature of 70 µK (violet solid line).

1.1 Phase transitions and strongly correlated systems

In classical physics, phase transitions occur at macroscopic scales and are governed by thermal fluctuations. These transitions occur at specific temperatures and are characterized by abrupt changes in the system's properties. The most common classical phase transitions are solid-to-liquid (melting), liquid-to-gas (evaporation), and liquid-to-solid (freezing) transitions. These classical phase transitions are well-described by classical statistical mechanics and do not involve quantum effects.

Unlike quantum phase transitions, which occur at zero temperature, these transitions pose challenges to experiments and are driven by quantum statistics. They arise from the competition between different quantum ground states and excited states of a system as a physical parameter is varied. Examples of quantum phase transitions include magnetic phases [16], superconducting-insulating phases [17], and superfluid-Mott insulator transitions [18].

The development of optical lattices provides a way to study strongly correlated systems. The first proposal realized in Hubbard systems in optical lattices [19] and later the experimental realization of Bose-Hubbard systems showed new possibilities of exploring many-body systems using ultracold atoms [18, 20]. Further reviews on this topic can be found in [21–23].

Meanwhile, fermions in optical lattices have been proposed to address questions regarding the Fermi-Hubbard model, which is expected to describe the origin of high-temperature superconductivity in cuprates [24]. A few years later, researchers achieved the first realization of Fermi-Hubbard systems in a square lattice using ultracold atoms, detected by absorption imaging [25, 26]. This milestone followed the discovery in 1986 of the first high-temperature superconductor in cuprates (LaBaCuO) with a transition temperature exceeding 30 K [27]. Several studies in condensed matter physics have focused on cuprates and observed antiferromagnetic Mott insulators at filling of one electron per unit cell [28, 29]. It is even more interesting in the regime of hole doping that exhibits d-wave superconductivity with short coherence length [30]. While the Fermi-Hubbard model can be analytically solved in one dimension (1d) [31], it remains challenging to handle higher-dimensional systems [32–34].

1.2 Complexity of many-body calculations and quantum simulators

Classical calculations are impractical for quantum systems due to fundamental differences in concepts between classical and quantum systems. The exponential growth of complexity, along with phenomena such as superposition and entanglement, poses challenges for many-body quantum systems. Present computers can diagonalize matrices of sizes up to $2^{40} \times 2^{40}$, allowing them to solve quantum systems with up to 40 spins exactly. With two possible configurations per spin, a chain of 40 spins has 2^{40} classical configurations, which leads to a basis size of 2^{40}. I note that while it might seem more straightforward to describe each spin with two complex numbers, the actual basis size required to describe the quantum system accurately through the classical representation is determined by the number of independent states. Adding just one more spin to the system necessitates a computer twice as powerful. Besides, when the system contained 300 spins, it would never be accessible because the number of matrix elements is approximately equal to the total number of protons in the universe (approximately 10^{80}). To address the limitations of classical computers, Richard P. Feynman proposed a solution in his seminal work [35, 36]. He famously stated,

> "Nature isn't classical, dammit, and if you want to make a simulation of nature, you'd better make it quantum mechanical, and by golly, it's a wonderful problem, because it doesn't look so easy."

This statement has inspired many researchers to gain insights into real quantum systems, particularly quantum materials, which are often challenging to access directly. Instead, researchers study well-controlled quantum systems to gain a deeper understanding of the complicated systems.

The quantum regime is reached when the de Broglie wavelength is either equivalent to or greater than the interparticle spacing. This is achieved by lowering the temperature of atoms in the trap. Ultracold gas in optical lattices offers a robust system

compared to crystalline materials. By cooling the system to a few nanokelvins, we maintain a similar ratio of the de Broglie wavelength to interparticle spacing. This allows us to observe similar phenomena in both real and artificial systems. Interacting systems of ultracold atoms extend models of condensed matter physics with complete control over microscopic parameters such as tunneling and interaction energy. The coherent nature and narrow linewidth of lasers enable the formation of optical lattices through the interference of laser beams. This results in optical potentials that are exceptionally clean and free from impurities. The observable timescale can be adjusted based on the natural properties of atoms while large interparticle spacing makes optical imaging possible. In addition, the capability of controlling interactions between atoms via Feshbach resonances offers new ways for studying condensed matter theory using ultracold-atom systems [37, 38]. Here, our study relies on ^{6}Li atoms which are fermions and are well-suited for many-body physics. The reasons are as follows: ^{6}Li atoms have light mass compared to other atoms typically studied (e.g., rubidium, potassium), resulting in rapid thermalization and dynamics. The atomic interaction of ^{6}Li can be tuned by a magnetic field owing to the Feshbach resonances. ^{6}Li atoms can form molecules, leading to the formation of molecular Bose-Einstein condensates (mBECs). In addition, the use of ^{6}Li atoms allows for more precise control and tunability in experiments. For the past few years, researchers have demonstrated the utility of both bosonic quantum gas microscopy [39–43] and fermionic quantum gas microscopy [44–49] in studying Hubbard models on optical lattices. Prominent examples of quantum simulation with ultracold atoms include the detection of antiferromagnetic correlations [49–56], the observation of many-body localization [57], and the detection of a triangular-lattice Mott insulator [58]. In the following, the dissertation's main focus on frustrated systems is introduced. There are only very few clean realizations of frustrated systems in condensed matter, and ultracold atoms allow for a systematic study in well-controlled systems.

1.3 Frustrated systems

A frustrated system exhibits a ground state with degeneracy, resulting in strong quantum fluctuations. This can lead to the emergence of exotic phases of matter, such as a quantum spin liquid, where spins exhibit strong correlations and remain highly fluctuating even at absolute zero temperature [59–62]. Recent studies have proposed exotic phases, including chiral order and topological superconductors in triangular lattices [63, 64].

The first realization of frustrated lattice geometries with absorption imaging was studied in a bosonic system [65]. During my Ph.D., we have realized Fermi-Hubbard model in a frustrated system and imaged the system using quantum gas microscopy. The system was implemented and used to study Mott insulator [58]. The implementation of frustrated quantum gas microscopy expands our understanding of condensed matter systems, addressing questions such as the ground state of the Heisenberg model. In bipartite square lattices, the ground state is an antiferromagnetic Neel state [66] as observed in many measurements of square-lattice quantum gas microscopy, showing antiferromagnetic correlations. In contrast, frustrated triangular lattices are expected to exhibit a 120° Neel state in the strongly interacting limit [67–70]. Evidence of the 120° order is revealed by the two distinct peaks of the hexagonal Brillouin zone in the spin structure factor. It is worth noting that the competition between charge dopants and magnetism in the triangular-lattice Fermi-Hubbard model results in particle-hole asymmetry [71] unlike square lattices where particle-hole symmetry is realized at half-filling. Additionally, kinetic magnetism in triangular lattices is predicted to exhibit effective antiferromagnetic correlations in hole-doped systems and ferromagnetic correlations in electron-doped systems even at high temperatures [72–76]. Recent measurements on kinetic magnetism in triangular lattices have confirmed the validity of the Nagaoka mechanism for electron-doped systems using three-point correlators [77, 78] and magnetic properties [79, 80].

List of publications

1. **J. Mongkolkiattichai**, L. Liu, D. Garwood, J. Yang, and P. Schauss, Quantum gas microscopy of fermionic triangular-lattice Mott insulators, Phys. Rev. A **108**, L061301 (2023).

2. D. Garwood, **J. Mongkolkiattichai**, L. Liu, J. Yang, and P. Schauss, Site-resolved observables in the doped spin-imbalanced triangular Hubbard model, Phys. Rev. A **106**, 013310 (2022).

3. D. Garwood, L. Liu, **J. Mongkolkiattichai**, J. Yang, and P. Schauss, A hybrid Zeeman slower for lithium, Rev. Sci. Instrum. **93**, 033202 (2022).

4. J. Yang, L. Liu, **J. Mongkolkiattichai**, and P. Schauss, Site-resolved imaging of ultracold fermions in a triangular-lattice quantum gas microscope, PRX Quantum **2**, 020344 (2021).

Outline

The outline of this dissertation is as follows: In Chapter 2, I present the single-atom resolved images in optical lattices that have revolutionized the study of ultracold-atom systems. I discuss the origin of Mott insulators and band insulators underlying harmonic confinement. Next, I describe algorithms used for detecting single atoms, lattice geometries, and reconstructing atoms to binary matrices.

In Chapter 3, I introduce the experimental setup, including laser locking to atomic transitions by spectroscopy, the operation of a Zeeman slower for atom deceleration, and atom trapping using a magneto-optical trap (MOT). I describe cooling processes in an optical dipole trap to achieve a degenerate Fermi gas and multiple steps before studying Hubbard physics. Next, I explain how we form optical lattices, the

techniques used to calibrate the lattice depth, and the implementation of single-site resolution via the Raman sideband cooling.

In Chapter 4, I provide a simple overview of the theoretical framework for the Fermi-Hubbard model with ultracold atoms in optical lattices, including key observables measured in experiments. I discuss the extreme cases of the model, such as the Mott insulator and non-interacting gas. Next, I indicate common observable quantities used for determining system properties.

In Chapter 5, I present the study of fermionic Mott insulators in a geometrically frustrated symmetric triangular lattice using a quantum gas microscope with single-site resolution. I demonstrate the detection of antiferromagnetic spin-spin correlations and discuss thermometry by comparison to numerical calculations. This discussion is based on our publication [58].

In Chapter 6, I describe the setup for spin-resolved imaging using a double light sheet approach, enhancing the capabilities of quantum gas microscopy. I demonstrate the thermometry based on correlations and the density fluctuation-dissipation theorem.

In Chapter 7, I apply spin-resolved imaging to investigate a three-component Fermi-Hubbard model in a square lattice. I discuss observable quantities such as doublon density and pairing correlation, using a simple model based on high-temperature series expansion in the atomic limit. The unique behavior of three-component fermions is highlighted, particularly in the regime where interactions exhibit both repulsive and attractive features simultaneously, a characteristic attributed to the Feshbach resonances.

In Chapter 8, I summarize the main points discussed in this dissertation and I provide future directions that our quantum gas microscope can offer insights into many-body systems beyond the Hubbard model.

Chapter 2

Single-Atom-Resolved Imaging

The development of detection techniques for individual atoms in optical lattices, so-called single-atom-resolved imaging, has expanded the understanding of ultracold atom systems. This imaging provides fruitful information at an unprecedented level. By taking snapshots of atoms confined in optical lattices, we can access atom occupation at individual lattice sites and observable quantities like correlation functions which give access to the quantum nature of the many-body state and serve as thermometers. The main purpose of this chapter is to introduce the Fermi-Hubbard model and the algorithms used for detecting single atoms and reconstructing them to obtain digitized occupation matrices.

2.1 From tight-binding to Fermi-Hubbard model

In condensed matter systems, the behavior of electrons in a crystalline solid can be described by the tight-binding model. This model assumes that electrons are tightly bound to individual atoms and can interact with neighboring atoms. The electrons are allowed to move between atoms due to a finite overlap between their wavefunctions, a phenomenon known as quantum tunneling. When considering a system of many particles, the energy levels of individual electrons merge, leading to the formation of energy bands (Fig. 2.1). In the following, the tight-binding model

for a triangular lattice is discussed.

For a two-dimensional (2d) triangular lattice with nearest-neighbor tunnelings t_1, t_2, and t_3 as shown in Fig. 2.2(a). The Hamiltonian of the lowest band is given by

$$H = -\sum_{\mathbf{R}} t_1 |\mathbf{R}\rangle \langle \mathbf{R} + \mathbf{a}_1| + t_2 |\mathbf{R}\rangle \langle \mathbf{R} + \mathbf{a}_2| + t_3 |\mathbf{R}\rangle \langle \mathbf{R} + \mathbf{a}_3| + \text{h.c.}, \tag{2.1}$$

where $|\mathbf{R}\rangle$ represents a localized state at lattice site $\mathbf{R}$ and $\mathbf{a}_i$ are the nearest neighbor lattice vectors i.e., $\mathbf{a}_1 = (1, 0)$, $\mathbf{a}_2 = (1/2, \sqrt{3}/2)$, and $\mathbf{a}_3 = \mathbf{a}_1 - \mathbf{a}_2$.

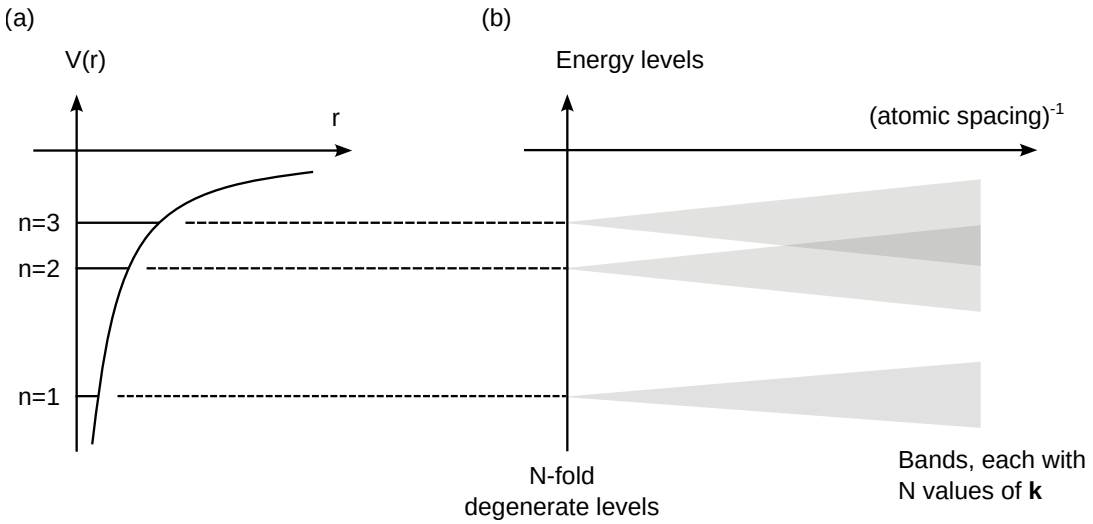

Figure 2.1: **The origin of energy bands in the tight-binding model.** (a) Non-degenerate electronic levels in atomic potential. (b) The energy level for N atoms in a periodic lattice. When the atomic spacing is much larger, energy levels are treated as non-degenerate electronic levels. With smaller atomic spacing, the overlap of electron wavefunctions becomes more pronounced and the levels broaden into bands. When bands begin to overlap, it becomes crucial to consider hybridization, which involves coherent mixing [81]. However, for our application, we are primarily interested in the ground band. As long as the ground band does not overlap with other bands, the tight-binding model remains applicable. Figure was reproduced from [82].

By applying a Fourier series expansion in plane waves with wavevectors, $\mathbf{k}$, in the direct lattice, expressed as

$$|\mathbf{R}\rangle = \frac{1}{\sqrt{N}} \sum_{\mathbf{k}} e^{i\mathbf{k}\cdot\mathbf{R}} |\mathbf{k}\rangle , \tag{2.2}$$

the Hamiltonian in the reciprocal lattice space is given by

$$H(\mathbf{k}) = \sum_{\mathbf{k}} \epsilon(\mathbf{k}) |\mathbf{k}\rangle \langle\mathbf{k}| , \tag{2.3}$$

where

$$\epsilon(\mathbf{k}) = -2 \left[t_1 \cos(\mathbf{k}\cdot\mathbf{a}_1) + t_2 \cos(\mathbf{k}\cdot\mathbf{a}_2) + t_3 \cos(\mathbf{k}\cdot(\mathbf{a}_1 - \mathbf{a}_2)) \right] , \tag{2.4}$$

and N is the number of unit cells [81]. The expression above simplifies to

$$\begin{aligned} \epsilon_{\mathbf{k}} &= \epsilon(k_x, k_y) \\ &= -2 \left[t_1 \cos(k_x) + t_2 \cos\Big(k_x/2 + \sqrt{3}k_y/2\Big) + t_3 \cos\Big(k_x/2 - \sqrt{3}k_y/2\Big) \right] . \end{aligned} \tag{2.5}$$

The band structure can be obtained through numerical calculations as discussed in detail in Chapter 4. It is worth noting that the analytic expression in Eq. 2.5 allows us to extract tunneling parameters from the known band structure, providing a precise determination of the tunneling strength in the experiment.

The tight-binding model serves as the starting point for understanding the electronic structure of solids. This model provides a foundation for more complex models such as the Fermi-Hubbard model, where the interaction term is introduced in addition to hopping. The formalism of the model will be discussed in Section. 4.3. In the Fermi-Hubbard model, the interplay between the two quantities provides insight into strongly correlated systems. Example phenomena include magnetism and superconductivity. The Fermi-Hubbard Hamiltonian in the lowest band is given by

$$\mathcal{H} = -t \sum_{\langle \mathbf{r},\mathbf{r}'\rangle,\sigma} \left(c^{\dagger}_{\mathbf{r},\sigma} c_{\mathbf{r}',\sigma} + \text{h.c.} \right) + U \sum_{\mathbf{r}} n_{\mathbf{r},\uparrow} n_{\mathbf{r},\downarrow}, \tag{2.6}$$

where $c^{\dagger}_{\mathbf{r},\sigma}, c_{\mathbf{r},\sigma}$ are the creation and annihilation operators. $n_{\mathbf{r},\sigma}$ is the number operators for spin σ. The first term describes the hopping of fermions from one site to neighboring sites with a strength of t. This term represents the kinetic energy

of the system where particles tend to delocalize over the system. The second term is the on-site interaction U, which favors localization for $U > 0$ and pairing for $U < 0$. This is because two fermions with the same spin are not allowed to stay in the same quantum state, as depicted in Fig. 2.2(b), due to the Pauli exclusion principle. However, if two atoms prefer to occupy the same lattice, an energy cost, referred to as an interaction energy, is required, and the spin states are different.

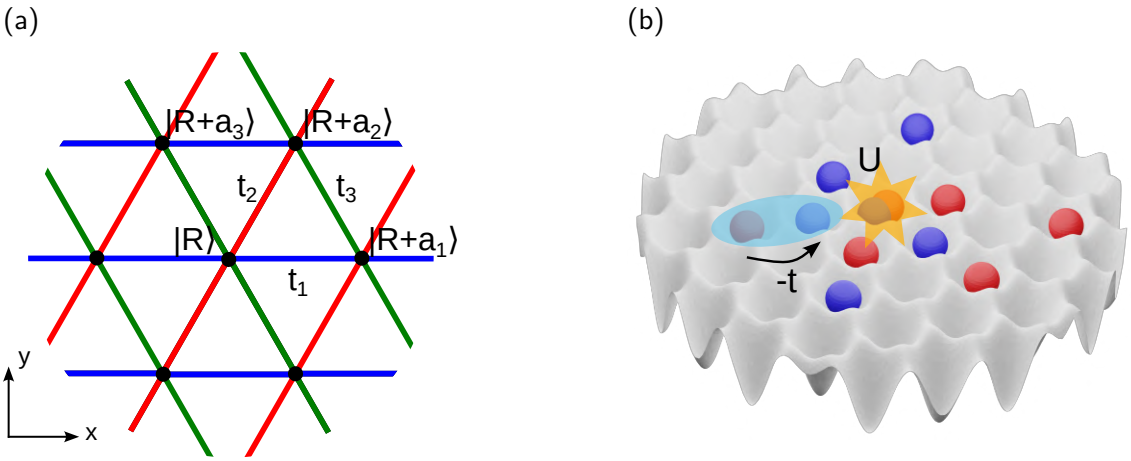

Figure 2.2: **Models in triangular lattices.** (a) Tight-binding model. Nearest-neighbor tunnelings are represented by blue, red, and green lines with strengths of t_1, t_2, and t_3. (b) Fermi-Hubbard model. Fermions can hop between neighboring lattices. When two fermions occupy the same site, there is an associated cost due to their interactions. Blue and red dots represent spin-up and spin-down atoms.

By considering atoms in the lowest band of the Fermi-Hubbard model, there are three possibilities for the site occupation within the system: empty sites (holes), singly-occupied sites (singles or singlons), and doubly-occupied sites (doubles or doublons). In the presence of interaction, the lowest band can be viewed as two sub-bands separated by interaction energy, and the optical lattice is curved by potential confinement from the Gaussian envelope of a laser beam (Figs. 2.3(a,b)). When the interaction is weak ($U/t \ll 1$) the two sub-bands almost overlap, leading to the delocalization of holes, singles, and doublons among the trap. Conversely, in

the case of strong interaction ($U/t \gg 1$) and a chemical potential, μ, less than $U/2$, atoms become localized and fill up the first sub-band as demonstrated in Fig. 2.3(a). This regime is referred to as the Mott insulator. As more atoms are filled into the system and with $\mu > U/2$, the second sub-band becomes occupied at the trap center first due to a lower energy offset compared to neighboring lattice sites. This phenomenon results in the formation of doublons and we refer to this regime as the band insulator (Fig. 2.3(b)). In Figs. 2.3(c-f), we show single atoms occupied in square and triangular lattices in the Mott and band insulator states. The imaging technique does not allow simple detection of doubly-occupied sites at the trap center due to light-assisted collisions [83], thus resulting in the detection of a doublon as a hole.

To verify the resolution of individual lattice sites, we measure the point spread function (PSF) averaged over a few hundred single atoms. We perform azimuthal averaging and fit the data to a Gaussian function and an Airy disk pattern, specifically $(2J_1(kr)/(kr))^2$, where J_1 is the Bessel function of the first kind of order one and k is the wavenumber of the light, (Fig. 2.4(a)). From the first minimum of an Airy fit, the resolution based on the Rayleigh criterion is extracted as 818(8) nm whereas our triangular lattice spacing of 1003 nm is larger. Therefore, we can resolve individual atoms in the triangular lattice without postprocessing.

2.2 Image analysis

After obtaining site-resolved images, we convert them into digitized occupation matrices of the lattice using a reconstruction algorithm [40]. These matrices are then used to construct observables in our measurements. There are two requirements for the reconstruction: lattice angles and lattice constants. These geometric parameters of the lattices can be extracted from individual isolated atoms in the images.

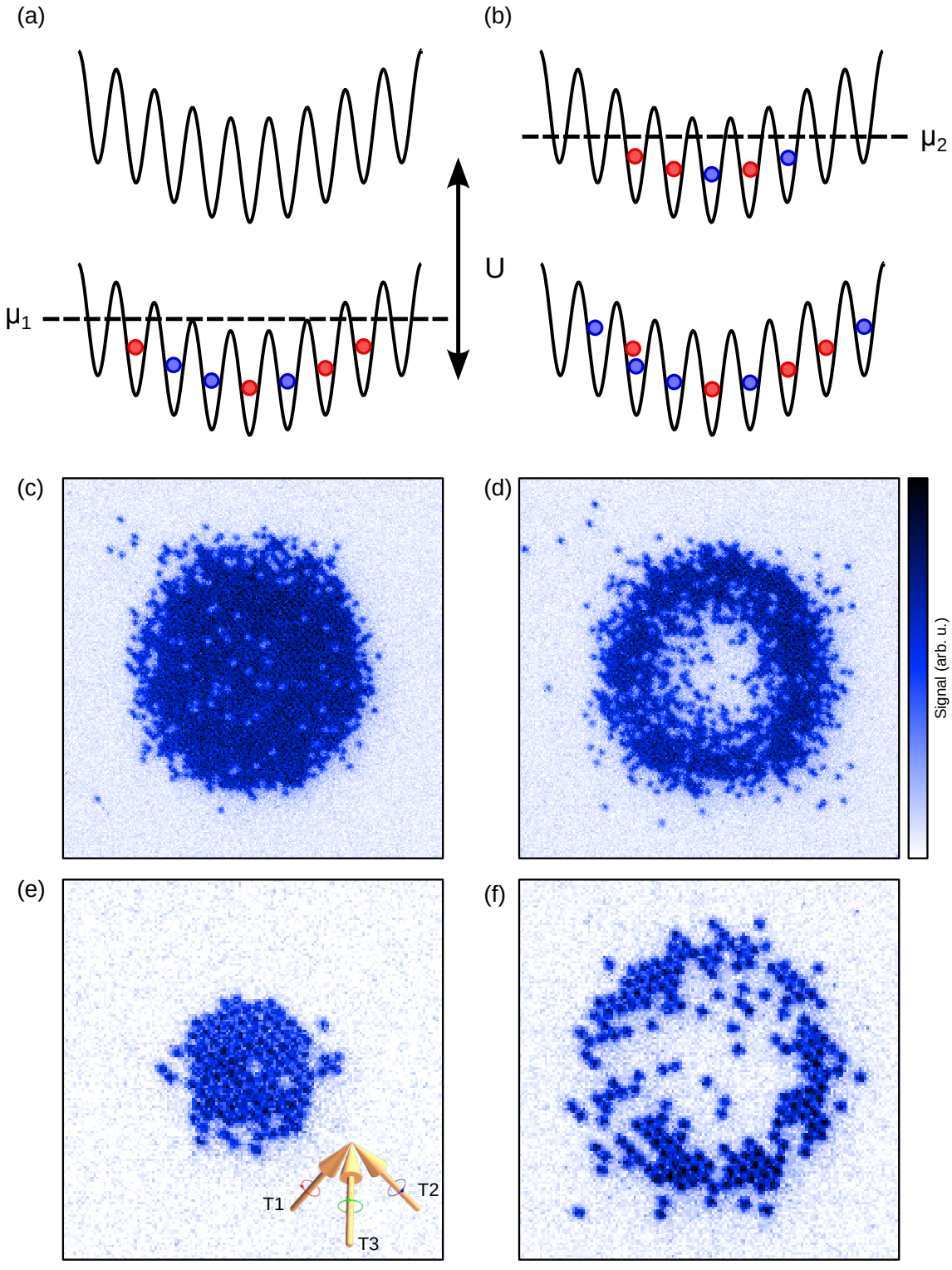

Figure 2.3: **Site-resolved imaging.** (a,b) Energy spectrum of a lattice Fermi gas underlying potential confinement. (a) Mott insulating limit where the interaction, U is much greater than the tunneling, t. Both spins (blue and red) fill the first Hubbard band up to the chemical potential, μ_1, determined by the total atom number and $\mu_1 < U/2$.

(b) In the band insulator, atoms are filled into the second Hubbard band and $\mu_2 > U/2$, leading to doubly-occupied sites at the trap center. This figure was inspired by [25]. (c) Mott and (d) band insulators on a 752 nm-square lattice consist of 1454 and 1123 atoms within a radius of 21 sites. The field of view is 60 μm$\times 60$ μm. (e) Mott and (f) band insulators on a 1003 nm-triangular lattice consist of 119 and 183 atoms within a radius of 8 and 14 sites. The field of view is 36 μm$\times 36$ μm. Images were taken from publication [58].

2.2.1 Detecting isolated atoms

Isolated atoms are essential for determining precise lattice angles and lattice constants. The atoms are detected by the following procedures. First, the image background is removed from the atom picture by estimating the mean signal from all pixels and applying a mean filter to the background-removed image. We set the cutoff to a certain value and only the signal beyond this cutoff is relevant to proceed to the next step. The filtered image is converted to a binary image using build-in function `imextendedmax` in MATLAB. Then we search for local maxima using `regionprops` which returns measurements for the set of properties (e.g., amplitude, area, and centroid position) for each object in the binary image. Here, we have candidates for isolated atoms. Next, we crop the region where the candidates are located by $w \times w$ pixels in raw images and are fitted to the Gaussian function. The candidates are accepted as isolated atoms when their amplitude, position, and waist satisfy criteria within tolerances.

2.2.2 Lattice angles and constants

Lattice angles and lattice constants define the geometry of the lattice. To obtain these parameters, we project isolated atom positions, (x_i, y_i), onto initial lattice vectors $\mathbf{b_1}$ and $\mathbf{b_2}$ using the following transformation

$$X_{ij} = x_j \cos\theta_i - y_j \sin\theta_i, \tag{2.7}$$

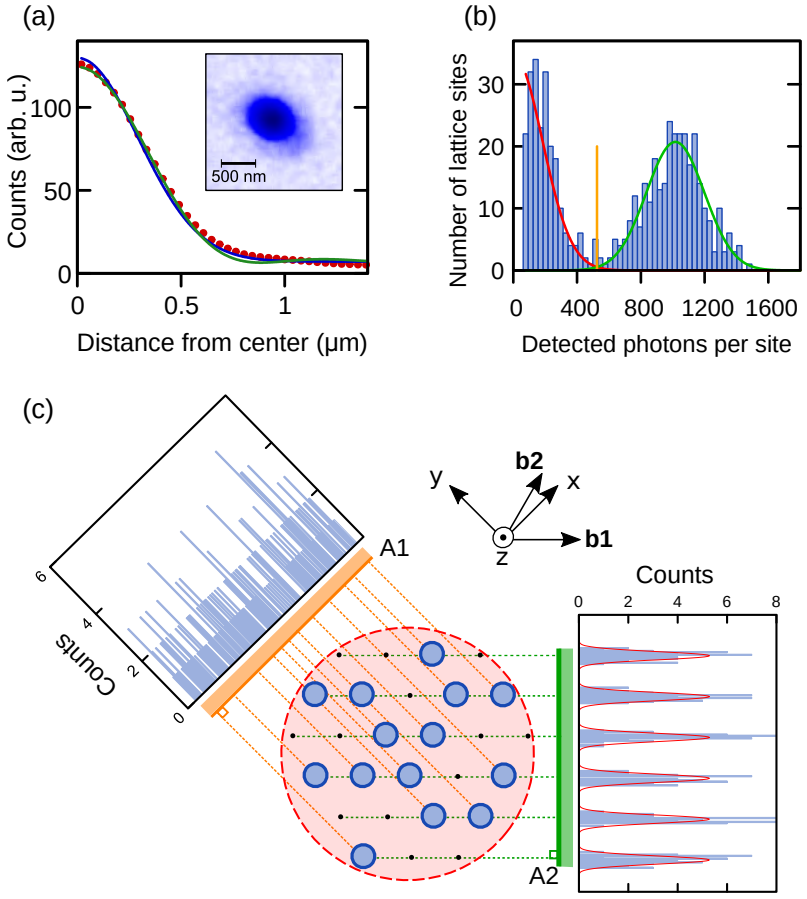

Figure 2.4: **Image analysis.** (a) Point spread function. Azimuthal average of the point spread function (red), with Gaussian fit (blue), and Airy fit (green). The measured FWHM of 720(18) nm of the PSF is consistent with the FWHM of 711 nm expected from the numerical aperture of the objective. The inset shows the PSF obtained by averaging isolated atoms. (b) Single atom count histogram. The left peak corresponds to empty sites and the right peak indicates sites occupied by single atoms. The threshold value between no atom and a single atom (vertical orange line) is determined as the intersection point of two Gaussian fits background and atom signal distribution, respectively. The reconstruction error caused by the overlap is negligible compared to the observed hopping and loss. (c) Determining lattice angles and lattice constants. Single-atom positions (exemplified in blue) are orthogonally projected onto a line of varying angle, here exemplified by A1 and A2. For each angle, a histogram of the projected positions is depicted. At the lattice angle, the experimental histogram has perfect contrast (right graph) corresponding to lattice vector b1. At other angles, for example, A2, there is almost no structure in the histograms. Figure was taken from previous work [84].

where (x_j, y_j) denotes the position of the isolated atom j^{th} in image coordinates and θ_i is the angle between lattice vector $\mathbf{b}_i$ with respect to x-axis. The angle is defined as positive in a clockwise direction.

In fact, lattice angles depend on the orientations of the lattice beams. We obtain the lattice angles by rotating the initial lattice vectors counterclockwise with a step of $\theta = 0.02$ rad and atom positions are projected onto the rotated lattice vectors. For each step, all isolated atoms are determined by their projection (X_{ij}) on $\mathbf{b}_i$ where j represents the j^{th} isolated atom. The difference of projections (e.g., $X_{ij} - X_{ik}$) is related to a relative lattice site by a constant factor determined by lattice geometry. When the rotation angle θ_i is perfectly matched to a certain value, saying (α_1, α_2), the histogram of the relative projection along $\mathbf{b}_i$ shows multiple peaks with a minimum width demonstrated in Fig. 2.4 (c). The separations between peaks $(\tilde{a}_x, \tilde{a}_y)$ are used to extract lattice constants (Fig. 2.5). Lattice constants, (a_1, a_2, a_3), and lattice angles, (β, γ), are related by the law of sine

$$\frac{a_1}{\sin(\pi - \gamma - \beta)} = \frac{a_2}{\sin\beta} = \frac{a_3}{\sin\gamma}. \tag{2.8}$$

By applying information extracted from the histogram (Fig. 2.5(b)), lattice constants are given by

$$a_1 = \frac{\tilde{a}_1}{\sin\gamma}, \tag{2.9}$$

$$a_2 = \frac{\sin\beta}{\sin\gamma} a_3, \tag{2.10}$$

$$a_3 = \frac{\tilde{a}_3}{\sin\beta}, \tag{2.11}$$

where

$$\beta = \alpha_2 - \alpha_1, \tag{2.12}$$

$$\gamma = \alpha_1 - \alpha_3 + \pi, \tag{2.13}$$

and α_i is the angle between the side a_i and y-axis.

For the triangular lattice (Figs. 2.3(e,f)), the lattice spacing is known as $a_{\text{latt}} = 2\lambda/(3\cos 45°) = 1.00(3)\,\mu\text{m}$ where the lattice laser wavelength λ is 1064 nm and the

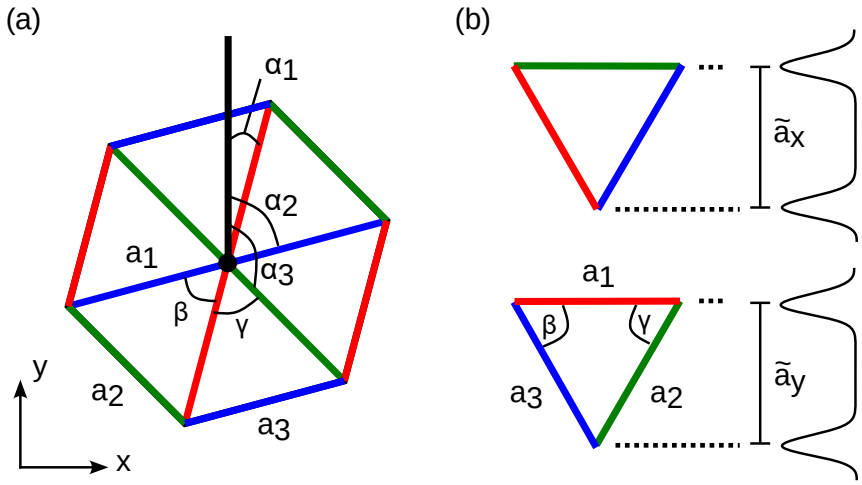

Figure 2.5: **Lattice angles and lattice constants.** (a) Determining lattice angles and lattice constants. The black solid line is the lattice vector. (b) Examples of configurations in which histograms of the projected positions have perfect contrast. Lattice constants are given by the peak separation multiplied by a factor i.e. $\tilde{a}_x = a_3 \sin(\pi - \beta - \gamma)$, $\tilde{a}_y = a_2 \sin\gamma$. The remaining side can be obtained by trigonometry.

cosine function accounts for the projection of the lattice beams onto the horizontal plane as shown in the inset of Fig. 2.3(e). The lattice spacing corresponds to about 5.10 pixels after taking into account the magnification of approximately 30 of the imaging system. The lattice angles are determined with high precision and have values of $-45.85(3)^\circ$ and $13.51(1)^\circ$. Theses angles are relative to the camera coordinates, which are registered to the xy-plane of the experiment sheared by 45° as defined in Fig. 3.11. The lattice constants in pixels are 5.09(9) and 5.10(4). Note that one of the lattice angles is the optimized angle along lattice vector $\mathbf{b_1}$ and the remaining is for the other lattice vector $\mathbf{b_2}$.

Now lattice angles and lattice constants are determined. Next, to perfectly overlap the lattice pattern with the single-atom image, lattice phases are extracted for every image. While the lattice angles only vary because of alignment changes, the phase of the lattice usually drifts due to thermal effects. To estimate the phase $\zeta_{1,2}$ in a picture, we generate the lattice structure and compare it to the position of isolated atoms, (x_j, y_j), and measure the phase difference between every single atom and the

nearest lattice site i.e.,

$$\begin{pmatrix} x_j \\ y_j \end{pmatrix} = (n + \zeta_1)\mathbf{b_1} + (m + \zeta_2)\mathbf{b_2}, \tag{2.14}$$

where $\zeta_{1,2}$ are defined within 0 and 1.

With information of the lattice angles, lattice constants, and lattice phases, the exact positions of all lattice sites in image coordinates are revealed through the reconstruction, discussed in the following.

2.2.3 Reconstruction

To obtain the occupation of each lattice site, we simultaneously fit 2d Gaussian functions to all lattice sites with a significant signal of more than about 100 detected photons per site. The resulting histogram of all Gaussian amplitudes in Fig. 2.4(b) shows a well-separated peak of a single atom signal. Owing to light-induced collisions, doubly-occupied sites are detected as empty sites. From the histogram, we obtain an optimized threshold between the signal of no atom and single atoms to decide whether a lattice site is occupied. As a result of the reconstruction, a matrix with entries zero (empty) or one (occupied) is generated. To handle the triangular lattice structure, we interpret it as a square lattice with diagonal tunneling, sheared by 30°. More details of the reconstruction algorithm can be found in [85].

Chapter 3

Triangular-Lattice Quantum Microscope Setup

Quantum gas microscopy is a powerful tool for the study of ultracold-atomic systems, offering unprecedented insights into the microscopic structure of quantum many-body systems. This technique relies on advanced laser and imaging technologies to achieve single-atom resolution. A quantum gas microscope is composed of several key components that work together. A lattice potential traps the atoms in an ordered array, while a tightly focused potential completes the three-dimensional confinement of the atoms. Additionally, the Raman sideband cooling technique is employed to cool the atoms to the ground state of the trap in the presence of spontaneous emission. This combination of components enables site-resolved imaging of ultracold-atomic systems. Achieving this imaging requires a complex experimental system, which will be discussed in detail here as follows: I explain the process of preparing cold ^{6}Li gases, starting with the deceleration of a thermal ^{6}Li atomic beam and progressing to the loading of a magneto-optical trap (MOT). I present the evaporation process in an optical dipole trap, obtaining a degenerate Fermi gas. In addition, I discuss the loading procedure for optical lattices and the methods used to calibrate the alignment. Finally, I exhibit detection schemes using absorption and single-site fluorescence imaging techniques.

3.1 ^{6}Li spectroscopy

For laser cooling of ^{6}Li, near-resonant laser beams are required and we stabilize the frequency using spectroscopy as a frequency reference, shown in Fig. 3.1(a). The laser beams are generated by a tunable laser diode (Toptica DL Pro). Note that the laser used for spectroscopy is derived from the Raman repump laser, which is discussed later in Section 3.5 and serves as a master laser. The spectroscopy is performed in a heat tube filled with ^{6}Li atoms, heated to 400°C for sublimation. Two laser beams are used as the pump beam and the probe beam. The pump beam has a high power of about 3 mW, while the counter-propagating probe beam has a weaker power of approximately 0.5 mW. Atoms absorb the probe beam less than the pump beam due to the pump beam saturating the atomic transition. This is a simple picture of how Doppler-free spectroscopy works. To address the limitations of basic Doppler-free spectroscopy, such as non-zero background and difficulty in resolving closed atomic transitions, we employ modulation transfer spectroscopy. This technique improves signal quality for laser frequency locking and benefits our applications, particularly when hyperfine transitions are closely spaced [86]. The schematic of modulation transfer spectroscopy is shown in Fig. 3.1(a).

Specifically, we apply phase modulation using an electro-optic modulator (EOM) to the pump beam which counter-propagates and overlaps with an unmodulated probe beam. The high intensity of the pump beam saturates the atomic transition, causing a fraction of the atoms to be in the excited state. As a result, the absorption of the weaker probe beam is reduced. The non-linear interaction between the pump and the probe beam occurs through the light-atom interaction by a 4-wave mixing process [87], thus leading to the pump beam transferring phase modulation to the probe beam (Fig. 3.1(b)). The probe beam is detected using a photodiode (Thorlabs PDA36A2) and the error signal is obtained by combining the detected signal with a local oscillator (RIGOL DG102), driven at 5.28 MHz, via a frequency mixer (Mini-circuits ZLW-3+). Finally, the error signal is fed to the diode laser for locking. In Fig. 3.1(c), the error signal for the D_1 transition is shown. Mod-

ulation transfer spectroscopy produces dispersive-like lineshapes that are flat and have zero background. The error signal is dominated by closed transitions, leading to zero crossings with a large peak-to-peak amplitude for each hyperfine transition. To drive the EOM, we design an LC circuit that resonantly enhances the electric field in the EOM crystal, leading to stronger phase modulation (Fig. 3.1(d)) and the working principle can be found in Appendix A.2.

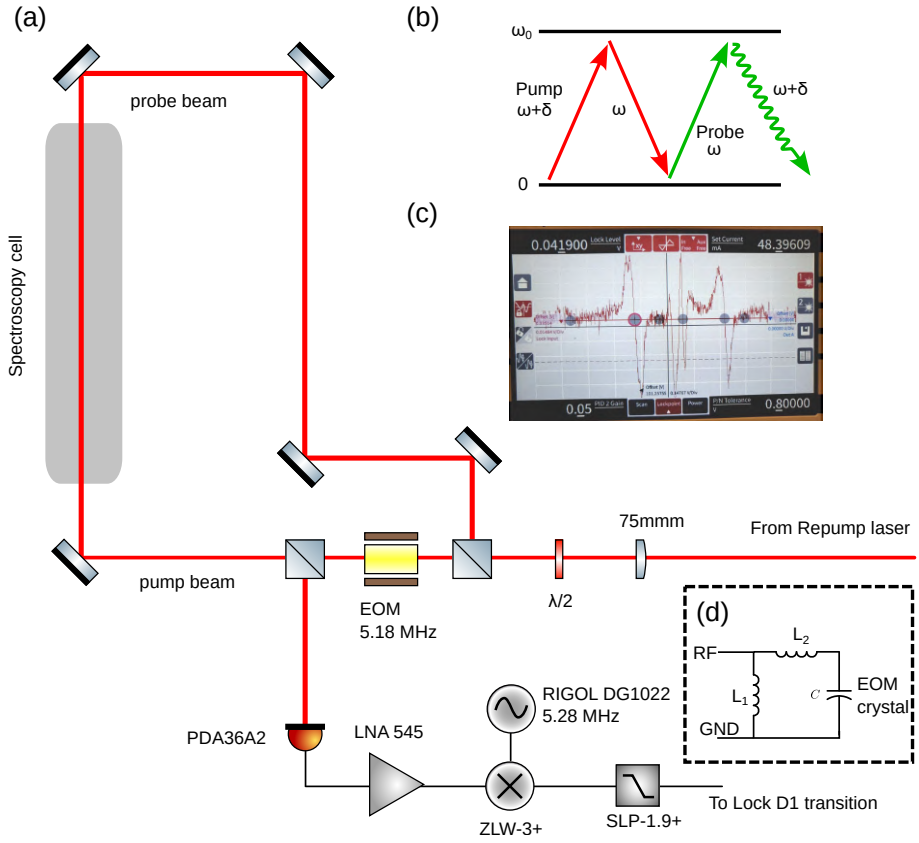

Figure 3.1: **^{6}Li spectroscopy.** (a) Schematic of the modulation transfer spectroscopy setup. (b) Modulation transfer process between the probe beam and the pump beam modified from [87]. (c) D_1 line signal of ^{6}Li atoms. We lock to the leftmost zero-crossing of the signals. (d) EOM driver circuit. The circuit allows us to imprint a phase modulation on the pump beam.

3.2 Zeeman slower

As seen, laser spectroscopy enables precise locking of its frequency to an atomic transition. This allows near-resonant laser beams to be used for decelerating atoms, a technique known as Doppler cooling. In our experimental setup, ^{6}Li atoms are located inside the oven on the experimental table. The atoms move rapidly with an average speed of approximately 600 m/s at an oven temperature of 320°C. Consequently, it is necessary to slow down the atoms to the MOT capture velocity of about 30 m/s before trapping them. This is achieved using a Zeeman slower, which exploits the Zeeman shift induced by a magnetic field [88]. In particular, atoms propagate along the z-axis of the tapered solenoid and the atoms experience energy shifts due to the spatial dependence of the magnetic field along the propagation direction, $B(z)$. When the cooling beam frequency is on-resonant with the atomic transition, the atoms absorb photons and emit scattered photons in random directions. Overall, the atoms are slowed down, and their speed is reduced. The scattering force depends on beam intensity and frequency detuning. The maximum scattering force for a large intensity limit compared to saturated intensity ($I/I_{\text{sat}} \gg 1$) is given by

$$F_{\text{scatt}} = \hbar k \Gamma/2, \tag{3.1}$$

where k is the photon momentum and Γ is the decay rate of an excited state.

During the slow-down process, we simplify the model by assuming atoms have an initial velocity, v_0, and an instantaneous velocity, v, at a later time. Atoms absorb photons when the detuning frequency from the atomic transition satisfies the condition given by

$$\delta = \omega + kv - \left(\omega_0 + \frac{\mu_B B(z) \Delta(g_F M_F)}{\hbar}\right) = 0. \tag{3.2}$$

This condition ensures that the atoms experience the maximum scattering force in the presence of the Doppler effect and the Zeeman shift. Here, $\Delta(g_F M_F)$ denotes the difference in the product of the magnetic quantum number, M_F, and the Lande g-factor, g_F, of the hyperfine structure between the final and initial state, ω is the free-space laser frequency, and ω_0 is the atomic transition frequency.

While a scattering force acts on atoms, they are constantly decelerating, and their instantaneous velocity at a distance z from the initial position is obtained by

$$v = v_0\Big(1 - \frac{z}{L_0}\Big)^{1/2}, \tag{3.3}$$

where $L_0 = v_0^2\lambda m/(\pi\hbar\Gamma)$ is the stopping distance under the assumption that the deceleration being used is half of the maximum deceleration calculated by Eq. 3.1, ensuring no atoms are left behind. Here, m is the atomic mass, and λ is the laser wavelength.

With the use of Eqs. 3.2 and 3.3, we obtain a designed magnetic field, expressed as

$$B(z) = \frac{2\pi\hbar v_0}{\lambda\mu_B\Delta(g_F M_F)}\Big(1 - \frac{z}{L_0}\Big)^{1/2} + \frac{\hbar}{\mu_B\Delta(g_F M_F)}(\omega - \omega_0), \quad 0 \le z \le L_0. \tag{3.4}$$

The designed magnetic profile suggests a spatial dependence of the magnetic field along the z-direction. With a spatially varying winding pattern, we can achieve the desired magnetic profile (Fig. 3.2). For increased accuracy, we use the Radia package [89] to design the field strength as a function of position, and the final design is shown in Fig. 3.2(a). The software allows us to calculate the combined magnetic field of Zeeman coils and MOT coils. In the experiment, Zeeman slowing beams consist of a cooling beam with a power of 30 mW and a repump beam with a power of 1 mW. Each beam is further red-detuned by 70 MHz with respect to the MOT cooling and MOT repump transitions (Fig. 3.3(b)). To improve the MOT loading rate, we implemented a Zeeman slower extension by installing permanent magnets that extend the magnetic field of the tapered coils. As a result, we obtain an increase by a factor of 1.8(4) in the MOT loading rate [90].

3.3 Magneto-optical trap

After atoms are decelerated by the Zeeman slower, they continue to move freely in space within the main chamber. Despite their speed being on the order of a few tens meters per second, the atoms remain energetically high and the density sparse. This state is still not suitable for studying quantum physics. To address this, we apply

3d Doppler cooling using three pairs of cooling and repump beams, similar to the concept discussed in Section 3.2. Additionally, we confine the atoms to the center of the science chamber using a quadrupole magnetic field formed by anti-Helmholtz coils. This field provides forces between a pair of counter-propagating lasers when the atoms are not in the center of the trap, resulting in a restoring force towards the center and trapping the atoms. This technique is known as a magneto-optical trap (MOT).

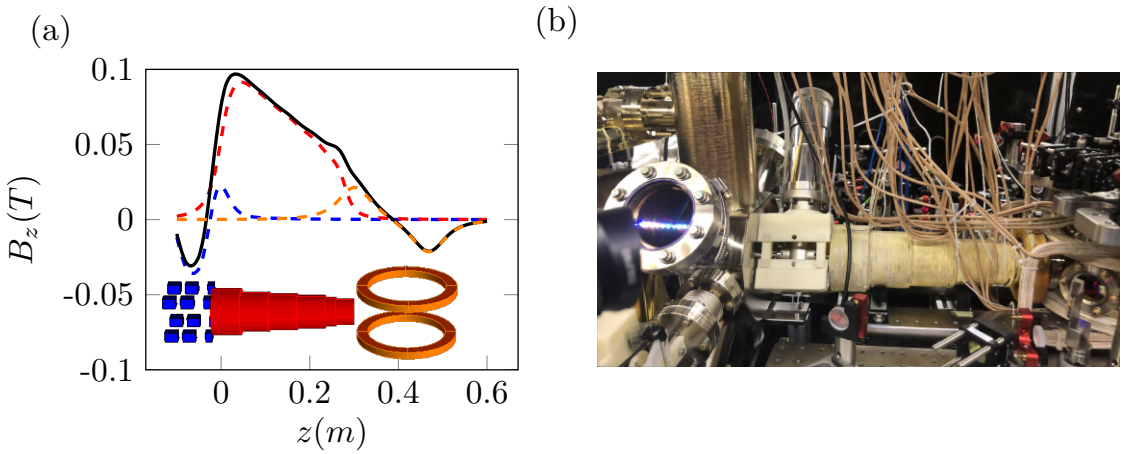

Figure 3.2: **Hybrid Zeeman slower and its magnetic field configuration.** (a) Contributions of the individual slower components to the total magnetic field along the atomic beam along the z-axis. The fields of the coils are calculated from the experimentally optimized currents using the Radia package. A 3d model showing the extension (blue), the wire-wound section (red) or Zeeman slower main section, and the MOT coils (orange) with their corresponding magnetic fields depicted in dashed lines. The black solid line is the total field. (b) Photograph of Zeeman slower setup. The extension permanent magnets are held by a 3d-printed plastic frame, which is inserted between the oven and the Zeeman coils. Figure was adapted from previous work [90].

For more details, let us consider a simple 2-level system that undergoes a transition between quantum states $F = 0$ and $F = 1$. At this point, we overlap the chamber center with the center of the MOT coils, therefore, there is no Zeeman shift due to a zero magnetic field i.e., the magnetic fields from the MOT coils cancel out at the

center. However, as we move away from the center along the axial direction, the z-axis, the magnetic field is non-zero and perturbs the atomic energy levels. For the $F = 1$ level, there are three possible magnetic quantum numbers $M_F = 0, \pm 1$. At a position close to the center, the energy shift can be approximated by the linear dependence of the magnetic field. In other words, the energy shift linearly varies with the position of the atoms (Fig. 3.3(a)) from the origin. When a red-detuned laser (refer to the MOT cooling beam) is applied, only atoms are displaced along $z < 0$ absorb σ^+ photons ($\Delta M_F = +1$), pushing back toward the trap center. Similarly, displaced atoms along $z > 0$ absorb σ^- photons and are kicked toward the trap center.

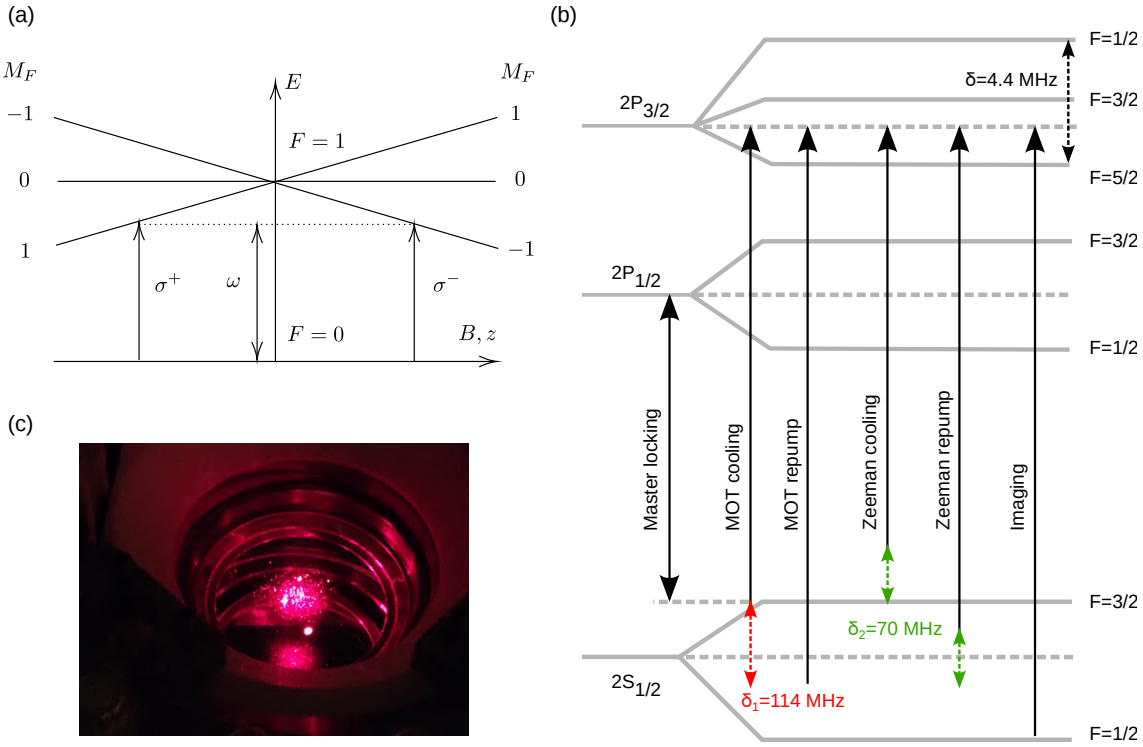

Figure 3.3: **Magneto-optical trap.** (a) Schematic of MOT operation in a simple picture of a 2-level system. Atoms experience Zeeman shifts in energy as they move away from the center. At this position, the atoms absorb counter-propagating photons, resulting in a restoring force that pushes them back toward the center. (b) A laser locking diagram is used in the experiment. The substructure of the $2P_{3/2}$ state is not resolved. (c) Picture of our MOT in the experiment (red spot).

To gain a more quantitative understanding of how the MOT operates, let us examine it mathematically [91]. The total scattering force due to the absorption of σ^+ and σ^- photons is given by

$$F_{\mathrm{MOT}} = F^{\sigma^+}_{\mathrm{scatt}}(\omega - kv - (\omega_0 + \beta z)) - F^{\sigma^-}_{\mathrm{scatt}}(\omega + kv - (\omega_0 - \beta z)). \tag{3.5}$$

We apply a series expansion to F_{scatt} about ω and ω_0, assuming that $kv, \beta z \ll \Gamma$. The expansion results in

$$F_{\mathrm{MOT}} \simeq -2\frac{\partial F}{\partial \omega} kv + 2\frac{\partial F}{\partial \omega_0}\beta z = -2\frac{\partial F}{\partial \omega}(kv + \beta z), \tag{3.6}$$

where $\beta = (\Delta(g_F M_F)\mu_B/\hbar)dB/dz$ and B is the magnetic field along the axial direction of anti-Helmholtz coils. As can be seen, F_{MOT} consists of restoring force and damping force, which push atoms towards the trap center and reduce velocity through damping.

The schematic of the MOT laser setup is illustrated in Fig. 3.4. The MOT laser (Toptica DL Pro) has an output power of approximately 20 mW and is amplified by the repump tapered amplifier (TA), Moglabs MOA003, to approximately 200 mW. The repump TA output is split into a MOT cooling seed and a MOT repump beam. We derive about 1 mW of light from the MOT cooling seed for phase locking to a master laser. The MOT repump beam goes through AOM1 (Intraaction ATM-1141A1) and its frequency is shifted by +114 MHz. The MOT cooling seed goes to the second tapered amplifier, Moglabs MOA003, followed by AOM2 (Intraaction ATM-1141A1) which shifts its frequency by −114 MHz. After that, both MOT cooling and repump beams are combined by a beamsplitter and distributed to four beams, called MOT1, MOT2, MOT3, and Zeeman slower beams. The MOT1 and MOT2 are used for horizontal cooling and trapping while the MOT3 is for vertical cooling and trapping. Overall, the MOT cooling beams have a power of 10 mW ($I/I_{\mathrm{sat}} = 10$) while the MOT repump beams have a power of 5 mW ($I/I_{\mathrm{sat}} = 5$) each. Both beams have a diameter of 10 mm. The schematic of laser locking is summarized in Fig. 3.3(b).

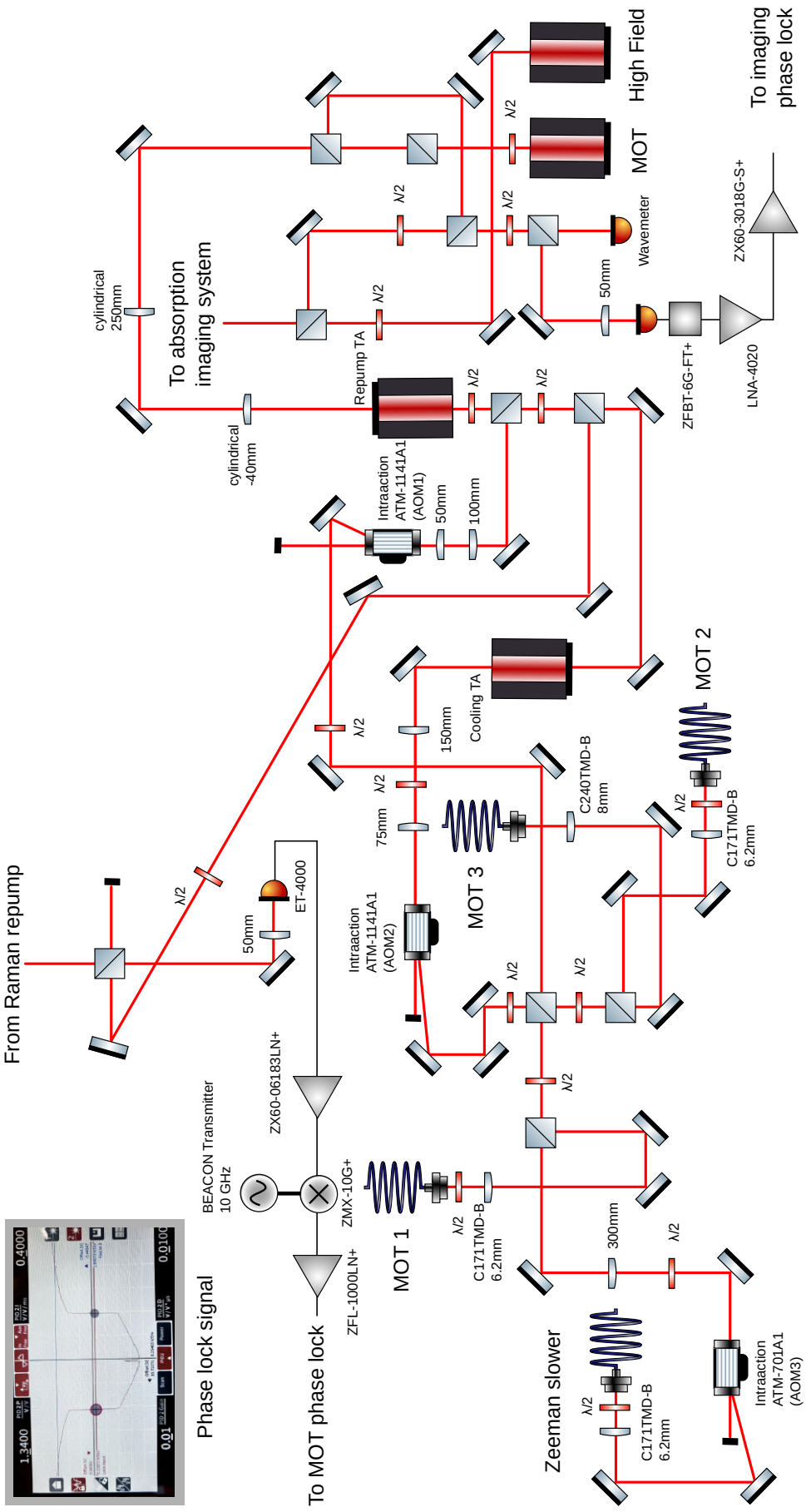

Figure 3.4: **Schematic of MOT laser setup.** Inset represents the phase lock signal of the MOT laser with the correct edge selected (leftmost). The beat lock signal of 10.06 GHz is generated by the mixing of the D_1 line and the MOT laser at a photodiode. The beat signal is further mixed with a local oscillator at 10.37 GHz and fed to the phase lock circuit.

In the MOT technique, a $\sigma^+ - \sigma^-$ configuration is required. Therefore, we place quarter-wave plates at the output of the fibers (P3630-PM-FC-10) as depicted in Fig. 3.5. The quarter-waveplates change the π polarization to σ^+ polarization while the half-waveplates on the retro sides convert retro-reflected beams to σ^- polarization. The Zeeman slower beams pass through AOM3 (Intraaction ATM-701A1) shifting frequency further by -70 MHz from the two previous MOT cooling and repump transitions. It is important to note that MOT repump beams are necessary because the cooling beams operate between $\left|^2S_{1/2}, F = 3/2\right\rangle$ and $\left|^2P_{3/2}\right\rangle$ and there is a non-zero chance to decay back to the dark state $\left|^2S_{1/2}, F = 1/2\right\rangle$. Atoms in the dark state are essentially lost from the cooling transition. By completing all requirements, we obtain our MOT, as shown in Fig. 3.3(c).

To lock the MOT laser to the D_2 transition, a fraction of light from the MOT laser and the Raman repump laser, which serves as a master laser, are derived and directed to a GaAs Photodetector (ET-4000). We work at a beat signal of 10.06 GHz which is created and detected by the photodiode. The beat signal is then mixed with a local oscillator (BEACON Transmitter) that provides a 10.37 GHz frequency reference which we use to mix down the signal to $10.37 - 10.06 = 310$ MHz. We finally connect the beat signal to the phase lock circuit with an external voltage-controlled oscillator (Pasternack PE1V31000), producing an error signal from a digital phase discriminator (AD9901KQ) for laser locking to the MOT transition as depicted in the inset of Fig. 3.4.

3.4 Low field and high field imaging

Following the capture of atoms in a MOT, properties of atom ensembles within the system, such as density profile, atom number, and energy shifts, can be observed using imaging techniques. Here, we rely on two types of imaging typically used in ultracold-atom experiments: fluorescence and absorption imaging. Fluorescence imaging is utilized to detect the number of atoms based on atoms emitting light

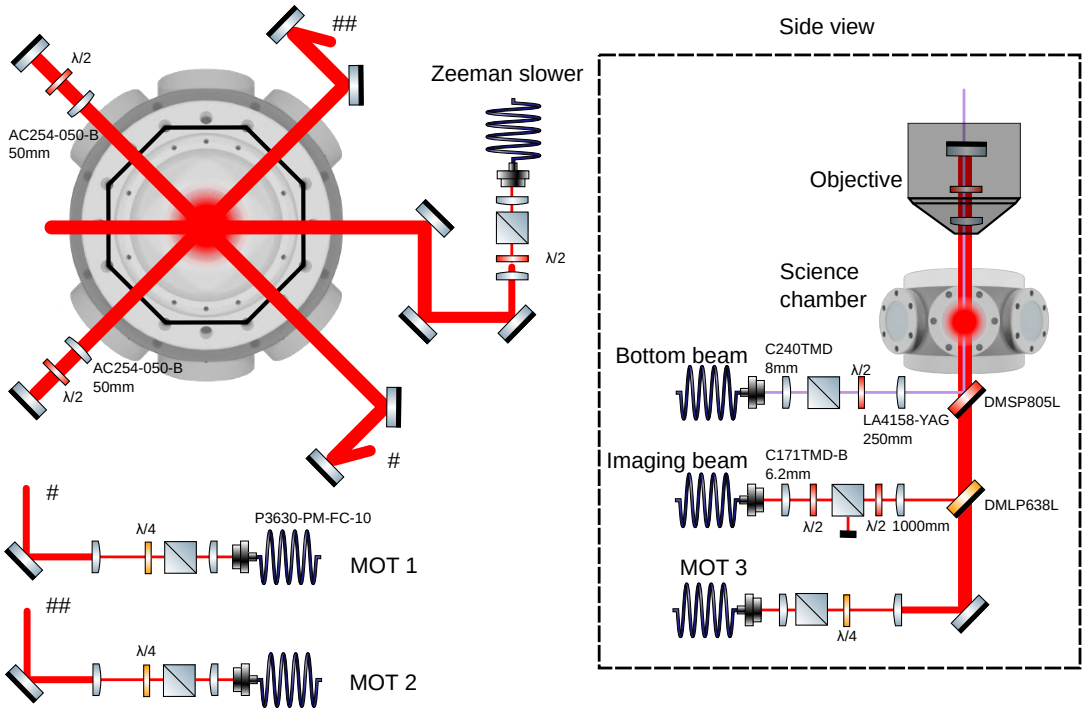

Figure 3.5: **Schematic of MOT on the experimental table.** (Left) Top view of the MOT setup. MOT cooling and repump beams are coupled to fibers and form $\sigma^+ - \sigma^-$ configuration on the experimental table. These beams have a diameter of $10\,\mathrm{mm}$. Zeeman slower beam propagates along the axial direction of Zeeman slower coils (not shown). (Right) Side view of the MOT setup. The vertical imaging beam and MOT beam are overlapped by a long-pass dichroic mirror (DMLP638L) and a short-pass dichroic mirror (DMSP805L) is added to coincide with the bottom beam, thus allowing the 1070 nm and 670 nm beams to propagate in vertical direction.

when the laser is tuned close to the atomic transition. We use fluorescence imaging in the early stages of the experiment, such as in the MOT (see Appendix C.2). Later, fluorescence imaging will be discussed again in our applications, specifically in manipulating atoms in optical lattices to emit fluorescence light based on the Raman sideband cooling technique. In this section, I mainly discuss absorption imaging used for optical alignment and measurements of atom number and temperature.

In the absence of a magnetic field, the imaging beam is on-resonant with the D_2 transition, or slightly off from the transition due to a small magnetic offset field.

We refer to this regime as low-field imaging. Whereas in the presence of a magnetic field i.e., Feshbach field, the imaging beam frequency is shifted by 0.5 MHz to 1 GHz. Therefore, we have to compensate for the Zeeman energy shift, and we realize it using a variable offset phase lock circuit. We refer to this regime as high-field imaging.

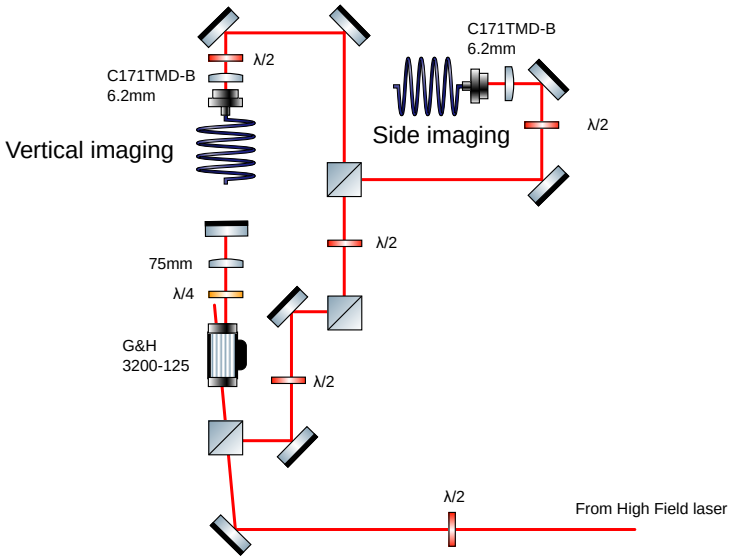

Figure 3.6: **Schematic of imaging laser.** An incoming beam from the high-field imaging laser is injected into the double-pass AOM. The outgoing beam is separated from the incoming beam by a beamsplitter and goes to fibers for vertical and side imaging. The power of both imaging beams is individually adjusted by the half-waveplates close to the AOM. Beam shutters (not shown) are added to the beam path to prevent residual light from entering the main experiment.

To produce the absorption imaging beam, we use a tunable laser diode (Toptica DL Pro) and lock the laser to the D_2 line using the MOT cooling transition as a reference (Fig. 3.3b). A double-pass AOM is implemented using the cat's-eye configuration and the frequency is red-detuned by 195 MHz for a single pass (Fig. 3.6). We finally distribute the imaging beam into two separate beams for side and vertical imaging. Both imaging beams are then guided to the experimental table via optical fibers (Thorlabs P3-630PM-FC-10). The beam waists for side and vertical imaging are

7 mm and 340(10) µm at the atom position. In the following section, we use imaging beams discussed in here to perform absorption imaging, detecting atom number in the ODT.

Spin mixture

During the MOT loading process, atoms are initially prepared in the ground state $\left|^2S_{1/2}\ F = 1/2\right\rangle$ and the repump beam prevents residual population in a dark state by transferring atoms that decay back to $\left|^2S_{1/2}\ F = 3/2\right\rangle$. Due to various parameters (e.g., cooling power, repump power), the mixture of two lowest hyperfine states, $|1\rangle = \left|^2S_{1/2}\ F = 1/2\ M_F = 1/2\right\rangle$ and $|2\rangle = \left|^2S_{1/2}\ F = 1/2\ M_F = -1/2\right\rangle$, could result in imbalanced population and can change over time. In Fig. 3.7(a), the mixture of the two lowest hyperfine states versus repump power is illustrated. The ratio of MOT cooling and repump power determines the population distribution in the ground state of the system.

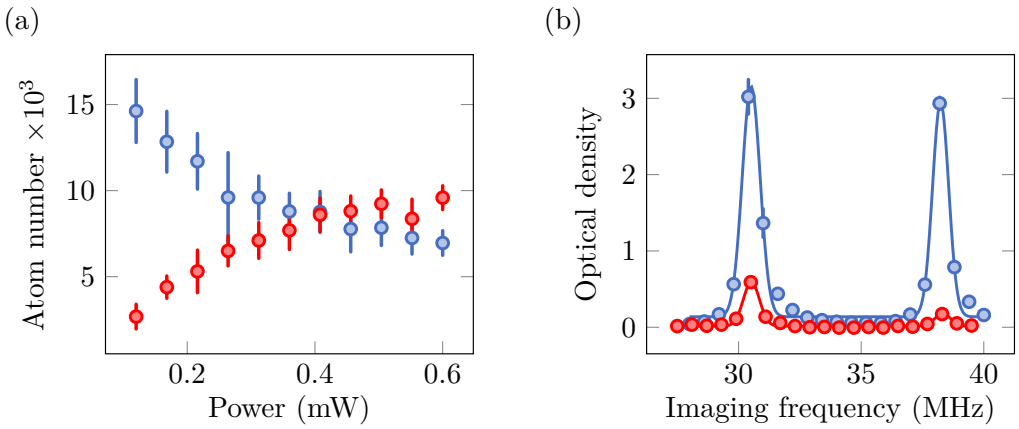

Figure 3.7: **Spin population.** (a) Two spin components as a function of the MOT repump power per beam. The MOT cooling power is fixed at 10 mW per beam. (b) Spin balance in the ODT (blue) and spin imbalance after evaporation in the ODT at significantly high scattering lengths (red).

We find that imbalance in population increases even more at high interactions beyond a magnetic field of 810 G during evaporation as shown in Fig. 3.7(b). Most

likely, one spin component gets lost or forms molecules. To achieve a stable balanced mixture, we apply a few consecutive radio-frequency sweep pulses between $|1\rangle - |2\rangle$ in the optical dipole trap, as discussed in a later Section 3.6.

3.5 Raman sideband cooling

An essential key to preventing system heating during fluorescence imaging is Raman sideband cooling, originally developed for cooling trapped ions to reach the zero point of motion. However, this technique can be applied to imaging atoms in deep optical lattices where atoms are strongly trapped in the Lamb-Dicke regime. By applying a two-photon process, atoms are driven from a harmonic quantum vibration number, ν, to a lower quantum number, $\nu - 1$. A complete process provides a scattering photon which is captured by an sCMOS camera (Andor Zyla 4.2 plus).

To implement Raman sideband cooling, the Raman repump laser is locked to the D_1 transition as mentioned in the ^{6}Li spectroscopy (see Section. 3.1). The Raman cooling beam laser is generated by a Toptica DL Pro and stabilized relative to the Raman repump laser with a red-detuning of 5.6 GHz. In Fig. 3.8, a beat signal of the Raman cooling laser and the Raman repump laser is detected using an ultrafast photodiode (G4176-03). Here, a bias tee (ZFBT-6G-FT+) blocks DC while radio-frequency signals are allowed to pass. A low-noise amplifier (LNA-6G) enhances the signal. Then a local oscillator (ZX95-5200) and the beat signal are fed to a mixer (ZMX-10G), resulting in the mixed-down beat signal at a frequency of $5.6 - 5.2$ GHz $= 400$ MHz. Finally, the second beat signal is amplified by an amplifier (ZFL-500HLN+) before being connected to a phase-frequency detector, providing an error signal for Raman cooling locking.

In Fig. 3.9(a), the schematic of the Raman cooling process is illustrated and the Raman cooling process is implemented as follows: Atoms are initially prepared in $\left|2S_{1/2}, F = 3/2, \nu\right\rangle$. The first Raman beam (R1) stems from the setup in Fig. 3.8 and further red-detuned by $(228.2 + \omega_{\text{lattice}}/2\pi)$ MHz (Fig. 3.9(b)) using a double-pass

AOM, called second Raman beam (R2). These Raman beams drive an oscillation between $\left|^2S_{1/2}, F = 3/2\right\rangle$ and $\left|^2S_{1/2}, F = 1/2\right\rangle$ via intermediate state $^2P_{1/2}$. The population in the intermediate state is minimized by detuning and can be optimized in the experiment. Therefore, atoms populate from $\left|2S_{1/2}, F = 3/2, \nu\right\rangle$ to $\left|2S_{1/2}, F = 1/2, \nu - 1\right\rangle$. It is important to note that the Raman cooling beams have an angle between them, allowing for momentum transfer, while co-propagating beams keep the vibrational quantum number unchanged.

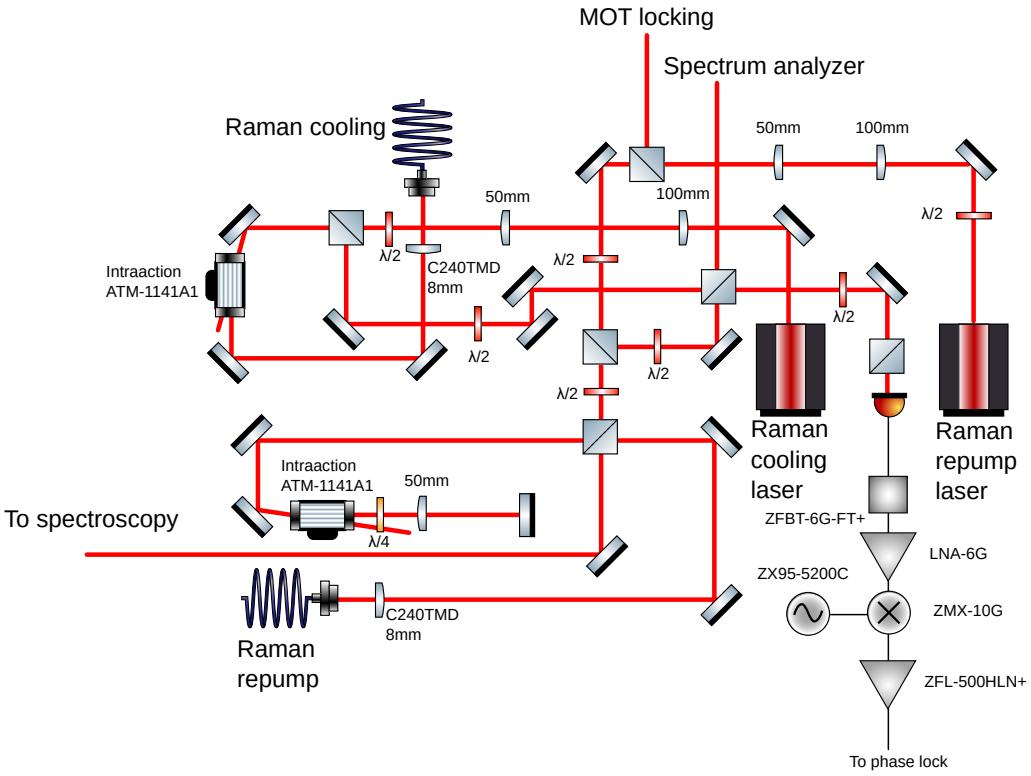

Figure 3.8: **Schematic of Raman laser systems.** The Raman imaging system consists of two individual lasers. The Raman cooling laser provides a cooling beam and is red-detuned by $5.6\,\mathrm{MHz}$ from the D_1 transition using phase locking. The single-pass AOM controls the Raman cooling power to a fiber. The Raman repump laser provides a repump beam for Raman sideband cooling technique as well as for spectroscopy. The Raman repump laser is locked to the D_1 transition by the spectroscopy cell and the Raman repump beam can be further red-detuned by a few tens MHz to the transition using double-pass AOM.

The Raman repump beam is blue-detuned by 9.6(5) MHz from the D_1 transition as shown in Fig. 3.9(a) and the beam is circularly polarized. The beam drives atoms from the ground state, $\left|2S_{1/2}, F = 1/2, \nu - 1\right\rangle$, to $^2P_{1/2}$ and the atoms finally decay back to $\left|2S_{1/2}, F = 3/2, \nu - 1\right\rangle$ where atoms occupy the same manifold, however, the quantum vibration level is lowered by one. The spontaneous photons emitted during the decay process are captured for fluorescence imaging. The atoms excited by the Raman repump beam are more likely to decay down into the $\left|2S_{1/2}, F = 3/2\right\rangle$ state rather than $\left|2S_{1/2}, F = 1/2\right\rangle$ with a branching ratio of 8 : 1. In Fig. 3.9(c), we demonstrate the successful implementation of the Raman sideband cooling system by performing Raman sideband spectroscopy, and we obtain the lattice trap frequency at full power of the lattice beams.

As can be seen, Raman laser systems are necessary for performing fluorescence imaging to capture spontaneous photons in a regime. Here, I discuss how we keep the atoms close to the vibrational ground state on each lattice site. Let us consider the transition probability between quantum states in a harmonic oscillator. Using the fact that atoms emit spontaneous photons and get kicked by momentum k that corresponds to momentum propagator $e^{-ik\hat{x}}$ which is equivalent to the well-known transition operator in coherent states $e^{-i\eta(\hat{a}+\hat{a}^\dagger)}$. The probability of atoms being driven from a quantum vibrational number ν to another quantum vibrational number ν' is given by

$$P_{\nu\to\nu'} = |\left\langle \nu | e^{ikx_0\left(\hat{a}+\hat{a}^\dagger\right)} | \nu' \right\rangle|^2. \tag{3.7}$$

By performing Taylor's series expansion about the Lamb-Dicke parameter which is defined as $\eta \equiv kx_0 = \sqrt{\hbar k^2/(2m\omega_{\text{latt}})}$, the transition probability is approximated by

$$P_{\nu\to\nu'} = \left| \left\langle \nu \left| \left(1 + i\eta\left(\hat{a} + \hat{a}^\dagger\right) - \frac{\eta^2}{2}\left(\hat{a} + \hat{a}^\dagger\right)^2 + \mathcal{O}\left(\eta^3\right)\right) \right| \nu' \right\rangle \right|^2. \tag{3.8}$$

In the Lamb-Dicke regime, higher transitions i.e., $\nu' - \nu > 2$ are suppressed. There-

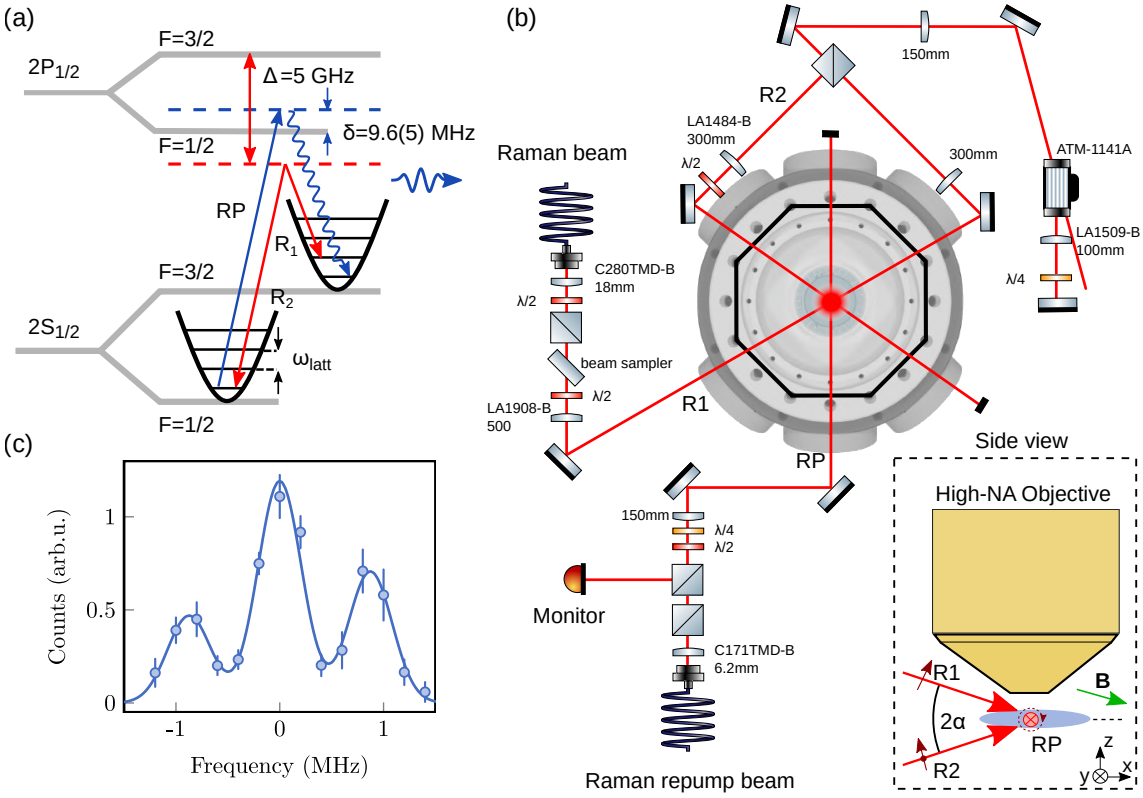

Figure 3.9: **Raman beams configuration and Raman cooling process.** (a) Schematic of the Raman cooling process. The Raman beams (red) are detuned by Δ from the D_1 line, driving vibrational-lowering transitions. The repump beam (blue) is blue detuned by $\delta = 9.6(5)$ MHz from the $\left|2S_{1/2}, F = 1/2\right\rangle$ to the $\left|2P_{1/2}, F = 1/2\right\rangle$; it pumps atoms back to the initial state without lowering the vibrational quantum number due to a small Lamb-Dicke parameter of 0.29. The spontaneous photons are used for fluorescence imaging. (b) Schematic of Raman setup on the experimental table. The inset shows lattices and Raman beams from the side view. The repump beam propagates in the plane formed by the lattice. Raman beam (R1) is horizontal linear polarized and propagates out of the plane with a shallow angle of $\alpha = 7.5(2)^\circ$. Raman beam (R2) is perpendicular to the R1 and has a mixture of both horizontal and vertical linear polarization in a ratio of $4:1$. A green arrow shows the projection of the magnetic field on the xz-plane with an angle of -70°. (c) Raman sideband spectroscopy of a triangular lattice. The sidebands show lattice vibrational spacing of $\omega_{\text{latt}} = (2\pi) \times 870$ kHz. Figure was reproduced from previous work [84].

fore, the probability of the transition is finally expressed as [92]

$$P_{\nu\to\nu'} = \eta^2\nu \qquad \nu \to \nu' = \nu - 1, \tag{3.9}$$

$$P_{\nu\to\nu'} = \left(1 - \frac{2\nu+1}{2}\eta^2\right)^2 \qquad \nu \to \nu' = \nu, \tag{3.10}$$

$$P_{\nu\to\nu'} = \eta^2(\nu+1) \qquad \nu \to \nu' = \nu + 1. \tag{3.11}$$

To ensure the cooling is efficient, the Lamb-Dicke parameter should be small to minimize changes in the quantum vibrational number during spontaneous emission. In the experiment, we obtain the Lamb-Dicke parameter η of 0.29. This condition is achieved by the cooling process occurring in a significantly deep lattice, implying a large trap frequency (ω_{latt}). An optimized Raman sideband cooling system can be accomplished by tuning the Raman parameters while minimizing atom hopping. This hopping plays a crucial role not only in image fidelity but also in observable quantities. The hopping of atoms occurs when the cooling process is unable to overcome the heating effects. Atoms then hop to nearest neighbors, with a suppressed probability of hopping to sites beyond the nearest neighbors. It is worth noting that directly transferring between quantum vibrational states using RF is impossible. The momentum transfer from photons to atoms in the RF regime is negligible. However, RF transfer can be used to drive atoms between hyperfine structures in the presence of a magnetic field without changing the motional state as demonstrated in Section 3.6.1.

By capturing spontaneous photons with a high-resolution objective (N.A.=0.5), individual atoms are detected at the camera as shown in Figs. 3.10(a,b). The imaging fidelity is measured by taking a series of five images with 500 ms exposure time each and 50 ms separation in between. Hopping and loss rates are estimated by comparing two adjacent images (Fig. 3.10(d)). We define the hopping rate as the fraction of sites detected as occupied in the second image only, while the loss rate is given by the fraction of atoms lost from picture to picture. The imaging fidelity is defined by the fraction of atoms remaining in the same lattice sites. As a result of hopping and loss, the imaging fidelity is determined to be 97.6(3)% in 500 ms. In the

subsequent section, the idea of evaporative cooling, mentioned earlier in Chapter 1, is implemented in the experiment to achieve degenerate Fermi gases.

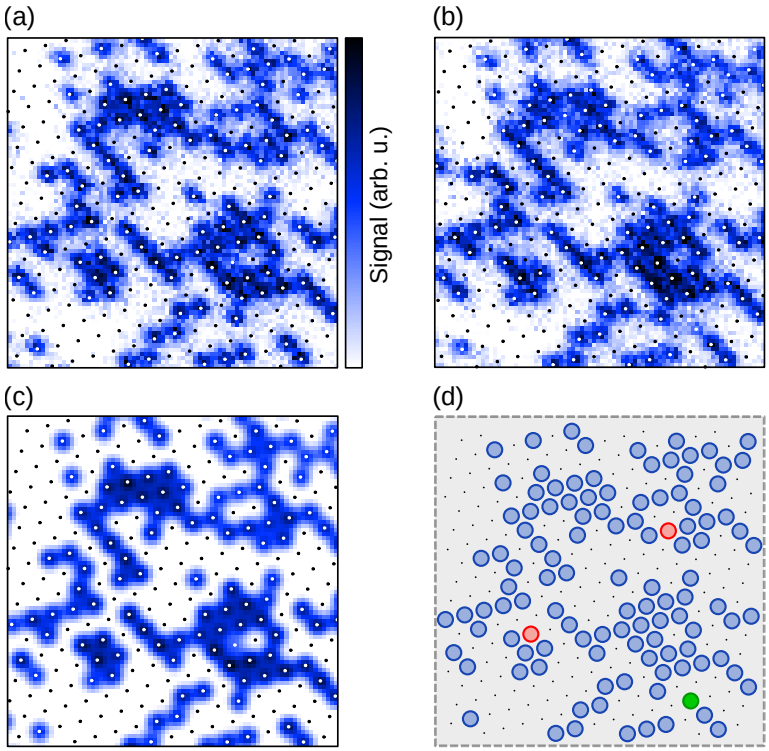

Figure 3.10: **Imaging fidelity.** (a,b) Two consecutive images of individual ^{6}Li atoms (white dots) in a triangular lattice (black dots) imaged with 500 ms exposure and separation of 50 ms. The single-site imaging has a field of view of $25\,\mu\text{m} \times 25\,\mu\text{m}$. (c) Reconstructed occupation of picture (a) convolved with the point spread function (PSF). (d) Hopping and loss during imaging, stationary atoms (blue), hopped atoms (green) and lost atoms (red). We obtain a hopping rate of 2.0(2)% and a loss rate of 0.4(2)% at a detected occupation of up to 50% by averaging over twelve pairs of pictures, thus demonstrating an imaging fidelity of 97.6(3)%. Figure was taken from our work [84].

3.6 Optical dipole trap

Atoms in the MOT are sparsely spaced, with interparticle spacing that is quite large, and their wavefunctions do not overlap. Here, we discuss ways to enhance the phase-space density as follows: After atoms are trapped in the MOT, we transfer

them to the optical dipole trap (ODT) by compressing the MOT. In particular, the MOT cooling and MOT repump frequencies are swept from −30 MHz to −5 MHz compared with the atomic transitions, represented in Fig. 3.3, while simultaneously decreasing in powers. This compression enhances the overlap between the MOT and the ODT, as the MOT size of approximately 3 mm is much larger than that of the ODT.

The ODT is generated by a 1070 nm laser (IPG YLR-300-LP-AC-Y14) with a power output of 125 W and a beam waist of 90 µm. We tested the laser at a power of 200 W without any issues. However, the laser is not running at that high power because of saturation in atom number beyond 125 W. The two ODT beams intersect at a small angle of 2θ, where $\theta \approx 10°$. This configuration is referred to as the crossed dipole trap (CDT), as illustrated in Fig. 3.11.

The potential of the CDT can be understood by considering the atom-light interaction through a light shift, expressed as

$$U_{\text{dip}} = -\frac{1}{2}\langle \mathbf{p} \cdot \mathbf{E} \rangle = -\frac{1}{2\epsilon_0 c}\,\text{Re}(\alpha) I, \tag{3.12}$$

where $\alpha(\omega)$ is the complex polarizability which depends on the driving frequency ω and can be calculated by Lorentz's model. This model treats the electrons as being attached to the atomic nucleus by springs, representing the restoring force of the electron cloud in the presence of a time-dependent external electric field. As a result, the dipole potential can be written as [93, 94]

$$U_{\text{dip}}(\mathbf{r}) = -\frac{3\pi c^2}{2\omega_0^3}\left(\frac{\Gamma}{\omega_0 - \omega} + \frac{\Gamma}{\omega_0 + \omega}\right) I(\mathbf{r}), \tag{3.13}$$

and the scattering rate in this potential is given by

$$\begin{aligned} \Gamma_{\text{sc}}(\mathbf{r}) &= \frac{1}{\hbar\epsilon_0 c}\,\text{Im}(\alpha) I(\mathbf{r}) \\ &= \frac{3\pi c^2}{2\hbar\omega_0^3}\left(\frac{\omega}{\omega_0}\right)^3 \left(\frac{\Gamma}{\omega_0 - \omega} + \frac{\Gamma}{\omega_0 + \omega}\right)^2 I(\mathbf{r}), \end{aligned} \tag{3.14}$$

where ω_0 is the atomic transition and Γ is the natural linewidth related to the lifetime of the excited states.. A simple picture of the light shift using a 2-level system approximation can be found in Appendix C.9.

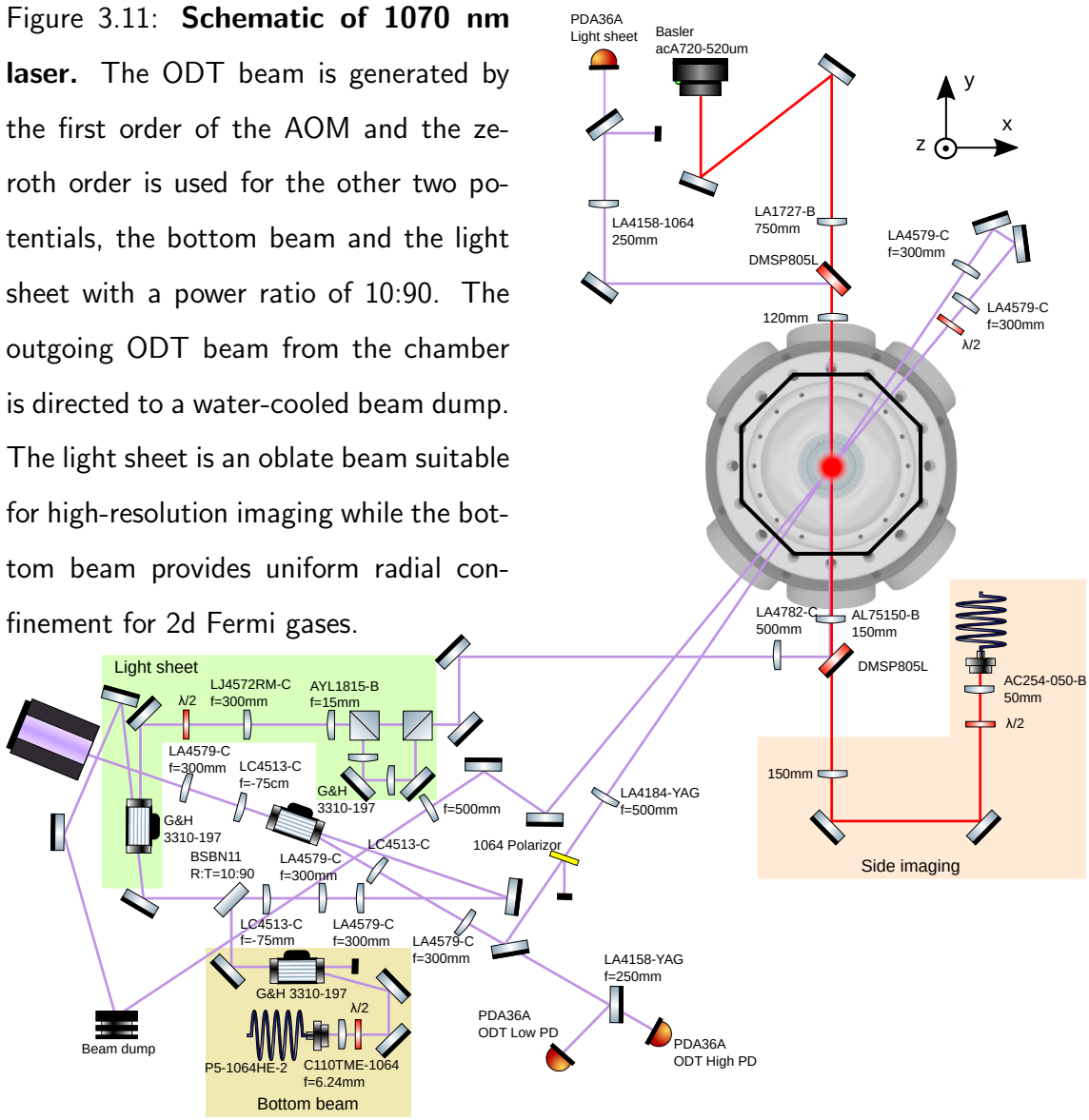

Figure 3.11: **Schematic of 1070 nm laser.** The ODT beam is generated by the first order of the AOM and the zeroth order is used for the other two potentials, the bottom beam and the light sheet with a power ratio of 10:90. The outgoing ODT beam from the chamber is directed to a water-cooled beam dump. The light sheet is an oblate beam suitable for high-resolution imaging while the bottom beam provides uniform radial confinement for 2d Fermi gases.

As can be seen, the optical dipole potential in Eq. 3.13 is proportional to the laser intensity at the atom position. The total complex electric field is a superposition of the fields from the two ODT beams i.e., $\mathbf{E} = \mathbf{E}_1 + \mathbf{E}_2$, and the intensity is given by

$$I = \frac{1}{2}\varepsilon c|\mathbf{E}_1 + \mathbf{E}_2|^2 = \frac{1}{2}\varepsilon c(\mathbf{E}_1 + \mathbf{E}_2)(\mathbf{E}_1 + \mathbf{E}_2)^*,$$

where c is the speed of light in vacuum and ε is the permittivity of free space. Here, we use an orthogonal configuration, i.e., $\mathbf{E}_1^* \cdot \mathbf{E}_2 = \mathbf{E}_1 \cdot \mathbf{E}_2^* = 0$. Because of no interference terms, the total intensity is simply the summation of each beam

intensity. It is important to adjust the crossed polarization configuration carefully to avoid interference terms. In fact, atoms occupied in the ground state experience attractive forces from the 1070 nm laser because the laser wavelength is longer than the atomic transition, as demonstrated in Fig. 3.12(a). Therefore, the CDT allows us to enlarge the trapping volume compared to a single ODT beam. The total intensity of this trap can be written in the cylindrical coordinates of two individual Gaussian beams propagating by $\pm\theta$ with respect to the z-axis (Fig. 3.12(b))

$$\begin{aligned} I(r,z) =& I_1\Big(r\cos\theta + z\sin\theta, -r\sin\theta + z\cos\theta\Big) \\ &+ I_2\Big(r\cos\theta - z\sin\theta, +r\sin\theta + z\cos\theta\Big), \end{aligned} \tag{3.15}$$

where a single Gaussian beam propagating along z′-direction, as defined in Fig. 3.12(b), has intensity given by

$$I_{1,2}(r',z') = I_0^{(1,2)}\left[\frac{w_0^{(1,2)}}{w_{1,2}(z')}\right]^2 \exp\left(\frac{-2r'^2}{w_{1,2}^2(z')}\right).$$

The definitions of parameters can be found in Appendix C.1.

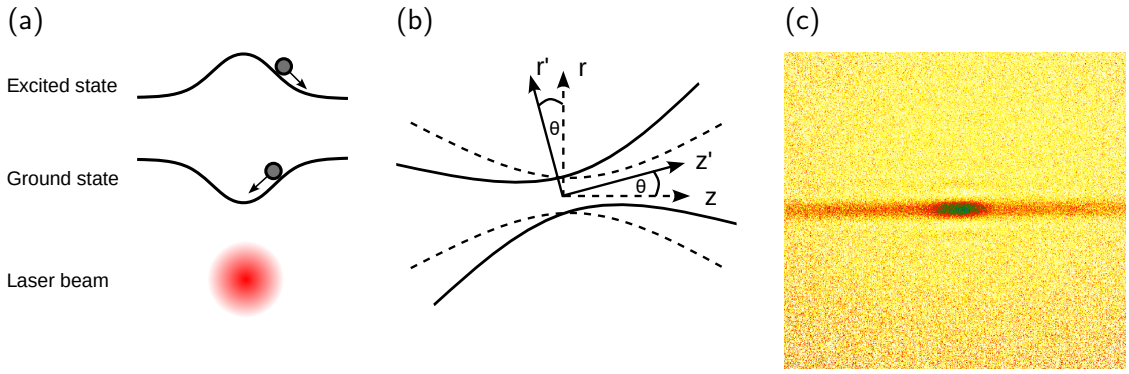

Figure 3.12: **Dipole force and crossed dipole trap.** (a) Light shift causes a gradient in energy, leading to repulsive and attractive forces. Red-detuned laser is used to trap atoms. (b) Rotated Gaussian beam with intensity $I(r',z')$. (c) Side imaging of the crossed dipole trap. The field of view is $600\,\mu\text{m} \times 600\,\mu\text{m}$.

By adjusting the CMOT parameters, ^{6}Li atoms are equally populated in the ground states $|1\rangle \equiv \left|^2\text{S}_{1/2}\ \text{F} = 1/2\ \text{M}_F = 1/2\right\rangle$ and $|2\rangle \equiv \left|^2\text{S}_{1/2}\ \text{F} = 1/2\ \text{M}_F = -1/2\right\rangle$ after

loading into the CDT, with an initial density of approximately $1 \times 10^{12}\,\mathrm{cm}^{-3}$ and a temperature of approximately 220 µK.

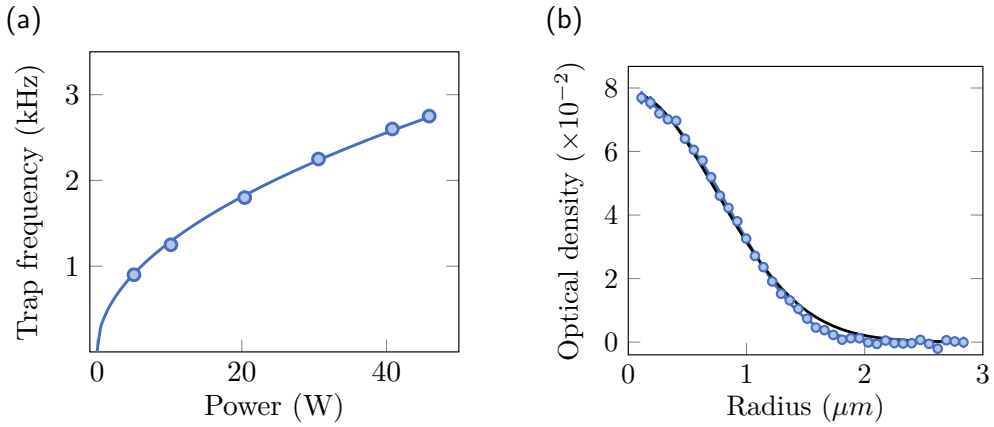

Figure 3.13: **ODT trap frequency and Fermi gas.** (a) Measurement of the ODT trap frequency as a function of power using amplitude modulation spectroscopy. The solid line represents the fit to power$^{1/2}$. (b) Fermi gas in ODT. The data (blue dots) are fit to 3d Fermi gas (blue solid line) and a Gaussian function (black solid line). The temperature is determined to be $0.20(5)\,\mathrm{T_F}$.

To achieve temperatures below the limitations of the MOT, we apply 3 steps of evaporative cooling to reach degenerate Fermi gases as follows [84]: First of all, plain evaporation is performed in 1 s by increasing a Feshbach field to 810 G, where the scattering length between state $|1\rangle$ and $|2\rangle$ is $a_s \approx 17{,}000 a_0$ [95, 96] with the Bohr radius a_0. The intensity of the dipole trap remains constant during plain evaporation, where the atoms naturally evaporate in the presence of gravity and significantly strong interactions. Next, we perform forced evaporation by reducing the intensity of the dipole trap to 6% of the initial value following an exponential decay curve with a time constant τ_1 of 300 ms with a duration of 0.7 s. Finally, forced evaporation II is applied for 5 s. The intensity of the dipole trap continues to reduce to 0.4% of the initial value with a time constant τ_2 of 6 s. To prevent the formation of deeply bound lithium molecules and obtain degenerate Fermi gases, the Feshbach magnetic field is switched from 810 G to 300 G ($a_s = -288 a_0$) within 10 ms and about 500 ms before the end of the forced evaporation stage II, where

the density is not sufficiently high to form lithium dimers via three-body collisions. With this experimental cycle of 12 s duration, we obtain a degenerate Fermi gas with about 3000 atoms and temperature below one-fifth of the Fermi temperature, determined by fitting the gas to the profile of a 3d non-interacting Fermi gas, as depicted in Fig. 3.13(b).

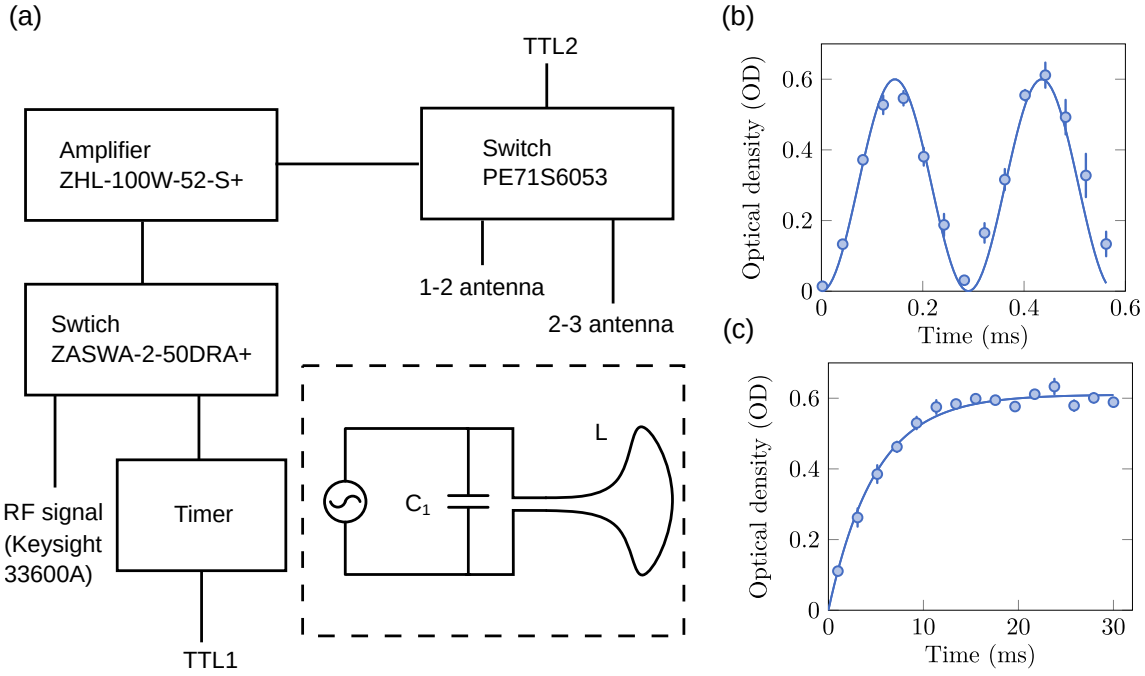

Figure 3.14: **Radio frequency transfer.** (a) Schematic of the antenna driver and antenna (inset). The resonance frequency is determined by capacitor C_1 and inductor L which depends on the shape of the antenna. (b) $|2\rangle - |3\rangle$ Rabi oscillation of $(2\pi) \times 3.6(3)$ kHz at a field of 795 G centered at $81.9297\,\mathrm{MHz}$. (c) $|2\rangle - |3\rangle$ frequency sweep spanned by $500\,\mathrm{kHz}$ centered at $81.9297\,\mathrm{MHz}$. By fitting to Eq. 3.18, a Rabi frequency of $(2\pi) \times 3.2(4)$ kHz is determined.

3.6.1 RF state preparation in ground state manifold

To expand the capability of tuning interactions, a spin mixture is not limited to the two lowest hyperfine states. It can, for example, involve the lowest state and the third lowest hyperfine state, $|3\rangle = \left|2^2\mathrm{S}_{1/2}\ \mathrm{F} = 3/2\ \mathrm{M}_F = -3/2\right\rangle$, because the $s-$wave scattering depends on occupied states with distinct magnetic moments. This

results in varied coupling between closed and open channels (see Appendix C.6). To access a desired spin mixture, radio frequency (RF) is applied, and the population transfer is determined by a pulse duration in the presence of a magnetic field. In Fig. 3.14(a), the implementation of a home-built RF antenna is depicted. The RF is generated by a wave generator (Keysight 33600A) and connected to a 100 W amplifier (ZHL-100W-52-S+) via a solid-state switch (ZASWA-2-50DRA+). We use a timer circuit to prevent overheating of the antenna by limiting the RF pulse duration to a few milliseconds. To switch between $|1\rangle - |2\rangle$ and $|2\rangle - |3\rangle$ antennas, a high power RF relay switch (PE71S6053) is added after the amplifier.

By applying an RF pulse to atoms in the presence of a magnetic field, the population in the two-level system can be described by the Rabi flopping formula [91]. At resonance, the transition probability is given by

$$P_{\mathrm{g}\to\mathrm{e}} = \sin^2\left(\frac{\Omega t}{2}\right), \tag{3.16}$$

where Ω is the Rabi frequency. We observe Rabi oscillations between the $|2\rangle$ and $|3\rangle$ states, as shown in Fig. 3.14(b). This is achieved by applying an RF pulse centered at 81.9297 MHz to a spin-balanced mixture of the $|1\rangle$ and $|2\rangle$ states in the ODT via the $|2\rangle - |3\rangle$ antenna, for varying durations. The oscillation is fitted to Eq. 3.16, and the Rabi frequency is extracted. It is worth noting that the Rabi frequency is power-dependent, and the antennas are optimized for a certain range of frequencies.

3.6.2 Radio frequency sweep

To completely transfer from one state to another state, Landau and Zener showed that the population can be transferred using an adiabatic sweep across the resonance [97]. The excitation probability from the ground state, $|g\rangle$, to the excited state, $|e\rangle$, is given by [98]

$$P_{\mathrm{g}\to\mathrm{e}} = 1 - \exp\left\{-\frac{2\Omega^2}{\dot{\delta}}\left[\tan^{-1}\left(\frac{\delta\left(t_f\right)}{\gamma/2}\right) - \tan^{-1}\left(\frac{\delta\left(t_i\right)}{\gamma/2}\right)\right]\right\}, \tag{3.17}$$

where γ is the decay rate of the Rabi oscillations and $\dot{\delta}$ is a constant detuning sweeping rate across a resonance. When the detuning δ starts from far below resonance at

initial time t_i, through the level crossing at $\delta = 0$, and ending up far above resonance at time $t = t_f$, Eq. 3.17 is simplified to

$$P_{\mathrm{g}\to\mathrm{e}} = 1 - e^{-2\pi\Omega^2/\dot{\delta}}. \tag{3.18}$$

It is worthwhile noting that a slow ramp through resonance, $\dot{\delta}/\Omega^2 \ll 1$, represents an adiabatic process and results in complete transfer to the excited state.

According to the scattering properties of a $|1\rangle - |3\rangle$ mixture, it can provide a stronger attractive interaction compared to other mixtures. We later work with this mixture to enhance evaporation for 2d Fermi gases. To prepare a $|1\rangle - |3\rangle$ mixture, we start with a balanced $|1\rangle - |2\rangle$ mixture in the ODT and we apply a sweeping pulse spanning 500 kHz and centered at 81.9297 MHz to transfer atoms from $|2\rangle$ to $|3\rangle$ at a magnetic field of 795 G. As a result, we obtain a $|1\rangle - |3\rangle$ mixture. The population in $|3\rangle$ is measured as a function of sweep time as illustrated in Fig. 3.14(c). As can be seen, a long sweep time completely transfers to the other state with a fidelity exceeding 95%.

3.7 Light sheet

Cold atoms trapped in an optical dipole trap naturally form a 3d cloud which does not meet the requirements for microscopy applications. To address this, atoms are prepared in a single plane, particularly for 2d systems, a strongly oblate cloud shape is necessary, referred to as a light sheet. The light sheet beam is derived from the zeroth order of the optical dipole trap AOM and the light sheet can reach powers of up to 100 W although the typical power used is 24 W. The beam waist is $(w_{0x}, w_{0y}, w_{0z}) = (50, 70, 4.2)$ µm with $p-$polarization. The setup of the light sheet is shown in Fig. 3.11. The light sheet can be treated as the elliptical Gaussian beam propagating along the y-axis in Cartesian coordinates, as demonstrated in Fig 3.15(a). The beam intensity is given by

$$I(x, y, z) = I_0 \left(\frac{w_{01}}{w_1(y)}\right) \left(\frac{w_{02}}{w_2(y)}\right) \exp\left[-2\left(\left(\frac{x}{w_1(y)}\right)^2 + \left(\frac{z}{w_2(y)}\right)^2\right)\right], \tag{3.19}$$

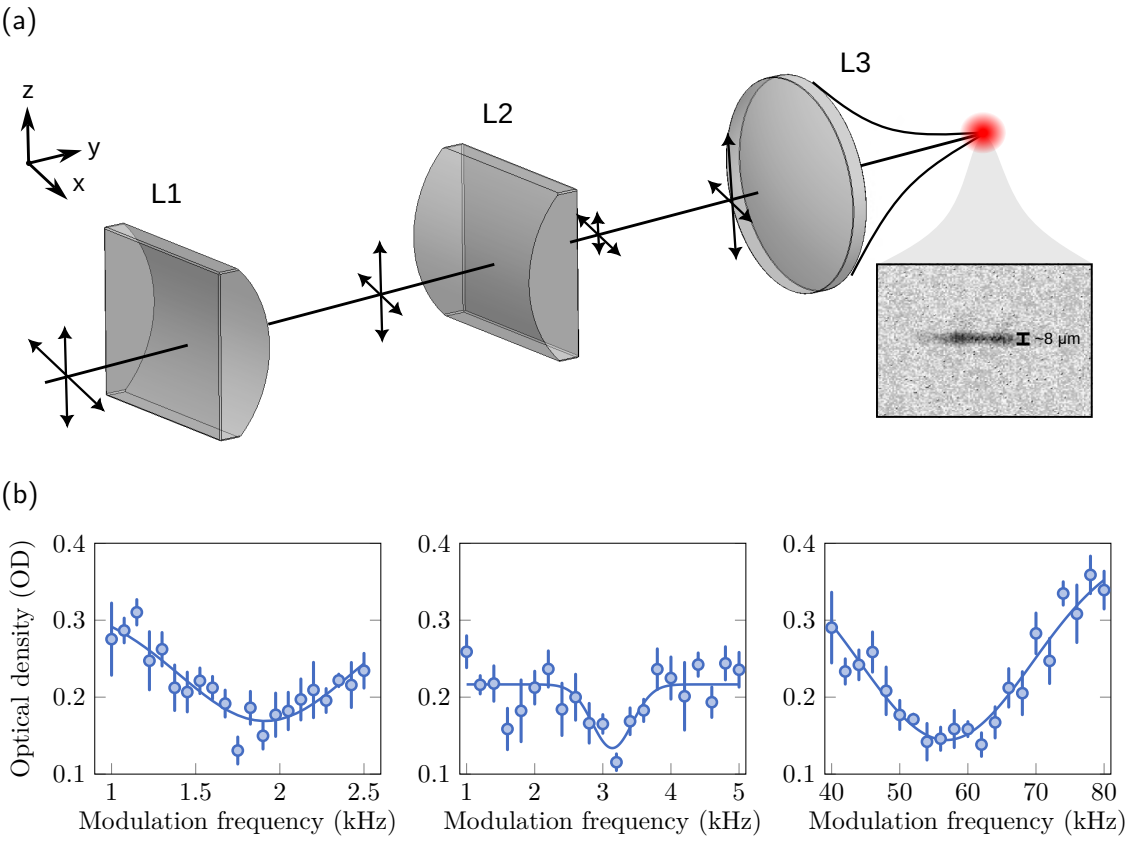

Figure 3.15: **Light sheet schematic and amplitude modulation spectroscopy.** (a) The creation of an oblate beam using two cylindrical lenses (L1, L2) and the beam is tightly focused to the atom position by an aspheric lens (L3). Arrows along the propagation direction indicate the beam size in vertical and horizontal directions. The inset presents the absorption imaging of the light sheet. More details on the setup can be found in Fig 3.11. (b) Amplitude modulation spectroscopy. Three resonances are observed using a power of $800\,\mathrm{mW}$, corresponding to a longitudinal frequency of $950(10)$ Hz and two transverse frequencies of $1.6(1)$ kHz and $29(2)$ kHz. Note that the trap frequency is half of the modulation frequency due to the parametric heating process [99]. Error bars are the standard error of the mean. Based on Eqs. 3.20 and 3.21, we expect that trap frequencies are $(1.2, 1.7, 28.9)$ kHz.

where the maximum intensity is $I_0 = 2P_0/(\pi w_{01} w_{02})$, P_0 is the beam power, beam waist $w_i = w_{0i}\sqrt{1 + (y/y_{Ri})^2}$, Rayleigh range in free space is $y_{Ri} = \pi w_{0i}^2/\lambda$, and w_{0i} is the beam waist at focus position.

To determine the trap frequency of the light sheet, We expand Eq. 3.19 as a series about either $x = 0$ or $z = 0$ at the focus position ($y = 0$) up to the second order. Equating the coefficient of the second order to that of a harmonic oscillator, allows us to determine the radial trap frequency, expressed as

$$f_{x,z} = \frac{1}{\pi w_{0x,0z}} \sqrt{\frac{2P_0\eta_{\text{dip}}}{m\pi w_{0x} w_{0z}}}. \tag{3.20}$$

Similarly, the longitudinal frequency is the trap frequency along the propagation direction and can be calculated by expanding about $y = 0$ while keeping $x = z = 0$, leading to

$$f_y = \frac{\lambda}{2\pi^2} \frac{\sqrt{w_{0x}^4 + w_{0z}^4}}{w_{0x}^2 w_{0z}^2} \sqrt{\frac{2P_0\eta_{\text{dip}}}{m\pi w_{0x} w_{0z}}}, \tag{3.21}$$

where η_{dip} is the conversion factor between intensity and dipole potential.

The creation of a light sheet using a system of cylindrical lenses is illustrated in Fig. 3.15. The trap frequency of the light sheet is verified by performing amplitude modulation spectroscopy and we compare it with the trap frequency calculated from the elliptical Gaussian beam as discussed in Eqs. 3.20 and 3.21.

3.8 Bottom beam

In the context of the light sheet and the optical dipole trap, their trap frequencies in the xy-plane are asymmetric due to their shapes. To achieve symmetry for 2d Fermi gas systems, we require uniform radial confinement. This is achieved using a 1070 nm laser propagating upward, referred to as the bottom beam. It provides uniform radial confinement with a beam waist of approximately 110 µm and a maximum power of 2 W. We confirm its properties by performing amplitude modulation spectroscopy in Fig. 3.16. In fact, the bottom beam facilitates atom loading to the accordion lattice, a 1d lattice in the vertical direction as discussed in Section 3.9. The bottom

beam provides an attractive force to hold the atoms and prevents them from being lost from the trap due to the presence of repulsive forces caused by the blue-detuned laser of the accordion lattice.

The setup of the bottom beam before and after the coupling to a high-power fiber (P5-1064HE-2) is illustrated in Figs. 3.5 and 3.11. We align the beam to the fiber at a lower power and optimize for higher power. Consequently, we achieve a fiber coupling efficiency of approximately 50% at both low and high power. We avoid the retroreflections from the viewports creating disturbances at the atom position by tilting the bottom beam a few degrees. In the upcoming section, we present the essential potential for studying 2d systems.

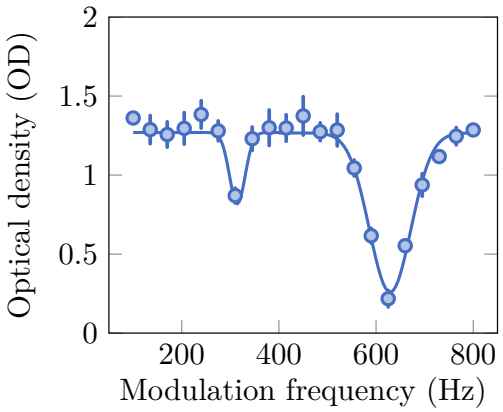

Figure 3.16: **Bottom beam spectroscopy.** Amplitude modulation is applied to the bottom beam with a power of 2 W, resulting in a trap frequency of approximately $(2\pi)\times 315$ Hz. The first dip is attributed to the excitation of subharmonics. Error bars are standard errors of the mean.

3.9 Accordion lattice

To allow for high-resolution imaging, we focus on 2d systems as our area of interest. We achieve a quasi 2d system by confining atoms to the ground state of the third dimension, saying in the vertical direction, where this condition satisfies $\hbar\omega_z \gg \hbar\omega_y, \hbar\omega_x$. Here, $\hbar\omega$ is the quantized energy of a quantum harmonic oscillator. To address this, we implemented the accordion lattice, a 1d optical lattice, similar to those described in [100–102]. The lattice is formed by a 532 nm laser and the discussion of generating this laser is detailed in Section 3.9.1. It is important to note that the light sheet cannot achieve 2d gases because its vertical confinement is not sufficiently strong, and the potential is non-uniform. This can be confirmed by

filling energy levels in the trap with fermions.

The concept of creating the accordion lattice involves crossing two laser beams at a variable angle, allowing for tunable lattice spacing. Smaller lattice spacing corresponds to a larger trap frequency at a fixed power. This can be viewed as the 1d potential being steeper, causing atoms to experience a stronger potential gradient in the trap. For further detail, let us consider the two plane waves with identical electric field amplitudes, E_0, given by

$$\mathbf{E}_1 = E_0 e^{-i(\mathbf{k}_1 \cdot \mathbf{r} + \omega t)}\, \hat{\mathbf{e}}_1, \tag{3.22}$$

$$\mathbf{E}_2 = E_0 e^{-i(\mathbf{k}_2 \cdot \mathbf{r} + \omega t)}\, \hat{\mathbf{e}}_2, \tag{3.23}$$

where $\hat{\mathbf{e}}_i$ represents the direction of electric field, $\mathbf{k}_i$ is the wavevector, and ω is the angular frequency. The setup illustrating the definition of Eqs. 3.22 and 3.23 is shown in Fig. 3.17(a).

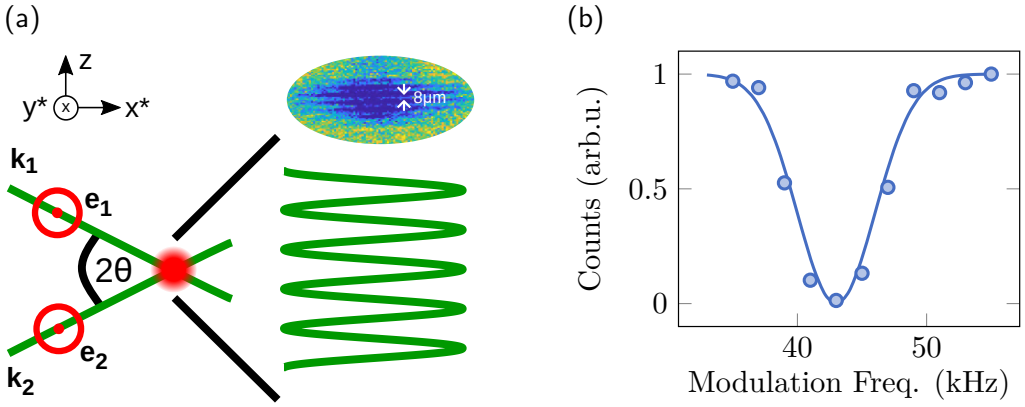

Figure 3.17: **Crossing beams.** (a) Two green beams with a wavelength of $532\,\mathrm{nm}$ are generated by frequency doubling and both beams cross at the atom position. By adjusting the proper polarization and crossing angle, we obtain the interference pattern shown in the inset with the largest spacing of $8\,\mu\mathrm{m}$. This 1d potential is referred to as the accordion lattice. (b) Amplitude modulation spectroscopy of the accordion lattice. The trap frequency is $(2\pi)\times 22\,\mathrm{kHz}$.

A strong contrast of the interference pattern is obtained by adjusting the half-waveplates such that the polarizations of the two beams are parallel to the optical table, leading to $\hat{\mathbf{e}}_1 \cdot \hat{\mathbf{e}}_2 = 1$. The total intensity is expressed as

$$I = \frac{1}{2}\varepsilon c \left(2E_0^2 + E_0^2 e^{-i(\mathbf{k}_2 - \mathbf{k}_1)\cdot\mathbf{r}} + E_0^2 e^{i(\mathbf{k}_2 - \mathbf{k}_1)\cdot\mathbf{r}}\right). \tag{3.24}$$

To simplify Eq. 3.24, we apply the fact that $\mathbf{k}_1$ and $\mathbf{k}_2$ have identical components, except for the vertical component, which points in opposite directions. This results in $\mathbf{k}_2 - \mathbf{k}_1 = 2|\mathbf{k}| \sin\theta \ \hat{z}$ where 2θ represents the crossing angle. Here, we obtain

$$I = I_0 \cos\left(\frac{2\pi}{a} z\right) + \text{offset}, \tag{3.25}$$

where I_0 is the maximum intensity and $a \equiv \lambda/(2\sin\theta)$ is the lattice spacing. As can be seen, the crossing angle determines the lattice spacing. As θ approaches $\pi/2$, it represents two identical waves with the same frequency propagating in opposite directions, leading to the formation of a standing wave with a spacing of $\lambda/2$.

3.9.1 Frequency doubling

To form the accordion lattice from the 532 nm laser, we generate the laser light by frequency doubling of the 1064 nm beam derived from the zeroth order of the square lattice AOM (Fig. 3.18(a)). We focus the beam waist of 30 µm onto the front face of the crystal (PPMgSLT, OXIDE Corporation) to minimize thermal lensing. The mount of the crystal attached to the thermoelectric cooler (TEC) is shown in the left inset of Fig. 3.18(a). We measure the second harmonic power as a function of seed power in Fig. 3.18(b). The maximum output power of 3 W is obtained at an optimal temperature of 44.0° (Fig. 3.18(c)) with a wavelength of 532 nm using a seed power of 16 W. Our fiber coupling has an efficiency of 60% in both low and high power, no saturation is observed. The mixture of 532 nm and 1064 nm lights is separated by a dichroic mirror (DMLP900). However, we observe that 1064 nm light is not fully suppressed. To prevent the residual light from the 1064 nm laser, a low pass filter (FESH0550) is added to the beam path. The 532 nm beam is coupled to a fiber (P3-488PM-FC-1) for the purpose of polarization cleaning. We add a motor shutter

in front of the fiber. The shutter is designed to automatically close within 6 s after a trigger to protect the fiber tip from excessive heating. Overall, we can obtain a maximum power of approximately 1.8 W at the other end of the fiber (Fig. 3.19). At this point, we have prepared the 532 nm laser for the accordion lattice. In the subsequent section, the setup of the lattice is detailed.

3.9.2 Accordion lattice setup

On the other end of the fiber, we prepare the accordion lattice beam as follows: We use a 400 mm cylindrical lens to focus the beam waist down to 80 µm at the center of the acoustic optical deflector (AOD). The schematic of the setup is shown in Fig. 3.19. Here, we tilt the beam upward by the mirror before the AOD and the AOD vertically deflects the beam. We use the first order that has a deflection angle depending on a driven frequency from 95 MHz to 105 MHz with a maximum efficiency of 80%. After the AOD, a $4-f$ system is implemented, consisting of of a 750 mm lens and a 150 mm cut lens to demagnify the beam by a factor of five at the atom position. The cut-lens is mounted on the rock-stone-obelisk shape attached to a translation stage (XRN25P), as shown in the right inset of Fig. 3.19. The tower indicated by the bottom inset of Fig. 3.19 contains a beamsplitter to split a single beam into two identical beams. The separation of the two beams is determined by the height of the input beam to the tower. The two mirrors after the tower adjust the beam parallel to the optical table (the top inset of Fig. 3.19).

We initially perform a coarse alignment of the accordion lattice using the optical dipole trap by changing the accordion lattice beams to cross-polarization, which results in no interference. We observe a hole at the center of the ODT due to the repulsive forces experienced by the atoms from the crossing of the accordion beams. To optimize loading, we adjust the accordion lattice to maximize the number of atoms loaded from the light sheet. For precise alignment, we modulate its intensity and search for the position where it exhibits the highest trapping frequency. This position serves as our best estimate for the center of the accordion lattice.

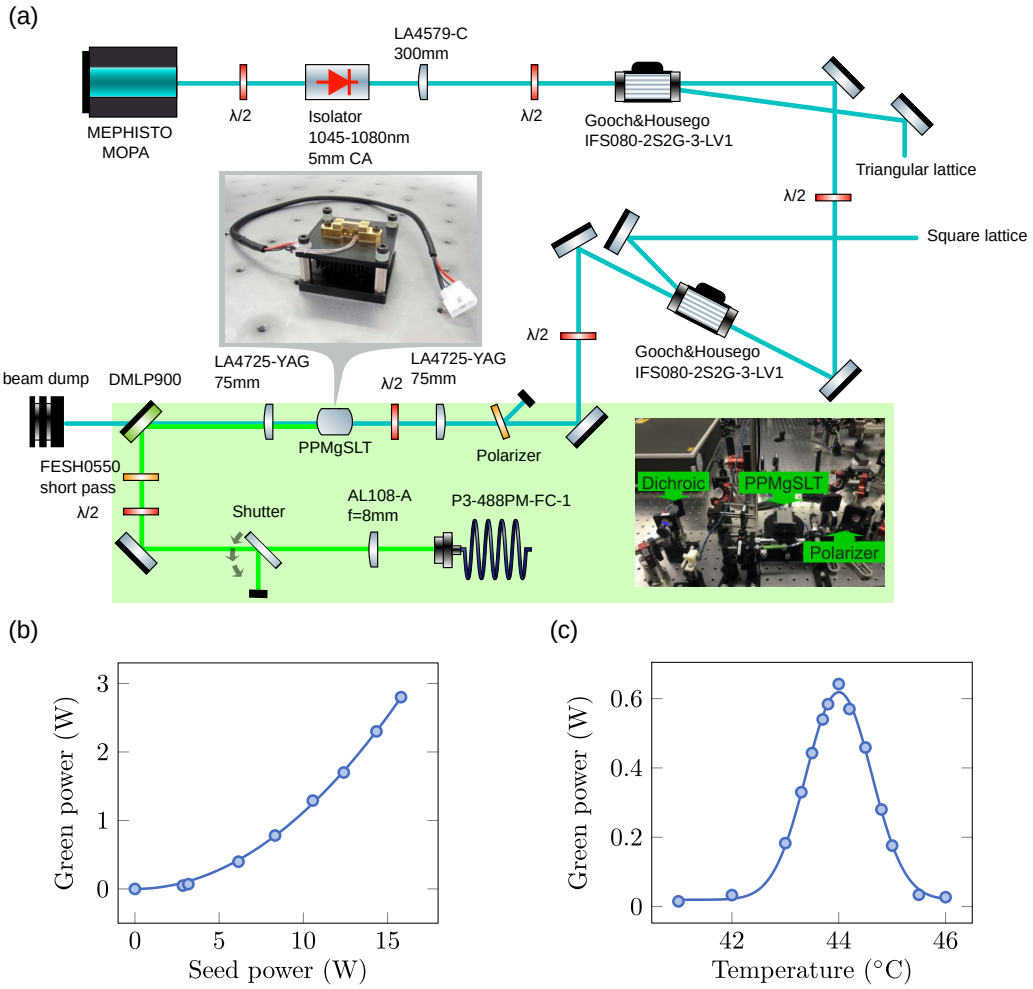

Figure 3.18: **Frequency doubling.** (a) Schematic of the frequency doubling setup. The seed laser is derived from the zeroth order of the square-lattice AOM. The center inset is a rendered image of a quasi-phase-matching (QPM) crystal mount with a thermoelectric cooler (TEC), taken from [103]. The bottom right inset is the image of the frequency doubling setup. (b) Second harmonic generation as a function of seed power. The blue dots represent the data and the solid line is the fit to the square of power, as expected for the 2$^{\text{nd}}$ harmonics process. (c) Second harmonic generation as a function of the crystal temperature. The data points are represented by dots, and the solid line is fit to a Gaussian function. The seed power is set to 8 W.

In the experiment, our 3d gas is compressed into a 2d regime by loading atoms from the light sheet into a single layer of the accordion lattice confined by the bottom

beam. We confirm the single layer by increasing the spacing for a short time and observing the time of flight measurement. The initial lattice spacing is 8 µm for capturing as many atoms as possible. After loading to the layer, we completely turn off the light sheet potential and shrink the spacing down to 3 µm where the trap frequency is $(2\pi)\times 22$ kHz. This trap frequency is measured by amplitude modulation spectroscopy using a single-site resolution shown in Fig. 3.17(b).

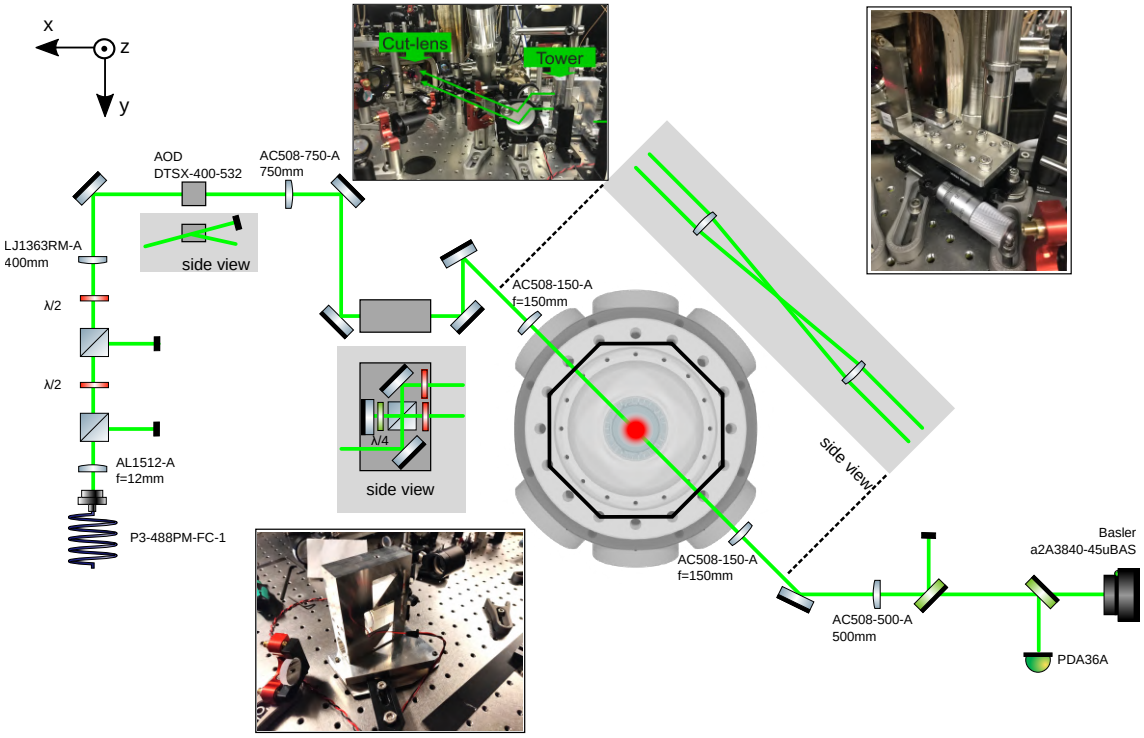

Figure 3.19: **Accordion lattice setup.** The schematic of the accordion lattice setup is illustrated. The bottom inset indicates the tower used to split the accordion lattice beam. In the right inset, the translation stage mounted by the cut-lens is shown with the cut-lens hidden behind the mount. The top inset shows an image of optical components after the tower, where two parallel beams are focused by the cut-lens to the atom position.

To verify the degenerate Fermi gases, we measure the atomic density in the light sheet and the accordion lattice shown in Figs. 3.20(a,b). The properties of the 2d Fermi gas confined in the accordion lattice are determined by fitting to Eq. C.27 while the atoms in the light sheet are fitted to a 3d Fermi gas because atoms occupy

higher levels than the ground state of the third dimension of a harmonics oscillator. We find that fitting elongated light sheet clouds is not trivial for the elliptical azimuthal average. To address this, we opt for a more effective approach by fitting the center cross-section instead. The temperature, expressed in terms of the Fermi temperature, is obtained from the fit and we determine the Fermi temperature using the known atom number and trap frequency. For reference, the atom number in different stages of experiments is tabulated in Table. 3.1 including temperature and phase space density. Now, we have almost all the necessary pieces to study Hubbard physics. Hereafter, we will primarily discuss how optical lattices can be created in the experiment.

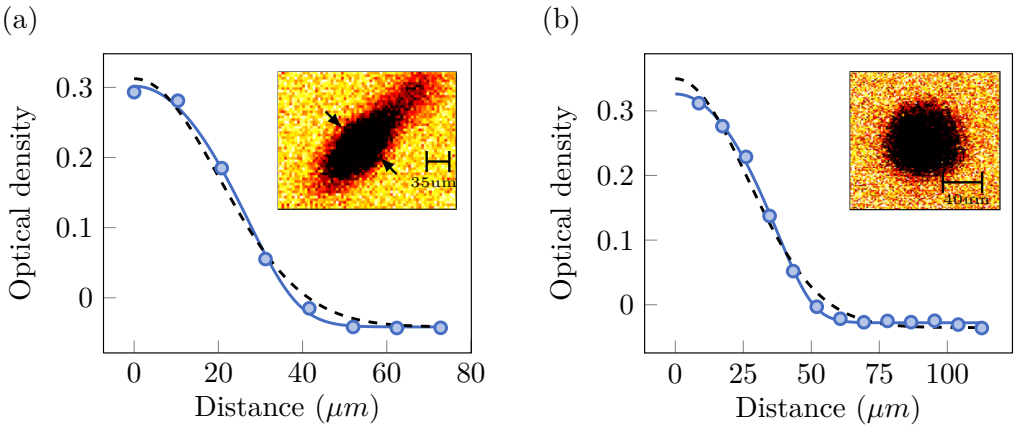

Figure 3.20: **Fermi gas in light sheet and accordion lattice.** (a) Fermi gas cross-section in the light sheet. The fit is aligned along the minor axis of the light sheet (indicated by arrows in the inset). The data points (blue dot) are fitted to the 3d Fermi gas model (blue solid line), a Gaussian fit (black dashed line). From the fit, we extract the temperature of $0.20\,\mathrm{T_F}$ where $\mathrm{T_F}$=3.5 µK and an atom number is 12,000 for a single spin component. The trap frequency of the light sheet at low power is $\omega = 2\pi \times (0.5, 0.8, 12)$ kHz. (b) An azimuthal average of 2d Fermi gas in both the accordion lattice and the bottom beam potentials. We extract a temperature of $0.35\,\mathrm{T_F}$ from the 2d Fermi gas fit where $\mathrm{T_F}$=2.5 µK with 10,000 of atoms. Error bars are smaller than the size of the dots. Note that the Fermi gas fit to the cross-section of (b) provides a temperature that agrees with the azimuthal fit.

	Atom number	Density(cm^{-3})	Temperature(μK)	Phase space density
MOT	4×10^8	2×10^9	2200	6×10^{-9}
CMOT	2.5×10^7	2×10^{10}	400	9×10^{-7}
ODT	5×10^5	1×10^{12}	200	1×10^{-4}
Free evap.	5×10^5		50	
Evap. ODT I	3×10^5		4	
Evap. ODT II	5×10^4	1×10^{12}	0.2-4	0.002-0.2
Light sheet	2×10^4	1.4×10^{12}	2	
Evap. Light sheet	1.5×10^4	1.1×10^{12}	0.3-2	
Accordion lattice	1×10^4	3×10^{12}	0.3-0.8	
Evap. accordion lattice [a]	$< 2.5 \times 10^3$		0.2-0.02	

Table 3.1: **Degenerate Fermi gas of one spin component in different stages.** Time of flight measurement is used to determine the temperature of a 3d cloud from the MOT to the second evaporation in the ODT. When the atomic cloud is in a 2d potential like an accordion lattice combined with a bottom beam, we use a 2d Fermi gas fitting. Density is extracted from absorption imaging.

[a] The atom number is determined by single-site imaging. Temperature is extracted from the Mott insulator fitting.

3.10 Triangular lattice

The last of the essential components for a quantum gas microscope is the optical lattices, which trap the atoms in an array of potential wells. These lattices provide a well-defined and controllable environment for the atoms. This setup allows for studying the Hubbard model, as discussed in Chapter 1, where ultracold atoms on optical lattices serve as a versatile platform for simulating and understanding complex quantum many-body systems. Here, I explain how the triangular lattice is formed using a recycled-beam approach, which facilitates a simple switch to square lattices.

In the experiment, we utilize the Mephisto MOPA, emitting light at a wavelength of 1064 nm, to create optical lattices. As shown in Fig. 3.21, the lattice beam propagates to an isolator which prevents retroreflections to the laser source. The first order of the AOM (Gooch&Housego IFS080-2S2G-3-LV1) is used to generate the triangular lattice beam while the zeroth-order output is directed to the second AOM. The triangular-lattice AOM operates at a frequency of 79.949 MHz for optimal efficiency. The first-order output of the second AOM is used for creating square lattices whereas the zeroth-order output is directed to the frequency doubling. It is worth noting that irregularities may occur in the lattice beam profile when the Mephisto MOPA operates at low power. For alignment purposes, such as aligning the triangular lattice, we apply full power to the triangular-lattice AOM and adjust the first-order output to the desired power level.

The first triangular lattice beam is prepared as illustrated in the inset of Fig. 3.21. The lattice beam is reflected down to the bottom layer of the optical table. To form the triangular lattice, all three lattice beams propagate from the negative z-direction (down) to the positive z-direction (up) at an angle of 45° out of the xy-plane through the science chamber (Fig. 3.22). Their projections onto the xy-plane intersect each other at an angle of 120.0(6)°. The power for each beam is 42 W, 40 W, and 38 W, respectively, due to losses caused by optics during the recycling.

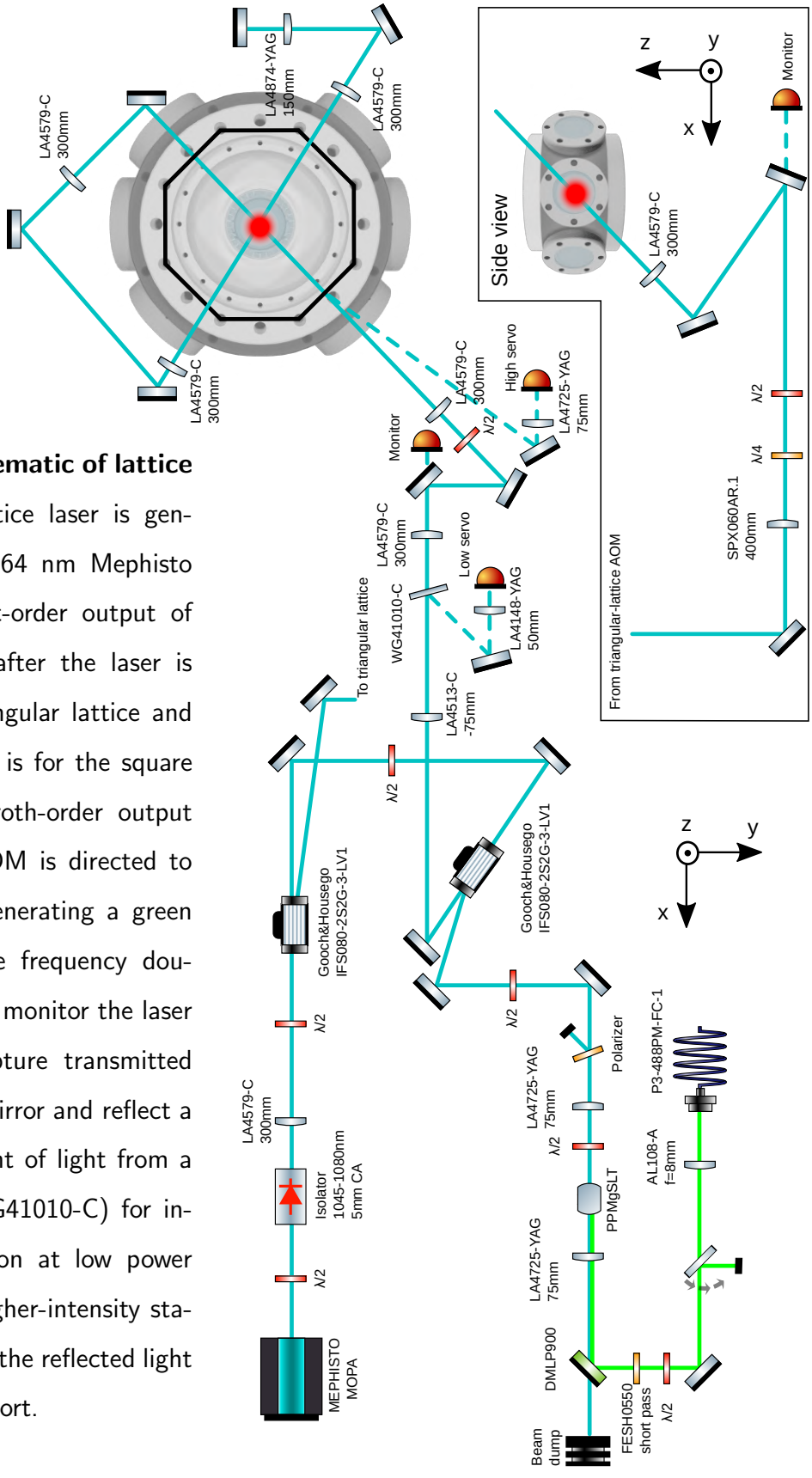

Figure 3.21: **Schematic of lattice setup.** The lattice laser is generated by the 1064 nm Mephisto MOPA. The first-order output of the AOM right after the laser is used for the triangular lattice and the second AOM is for the square lattice. The zeroth-order output of the square AOM is directed to the crystal for generating a green laser through the frequency doubling process. To monitor the laser intensity, we capture transmitted light through a mirror and reflect a reasonable amount of light from a thin window (WG41010-C) for intensity stabilization at low power ($< 1\,\mathrm{W}$). For higher-intensity stabilization, we use the reflected light from a side viewport.

All three beams have a Gaussian beam waist of about 30 µm at the focus. This configuration leads us to a triangular lattice with a lattice spacing of $a_{\mathrm{latt}} = 1003\,\mathrm{nm}$. Note that the configuration for the triangular lattice is compatible with a standard octagon vacuum chamber, however, it requires meticulous consideration of objective mount and magnetic field coils, which can obstruct optical access (Fig. 3.22).

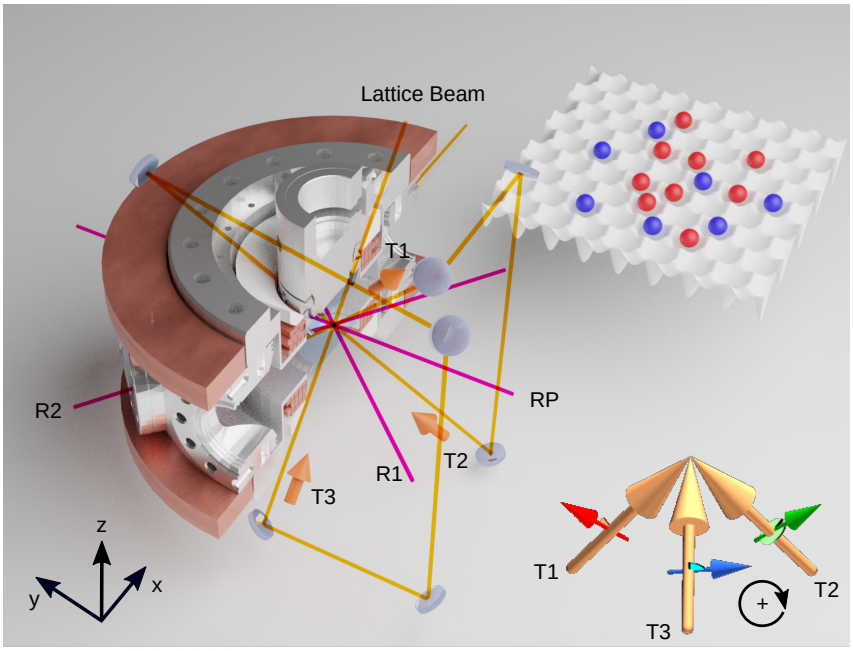

Figure 3.22: **Triangular lattice and Raman imaging beams.** (left) Sketch of triangular lattice and Raman sideband imaging beams and their alignment relative to the vacuum chamber. The stainless-steel octagon chamber is equipped with an outer copper coil pair for the MOT field and an inner coil pair for the Feshbach field. The triangular lattice is formed by recycling the lattice beam through the recessed top and bottom windows, leaving sufficient space for the objective at the top window. The second and third focus are created by 1:1 imaging system, which are not shown. Three orange arrows (T1, T2, and T3) indicate the direction of the three beams which cross at the position of the atoms where the triangular lattice is formed. The polarization configuration used for imaging in the lattice is illustrated in the bottom middle inset. The Raman cooling beams (R1 and R2) and the Raman repump beam (RP) are sent through the side windows. Figure was taken from previous work [84].

In addition, we have custom-designed anti-reflection coatings for the vacuum windows to reduce reflections at a 45° angle of incidence. These coatings can be achieved by carefully designing the coating thickness and refractive index regardless of the polarization state of the incident light. Since the interference pattern between the three crossing beams depends on both the wavevectors and polarizations, these parameters have to be carefully adjusted for each beam. The angles between the lattice beams are restricted to about 1° by the optical access and we use half-wave plates to control the polarizations of all lattice passes. For the experiments reported in [104], we adjusted these parameters to obtain the strongest possible interference pattern in the triangular lattice. We found that the lattice depth is maximal for incoming linear polarization angles of about 40°, −40°, and 80° for lattice beams L1, L2, and L3, respectively, relative to the vertical polarization closest aligned to the z-axis (Fig. 3.22).

Later, we realized that the sigma configuration of lattice beams allows us to obtain a symmetric triangular lattice which also exhibits the strongest interference contrast, enhancing the fidelity of fluorescence imaging.

3.10.1 Depth calibration of 1d optical lattices

To check the overlapping of two lattice beams, the most straightforward technique is using Kapitza-Dirac scattering. The working principle is based on the interaction between atoms and a standing light wave acting as a stationary field. When atoms pass through a periodic potential, the atoms experience the potential like a grating and are scattered [105]. This can be viewed as a momentum transferred from the standing wave to the atoms. The validity of Kapitza-Dirac scattering relies on the Raman-Nath approximation that neglects particle motion over the duration of the interaction. The interaction time τ is required to be extremely shorter than the inverse of recoil frequency ω_r, $\tau \ll 1/\omega_r$. This process is different from the Bragg scattering which requires the difference in wavevectors between incident and reflected light to be a reciprocal lattice vector of the periodic potential [106, 107].

Let us consider the standing wave that has a potential given by $V_0 \sin^2(k_L z)$ with a wavenumber $k_L = 2\pi/\lambda$. The potential is switched on and off by a duration τ. Here, we introduce dimensionless parameters,

$$\alpha \equiv (E_r^{(2)}/\hbar)\tau, \tag{3.26}$$

$$\beta \equiv (V_0/\hbar)\tau, \tag{3.27}$$

where $E_r^{(n)} = (n\hbar k_L)^2/(2m)$ represents the n-photon recoil energy. In the limit of Raman-Nath approximation, $\beta\alpha \ll 1$, the population of the n-th diffracted order is given by

$$P_n = J_n^2(\beta/2), \tag{3.28}$$

where J_n are Bessel functions of the first kind [108]. Derivations can be found in Appendix C.7.

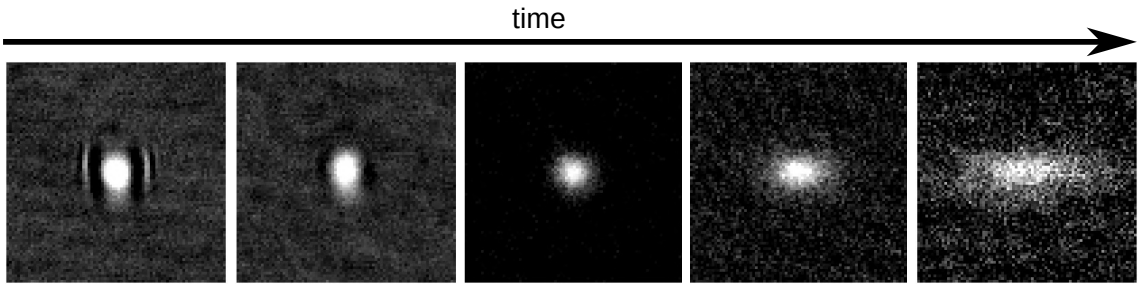

Figure 3.23: **mBECs time of flight.** The interaction of ^{6}Li is tuned to high interaction and a ^{6}Li pair forms a molecule that behaves like a boson. Each shot has 2 ms separation.

In the experiment, we prepare molecular Bose-Einstein condensates (mBECs) using a spin-balanced mixture of the two lowest hyperfine states. We sweep the Feshbach field at the vicinity of 810 G from high to low magnetic field and perform evaporation to achieve mBECs. To verify the mBECs, we employ the time of flight (TOF) for the cloud and illustrate the results in Fig. 3.23. The appearance of the cloud exhibits an inversion of aspect ratio as a function of time, indicating the presence of a condensed fraction. It is worth noting that the anisotropic shape at the initial time represents the isotropy of the trap potential, here, we perform the measurement in the optical

dipole trap. Next, we apply a pulse of the lattice beams and measure the population in momentum space using the TOF technique.

Later we realized that the lattice pulse is not perfectly square, and it is better to analyze by considering the pulse area $A = V_0\tau$. In fact, the lattice depth V_0 is proportional to the voltage V_i measured by a photodiode i.e., $V_0 = (2\hbar c)V_i$ where c is a constant. By fitting the zeroth order of the scattering to Eq. 3.28, we obtain the maximum 1d lattice depth of $732(152)\,\mathrm{E_r^{Tri}}$ at full power of approximately 40 W for the cross of two triangular-lattice beams (Fig. 3.24). Here, $\mathrm{E_r^{Tri}}$ denotes the recoil energy of the triangular lattice, which is equal to $h \times 8.2$ kHz, where h is Planck's constant.

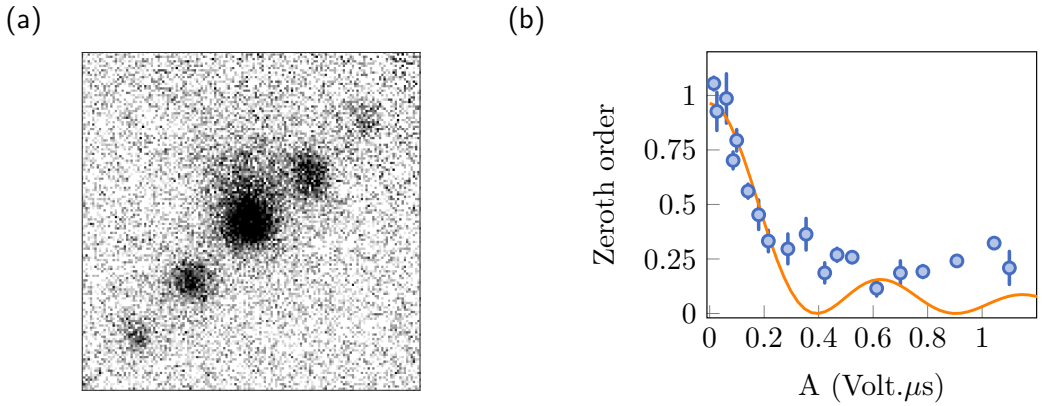

Figure 3.24: **1d Kapitza-Dirac scattering.** (a) Absorption image of the scattering generated by the interference of two triangular-lattice beams. The field of view is 260 µm × 260 µm. (b) The zeroth-order population is a function of the pulse area. The data (blue dots) are fitted to Eq. 3.28 which we treat c as a free parameter. The lattice depth is obtained using the relation $V_0 = (2\hbar c)V_i$.

3.10.2 Depth calibration of 2d optical lattices

When three triangular-lattice beams cross in a certain configuration, we can obtain a 2d triangular lattice. We simulate the 2d pattern based on the beam configuration that we have. To begin with, we apply the fact that the time evolution of Hamil-

tonian in the Raman-Nath regime can be approximated by $\exp[-i\tau V(\mathbf{r})/\hbar]$. The wavefunction at a later time τ can be written in terms of reciprocal lattices and is given by

$$e^{-\frac{i}{\hbar}\tau V(\mathbf{r})}\left|\Psi_0\right\rangle = \sum_{n_1=-\infty}^{\infty}\sum_{n_2=-\infty}^{\infty} c_{n_1,n_2} e^{i(n_1\mathbf{b_1}+n_2\mathbf{b_2})\cdot\mathbf{r}}\left|\Psi_0\right\rangle,$$

where $|\Psi_0\rangle$ represents the initial wavefunction and c_{n_1,n_2} is the scattering amplitude for diffraction order (n_1, n_2) such that

$$c_{n_1,n_2} = \int\int e^{-\frac{i}{\hbar}\tau V(\mathbf{r})} e^{-i(n_1\mathbf{b_1}+n_2\mathbf{b_2})\cdot\mathbf{r}} d\mathbf{r}.$$

Here, the probability being the order (n_1, n_2) is $P_{n_1,n_2} = |c_{n_1,n_2}|^2$. By solving for the analytic solution to the triangular lattice, the wavefunction after atoms are scattered by the lattice is given by

$$\begin{aligned}\left|\Psi\right\rangle &= e^{-iV(\mathbf{r})\tau/\hbar}\left|\Psi_0\right\rangle \\ &= e^{iV_0\tau/\hbar\cos(\mathbf{b_1}\cdot\mathbf{r})} e^{iV_0\tau/\hbar\cos(\mathbf{b_2}\cdot\mathbf{r})} e^{iV_0\tau/\hbar\cos(\mathbf{b_3}\cdot\mathbf{r})}\left|\Psi_0\right\rangle,\end{aligned} \tag{3.29}$$

where we use linear $s-$polarization to form the triangular lattice and here $V_0 = V_{12,ss} = V_{23,ss} = V_{13,ss}$ defined in Eq. 4.32 for a symmetric triangular lattice.

The population being in the (n_1,n_2) order is therefore

$$P_{(n_1,n_2)} = \left|\sum_{n_3=-\infty}^{\infty} i^{n_1+n_2-n_3} J_{n_1-n_3}(\frac{V_0\tau}{\hbar}) J_{n_2-n_3}(\frac{V_0\tau}{\hbar}) J_{n_3}(\frac{V_0\tau}{\hbar})\right|^2. \tag{3.30}$$

By picking up the zeroth order, $(n_1, n_2) = (0, 0)$, the density is expressed as

$$P_{(0,0)} = B\left|\sum_{n_3=-\infty}^{\infty} i^{-n_3} J_{n_3}^3(cA)\right|^2, \tag{3.31}$$

where A represents the pulse area. The lattice depth is expected to be $9V_0/2$ where the factor of $1/2$ takes into account the beam propagation direction $45°$ off-plane in the upward direction. Through fitting of the decay curve in the Fig. 3.25 to Eq. 3.31, we find a maximum lattice depth of approximately $5000\,\mathrm{E_r^{Tri}}$.

It is worthwhile noting that the asymmetry of the scattering from our triangular lattice shown in Fig. 3.25(a) was studied in more detail in [109] by considering the geometry phase. Recently, the diffraction pattern of honeycomb geometry has been demonstrated in [110].

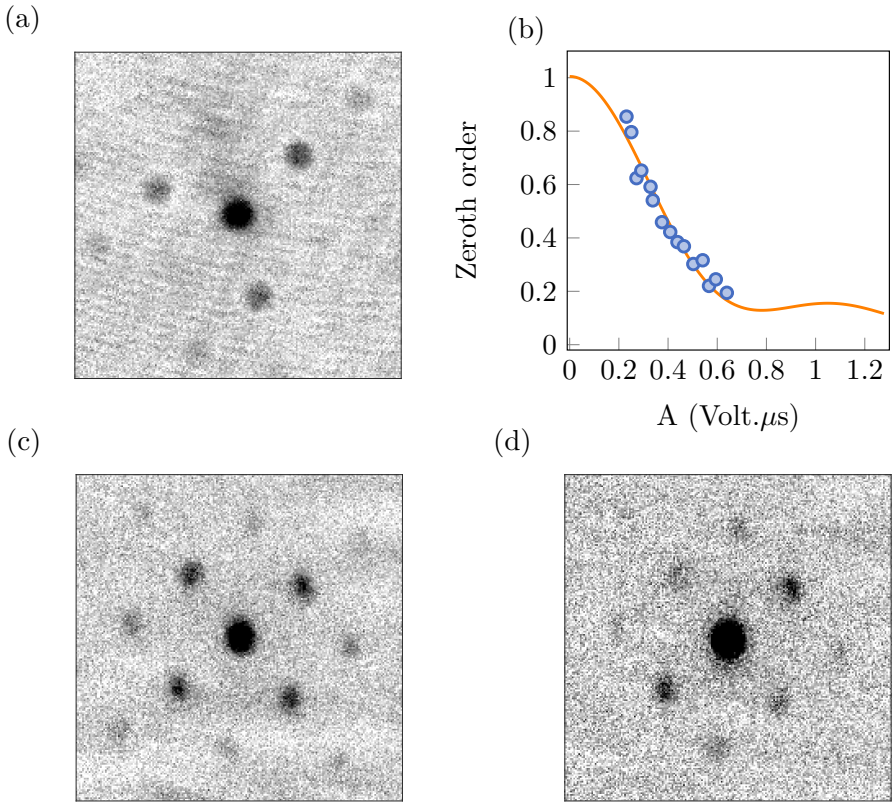

Figure 3.25: **2d Kapitza-Dirac scattering.** The scattering is generated by (a) a symmetric triangular lattice and (c) a square lattice. (d) An asymmetric square lattice is obtained by misaligning the lattice beams on purpose. The field of view is $160\,\mu\text{m}\times160\,\mu\text{m}$. (b) Zeroth-order population of triangular lattice scattering as a function of pulse area. Dots represent experimental data and the solid line is the fit to Eq. 3.31.

3.11 Square lattice

The triangular-lattice setup introduces additional complexity due to its non-trivial geometry in contrast to the square lattice, which offers a simpler and more intuitive geometry. Here, we implemented a versatile square lattice in the same experimental setup which can be superimposed with the triangular lattice. The square lattice setup can be used at 532 nm or 752 nm lattice spacing. Currently, we do not control the relative phase between the square lattices and the triangular lattice, however, this can be implemented by piezo mirror mounts and feedback from single-site re-

solved images of atoms in the individual lattices. We create the square lattices using the recycled lattice setup as described in [49, 111] (Fig. 3.26(a)). For vertical polarization, four-beam interference leads to a 752 nm spacing lattice, while an in-plane polarization creates a 532 nm spacing lattice. The power of the four passes is 41 W, 39 W, 37 W and 36 W, respectively, with a Gaussian beam waist of 70 µm. The trap depths are $1900\,E_r^{Sq,532}$ and $7500\,E_r^{Sq,752}$. Here, $E_r^{Sq,532}$ and $E_r^{Sq,752}$ denote the recoil energy of square lattices with lattice spacing of 532 nm and 752 nm, which are equal to $h \times 29.1$ and $h \times 14.6$ kHz, respectively. Trap frequencies are 1.36(2) MHz and 1.90(4) MHz for the 532 nm and 752 nm spacing lattices (Fig. 3.26(b)).

The square lattices have smaller lattice spacing than the triangular lattice, however, our reconstruction algorithm is able to determine the lattice occupation with an error only limited by the observed hopping and loss (Figs. 3.26(c,d)). We confirm this by comparing different fitting subroutines which lead to differences much smaller than the imaging infidelity. The 532 nm spacing lattice is imaged using the same Raman cooling configuration as the triangular lattice, while for the 752 nm square lattice the Raman beam R2 is the retroreflection of the incoming Raman beam R1, instead of the orthogonal configuration described above. For the triangular and 532 nm spacing square lattices with smaller trap frequencies, we observe that the orthogonal Raman beam configuration is necessary, however, for trap frequencies beyond 1.5 MHz, the retroreflected configuration works well. The square lattices have imaging fidelities of 84(3)% and 97(1)%, with detected filling up to 50%, in 532 nm and 752 nm spacing lattices, respectively.

Our imaging fidelity in the 532 nm spacing lattice is slightly lower than observed previously in a three-dimensional 532 nm spacing lattice, possibly caused by our weaker z confinement [47]. However, the imaging fidelity in the 752 nm spacing lattice is comparable with previous results [49]. Due to the large sideband frequency in our 752 nm spacing lattice, it would be possible to double the system size while maintaining sufficient lattice depth for high-fidelity imaging. Superimposing the triangular lattice with the square lattice can form a two-dimensional quasi-crystalline

lattice [112], which could be used to study many-body localization in a non-separable two-dimensional quasi-periodic lattice.

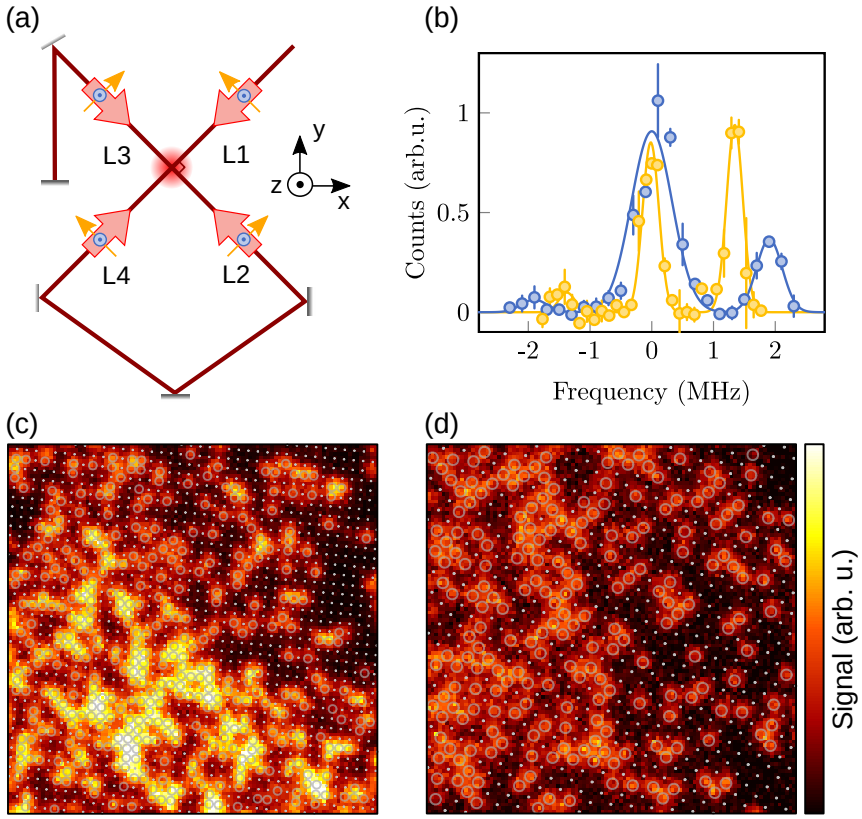

Figure 3.26: **Comparison to square lattices.** (a) Square lattice setup. Orange and blue arrows denote polarizations of $532\,\mathrm{nm}$ and $752\,\mathrm{nm}$ spacing square lattices, respectively. (b) Raman sideband spectra in $532\,\mathrm{nm}$ spacing (orange) and $752\,\mathrm{nm}$ spacing (blue) square lattice. The dots denote experimental data and solid lines are Gaussian fits. The sidebands are at $1.36(2)\,\mathrm{MHz}$ and $1.90(4)\,\mathrm{MHz}$ for $532\,\mathrm{nm}$ and $752\,\mathrm{nm}$ square lattices, respectively. The asymmetry of the sidebands shows that the atoms are predominantly in the 2d vibrational ground state after loading into the lattice. We find average number of vibrational quanta per dimension in 2d of $0.1(1)$ in the $532\,\mathrm{nm}$ lattice and $0.2^{+0.8}_{-0.2}$ in the $752\,\mathrm{nm}$ lattice. (c-d) Single-site-resolved images of ^{6}Li atoms with lattice structure overlay in the $532\,\mathrm{nm}$ spacing and $752\,\mathrm{nm}$ spacing lattice, respectively. The gray circles indicate occupied lattice sites. For the $532\,\mathrm{nm}$ lattice, the Raman configuration is the same as for the triangular, however, for the $752\,\mathrm{nm}$ lattice we use counter-propagating Raman beams. Figure was taken from previous work [84].

Our setup is prepared to superimpose both lattices by splitting the laser power between both simultaneously realized optical paths and will be capable of studying such systems on the single-atom level. We note that phase locking the lattices in our experiment is not required because the lattice beams are generated by the same laser source.

Chapter 4

The Triangular-Lattice Fermi-Hubbard Model

The Fermi-Hubbard model is a versatile platform for studying strongly correlated systems. To simulate quantum materials using ultracold-atomic systems, we are required to establish a connection between condensed matter theory and cold atom theory. This chapter presents the relevant background for studying the Fermi-Hubbard model with ultracold atoms in optical lattices, along with the observable quantities measured in experiments. The first section introduces a simple model of energy level in a solid-like system due to the overlapping of atomic orbitals in optical lattices, thus forming a band structure. Next, Wannier functions are discussed to construct localized wavefunctions that represent the electronic states in a crystal. Later, I present the Fermi-Hubbard model used to study the behavior of strongly correlated systems, where the interplay between atom motion and interaction plays a significant role. Limiting cases like the Mott insulator and non-interacting gas are discussed for this model. Finally, I indicate observable quantities typically used to determine the system's properties.

4.1 Band structure

The band structure plays a crucial role in comprehending the electronic properties of materials. It offers insights into the distribution of electrons across energy levels, or bands, within a solid material. The concept of band structure provides explanations of phenomena such as insulators, conductors, and semiconductors, thereby illuminating the diverse electrical behaviors exhibited by different materials.

For both condensed matter and optical lattice systems, the band structure exhibits different characteristics depending on the lattice structure. In this context, we will proceed by establishing a foundational understanding of band structure in 1d optical lattices, subsequently delving into higher dimensions like the 2d optical lattice, a focal point of this dissertation.

4.1.1 Band structure in 1d

A one-dimensional lattice is described by a periodic potential, $V_{\text{latt}} = V_0 \sin^2(k_L x)$, where V_0 is the lattice depth, the lattice spacing is $d = \lambda_L/2 = \pi/k_L$, lattice momentum $\hbar k_L$, and recoil energy associated with lattice spacing is $E_R = \hbar^2 k_L^2/2m_a$, given the laser wavelength λ_L and the mass of the atom m_a. In the following, the derivation and calculation are adapted from ref. [113]. Let $\hat{T}_d$ be the translational operator that translates the position by d, expressed as

$$\hat{T}_d = \exp(i\hat{p}d/\hbar), \tag{4.1}$$

where $\hat{p}$ is the momentum operator. We note that the eigenstate of $\hat{T}_d$ in real space, saying $u(x)$, is a periodic function with a period of d. The translational operator commutes with the lattice potential because the lattice is invariant under a translation by an amount of lattice spacing d,

$$\left[\hat{T}_d, \hat{V}_{\text{latt}}\right] = 0. \tag{4.2}$$

This implies the commutation of Hamiltonian, $\hat{H} = \hat{p}^2/2m_a + \hat{V}_{\text{latt}}$, and translational operator $\hat{T}_d$,

$$\left[\hat{T}_d, \hat{H}\right] = 0. \tag{4.3}$$

Let $|\phi\rangle$ be an eigenstate of the Hamiltonian. The projection onto position space $\langle x|\phi\rangle$ is $\phi(x)$ and the translation of ϕ by d in position space is given by

$$\langle x|\hat{T}_d|\phi\rangle = \phi(x+d). \tag{4.4}$$

According to Eq. 4.3, the eigenstate is invariant under the translational operator. In other words, they share the same basis. Therefore, the eigenstate of the Hamiltonian has to be written in the form of a plane wave multiplied by a periodic function,

$$\phi_{n,q}(x) = e^{iqx} u_{n,q}(x). \tag{4.5}$$

This expression is known as Bloch's theorem where $\phi_{n,q}$ is the Bloch wave, $u_{n,q}$ is the Bloch periodic function with period d, and q is the quantum number in momentum space. The value of q is in the first Brillouin zone and defined in range $[-k_L, k_L)$. We note that adding a phase e^{iqx} to $u(x)$ does not change the fact that it remains a solution to the Hamiltonian.

By expanding the periodic potential $V_{\text{latt}}(x)$ and the Bloch function $u_{n,q}(x)$ in terms of Fourier series, here we have

$$V_{\text{latt}}(x) = \sum_{m \in Z} \tilde{V}(m) e^{iQ_m x}, \tag{4.6}$$

$$u_{n,q}(x) = \sum_{m \in Z} \tilde{u}_{n,q}(m) e^{iQ_m x}, \tag{4.7}$$

where Q_m is defined as $2\pi m/d$ and m is an integer.

According to the time-independent Schrodinger equation,

$$-\frac{\hbar^2}{2m_a}\frac{d^2}{dx^2}\phi_{n,q}(x) + V_{\text{latt}}\phi_{n,q}(x) = E\phi_{n,q}(x). \tag{4.8}$$

We plug Eqs. 4.6, 4.7 into Eq. 4.8 and rewrite in terms of summations

$$-\frac{\hbar^2}{2m_a}\sum_{m\in Z}(iq+iQ_m)^2\tilde{u}_{n,q}(m)e^{i(q+Q_m)x}+\sum_{m\in Z}\sum_{m'\in Z}\tilde{V}(m')\tilde{u}_{n,q}(m)e^{i(Q_m+Q_{m'}+q)x} = \sum_{m\in Z}E_n\tilde{u}_{n,q}(m)e^{i(q+Q_m)x}. \tag{4.9}$$

By factorizing out $\tilde{u}_{n,q}(m)e^{i(Q_m+q)x}$, the expression becomes

$$\sum_{m\in Z}\left(\frac{\hbar^2}{2m_a}(q+Q_m)^2+\sum_{m'\in Z}\tilde{V}(m')e^{iQ_{m'}x}-E_n\right)\tilde{u}_{n,q}(m)e^{i(Q_m+q)x}=0. \tag{4.10}$$

To eliminate the complex exponential term, we multiply both sides by $\sum_{m''\in Z}e^{-i(Q_{m''}+q)x}$ and integrate over a unit cell

$$\left[\sum_{m\in Z}\sum_{m''\in Z}\frac{\hbar^2}{2m_a}(q+Q_m)^2\delta_{m,m''}+\sum_{m\in Z}\sum_{m'\in Z}\sum_{m''\in Z}\tilde{V}(m')\delta_{m+m',m''}\right]\tilde{u}_{n,q}=E_n\mathbb{1}\tilde{u}_{n,q}. \tag{4.11}$$

Here, it is convenient to represent this in matrix form, such as

$$\begin{pmatrix} \ddots & \vdots & \vdots & \vdots & \iddots \\ \dots & \frac{\hbar^2(q+Q_{m-1})^2}{2m_a} & \tilde{V}(-1) & \tilde{V}(-2) & \dots \\ \cdots & \tilde{V}(1) & \frac{\hbar^2(q+Q_m)^2}{2m_a} & \tilde{V}(-1) & \cdots \\ \dots & \tilde{V}(2) & \tilde{V}(1) & \frac{\hbar^2(q+Q_{m+1})^2}{2m_a} & \dots \\ \iddots & \vdots & \vdots & \vdots & \ddots \end{pmatrix}\begin{pmatrix} \vdots \\ \tilde{u}_{n,q}(m-1) \\ \tilde{u}_{n,q}(m) \\ \tilde{u}_{n,q}(m+1) \\ \vdots \end{pmatrix} = \left(\varepsilon_n(q)-\tilde{V}(0)\right)\begin{pmatrix} \vdots \\ \tilde{u}_{n,q}(m-1) \\ \tilde{u}_{n,q}(m) \\ \tilde{u}_{n,q}(m+1) \\ \vdots \end{pmatrix}. \tag{4.12}$$

This form resembles an eigenproblem, $AX = aX$, therefore, one can solve the characteristic equation and find the eigenenergy $\varepsilon_n(q)$ associated with q. An example is demonstrated in Fig. 4.1.

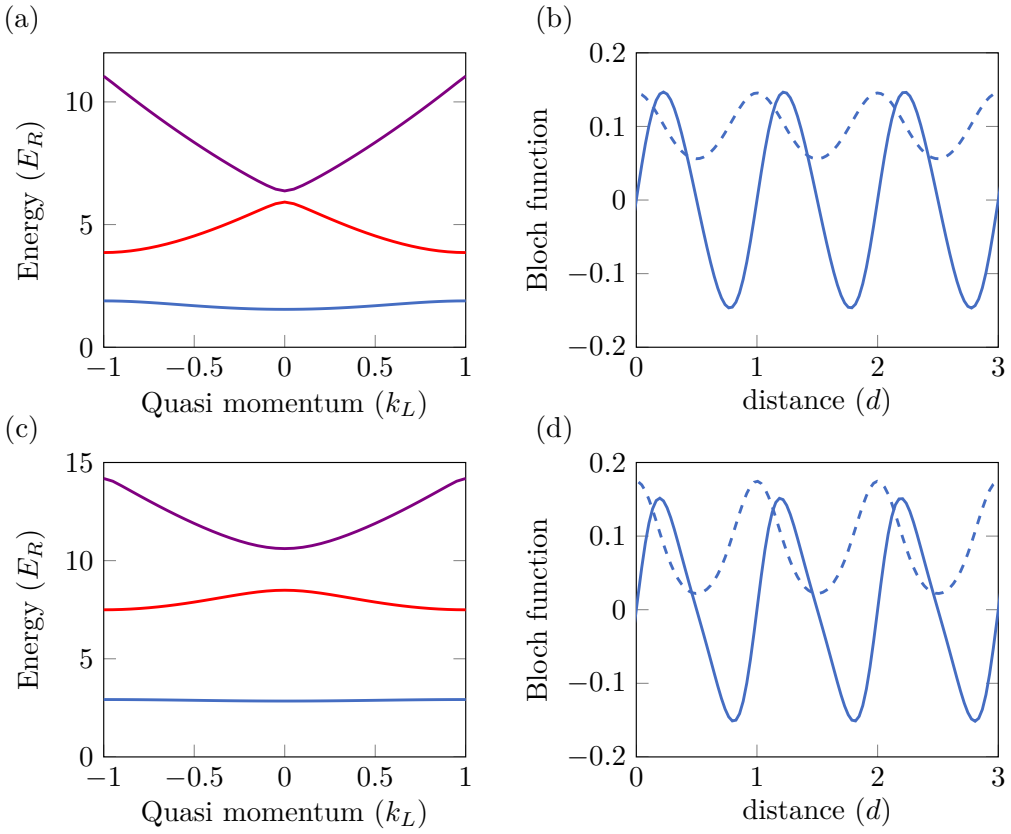

Figure 4.1: **Band structures and Bloch functions of a 1d lattice.** Band structure for $4\,\mathrm{E_R}$ (a) and $10\,\mathrm{E_R}$ (c). The blue, red, and violet solid lines are the ground band, first excited band, and second excited band. (b) Bloch functions for the ground and first excited bands at $q = 0$, $u_{0,0}$ (dashed line) and $u_{1,0}$ (solid line) are shown for a lattice depth of $4\,\mathrm{E_R}$. (d) the same as (b) with a lattice depth of $10\,\mathrm{E_R}$. Here, the potential $V_{\mathrm{latt}}(x) = V_0 \sin^2(\pi x/d)$ is used to generate a periodic potential over 30 lattice sites where V_0 is the lattice depth, d is the lattice spacing and $\mathrm{E_R} = \hbar^2/(2m_a)(\pi/d)^2$. The Fourier coefficients of this potential are $\tilde{V}(0) = V_0/2$ and $\tilde{V}(\pm 1) = -V_0/4$, and zero otherwise.

4.1.2 Band structure in 2d

Higher-dimensional band structures exhibit more interesting phenomena. For instance, in the honeycomb structure of graphite, there are six Dirac points between the lowest and the first excited bands, representing the touching points between

the valence and conduction bands, whereas complicated structures are not possible in one-dimensional (1d) systems. Moving to two dimensions (2d), we expect more complicated calculations to obtain the band structure and Bloch states. Note that 2d lattices can be simplified to the 1d calculation when the lattices are separable. In the following, we calculate the two-dimensional band structure, as discussed in ref. [114]. Here, the Bloch theorem remains valid for higher dimensions, therefore, the Bloch state at the crystal momentum $\mathbf{q}$ of the n^{th} band index is given by

$$\phi_{n,\mathbf{q}} = e^{i\mathbf{q}\cdot\mathbf{r}} u_{\mathbf{q},n}(\mathbf{r}), \tag{4.13}$$

where $u_{\mathbf{q},n}(\mathbf{r})$ is the periodic function. It can be expanded by the Fourier series as

$$u_{n,\mathbf{q}}(\mathbf{r}) = \sum_{m_1,m_2\in Z} \tilde{u}_{n,\mathbf{q}}(m_1,m_2) e^{i(m_1\mathbf{b}_1+m_2\mathbf{b}_2)\cdot\mathbf{r}}. \tag{4.14}$$

Similar to the periodic potential, it can be expressed as

$$V(\mathbf{r}) = \sum_{m_1,m_2\in Z} \tilde{V}(m_1,m_2) e^{i(m_1\mathbf{b}_1+m_2\mathbf{b}_2)\cdot\mathbf{r}}, \tag{4.15}$$

where Fourier coefficients are

$$\tilde{V}(m_1,m_2) = \int_{\text{a unit cell}} V(\mathbf{r}) e^{-i(m_1\mathbf{b}_1+m_2\mathbf{b}_2)\cdot\mathbf{r}}\, d^3\mathbf{r}. \tag{4.16}$$

By plugging $V(\mathbf{r})$ and $\phi_{n,\mathbf{q}}(\mathbf{r})$ into the Schrodinger equation

$$\left[-\frac{\hbar^2}{2m_a}\nabla^2 + V(\mathbf{r})\right]\phi_{n,\mathbf{q}} = \epsilon_{n,\mathbf{q}}\phi_{n,\mathbf{q}}. \tag{4.17}$$

The first term, representing kinetic energy, becomes

$$-\frac{\hbar^2}{2m_a}\nabla^2\phi_{n,\mathbf{q}}(\mathbf{r}) = \sum_{m_1,m_2\in Z} \frac{\hbar^2}{2m_a}\left(m_1\mathbf{b}_1 + m_2\mathbf{b}_2 + \mathbf{q}\right)^2 \tilde{u}_{n,\mathbf{q}}(m_1,m_2) e^{i(m_1\mathbf{b}_1+m_2\mathbf{b}_2+\mathbf{q})\cdot\mathbf{r}}, \tag{4.18}$$

and the second term, which describes the influence of the potential, is

$$V(\mathbf{r})\phi_{n,\mathbf{q}}(\mathbf{r}) = \sum_{m_1',m_2'\in Z}\sum_{m_1,m_2\in Z} \tilde{V}(m_1',m_2')\tilde{u}_{n,\mathbf{q}}(m_1,m_2) e^{i\left[(m_1+m_1')\mathbf{b}_1+(m_2+m_2')\mathbf{b}_2+\mathbf{q}\right]\cdot\mathbf{r}}. \tag{4.19}$$

One can show that the matrix elements of the kinetic energy and potential energy are

$$\begin{aligned} T_{\{m_1,m_2,\mathbf{q}\},\{n_1,n_2,\mathbf{s}\}} &= \int\limits_{\text{a unit cell}} e^{-i(n_1\mathbf{b}_1+n_2\mathbf{b}_2+\mathbf{s})\cdot\mathbf{r}} \left[-\frac{\hbar^2}{2m_a}\nabla^2 e^{i(m_1\mathbf{b}_1+m_2\mathbf{b}_2+\mathbf{q})\cdot\mathbf{r}}\right] d^3\mathbf{r} \\ &= \frac{\hbar^2}{2m_a}\left(m_1\mathbf{b}_1+m_2\mathbf{b}_2+\mathbf{q}\right)^2 \delta_{m_1,n_1}\delta_{m_2,n_2}\delta_{\mathbf{q},\mathbf{s}}, \end{aligned} \tag{4.20}$$

and

$$\begin{aligned} V_{\{m_1,m_2,\mathbf{q}\},\{n_1,n_2,\mathbf{s}\}} &= \int\limits_{\text{a unit cell}} e^{-i(n_1\mathbf{b}_1+n_2\mathbf{b}_2+\mathbf{s})\cdot\mathbf{r}} \\ &\quad\times \left[\sum_{m_1',m_2'\in Z} \tilde{V}(m_1',m_2') e^{i(m_1'\mathbf{b}_1+m_2'\mathbf{b}_2)\cdot\mathbf{r}}\right] e^{i(m_1\mathbf{b}_1+m_2\mathbf{b}_2+\mathbf{q})\cdot\mathbf{r}} d^3\mathbf{r} \\ &= \sum_{m_1',m_2'\in Z} \tilde{V}(m_1',m_2')\delta_{m_1+m_1',n_1}\delta_{m_2+m_2',n_2}\delta_{\mathbf{q},\mathbf{s}} \\ &= \tilde{V}(n_1-m_1,n_2-m_2)\delta_{\mathbf{q},\mathbf{s}}. \end{aligned} \tag{4.21}$$

The kinetic and potential energy matrices have dimensions higher than two and cannot be diagonalized in a normal way. Here, we map $\{m_1,m_2\},\{n_1,n_2\}$ to a 2d array and assume $\mathbf{q}=\mathbf{s}$ for quasimomentum. Let us consider constructing N^2 bands, where n_1,n_2,m_1,m_2 are integers, satisfying

$$-\frac{N-1}{2} \le n_1,n_2,m_1,m_2 \le \frac{N-1}{2}. \tag{4.22}$$

We introduce an index

$$u \equiv Nn_1+n_2+\frac{N^2+1}{2}, \tag{4.23}$$

which has values ranging from 1 to N^2. The inverse map from u to (n_1,n_2) is given by

$$n_1(u) = \left\lceil \frac{u}{N} \right\rceil - \frac{N+1}{2}, \tag{4.24}$$

$$n_2(u,n_1) = u - Nn_1 - \frac{N^2}{2} - \frac{1}{2}, \tag{4.25}$$

where $\lceil \dots \rceil$ denotes the ceiling function.

Similarly, the index v is introduced in the same manner

$$v \equiv Nm_1 + m_2 + \frac{N^2+1}{2}. \tag{4.26}$$

Therefore, the difference between u and v yields

$$u - v = N(n_1 - m_1) + (n_2 - m_2). \tag{4.27}$$

The above expression implies that any pairs $\{m_1, n_1\}, \{m_2, n_2\}$ specify the location of components u, v in the new matrix. For example, $(n_1 - m_1) = 1,\ (n_2 - m_2) = 1 \rightarrow\ u - v = N$ or $v = u - N$. The matrix element of new $N^2 \times N^2$ Hamiltonian is written as

$$\begin{aligned} H_{u,v} = H_{u,u-N} =& \frac{\hbar^2}{2m_a} \left(m_1\mathbf{b}_1 + m_2\mathbf{b}_2 + \mathbf{q}\right)^2 \delta_{m_1,n_1}\delta_{m_2,n_2} + \tilde{V}(1,1) \\ =& \frac{\hbar^2}{2m_a} \left(m_1\mathbf{b}_1 + m_2\mathbf{b}_2 + \mathbf{q}\right)^2 \delta_{m_1,m_1+1}\delta_{m_2,m_2+1} + \tilde{V}(1,1) \\ =& \tilde{V}(1,1). \end{aligned} \tag{4.28}$$

However, in the case of imposing $n_1 - m_1 = n_2 - m_2 = 0$, we have $u - v = 0$ and

$$H_{u,v} = H_{u,v=u} = \frac{\hbar^2}{2m_a} \left(m_1\mathbf{b}_1 + m_2\mathbf{b}_2 + \mathbf{q}\right)^2 + \tilde{V}(0,0). \tag{4.29}$$

By constructing $H_{u,v}$ for all possible n_1, n_2, m_1, m_2, the Hamiltonian reveals N^2 bands of the 2d lattice. In particular, we diagonalize the Hamiltonian to obtain eigenvectors and their associated eigenvalues. Let us denote an eigenvector corresponding to its eigenvalue $\lambda_{n,\mathbf{q}}$ for the band n^{th} as $[c_1(n,\mathbf{q}), c_2(n,\mathbf{q}), \ldots, c_{N^2}(n,\mathbf{q})]^T$. Note that eigenvalues obtained from numerical calculations have to be sorted before constructing the band structure. The band structure is finally generated by spanning $\mathbf{q}$ in the first Brillouin zone (e.g., $\mathbf{q} = \beta_1\mathbf{b}_1 + \beta_2\mathbf{b}_2$ with $0 \leq \beta_1, \beta_2 < 1$). In addition, the Bloch states of the band index n^{th} at lattice momentum $\mathbf{q}$ is

$$\phi_{n,\mathbf{q}}(\mathbf{r}) = e^{-i\mathbf{q}\cdot\mathbf{r}} \sum_{u=1}^{N^2} c_u(n,\mathbf{q}) e^{-i\mathbf{k}_u\cdot\mathbf{r}}, \tag{4.30}$$

where $\mathbf{k}_u = m_1(u)\mathbf{b}_1 + m_2(u, m_1)\mathbf{b}_2$.

In the experiment, we are interested in triangular lattices generated by the interference of three laser beams tilted by 45° off-plane in an upward direction as depicted

in the inset of Fig 3.22. The beams are crossing at an angle of 120° projected onto the horizontal plane. Each beam is not required to have identical intensity. The following shows the calculation of optical lattice potential. Let us assume an electric field $\mathbf{E}_j$ with wavevector $\mathbf{k}$, angular frequency ω and global phase ϕ_j, is given by

$$\mathbf{E}_j(\mathbf{r}) = \sqrt{\frac{2I_j}{c\epsilon_0}} \exp\left[i(\mathbf{k}_j \cdot \mathbf{r} + \phi_j)\right] \left(\cos\theta_j \hat{\mathbf{e}}_{p,j} + \exp(i\alpha_j) \sin\theta_j \hat{\mathbf{e}}_{s,j}\right), \ j = 1, 2, 3, \tag{4.31}$$

where $\sqrt{2I_j/(c\epsilon_0)}$ represents the field amplitude and $\hat{\mathbf{e}}_{p,j}, \hat{\mathbf{e}}_{s,j}$ are unit vectors of $p-$ and $s-$polarizations. θ_j determines the ratio between polarizations and α_j is the phase difference between polarizations.

By applying a superposition of electric fields, the optical lattice potential is given by

$$V(\mathbf{r}) = \frac{1}{2} c\epsilon_0 |\mathbf{E}_1 + \mathbf{E}_2 + \mathbf{E}_3|^2 = V_{12} + V_{23} + V_{13} + \text{offset}, \tag{4.32}$$

where

$$\begin{aligned} V_{ij} =& (1/2) c\epsilon_0 (\mathbf{E}_i \cdot \mathbf{E}_j^* + \mathbf{E}_i^* \cdot \mathbf{E}_j) \\ =& \, 2\sqrt{I_i I_j} \cos\theta_i \cos\theta_j \cos\left((\mathbf{k}_i - \mathbf{k}_j) \cdot \mathbf{r} + \phi_i - \phi_j\right) \hat{\mathbf{e}}_{p,i} \cdot \hat{\mathbf{e}}_{p,j} \\ &+ 2\sqrt{I_i I_j} \sin\theta_i \sin\theta_j \cos\left((\mathbf{k}_i - \mathbf{k}_j) \cdot \mathbf{r} + \phi_i - \phi_j + \alpha_i - \alpha_j\right) \hat{\mathbf{e}}_{s,i} \cdot \hat{\mathbf{e}}_{s,j} \\ &+ 2\sqrt{I_i I_j} \cos\theta_i \sin\theta_j \cos\left((\mathbf{k}_i - \mathbf{k}_j) \cdot \mathbf{r} + \phi_i - \phi_j - \alpha_j\right) \hat{\mathbf{e}}_{p,i} \cdot \hat{\mathbf{e}}_{s,j} \\ &+ 2\sqrt{I_i I_j} \sin\theta_i \cos\theta_j \cos\left((\mathbf{k}_i - \mathbf{k}_j) \cdot \mathbf{r} + \phi_i - \phi_j + \alpha_i\right) \hat{\mathbf{e}}_{s,i} \cdot \hat{\mathbf{e}}_{p,j}. \end{aligned}$$

To simplify V_{ij} further, we define

$$V_{ij,pp} \equiv 2\sqrt{I_i I_j} \cos\theta_i \cos\theta_j \hat{\mathbf{e}}_{p,i} \cdot \hat{\mathbf{e}}_{p,j}, \tag{4.33}$$

$$V_{ij,ss} \equiv 2\sqrt{I_i I_j} \sin\theta_i \sin\theta_j \hat{\mathbf{e}}_{s,i} \cdot \hat{\mathbf{e}}_{s,j}, \tag{4.34}$$

$$V_{ij,ps} \equiv 2\sqrt{I_i I_j} \cos\theta_i \sin\theta_j \hat{\mathbf{e}}_{p,i} \cdot \hat{\mathbf{e}}_{s,j}, \tag{4.35}$$

$$V_{ij,sp} \equiv 2\sqrt{I_i I_j} \sin\theta_i \cos\theta_j \hat{\mathbf{e}}_{s,i} \cdot \hat{\mathbf{e}}_{p,j}. \tag{4.36}$$

Therefore, the potential due to a pair of lattice beams, V_{ij}, is given by

$$\begin{aligned} V_{ij} =& V_{ij,pp}\cos\left((\mathbf{k}_i-\mathbf{k}_j)\cdot\mathbf{r}+\phi_i-\phi_j\right) \\ &+V_{ij,ss}\cos\left((\mathbf{k}_i-\mathbf{k}_j)\cdot\mathbf{r}+\phi_i-\phi_j+\alpha_i-\alpha_j\right) \\ &+V_{ij,ps}\cos\left((\mathbf{k}_i-\mathbf{k}_j)\cdot\mathbf{r}+\phi_i-\phi_j-\alpha_j\right) \\ &+V_{ij,sp}\cos\left((\mathbf{k}_i-\mathbf{k}_j)\cdot\mathbf{r}+\phi_i-\phi_j+\alpha_i\right). \end{aligned} \tag{4.37}$$

Applying our lattice beam directions, the wavevectors for individual beams are

$$\mathbf{k}_1=\frac{1}{\sqrt{2}}\begin{pmatrix}1\\0\\1\end{pmatrix}k_L,\qquad \mathbf{k}_2=\frac{1}{2\sqrt{2}}\begin{pmatrix}-1\\-\sqrt{3}\\2\end{pmatrix}k_L,\qquad \mathbf{k}_3=\frac{1}{2\sqrt{2}}\begin{pmatrix}-1\\\sqrt{3}\\2\end{pmatrix}k_L.$$

The magnitude of the wavevectors is $k_L=2\pi/\lambda$. Each lattice beam has its polarization pointing in a direction spanned by $s-$ and $p-$polarizations. The unit vectors of polarizations are given by

$$\hat{\mathbf{e}}_{s,1}=\frac{1}{\sqrt{2}}\begin{pmatrix}-1\\0\\1\end{pmatrix},\qquad \hat{\mathbf{e}}_{s,2}=\frac{1}{2\sqrt{2}}\begin{pmatrix}1\\\sqrt{3}\\2\end{pmatrix},\qquad \hat{\mathbf{e}}_{s,3}=\frac{1}{2\sqrt{2}}\begin{pmatrix}1\\-\sqrt{3}\\2\end{pmatrix},$$

and

$$\hat{\mathbf{e}}_{p,1}=\begin{pmatrix}0\\1\\0\end{pmatrix},\qquad \hat{\mathbf{e}}_{p,2}=\frac{1}{2}\begin{pmatrix}\sqrt{3}\\-1\\0\end{pmatrix},\qquad \hat{\mathbf{e}}_{p,3}=\frac{1}{2}\begin{pmatrix}-\sqrt{3}\\-1\\0\end{pmatrix}.$$

The reciprocal vectors of this lattice are

$$\begin{aligned} \mathbf{b}_1&=\mathbf{k}_1-\mathbf{k}_2, \\ \mathbf{b}_2&=\mathbf{k}_2-\mathbf{k}_3, \\ \mathbf{b}_3&=\mathbf{b}_1+\mathbf{b}_2=\mathbf{k}_1-\mathbf{k}_3. \end{aligned} \tag{4.38}$$

For example, let us consider the potential V_{12} created by the first and second lattice beams,

$$\begin{aligned} V_{12} =& V_{12,pp}\cos\left(\mathbf{b}_1\cdot\mathbf{r}+\phi_1-\phi_2\right) \\ &+V_{12,ss}\cos\left(\mathbf{b}_1\cdot\mathbf{r}+\phi_1-\phi_2+\alpha_1-\alpha_2\right) \\ &+V_{12,ps}\cos\left(\mathbf{b}_1\cdot\mathbf{r}+\phi_1-\phi_2-\alpha_2\right) \\ &+V_{12,sp}\cos\left(\mathbf{b}_1\cdot\mathbf{r}+\phi_1-\phi_2+\alpha_1\right). \end{aligned} \tag{4.39}$$

By applying Euler's formula, the above equation becomes

$$\begin{aligned} V_{12} =& \frac{V_{12,pp}}{2}\left(e^{i(\mathbf{b}_1\cdot\mathbf{r}+\phi_1-\phi_2)}+e^{-i(\mathbf{b}_1\cdot\mathbf{r}+\phi_1-\phi_2)}\right) \\ &+\frac{V_{12,ss}}{2}\left(e^{i(\mathbf{b}_1\cdot\mathbf{r}+\phi_1-\phi_2+\alpha_1-\alpha_2)}+e^{-i(\mathbf{b}_1\cdot\mathbf{r}+\phi_1-\phi_2+\alpha_1-\alpha_2)}\right) \\ &+\frac{V_{12,ps}}{2}\left(e^{i(\mathbf{b}_1\cdot\mathbf{r}+\phi_1-\phi_2-\alpha_2))}+e^{-i(\mathbf{b}_1\cdot\mathbf{r}+\phi_1-\phi_2-\alpha_2)}\right) \\ &+\frac{V_{12,sp}}{2}\left(e^{i(\mathbf{b}_1\cdot\mathbf{r}+\phi_1-\phi_2+\alpha_1)}+e^{-i(\mathbf{b}_1\cdot\mathbf{r}+\phi_1-\phi_2+\alpha_1)}\right). \end{aligned} \tag{4.40}$$

We compare each term of Eq. 4.40 to Eq. 4.15 and Fourier coefficients are

$$\tilde{V}(\pm1,0)=\frac{1}{2}e^{\pm i(\phi_1-\phi_2)}\left(V_{12,pp}+V_{12,ss}e^{\pm i(\alpha_1-\alpha_2)}+V_{12,ps}e^{\mp i\alpha_2}+V_{12,sp}e^{\pm i\alpha_1}\right). \tag{4.41}$$

Similar to the other potentials, V_{23} and V_{13}, the Fourier coefficients are

$$\tilde{V}(0,\pm1)=\frac{1}{2}e^{\pm i(\phi_2-\phi_3)}\left(V_{23,pp}+V_{23,ss}e^{\pm i(\alpha_2-\alpha_3)}+V_{23,ps}e^{\mp i\alpha_3}+V_{23,sp}e^{\pm i\alpha_2}\right), \tag{4.42}$$

$$\tilde{V}(\pm1,\pm1)=\frac{1}{2}e^{\pm i(\phi_1-\phi_3)}\left(V_{13,pp}+V_{13,ss}e^{\pm i(\alpha_1-\alpha_3)}+V_{13,ps}e^{\mp i\alpha_3}+V_{13,sp}e^{\pm i\alpha_1}\right). \tag{4.43}$$

Here, the matrix element of the triangular-lattice potential is

$$\begin{aligned} V_{\{m_1,n_1,\mathbf{q}\},\{m_2,n_2,\mathbf{s}\}} &= \int e^{-i(m_1\mathbf{b_1}+n_1\mathbf{b_2}+\mathbf{q})}V(\mathbf{r})e^{i(m_2\mathbf{b_1}+n_2\mathbf{b_2}+\mathbf{s})}\,d^3r \\ &= \delta_{\mathbf{q},\mathbf{s}}\times\begin{cases}\tilde{V}(\pm1,0) & m_1-m_2=\pm1, n_1-n_2=0\\ \tilde{V}(0,\pm1) & m_1-m_2=0, n_1-n_2=\pm1\\ \tilde{V}(\pm1,\pm1) & m_1-m_2=\pm1, n_1-n_2=\pm1,\end{cases} \end{aligned} \tag{4.44}$$

where the Fourier coefficients in Eq. 4.44 are analytically obtained from Eqs. 4.41-4.43. The matrix element of the kinetic energy is

$$T_{\{m_1,m_2,\mathbf{q}\},\{n_1,n_2,\mathbf{s}\}} = \frac{\hbar^2}{2m}\left(m_1\mathbf{b}_1 + m_2\mathbf{b}_2 + \mathbf{q}\right)^2 \delta_{m_1,n_1}\delta_{m_2,n_2}\delta_{\mathbf{q},\mathbf{s}}.$$

Next, we apply the fact that a quasimomentum $\mathbf{q}$ is within a reciprocal unit cell that means $\mathbf{q} = \beta_1\mathbf{b}_1 + \beta_2\mathbf{b}_2$ where $0 \leq \beta_1, \beta_2 < 1$ and $|\mathbf{b}_1|^2 = |\mathbf{b}_2|^2 = 3k_L^2/2$, $\mathbf{b}_1 \cdot \mathbf{b}_2 = -3k_L^2/4$. Therefore, the matrix element of the kinetic energy is expressed as

$$\begin{aligned} T_{\{m_1,m_2,\mathbf{q}\},\{n_1,n_2,\mathbf{s}\}} =& \frac{3}{2}E_{\mathrm{R}}\left[(m_1+\beta_1)^2 + (m_2+\beta_2)^2 - (m_1+\beta_1)(n_2+\beta_2)\right] \\ & \times \delta_{m_1,n_1}\delta_{m_2,n_2}\delta_{\mathbf{q},\mathbf{s}}. \end{aligned} \tag{4.45}$$

We apply Eqs. 4.44 and 4.45 to construct the Hamiltonian, where the matrix element is denoted by a pair of indices $\{u, v\}$ using a mapping described in Eqs. 4.23 and 4.26. We impose $\mathbf{s} = \mathbf{q}$, and thus, the $N^2 \times N^2$ Hamiltonian matrix element for each quasimomentum $\mathbf{q}$ is expressed as follows:

$$H_{uv}^{\mathbf{q}} = \begin{cases} 1.5E_{\mathrm{R}}\left[(m_1+\beta_1)^2 + (m_2+\beta_2)^2 - (m_1+\beta_1)(n_2+\beta_2)\right] & u = v \\ \tilde{V}(\pm 1, 0) & u - v = \pm N \\ \tilde{V}(0, \pm 1) & u - v = \pm 1 \\ \tilde{V}(\pm 1, \pm 1) & u - v = \pm(N+1). \end{cases} \tag{4.46}$$

To discretize quasimomentum, we introduce dimensionless quantities q_x, q_y. Quasimomentum is inside the first Brillouin zone, meaning that $\mathbf{q} = |\mathbf{b}_1|(q_x, q_y, 0) = \sqrt{6}/2k_L(q_x, q_y, 0)$. With the use of $\mathbf{q} = \beta_1\mathbf{b}_1 + \beta_2\mathbf{b}_2$, one can write β_1, β_2 in terms of q_x, q_y,

$$\beta_1 = \frac{2q_x}{\sqrt{3}}, \qquad \beta_2 = q_y + \frac{1}{\sqrt{3}}q_x.$$

Finally, we obtain the band structure of the triangular lattice, as shown in Fig. 4.2.

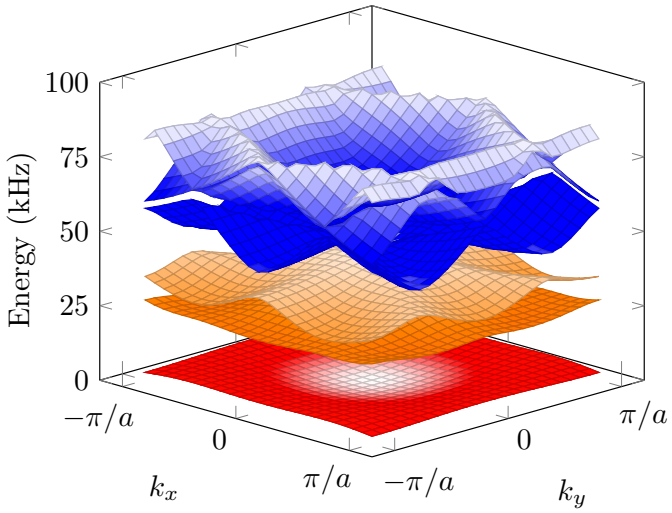

Figure 4.2: **Triangular-lattice band structure.** The band structure is calculated using a lattice depth of $9.7\,\mathrm{E_r^{Tri}}$ and a spacing of $a = 1003$ nm. $k_{x,y}$ represent quasimomenta. Here we use the sigma polarization by imposing $\alpha_j = -\pi/2$, $\theta_j = \pi/4$, and $\phi_j = 0$. $S-$band (red), $P-$bands (orange), and $D-$bands (blue). Figure was taken from previous work [58].

4.2 Wannier functions

Various sets of orthogonal functions can describe electronic states in specific potentials, such as a plane-wave basis. However, an intriguing alternative is the Wannier function basis. This function holds a unique property: It is localized at a certain lattice site, unlike the plane-wave basis which is spread across space. When discussing interactions and hopping of atoms between lattices the Wannier basis allows the calculations of interactions and tunneling through determination of wavefunction overlaps. To obtain the Wannier function in a periodic potential, I provide two robust ways to calculate it. The first method uses a complex Fourier series (plane-wave basis) to form maximally localized states and the second method is the projection method, where the Wannier function represents the projection of eigenstates onto the position operator. For simplicity, let us begin with Wannier functions in one dimension.

4.2.1 Maximally localized states

Maximally localized states are often used to describe electronic states in crystals. These states are highly localized around certain atomic sites or regions within the crystal lattice. An example of such a state is the Wannier function, denoted as $w_n(x - x_i)$ for the band n centered at x_i can be obtained through the Fourier transform of the Bloch states,

$$w_n(x - x_i) = \frac{1}{\sqrt{N_s}} \sum_{q \in \mathrm{BZ}_1} e^{-iqx_i} \phi_{n,q}(x), \tag{4.47}$$

where N_s is the total number of unit cells in the crystal and the sum runs over all allowed quasimomenta in the Brillouin zone.

As can be seen in Eq. 4.47, $\phi_{n,q}(x)$ can have arbitrary phase, making the sum of the $\phi_{n,q}(x)$ to various shapes and most configurations do not result in a localized wavefunction due to the phase mismatch of each $\phi_{n,q}(x)$. To ensure that the Wannier function is localized, we apply a trick such that a state with momentum $q = q_i$ constructively interferes with the state with momentum $q = -q_i$ in real space, thus leading to the existence of only real part and implying maximally localize wavefunction [115]. Specifically, for even excited states i.e., $\phi(x) = \phi(-x)$, we require $\phi_{\mathrm{even},q}(x) + \phi_{\mathrm{even},-q}(x)$ to be real and the summation is non-zero at $x = 0$. As a result, we ensure that numerical calculations for $\phi_{\mathrm{even},\pm q}(x)$ have the same phase by choosing this state and dividing by its sign at $x = 0$. A new Bloch state for even excited state is

$$\phi^{\mathrm{new}}_{\mathrm{even},q}(x) = \frac{\phi_{\mathrm{even},q}(x)}{\mathrm{sign}(\phi_{\mathrm{even},q}(0))}, \tag{4.48}$$

where the $\mathrm{sign}(z)$ is defined as $z/|z|$.

For odd excited states i.e., $\phi(-x) = -\phi(x)$, this summation $\phi_{\mathrm{odd},q}(x) + \phi_{\mathrm{odd},-q}(x)$ is required to be real. The odd function is zero at $x = 0$. However, to determine its phase, we can pick its values at $x = 0 \pm \delta x$ instead where δx is a small number but close to zero and assigns a new Bloch state for odd excited state

$$\phi^{\mathrm{new}}_{\mathrm{odd},q}(x) = \frac{\phi_{\mathrm{odd},q}(x)}{\mathrm{sign}(\phi_{\mathrm{odd},q}(\delta x) - \phi_{\mathrm{odd},q}(-\delta x))}. \tag{4.49}$$

After the proper phase adjustment, the Wannier function is achieved by

$$w_n(x - x_i) = \frac{1}{\sqrt{N_s}} \sum_{q \in \mathrm{BZ}_1} e^{-iqx_i} \phi^{\mathrm{new}}_{n,q}(x). \tag{4.50}$$

By applying the criteria discussed here, we obtain the Wannier function demonstrated in Fig. 4.3. As can be seen, handling the phase adjustment in one dimension is feasible, however, there is another approach to tackle the Wannier function, as presented below.

4.2.2 Eigenstates of the projection operator

The projection method can be used to calculate the Wannier function. It involves projecting the eigenstates onto localized functions centered at each lattice site. Here, we use a delta function as a localized function. To obtain the eigenstates, we first express the Hamiltonian in a matrix form such that

$$\hat{H}\psi = (\hat{T} + \hat{V})\psi = E\psi, \tag{4.51}$$

where E is the eigenvalue of the Hamiltonian and ψ is the eigenvector.

To generate this matrix, we consider writing the second derivatives in terms of the zeroth order,

$$\frac{d^2}{dx^2}\psi(x) = \lim_{\delta x \to 0} \frac{\psi(x + \delta x) - 2\psi(x) + \psi(x - \delta x)}{\delta x^2}. \tag{4.52}$$

When the numerical calculations are performed, we specify the spatial coordinate, x, by setting $x_{\min} = x_1$ and $x_{\max} = x_{n+1}$ with a step size of $\delta x = (x_{n+1} - x_1)/n$. Here, n is the number of discretization points. The second derivative at $x = x_i$ is approximated by a second-order centered difference scheme

$$\frac{d^2}{dx^2}\psi(x_i) \approx \frac{\psi(x_i + \delta x) - 2\psi(x_i) + \psi(x_i - \delta x)}{\delta x^2} \tag{4.53}$$

$$= \frac{\psi(x_{i+1}) - 2\psi(x_i) + \psi(x_{i-1})}{\delta x^2}. \tag{4.54}$$

With the use of the Kronecker delta function, the second derivative is expressed as

$$\frac{d^2}{dx^2}\psi(x_i) = \frac{1}{\delta x^2} \sum_{i'=1}^{n} \psi(x_{i'}) \left(\delta_{i',i+1} - 2\delta_{i',i} + \delta_{i',i-1}\right). \tag{4.55}$$

To write the second derivatives in a matrix form, an additional summation on i is added without losing any information,

$$\frac{d^2}{dx^2}\psi(x) = \frac{1}{\delta x^2}\sum_{i=1}^{n}\sum_{i'=1}^{n}\psi(x_{i'})\left(\delta_{i',i+1} - 2\delta_{i',i} + \delta_{i',i-1}\right). \tag{4.56}$$

Here, we apply periodic boundary conditions, and the matrix form of the kinetic energy is given by

$$\hat{T}\psi = -\frac{\hbar^2}{2m_a}\frac{d^2}{dx^2}\psi(x) = -\frac{\hbar^2}{2m_a}\begin{pmatrix} -2 & 1 & 0 & \cdots & 0 & 1 \\ 1 & -2 & 1 & \cdots & 0 & 0 \\ 0 & 1 & -2 & \cdots & 0 & 0 \\ \vdots & \vdots & \vdots & \ddots & 0 & 0 \\ 0 & 0 & 0 & \cdots & -2 & 1 \\ 1 & 0 & 0 & \cdots & 1 & -2 \end{pmatrix}_{n\times n}\begin{pmatrix} \psi(x_1) \\ \psi(x_2) \\ \vdots \\ \psi(x_i) \\ \vdots \\ \psi(x_n) \end{pmatrix}. \tag{4.57}$$

For the potential energy, which is a function of spatial coordinates and has no derivative dependence, the potential matrix consists only of diagonal entries,

$$\hat{V}\psi = \begin{pmatrix} V(x_1) & 0 & 0 & \cdots & 0 & 0 \\ 0 & V(x_2) & 0 & \cdots & 0 & 0 \\ 0 & 0 & V(x_3) & \cdots & 0 & 0 \\ \vdots & \vdots & \vdots & \ddots & 0 & 0 \\ 0 & 0 & 0 & \cdots & V(x_{n-1}) & 0 \\ 0 & 0 & 0 & \cdots & 0 & V(x_n) \end{pmatrix}\begin{pmatrix} \psi(x_1) \\ \psi(x_2) \\ \vdots \\ \psi(x_i) \\ \vdots \\ \psi(x_n) \end{pmatrix}. \tag{4.58}$$

By combining the kinetic and the potential energy matrix, the Hamiltonian is constructed. Next, the Hamiltonian matrix is diagonalized to obtain its eigenvalues and eigenvectors. It is important to ensure that the eigenvalues and eigenvectors are properly sorted from the smallest eigenvalue to the largest eigenvalue in order to later identify them as the ground state, first excited state, and so on.

As mentioned earlier the localized function used is the delta function. Here, we apply the fact that the delta function is an eigenfunction of the position operator, $\hat{X}$, associated with the observable position x_0,

$$\hat{X}\,|x\rangle \equiv x\,|x\rangle = x_0\,|x\rangle\,, \tag{4.59}$$

where eigenfunction $|x\rangle$ is the delta function centered at x_0, $\delta(x - x_0)$. The matrix element of projection operator $\hat{\mathcal{P}}_{X,ij}$ is given by

$$\hat{\mathcal{P}}_{X,ij} = \langle\psi_i|\hat{X}|\psi_j\rangle\,. \tag{4.60}$$

The projection operator onto the lowest band can be obtained using the m lowest-energy states, where $m < n$. It can be represented in matrix form as

$$\hat{\mathcal{P}}_X = \begin{pmatrix} \langle\psi_1| \\ \langle\psi_2| \\ \vdots \\ \langle\psi_m| \end{pmatrix}_{m\times n} \begin{pmatrix} x_1 & 0 & \cdots & 0 \\ 0 & x_2 & \cdots & 0 \\ \vdots & \vdots & \ddots & \vdots \\ 0 & 0 & \cdots & x_n \end{pmatrix}_{n\times n} \begin{pmatrix} |\psi_1\rangle & |\psi_2\rangle & \cdots & |\psi_m\rangle \end{pmatrix}_{n\times m}. \tag{4.61}$$

Note that $|\psi_i\rangle$ has n elements i.e., $\begin{pmatrix} \psi_i(x_1) & \psi_i(x_2) & \ldots & \psi_i(x_n) \end{pmatrix}^T$. After diagonalization the $\hat{\mathcal{P}}_X$ matrix, the projection operator transforms into

$$\hat{\tilde{\mathcal{P}}}_X = \begin{pmatrix} \tilde{x}_1 & 0 & \cdots & 0 \\ 0 & \tilde{x}_2 & \cdots & 0 \\ \vdots & \vdots & \ddots & \vdots \\ 0 & 0 & \cdots & \tilde{x}_m \end{pmatrix}, \tag{4.62}$$

with eigenvector $|\tilde{x}_i\rangle$,

$$|\tilde{x}_i\rangle = \begin{pmatrix} a_{i1} & a_{i2} & \ldots & a_{im} \end{pmatrix}^T, \tag{4.63}$$

associated with eigenvalue $\tilde{x}_i$.

Finally, we achieve the Wannier function w_i centered at $x = \tilde{x}_i$ for the lowest band using a superposition of the wavefunctions $|\psi_m\rangle$ with coefficients a_{im} determined by Eq. 4.63,

$$\begin{aligned} w_i &= a_{i1} |\psi_1\rangle + a_{i2} |\psi_2\rangle + \cdots + a_{im} |\psi_m\rangle \\ &= \sum_{j=1}^{m} a_{ij} |\psi_j\rangle \\ &= \sum_{j=1}^{m} a_{ij} \psi_j(x). \end{aligned} \tag{4.64}$$

In Fig. 4.3, the Wannier functions for the lowest band using the maximally localized states (Section. 4.2.1) and the projection method are demonstrated. The results show good agreement between methods. Note that the latter method does not require phase adjustment, making it more general to handle. In fact, the projection method provides a general framework for obtaining Wannier functions in higher dimensions, as demonstrated below.

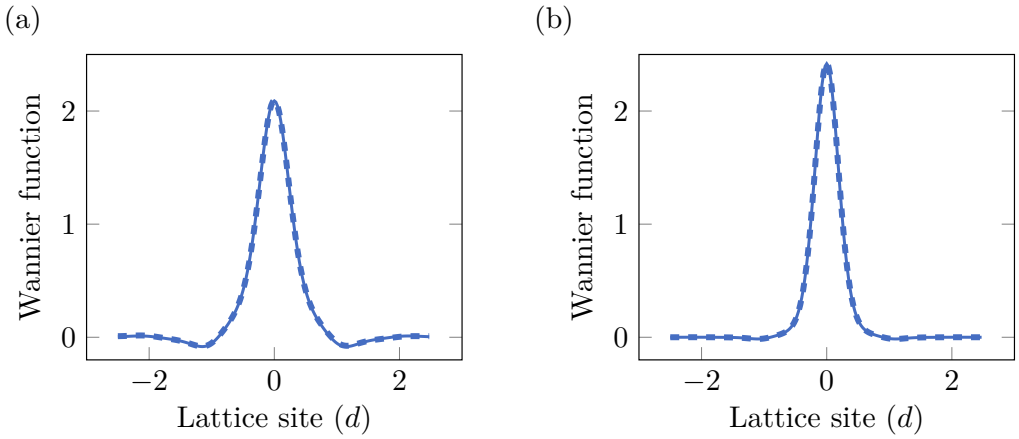

Figure 4.3: **Wannier function for the lowest band of a 1d lattice.** (a,b) Lattice depths of $4\,\mathrm{E_R}$ and $10\,\mathrm{E_R}$. Solid lines represent the calculation using the maximally localized states and dashed lines are calculated by the projection method.

To determine the Wannier functions in a 2d lattice system, we initialize the Hamiltonian with kinetic energy $\hat{T}$ and potential energy $\hat{V}$ in the position basis similar to the discussion in 1d case. We then diagonalize the Hamiltonian and rewrite projection

operators $\hat{\mathcal{P}}_X, \hat{\mathcal{P}}_Y$ in terms of the ground band of the Hamiltonian. We simultaneously diagonalize $\hat{\mathcal{P}}_X$ and $\hat{\mathcal{P}}_Y$. This simultaneous diagonalization is approximate when the lattice is not exactly separable. Next, we search for simultaneous eigenvectors of these projection operators [116]. We finally transform the component in the lowest band to the position basis. This procedure is effectively the projection of a spatial delta function to the ground band which corresponds to the Wannier function on a site [117]. In Fig. 4.4, we demonstrate Wannier functions for triangular and square lattices at depth of $9.6\,\mathrm{E_r^{Tri,Sq}}$. It is worth noting that the Wannier function obtained here will be used to extract the tunneling parameter in the Hubbard system, as discussed in the following.

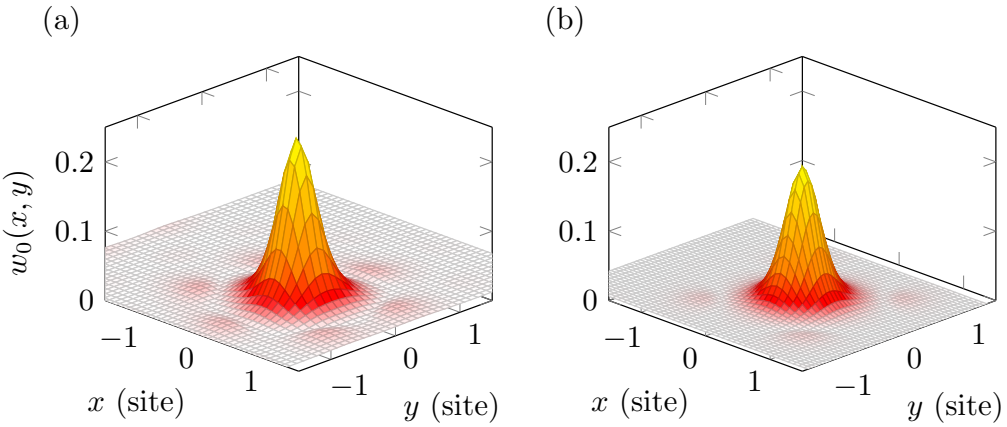

Figure 4.4: **Wannier functions of 2d optical lattices**. (a) Triangular lattice with a depth of $9.6\,\mathrm{E_r^{Tri}}$ and a spacing of $1003\,\mathrm{nm}$ and (b) Square lattice with a depth of $9.6\,\mathrm{E_r^{Sq}}$ and a spacing of $752\,\mathrm{nm}$. Here, we use $\mathrm{E_r^{Sq}}$ to represent $\mathrm{E_r^{Sq,752}} = h \times 14.6$ kHz, as defined in Section 3.11.

4.2.3 Tunneling parameter

As shown in Figs. 4.3 and 4.4, the Wannier functions can extend beyond a specific site, indicating that the wavefunctions have an amount of overlap with neighboring atoms. This overlap of wavefunctions allows quantum tunneling to occur and atoms can tunnel through potential barriers. To understand this tunneling phenomenon, let us consider a band structure $E_{\mathbf{q},\alpha}$ with a band index α. The corresponding

Hamiltonian is given by

$$H = \sum_{\mathbf{q},\alpha} E_{\mathbf{q},\alpha} \left|\phi_{\alpha,\mathbf{q}}\right\rangle \left\langle\phi_{\alpha,\mathbf{q}}\right| . \tag{4.65}$$

We apply the fact that the Wannier function is a complete and orthogonal basis set. The momentum basis $|\phi_{\alpha,\mathbf{k}}\rangle$ can be mapped to the Wannier basis $|\ell,\alpha\rangle$. The Hamiltonian is transformed into

$$H = \sum_{\ell,\ell',\alpha} J^{(\alpha)}_{\ell,\ell'} \left|w_{\alpha,\ell}\right\rangle \left\langle w_{\alpha,\ell'}\right| , \tag{4.66}$$

where α represents the band index and ℓ indicates the lattice site. $J^{(\alpha)}_{\ell,\ell'}$ is the tunneling strength between sites ℓ and ℓ' at the specific band α.

By multiplying $\langle w_{\ell,\alpha}|$ on both sides, the tunneling parameter is simply an expectation value of the Hamiltonian by two different Wannier bases on the band α. Here the tunneling strength is given by

$$\begin{aligned} J^{(\alpha)}_{\ell,\ell'} &= \langle w_{\alpha,\ell}|H|w_{\alpha,\ell'}\rangle = \langle w_{\alpha,\ell}| H \sum_{\mathbf{q},\alpha} |\phi_{\alpha,\mathbf{q}}\rangle \langle\phi_{\alpha,\mathbf{q}}| w_{\alpha,\ell'}\rangle \\ &= \sum_{\mathbf{q},\alpha} \langle w_{\alpha,\ell}| H|\phi_{\alpha,\mathbf{q}}\rangle \frac{1}{\sqrt{N_s}} e^{-i\mathbf{q}\cdot\mathbf{R}_{\ell'}} \\ &= \frac{1}{N_s} \sum_{\mathbf{q}} E_{\mathbf{q},\alpha} e^{i\mathbf{q}\cdot(\mathbf{R}_\ell - \mathbf{R}_{\ell'})}, \end{aligned} \tag{4.67}$$

where $\mathbf{R}_\ell$ is the position of lattice site, ℓ. The tunneling parameter exponentially decays when the two sites are far away from each other. This is due to the fact that the Wannier function is localized at a given lattice site and rapidly decays with distance. As a result, there is a smaller overlap integral, and the tunneling parameter is weaker for more localized Wannier functions, which occur in deeper lattices. Note that we calculate the tunneling parameters using $\langle w_{\alpha,\ell}|H|w_{\alpha,\ell'}\rangle$ in Eq. 4.67 because the Wannier function is numerically obtained from the method described in Section 4.2.2. Alternatively, the tunneling strength can be calculated using a plane-wave basis in Eq. 4.67, which requires additional steps.

4.3 Fermi-Hubbard model

The Fermi-Hubbard model is a prominent extension of the tight-binding model. The model addresses phenomena in strongly correlated systems that are not captured by the tight-binding model. As I briefly introduced the Fermi-Hubbard model in Chapter 2, let us delve into its fundamental formalism here. To understand the model, we begin with electrons in materials moving around their ionic cores. Electrons interact with each other via Coulomb's force. In general, the Hamiltonian describing the system of N electrons is given by

$$\mathcal{H} = \sum_{i=1}^{N} \left(\frac{\mathbf{p}_i^2}{2m_a} + V_L\left(\mathbf{r}_i\right) \right) + \sum_{\mathbf{r}_i \neq \mathbf{r}_j} V_C\left(\mathbf{r}_i - \mathbf{r}_j\right), \tag{4.68}$$

where the i^{th} electron has momentum $\mathbf{p}_i$ and the electrons are under the potential V_L, caused by their core ion while Coulomb's interaction between electrons is represented by V_C.

This Hamiltonian can be formulated in terms of second quantization. As demonstrated by [19] in the case of bosonic systems, interacting bosonic atoms within an optical lattice can be transformed into the Bose-Hubbard model. Similarly, for fermionic atoms, the Hamiltonian operator for fermionic atoms confined within a trapping potential is given by

$$\hat{\mathcal{H}} = \int \hat{\psi}^\dagger(\mathbf{r}) \left(-\frac{\hbar^2}{2m_a}\nabla^2 + V_{\text{latt}}(\mathbf{r}) \right) \hat{\psi}(\mathbf{r})\ d^3r + \frac{4\pi a_s \hbar^2}{m_a} \int \hat{\psi}^\dagger(\mathbf{r})\hat{\psi}^\dagger(\mathbf{r})\hat{\psi}(\mathbf{r})\hat{\psi}(\mathbf{r}). \tag{4.69}$$

Here, $\hat{\psi}(\mathbf{r})$ stands for a fermion field operator describing atoms in a particular internal atomic state at position $\mathbf{r}$, while $V_{\text{latt}}(\mathbf{r})$ symbolizes the optical lattice potential. The interaction between atoms is approximated by a short-range pseudopotential, with a_s denoting the $s-$wave scattering length.

Assuming that the fermions occupy the lowest band of an optical lattice, the field operator can be expanded using Wannier functions, expressed as

$$\hat{\psi}_\sigma(\mathbf{r}) = \sum_i w_i(\mathbf{r})\hat{c}_{i,\sigma}. \tag{4.70}$$

Here, $\hat{c}_{i,\sigma}$ represents the annihilation operator for a fermion at site i with spin $\sigma =\uparrow$ or $\downarrow$.

By substituting Eq. 4.70 into Eq. 4.69, we can express the Fermi-Hubbard model in the lowest band under certain assumptions. These assumptions include the tight-binding approximation, allowing tunneling only between neighboring sites and localizing electrons to a single site. Additionally, we assume strong short-range interactions between fermions without the overlap of Wannier functions beyond nearest neighbor sites. This elegant formulation was presented in the seminal work by Hubbard [118] and the Hamiltonian is given by

$$\mathcal{H} = -t \sum_{\langle \mathbf{r},\mathbf{r}'\rangle,\sigma} \left(c^{\dagger}_{\mathbf{r},\sigma} c_{\mathbf{r}',\sigma} + \text{h.c.}\right) + U \sum_{\mathbf{r}} n_{\mathbf{r},\uparrow} n_{\mathbf{r},\downarrow}, \tag{4.71}$$

where $c^{\dagger}_{\mathbf{r},\sigma}, c_{\mathbf{r},\sigma}$ are the creation and annihilation operators. $n_{\mathbf{r},\sigma}$ is the number operators for spin σ.

The tunneling strength between two sites is determined by the overlap of two Wannier functions with the Hamiltonian $\hat{H}$ [119], similar to the discussion in Section 4.2.3. The tunneling strength is therefore given by

$$t = \int w_0^{\dagger}(\mathbf{r}) \left[-\frac{\hbar^2}{2m_a}\nabla^2 + V_{\text{latt}}(\mathbf{r})\right] w_0(\mathbf{r}-\mathbf{a})\ d^3\mathbf{r}, \tag{4.72}$$

where w_0 is the Wannier function of the lowest band in the optical lattice.

On-site interaction U can be obtained by integrating over two Wannier functions localized at the same lattice site whereas the Wannier function in the vertical direction is treated as a harmonic oscillator ground state wavefunction. Here, the on-site Hubbard interaction is written as

$$\begin{aligned} U &= \frac{4\pi\hbar^2 a_s}{m_a} \int |w_0(\mathbf{r})|^4\ dxdydz \\ &= \frac{4\pi\hbar^2 a_s}{m_a} \sqrt{\frac{m_a\omega_z}{h}} \int |w_0(x,y)|^4\ dxdy, \end{aligned} \tag{4.73}$$

where ω_z is the confinement in the vertical direction.

Combining all the knowledge from these discussions, we can extract the Hubbard parameters in the optical lattice as a function of the lattice depth, as shown in

Fig. 4.5. Here, we have calculations for Hubbard parameters, which will be used to calibrate our optical lattices, as presented in the following.

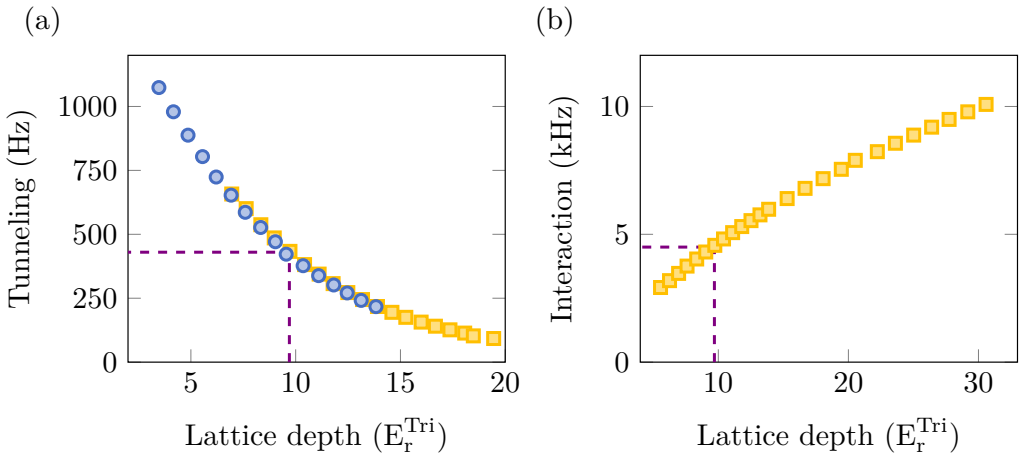

Figure 4.5: **Triangular-lattice Hubbard parameters as a function of lattice depth.** (a) Tunneling using band structure calculation (blue dots) and Wannier functions (orange squares). The tunneling t is 9 times the bandwidth of the $S-$band. The dashed line marks the lattice depth of $9.7\,E_r^{Tri}$. (b) Interaction calculated by Wannier functions by assuming $\omega_z = (2\pi)\times 20\,\mathrm{kHz}$ and scattering length $a_s = 1000a_0$ where a_0 is the Bohr radius. Images were reproduced from previous work [58].

4.3.1 Hubbard tunneling calibrations

Important parameters in the Hubbard model are tunneling (t) and interaction (U). Measuring tunneling is not simple because the tunneling energy is small, a few hundred Hz, compared to other energy scales. Modulation of the tunneling energy may not isolate the tunneling process from other effects, such as interaction-induced changes in the band structure. In the experiment, we calibrate the tunneling energy using band excitation spectroscopy, which depends on the lattice depth. We infer the tunneling parameter by comparison to a band structure calculation.

Lattice depth for 752 nm square lattice

To measure lattice depth, we perform amplitude modulation spectroscopy by combining a tunable external wave oscillator, operating over 200 kHz, with a reference lattice intensity using a bias tee (Fig. 4.6(a)). We feed the combined signal to the lattice stabilization. Note that we cannot generate the combined signal directly from the experiment control because the resolved transitions from the ground band to the $D-$bands are greater than the maximum frequency we can generate (200 kHz). Our measurement is shown in Fig. 4.6(b). The overall result is consistent with our expectations. The second and third peaks are slightly shifted from the expected frequency, this indicates that our square lattice is slightly imbalanced. The imbalance can be fixed by attenuating the retroreflection of the square lattice beam (see Section. 3.11).

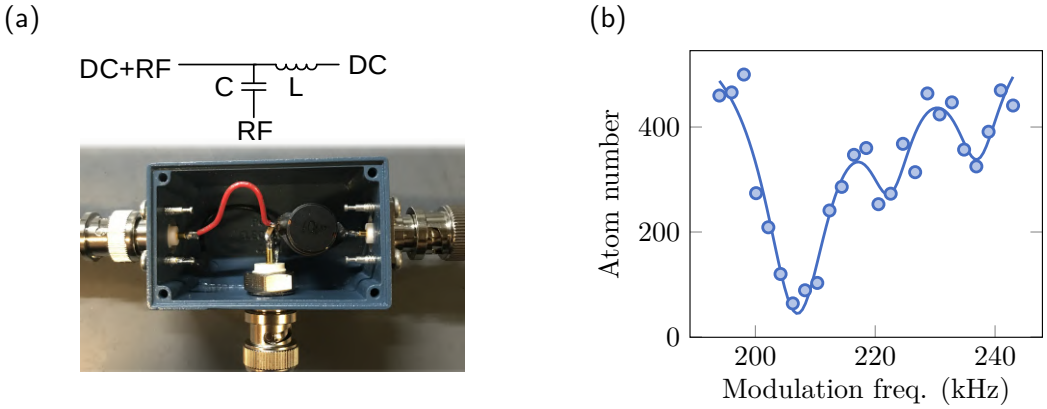

Figure 4.6: **Lattice depth calibration.** (a) Bias tee image. Lattice intensity is connected to the DC channel and the external oscillator is connected to the RF channel. The combined signal goes to the mixer in the lattice AOM driver. (b) Lattice modulation spectroscopy. Dots are experimental data and the solid line is a fit to a triple Gaussian function. Three resonances (206.9, 222.5, 237.1) kHz are observed for a lattice depth of $25.4\,\mathrm{E_r^{Sq}}$.

Lattice depth for triangular lattice

We calibrate our lattice depths in the range from $18\,\mathrm{E_r^{Tri}}$ to $30\,\mathrm{E_r^{Tri}}$ in the non-interacting regime of a $|1\rangle - |2\rangle$ mixture at a Feshbach field of 527 G. This configuration simplifies the Fermi-Hubbard model to a single-particle Hamiltonian approximated by a tight-binding model, and we can calculate all band energies via a band structure calculation. We apply lattice modulation spectroscopy to characterize the lattice depth. After modulating the lattice beam power with an amplitude of approximately 1% for 20 ms, we increase the lattice depth to maximum and measure atom number. We clearly observe two separated loss features whereas the third expected feature overlaps with the second. The resonance is fit to our band structure calculations and we extract the lattice depth (Fig. 4.7). The error bar of lattice depth is approximately 10% determined using a nonlinear fit to the band structure calculation with the lattice depth as a free parameter. As can be seen, we successfully extracted the tunneling energy from the indirect measurement. In the following, the other important Hubbard parameter, interaction, is calibrated. A higher interaction energy compared with tunneling energy provides several opportunities to perform direct measurements.

4.3.2 Hubbard interaction calibrations

The Hubbard interaction (U) occurs between two fermionic atoms with opposite spins, representing the energy cost associated with the fermions occupying the same lattice site. The interaction can be measured using various techniques, such as doublon formation spectroscopy and radio-frequency (RF) spectroscopy, as discussed in below.

Doublon formation spectroscopy

To measure our Hubbard interactions, we prepare atoms in a lattice of depth $9\,\mathrm{E_r^{Tri}}$ and perform amplitude modulation spectroscopy at varying Feshbach fields corresponding to scattering lengths i.e., 500, 675, 900, and $1400a_0$. We modulate the

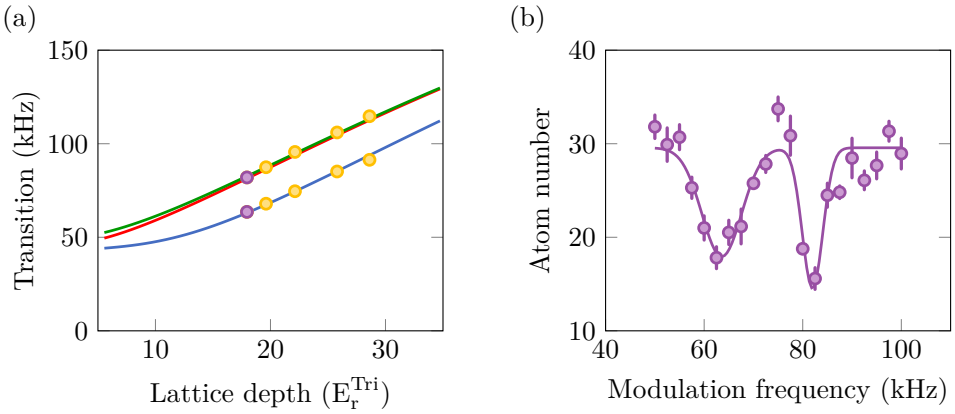

Figure 4.7: **Band excitation spectroscopy.** (a) Transitions between band structures. Orange dots show experimental data evaluated by Gaussian fit to atoms loss as a function of transition frequency. Red, blue, and green solid lines are transition frequencies from $S-$band to $D-$bands for different lattice depths calculated with band structure in the tight-binding limit. Transitions to the $P-$band are suppressed by the symmetry of the amplitude modulation. Error bars are smaller than the dots and evaluated by the standard error of the mean. (b) Lattice amplitude modulation. Data (violet points) are fit to a double Gaussian function (solid line). Image (a) was reproduced from previous work [58].

lattice with an amplitude of approximately 5% of the lattice depth for 20 ms then measure atom number in fluorescence. When the modulation frequency is in resonance with the interaction energy, pairs of singlons form doublons [120] and we observe a decrease of 20% in detected atoms in fluorescence imaging due to light-assisted collisions [40, 121]. According to Eq. 4.73, the on-site Hubbard interaction energy is linearly fit to scattering length (a_0) shown in Fig. 4.8 and we find the expected linear dependence within error bars.

RF spectroscopy

As can be seen in Fig. 4.8, the precision of measuring interaction from modulation is limited by several factors including total atom number, amplitude, and time duration. However, the Hubbard interaction can be precisely measured using radio-frequency spectroscopy. Let us consider the energy levels of singles (one atom per

site) and doublons (two atoms per site). The separation in energy between those represents Hubbard interaction energy. The $|1\rangle - |3\rangle$ mixture is initially prepared with interaction U_{13}. Radio frequency is applied to transfer the initial state to $|2\rangle - |3\rangle$ mixture at the same magnetic field and the interaction becomes U_{23}. According to Eq. 4.73, the interaction is proportional to scattering length i.e.,

$$a_{13} \propto U_{13}, \tag{4.74}$$

$$a_{23} \propto U_{23} = U_{13} - \delta U, \tag{4.75}$$

where δU is the energy difference between singlons and doublons shown in Fig. 4.9(a).

By solving above equations, the interaction of a $|1\rangle - |3\rangle$ mixture is given by

$$U_{13} = \delta U \frac{a_{13}}{a_{13} - a_{23}}. \tag{4.76}$$

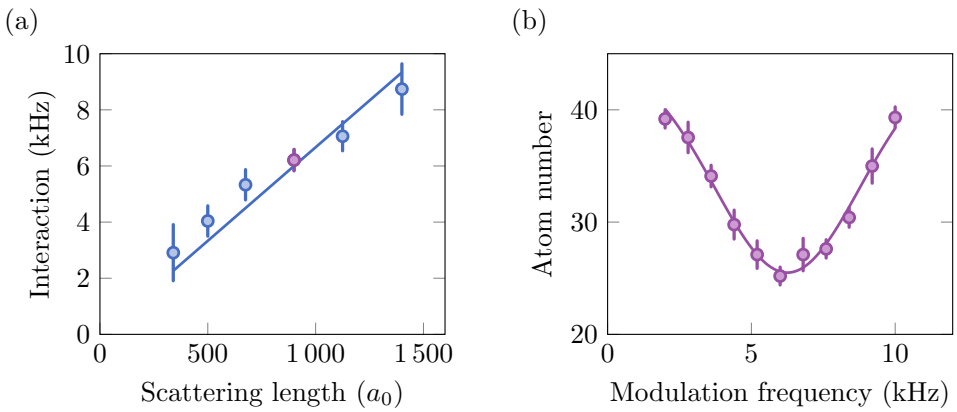

Figure 4.8: **Doublon modulation spectroscopy.** (a) Detected interaction frequency as a function of scattering length (blue dots). The interaction is determined by a decrease of singles in fluorescence images due to doublon formation during modulation. We calibrate the magnetic field from the narrow Feshbach resonance at 543.3 G by comparing the field to the scattering length from [96]. The blue solid line is a linear fit to the data as expected in Eq. 4.73. (b) Amplitude modulation spectroscopy of the violet dot in (a). The violet solid line is fitted to a Gaussian function. Error bars are the standard error of the mean. Image (a) was reproduced from previous work [58].

Typically, the calibration of interaction is performed in a deep lattice to prevent many-body effects and in the tight-binding limit. For example, we calibrate interaction at lattice depth of $15\,E_r^{Sq}$ and a field of 600 G as depicted in Fig. 4.9(b). Later, assuming that we set the lattice depth to $8.3\,E_r^{Sq}$ with tunneling of 660 Hz. We scale the result to the desired depth using a numerical table that relates lattice depths to the integral term in Eq. 4.73, thus yielding $U/t = 7.4(3)$. Note that RF spectroscopy offers faster calibration with higher precision. As a result, we can obtain a clean RF spectrum of singles and doublons transfer. Finally, we effectively determine the Hubbard parameters of our optical lattices, preparing us to investigate Hubbard physics as discussed in the following.

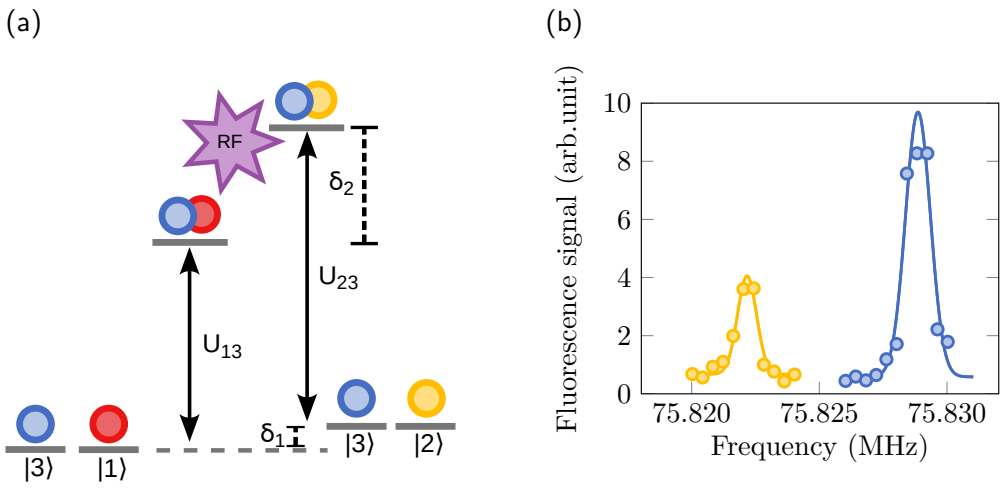

Figure 4.9: **Singlon and doublon transfer.** (a) Schematic of RF spectroscopy. The relation between $|2\rangle - |3\rangle$ interaction and $|1\rangle - |3\rangle$ interaction is $U_{23} = U_{13} + \delta_2 - \delta_1$. Here, $\delta U \equiv \delta_1 - \delta_2$. (b) RF sweep is applied to transfer $|1\rangle - |3\rangle$ to $|2\rangle - |3\rangle$ mixture at a lattice depth of $15\,E_r^{Sq}$ and a field of 600 G. The left and right peaks are doublons and singles transfer with RF frequencies of $75.8221(3)$, $75.8288(4)$ MHz. The spacing between the peaks is $\delta U = +7.8(3)$ kHz, thus yielding U=$8.1(2)\,$kHz. The peak from singles transfer can be used to precisely measure the magnetic field.

4.4 Mott insulator

A Mott insulator is a state in which each lattice site is occupied by one particle. The term "insulator" in this context refers to a state in which electrons are localized, with their movement inhibited by the strong Coulomb repulsion between them. The Mott insulating state occurs when the interaction is larger than tunneling ($U \gg 8t$ for 2d square lattice) and is typically observed in a deep lattice depth in which tunneling is suppressed. To understand the Mott insulator, we use a simple approach via grand canonical ensemble and employ the local density approximation, assuming that the chemical potential gradient is negligible [40]. The atom occupation as a function of radius r is given by

$$P_r(n) = \frac{1}{Z(r)} e^{\beta(\mu_{\rm loc} n - E_n)}, \tag{4.77}$$

where $Z(r) = \sum_n e^{\beta(\mu_{\rm loc} n - E_n)}$, $\mu_{\rm loc}$ is the local chemical potential and the interaction energy $E_n = Un(n-1)/2$. Here, $\beta = 1/(k_B T)$ for a given temperature T. Note that the approach we use in Eq. 4.77 corresponds to the high-temperature series expansion (HTSE) in the atomic limit. Here, our system is fermionic and therefore the atom number per lattice site is limited to $n_{\rm max} = 2$ (0 for empty, 1 for one fermion either spin up or down, and 2 for two fermions). We also take into account the harmonic trapping confinement generated by Gaussian laser beams. We apply a local density approximation, $\mu_{\rm loc} = \mu - (1/2) m_a \omega^2 r^2$ where μ is the global chemical potential and ω is the confinement, which can be obtained from a separate measurement, as discussed in Section 4.5.

In the experiment, we start searching Mott insulator in the 752 nm square lattice because our system is not optimized i.e., bad alignment, heating up during loading, low atom number, and it is harder to align in the triangular lattice. We load atoms from the light sheet to the accordion lattice combined with the bottom beam that is pointing upward from the bottom of the chamber. The accordion lattice provides confinement in the vertical direction and cannot hold atoms by itself. To address this, we turn on the bottom beam to provide radial confinement. Atoms are loaded to the accordion lattice at the largest spacing (8 µm) to capture as many atoms as

possible and we squeeze the accordion lattice to the smallest spacing (3 µm). After that, we perform evaporation using the bottom beam before loading it into a square lattice with the depth of $10.2\,\mathrm{E_r^{Sq}}$ at 603 G, yielding interaction $U/t = 14.3$. We observe a Mott insulator for various atom numbers shown in Fig. 4.10. The atom numbers are adjusted during the last evaporation before loading into the lattice. Doublons appear at the center of the cloud, showing that we exceed half-filling, and doublons are observed as empty sites because of light-assisted collisions [83]. We note that in Eq. 4.77 there are three free parameters for fitting: β, μ, and ω. The fit converges more effectively when we reduce the number of free parameters. For example, we can impose ω as a known parameter, which can be obtained from the following.

4.5 Non-interacting Fermi gas

A non-interacting Fermi gas can be used to determine the radial confinement of Mott insulators. According to Eq 4.77, we can eliminate one fit parameter i.e., interaction, and treat the confinement as a free parameter. However, fitting this expression does not work because we assume that the interaction is significantly stronger than the tunneling. Alternately, for a non-interacting gas, we apply another approach by filling up the Fermi-Dirac distribution with energy calculated from the tight-binding model and considering local density variation due to confinement. For the square lattice, energy dispersion is given by

$$\varepsilon^{\mathrm{sq}}(\mathbf{k}) = -2t[\cos(k_x a) + \cos(k_y a)], \tag{4.78}$$

where t is the tunneling parameter, k_i is the lattice momentum defined in the first Brillouin zone, $k \in [-\pi/a, \pi/a)$.

The density profile of non-interacting gases in a square lattice can be calculated by summing up all allowed momenta,

$$n^{\mathrm{sq}}_{\text{non-int}}(r) = \sum_{\mathbf{k}\in 1\text{st Brillouin}} \frac{1}{e^{\beta(\varepsilon^{\mathrm{sq}}(\mathbf{k}) - \mu_{\mathrm{loc}}(r))} + 1}. \tag{4.79}$$

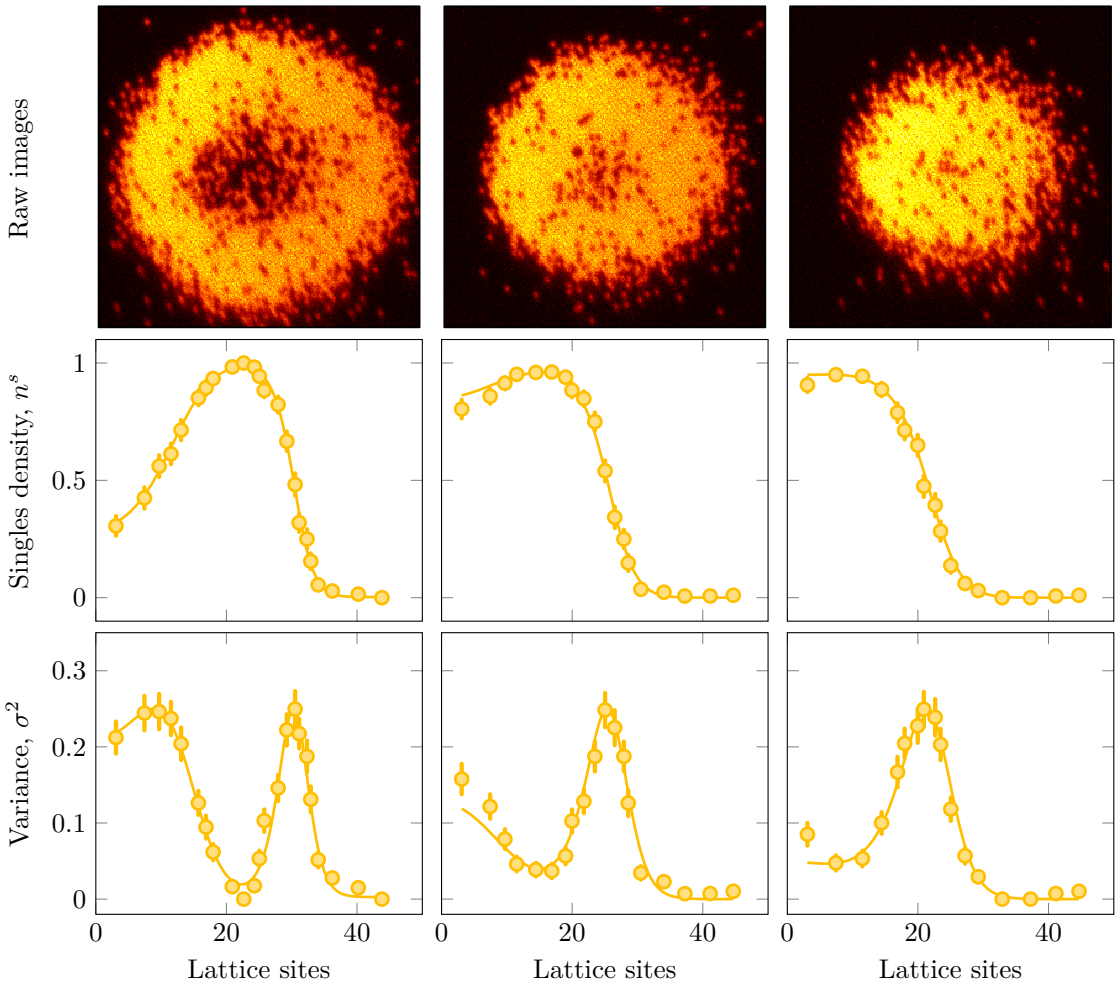

Figure 4.10: **Mott insulators in square lattices.** (Top) Fluorescence imaging. (Middle) Singles density. The fit is shown by solid line using Eq. 4.77 and yield $k_BT/t = 1.6(2),\ 1.9(2),\ 2.0(3)$ with chemical potentials of $\mu/t = 15.7(1),\ 11.0(2),\ 7.8(2)$ at $U/t = 14.3$. There are 2544, 1945, and 1421 atoms inside radii of 40, 38, and 32 sites. (Bottom) Variance of singles density calculated using $\sigma^2 = n^s - (n^s)^2$.

In other words, the double summation can be approximated by double integrations,

$$n^{\mathrm{sq}}_{\text{non-int}}(r) = \frac{1}{(2\pi)^2}\int_{-\pi/a}^{\pi/a}\int_{-\pi/a}^{\pi/a}\frac{1}{e^{\beta(\varepsilon^{\mathrm{sq}}(\mathbf{k})-\mu_{\mathrm{loc}}(r))}+1}\,dk_x dk_y. \tag{4.80}$$

We obtain the non-interacting Fermi gas similar to the Mott insulator sequence using a $|1\rangle - |2\rangle$ mixture. In addition, we ramp up the Feshbach field to the zero-crossing point (527 G) immediately after evaporation in the accordion lattice and the bottom beam. Then the lattice depth is set to $7.4\,\mathrm{E_r^{Sq}}$ and $25\,\mathrm{E_r^{Sq}}$. The azimuthal average

of the cloud is shown in Fig. 4.11. Overall, this technique allows us to measure the harmonic trapping in the lattice and we can scale to a desired lattice depth using the relation i.e., $\omega \propto \sqrt{s}$, where s is the lattice depth. Here, we have examined two limiting cases of the Fermi-Hubbard model. The model's intriguing features emerge at U/t between 4 and 14. Before investigating that, I will introduce observables that are remarkably useful for detecting quantum systems.

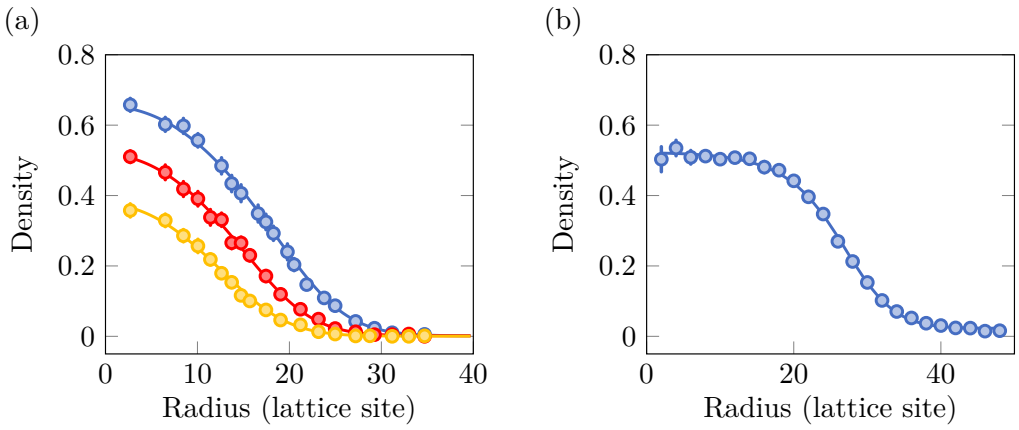

Figure 4.11: **Azimuthal average of fermionic non-interacting gases.** (a) Lattice depth of $7.4\,\mathrm{E_r^{Sq}}$ at $k_BT/t \simeq 1$ with the center chemical potential μ/t of 1.2 (blue), 0.2 (red), -0.7 (orange), leading to confinement of $(2\pi)\times147(24)\,\mathrm{Hz}$. (b) Lattice depth of $27\,\mathrm{E_r^{Sq}}$. Essential parameters are extracted from the fit, $k_BT/t = 5.1$, $\mu/t = 17.6$ and confinement is determined to $(2\pi)\times302(10)\,\mathrm{Hz}$.

4.6 Observables in the quantum gas microscope

When we measure a quantum system, the many-body wavefunction collapses to a measurement basis, revealing captivating insights while destroying its state. Here, we explore diverse measurement techniques that shed light on the interesting features of the Fermi-Hubbard model.

4.6.1 Density

In the context of Raman imaging, we encounter several density components that provide crucial insights into the Fermi-Hubbard model. One of the fundamental quantities is the singles density, denoted as n^s. This density accounts for the loss of doubly-occupied sites due to light-assisted collisions. The singles density is defined as

$$n_i^s = n_{i,\uparrow} + n_{i,\downarrow} - 2n_{i,\uparrow}n_{i,\downarrow}, \tag{4.81}$$

here, i represents the lattice site index. The first two terms, $n_{i,\uparrow} + n_{i,\downarrow}$, collectively reflect the full density, while the last term, $n_{i,\uparrow}n_{i,\downarrow}$, quantifies the doublon density.

To obtain single-species densities, $n_{i,\sigma=\uparrow,\downarrow}$, we employ a spin removal technique. This process effectively eliminates the non-targeted spin and converts doublons into a single component. Further details on this technique will be discussed in Section 4.6.2.

Another valuable density parameter is the single-species singles density, denoted as $n^s_{i,\sigma=\uparrow,\downarrow}$. This density specifically measures the single-species density after the removal of doublons. It can be obtained by applying a doublon hiding technique before applying the spin removal process (see Section 4.6.3), and it is defined as

$$n^s_{i,\sigma} = n_{i,\sigma} - n_{i,\uparrow}n_{i,\downarrow}. \tag{4.82}$$

Doublon density, d_i, can be directly obtained through spin-resolved imaging or by employing an RF technique to transfer a component of the doublon to another state, similar to the procedure demonstrated in Fig. 4.9. The doublon density is defined as

$$d_i = n_{i,\uparrow}n_{i,\downarrow}. \tag{4.83}$$

As can be seen, this systematic breakdown of density components allows for a more comprehensive understanding of the Fermi-Hubbard model and its behavior under various experimental conditions.

All the densities mentioned above can be obtained using the high-temperature series expansion (HTSE) in the atomic limit (see Section. 4.4), applicable when $k_BT/t \geq 1$.

However, when considering tunneling effects that delocalize atoms in the lattice, higher-order HTSE can estimate the effect, however, it fails to capture quantum fluctuations at very low temperatures ($k_BT/t \ll 1$). This raises the question of how to calculate observables at low temperatures. While a small system of few atoms can be analytically solved by diagonalizing the Hamiltonian, it cannot accurately represent a large system where collective behavior occurs and cannot be captured by a small system. To address this challenge, numerical techniques like Determinantal Quantum Monte Carlo (DQMC) and Numerical Linked-Cluster Expansion (NLCE) can be used. For this DQMC calculation, we rely on a Fortran 90/95 package, the QUantum Electron Simulation Toolbox (QUEST) [122]. DQMC is based on sampling the possible configurations of a system and using statistical averages, providing insights into the ground state. Unfortunately, the calculations suffer from a severe sign problem for triangular Hubbard systems when approaching low temperatures [123] and we rely on extensive averaging for low temperatures. In addition, we developed our NLCE as a tool for many-body calculations, however, it is not the main subject of this dissertation. More details can be found in [124].

In Fig. 4.12, singles density and full density calculated by DQMC simulation for triangular lattices are demonstrated. Singles density increases as higher chemical potential and it reduces at $\mu \simeq 0$ because doubly-occupied sites are formed, nevertheless, it gets lost during the imaging process (Fig. 4.12 (a)) while full density is unity around $\mu = 0$ (Fig. 4.12 (b)). Specifically, the unity filling is not exactly at $\mu = 0$ because of particle-hole asymmetry in the triangular lattice and we determine the chemical potential at half-filling shown in Fig. 4.12 (c) for various interactions. By measuring singles density, this observable quantity is not sensitive to temperature as depicted in Fig. 4.12 (d). Later, we use correlation functions to perform the thermometry of the system.

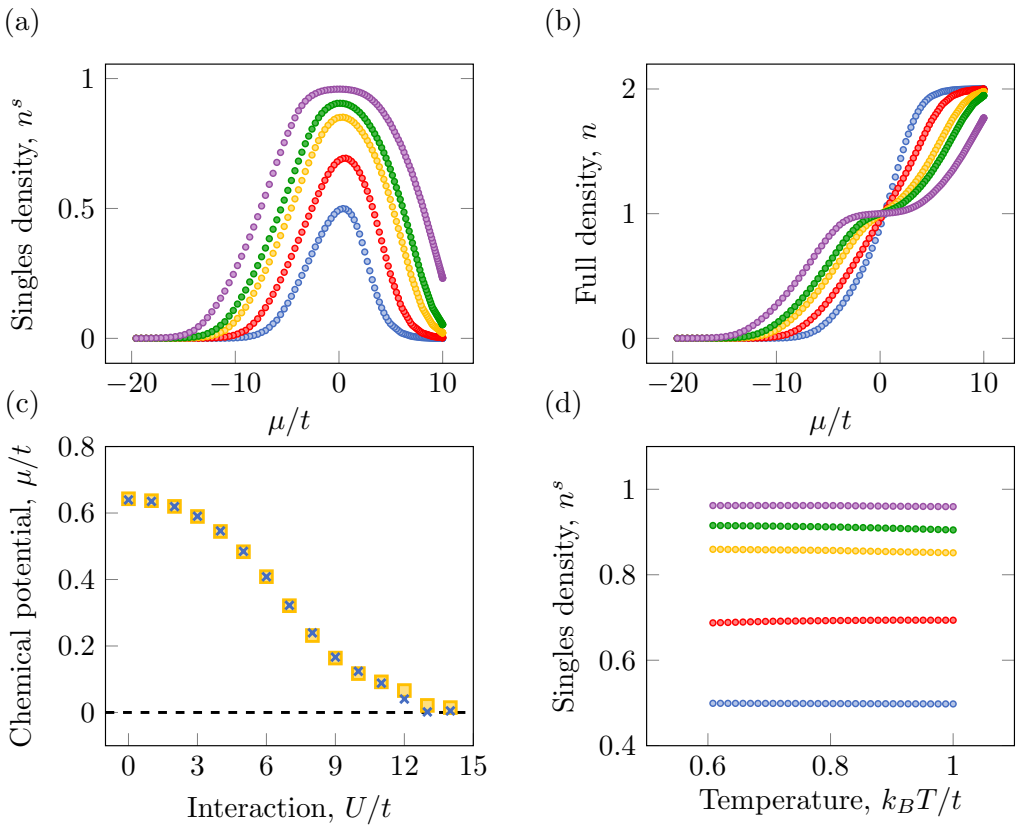

Figure 4.12: **DQMC calculation for full density and singles density in the triangular Hubbard model.** (a) Singles density as a function of chemical potential for $U/t = 0$ (blue), 4 (red), 8 (orange), 10 (green), and 14 (violet). The chemical potentials shown here are offset by $U/2$. (b) Full density as a function of chemical potential. (c) Chemical potential as a function of interaction at half-filling. The variation of μ/t at half-filling is caused by particle-hole asymmetry in this system. DQMC simulation is performed using imaginary time slices $L = 40$ (blue crosses) and $L = 200$ (orange squares) to obtain full density used to estimate chemical potential at half-filling. The Black dashed line indicates $\mu/t = 0$. Error bars are estimated by the deviation between $L = 40$ and $L = 200$ datasets. (d) Singles density at half-filling as a function of temperature. All densities are calculated by DQMC simulations that rely on a homogeneous 8×8 lattice with periodic boundary conditions. The inverse temperature $\beta = Ld\tau$ was split into $L = 40$ imaginary time slices. the simulations were averaged over ten runs, 5,000 warmup sweeps, and 20,000 measurement sweeps each.

4.6.2 Spin removal

The spin degree of freedom can be studied by selectively eliminating undesired spin components using on-resonant light. This technique is known as spin removal. To access spin-spin correlations, assuming we work with a $|1\rangle - |2\rangle$ mixture, site-resolved imaging of only a single spin component is necessary. We follow the spin removal technique demonstrated in [52]. We push out the other spin component using the vertical imaging light that is on resonance from $\left|^2S_{1/2}\ F = 1/2\ M_F = \pm 1/2\right\rangle$ to $\left|^2P_{3/2}\right\rangle$ and image the remaining atoms in fluorescence with a fidelity of approximately 98% [84]. We determine the imaging fidelity for this process by preparing a Mott insulator at $U/t = 17$ and we freeze the atom motion by ramping up the lattice depth to $100\,\mathrm{E_r^{Tri}}$ within 8 ms and reduce Feshbach field to the non-interacting point (527 G). It is important to note that an 8 ms ramp-up time is determined to be optimal for the experiment, providing a balance between suppressing tunneling and ensuring minimal band excitations [125]. Additionally, a similar ramp-up time can be found in [126]. We use a vertically propagating resonant laser beam with $I/I_{\mathrm{sat}} = 10$. The pulse duration is 50 µs determined by a double decay graph shown in Fig. 4.13 similar to [52]. By comparing the remaining atoms from the MI with and without pushing we can extract the spin removal fidelity to $\varepsilon_s = 94(1)\%$ for both spins.

4.6.3 Doublon hiding

Doublon hiding allows for the suppression of certain doubly-occupied sites, providing information on spin states that originate from singly-occupied sites. In fact, we observe that during the removal of one spin component, doublons of a spin mixture, i.e., $|1\rangle - |2\rangle$, are not reliably lost via light-induced collisions. Therefore, we apply a doublon removal technique [49], to eliminate doubly-occupied sites before applying spin removal. After we ramp up our lattice to $100\,\mathrm{E_r^{Tri}}$ we slowly sweep the Feshbach field over the narrow Feshbach resonance centered at 543.3 G from high to low magnetic field (Fig. 4.14 (a)). The fidelity of doublon hiding is determined by preparing a band insulator, and taking three separate datasets: no doublon hiding

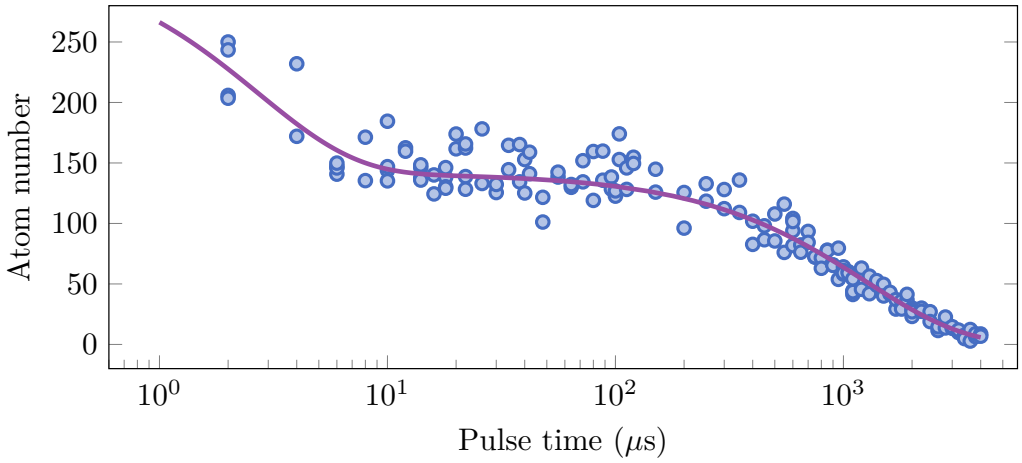

Figure 4.13: **Atom number as a function of resonant light pulse time.** On-resonant pulse is applied for a variable time. Experimental data (blue dots) are fitted to a double decay function (violet solid line), resulting in $2.7(9)$ µs and $1250(190)$ µs for on-resonant and off-resonant removal time. The image was reproduced from previous work [58].

and no spin removal (n_s^{BI}), only spin removal ($n_{s,p}^{\mathrm{BI}}$), and both doublon hiding and spin removal ($n_{s,hp}^{\mathrm{BI}}$). Here, we obtain three singles densities from the measurements of a spin-balanced gas and consider a band-insulating core (Fig. 4.14),

$$n_s^{\mathrm{BI}} = 1 - n_d^{\mathrm{BI}}, \tag{4.84}$$

$$n_{s,p}^{\mathrm{BI}} = n_d^{\mathrm{BI}}\varepsilon_d + \frac{1}{2}\varepsilon_s n_s^{\mathrm{BI}}, \tag{4.85}$$

$$n_{s,hp}^{\mathrm{BI}} = n_d^{\mathrm{BI}}\varepsilon_d(1-\eta_h) + \frac{1}{2}\varepsilon_s n_s^{\mathrm{BI}}, \tag{4.86}$$

where n_d is doublon density, ε_d is spin-removal fidelity of doublons being singlons, ε_s is spin-removal fidelity of singlons and η_h is doublon hiding fidelity. Note that we assume the majority at the center of the band insulator are doublons and singlons. Only doublons are lost during the doublon hiding because of the formation of weakly bound molecules. We solve these equations, resulting in the doublon hiding fidelity $\eta_h = 98(6)\%$.

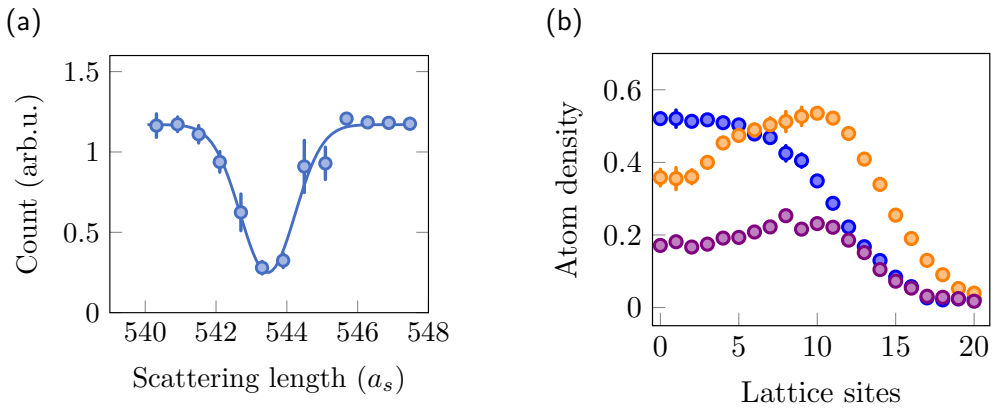

Figure 4.14: **Doublon hiding.** (a) Narrow Feshbach resonance for a $|1\rangle - |2\rangle$ mixture. Atoms are held in the ODT and atom loss is measured as a function of scattering length at a certain magnetic field. (b) Doublon hiding fidelity. To determine the doublon hiding fidelity, we should to take into account imperfections in the band insulator. The core region of the band insulator contains a mix of single and double occupations (n_s^{BI}, orange) due to finite temperature. To determine an accurate fidelity nevertheless, doublon hiding and spin-removal techniques are applied to the band insulator ($n_{s,hp}^{\mathsf{BI}}$, violet) whereas only spin-removal technique is performed to the band insulator resulting in the transformation from doublons to singlons ($n_{s,p}^{\mathsf{BI}}$, blue). We apply Eqs. 4.84, 4.85, and 4.86 to the core region within three lattice sites from the center, therefore yielding the fidelity of doublon hiding technique $\eta_h = 98(6)\%$. Image (b) was taken from previous work [58].

4.6.4 Correlations

Spin-spin correlations are a very sensitive tool to probe properties of a system i.e., temperature and lattice symmetry. To measure these correlations, we use a spin-removal technique described in Section 4.6.2 to resolve spin components and take images of only one spin-species spin (spin up or down). These images are analyzed via correlation functions [52] i.e.,

$$C_{\mathbf{d}}^{z}(\mathbf{r}) = 4\Big(\left\langle S_{\mathbf{r}}^{z} S_{\mathbf{r}+\mathbf{d}}^{z} \right\rangle - \left\langle S_{\mathbf{r}}^{z} \right\rangle \left\langle S_{\mathbf{r}+\mathbf{d}}^{z} \right\rangle \Big), \tag{4.87}$$

where the spin operator is defined as $S_{\mathbf{r}}^{z} = (\hat{n}_{\mathbf{r}}^{\uparrow} - \hat{n}_{\mathbf{r}}^{\downarrow})/2$ and $\langle \ldots \rangle$ denotes the expectation value. $\hat{n}_{\mathbf{r}}^{\sigma}$ represents the number of particles of spin σ on the site at $\mathbf{r}$,

and $\mathbf{d}$ can be the nearest neighbor, next-nearest neighbor and so on. For example, in a symmetric triangular lattice, the nearest neighbors are denoted as $(1, 0)$, $(1/2, \sqrt{3}/2)$, and $(1/2, -\sqrt{3}/2)$. The correlations are expected to be identical along the lattice axes. Unfortunately, the spin-spin correlation defined in Eq. 4.87 is not trivial to obtain because it requires information on both spin up and spin down at a given site. It is impossible to know by taking a snapshot of a parity projected image. Owing to spin-removal and doublon hiding techniques, the spin-spin correlation can be written as [49, 54]

$$C^z_{\mathbf{d}}(\mathbf{r}) = 2\Big(C^s_{\uparrow}(\mathbf{r}) + C^s_{\downarrow}(\mathbf{r})\Big) - C^s(\mathbf{r}), \tag{4.88}$$

where the single-species singles correlation for spin σ is given by

$$C^s_{\sigma}(\mathbf{r}) = \left\langle n^s_{\sigma,\mathbf{r}} n^s_{\sigma,\mathbf{r}+\mathbf{d}} \right\rangle - \left\langle n^s_{\sigma,\mathbf{r}} \right\rangle \left\langle n^s_{\sigma,\mathbf{r}+\mathbf{d}} \right\rangle, \tag{4.89}$$

and the singles correlation is

$$C^s(\mathbf{r}) = \left\langle n^s_{\mathbf{r}} n^s_{\mathbf{r}+\mathbf{d}} \right\rangle - \left\langle n^s_{\mathbf{r}} \right\rangle \left\langle n^s_{\mathbf{r}+\mathbf{d}} \right\rangle. \tag{4.90}$$

We obtain the single-species singles density (n^s_σ) by removing doubly-occupied sites using doublon hiding, discussed in Section 4.6.2, and remove either spin states using spin removal technique (see Section 4.6.3). The singles density (n^s) is naturally measured during fluorescence imaging without any additional removal procedures. Combining all the information from $C^s(\mathbf{r})$ and $C^s_\sigma(\mathbf{r})$, we can access spin-spin correlations from the experiment.

In Fig. 4.15, we illustrate calculated spin-spin correlations as a function of temperature, density, and interaction. These demonstrate the sensitivity of the correlations to the system parameters. It is important to note that in the Heisenberg model, the Neel state is expected at zero temperature, implying a classical interpretation where spin-up and spin-down atoms are alternately located next to each other. However, in the Fermi-Hubbard system, as the temperature approaching zero, the nearest spin-spin correlation exhibits a stronger correlation, reaching approximately -0.3 for a square lattice, as reported in the coldest Fermi-Hubbard system [126]. In this case,

the Heisenberg Neel state is no longer applicable due to quantum superposition, where the correlations are projected onto the measurement basis. For the triangular lattice, it behaves differently due to the nature of frustration. We will discuss this in detail in the following chapter.

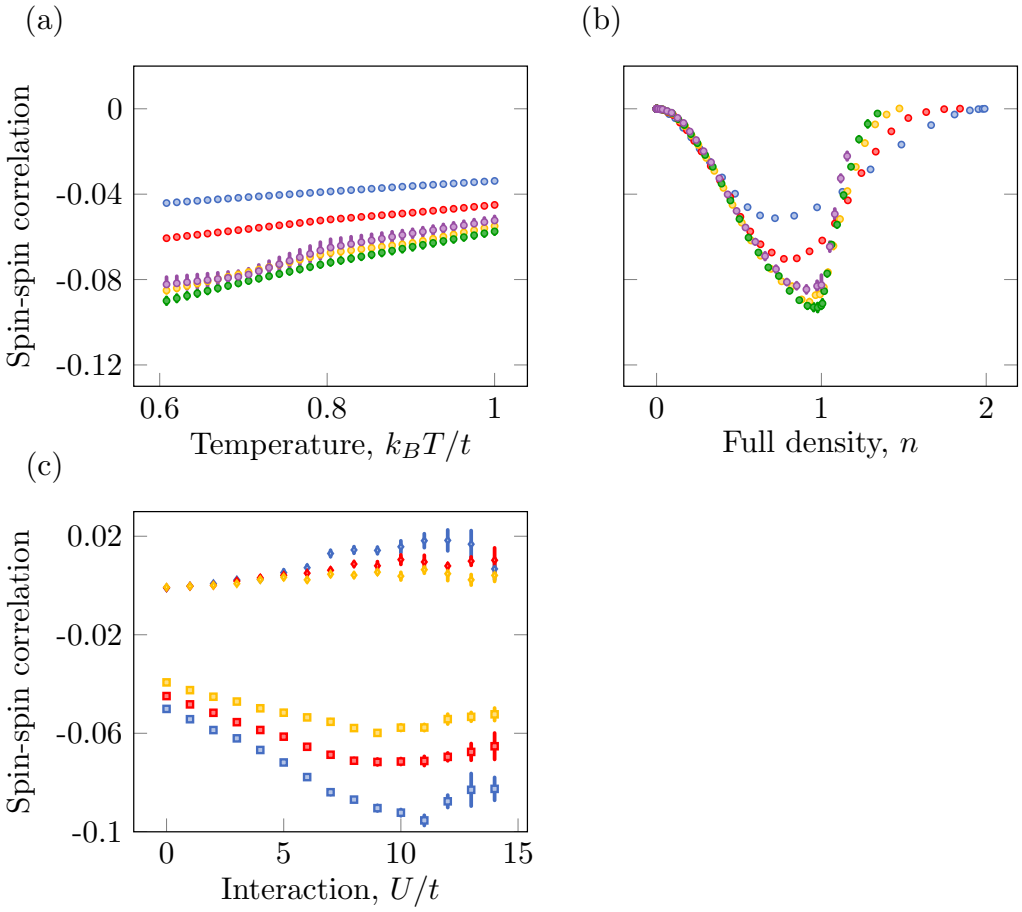

Figure 4.15: **Calculated spin-spin correlations in the triangular lattice.** (a) Temperature dependence of nearest spin-spin correlations for $U/t = 0$ (blue), 4 (red), 8 (orange), 10 (green), and 14 (violet). (b) Density dependence of nearest spin-spin correlations. The strongest correlation occurs approximately at a unity density and the correlations are asymmetric as opposed to square lattices. (c) Spin-spin correlations as a function of interaction for various temperatures, $k_BT/t = 0.6$ (blue), 0.8 (red), and 1.0 (orange). Squares are nearest neighbors and diamonds are next-nearest neighbors. All correlations are calculated by DQMC simulations with the same datasets from Fig. 4.12.

Chapter 5

Quantum Gas Microscopy of Fermionic Triangular-Lattice Mott Insulators

This chapter presents the previous work published as

> **J. Mongkolkiattichai**, L. Liu, D. Garwood, J. Yang, and P. Schauss, Quantum gas microscopy of fermionic triangular-lattice Mott insulators, Phys. Rev. A **108**, L061301 (2023).

5.1 Introduction

Electronic systems typically establish long-range order at zero temperature. Surprisingly, there are systems that do not have this fundamental property. For example, quantum spin liquids [127, 128] form in the presence of conflicting energetic constraints that prevent long-range ordering. Interestingly, the absence of ordering opens the door to a variety of exotic phenomena. Quantum spin liquids can show fractional quasi-particle statistics analogous to those underlying the quantum Hall effect [129].

Time-reversal symmetry breaking has been predicted in numerical studies on frustrated systems and kinetic constraints caused by the frustration lead to complex time-evolution [61, 130, 131]. While frustrated systems with small number of particles can be accurately simulated with tremendous computational resources, predictions for the low-temperature phases in the thermodynamic limit are scarce and often debated [63, 132, 133]. Existing condensed matter realizations are complicated materials [61], making well-controlled model systems a valuable alternative for gaining insight into the physics of frustration.

Ultracold atoms provide a unique way to explore quantum many-body physics through quantum simulation based on first principles. Prominent examples of quantum simulation with ultracold atoms include the realization of Hubbard models [134] and the observation of many-body localization [135]. While there is widespread evidence for insulating phases without magnetic ordering in frustrated Hubbard models, their existence and properties are still controversial on many lattice geometries, including the triangular lattice which has been proposed as paradigm model for geometric frustration [128]. Ultracold atoms in optical lattices implement Hubbard models [21–23], where neighboring sites are coupled by hopping, and atoms on the same lattice site interact. Atomic Fermi-Hubbard systems were first realized with ultracold atoms in square lattices [25, 26].

With the realization of quantum gas microscopes for fermions, it became possible to image fermionic atoms on the single-atom level [44–47, 101]. Later, two-dimensional (2d) fermionic Mott insulators (MI) were detected with quantum gas microscopes using ^{6}Li ref. [136] and ^{40}K ref. [120]. In particular, the characteristic antiferromagnetic correlations in the repulsive Hubbard model have been studied in detail [49–54, 137]. Frustration has been studied with various ultracold-atomic systems, starting with Bose-Einstein condensates in frustrated lattices [65, 138] and recently by the realization of frustrated spin systems with Rydberg atoms in optical tweezers [139, 140]. Here, we expand quantum simulation of frustrated systems to fermions in a Hubbard model on a triangular lattice structure, and report on the site-resolved

imaging of fermionic atomic Mott insulators in a triangular lattice. Although the triangular geometry suppresses anti-ferromagnetic ordering, short-range correlations persist over a wide range of parameters, and we measure these correlations and perform thermometry by comparison with numerical calculations, realizing for the first time a detailed comparison between theory and experiment of the equilibrium properties of the triangular Hubbard model in an optical lattice. Our work establishes a novel platform for the study of frustrated Hubbard physics.

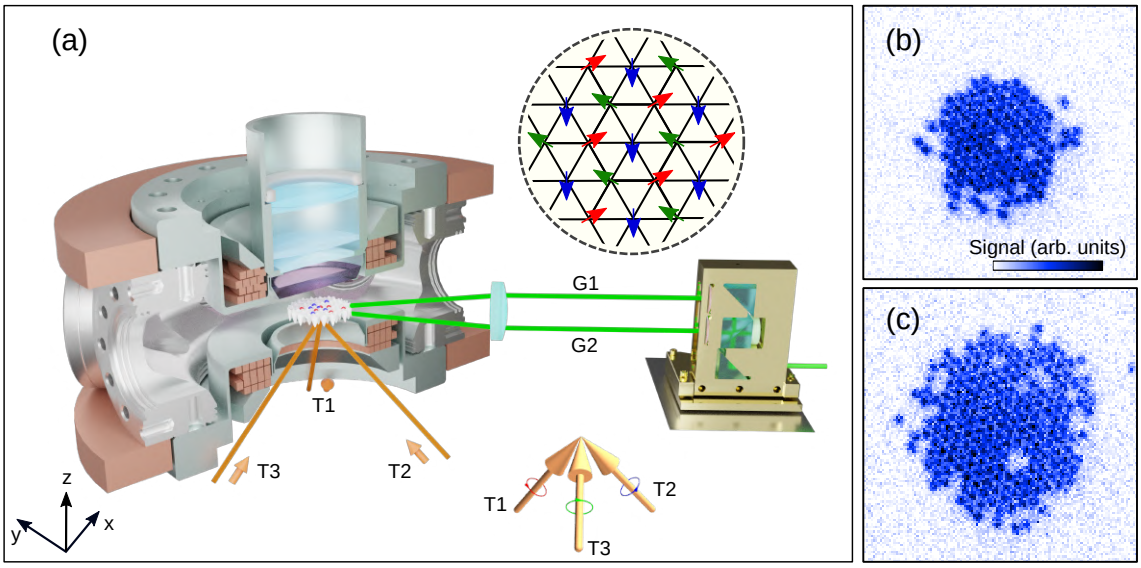

Figure 5.1: **Triangular-lattice quantum gas microscope.** (a) A triangular optical lattice is realized by interfering three circularly polarized laser beams ($T1$, $T2$, and $T3$) using 1064 nm light in the center of a vacuum chamber. The confinement of the atoms into two dimensions is achieved by a 1d accordion lattice in vertical direction, formed by the 532 nm laser beams $G1$ and $G2$. A combination of a beam splitter and mirrors allows us to vary the distance between $G1$ and $G2$ via the height of the input beam, therefore forming a lattice with a variable spacing between $3\,\mu\mathrm{m}$ and $8\,\mu\mathrm{m}$. A high-resolution objective enables single-site resolved imaging of the atoms in the triangular lattice. The inset demonstrates $120°$ order which is the classical analog of the spin ordering expected at large interactions. (b), (c) Triangular-lattice Mott insulators at $U/t = 10(1)$ with 109 atoms (top right) and $U/t = 26(3)$ with 203 atoms (bottom right). The field of view is $32\,\mu\mathrm{m} \times 32\,\mu\mathrm{m}$.

The Hamiltonian of the fermionic system in a two-dimensional lattice is

$$\mathcal{H} = -t \sum_{\langle \mathbf{r}\mathbf{r}\prime\rangle,\sigma} (c^{\dagger}_{\mathbf{r},\sigma} c_{\mathbf{r}\prime,\sigma} + c^{\dagger}_{\mathbf{r}\prime,\sigma} c_{\mathbf{r},\sigma}) + U \sum_{\mathbf{r}} n_{\mathbf{r},\uparrow} n_{\mathbf{r},\downarrow} - \mu(\mathbf{r}) \sum_{\mathbf{r}} (n_{\mathbf{r},\uparrow} + n_{\mathbf{r},\downarrow}), \tag{5.1}$$

where t is the tunneling strength between nearest-neighbor lattice sites, U is the on-site interaction, $c_{\mathbf{r},\sigma}(c^{\dagger}_{\mathbf{r}\prime,\sigma})$ is the annihilation (creation) operator for a fermion with spin σ on site $\mathbf{r}$, $n_{\mathbf{r},\sigma} = c^{\dagger}_{\mathbf{r},\sigma} c_{\mathbf{r},\sigma}$ is the number operator, and $\mu(\mathbf{r})$ is the chemical potential. This model describes the transition from a metal to a fermionic Mott Insulator. The insulating behavior originates from the electron-electron correlations and cannot be explained in a non-interacting electron picture. At temperatures below U/k_B, double occupation of sites is suppressed. Single occupation is energetically preferred at $\mu \sim U/2$ and the density variance approaches zero, leading to a MI. When the chemical potential is larger than the energy gap, doublons (two atoms on a site) are formed. They first appear at the center of the trap, forming a band insulating core, because of the lower harmonic potential. More than two atoms per site in the lowest band are forbidden by the Pauli exclusion principle, and higher band population is strongly suppressed energetically at such low temperatures. Short-range antiferromagnetic ordering can be observed in MIs when the temperature is comparable to the exchange energy $J = 4t^2/U$ ref. [141]. In this study, we acquired experimental data in this temperature regime, demonstrated consistency of numerical calculations and measurements characterizing the equation of state of the triangular Hubbard model, and observed antiferromagnetic correlations on the triangular lattice.

5.2 Experimental setup

We started the experiment by preparing a spin-balanced Fermi gas in a single layer of a one-dimensional (1d) accordion lattice (Fig. 5.1(a)) with a variable spacing. The gas is a mixture of the two lowest hyperfine ground states $|\uparrow\rangle = |F = 1/2, m_F = 1/2\rangle$ and $|\downarrow\rangle = |F = 1/2, m_F = -1/2\rangle$ of ^{6}Li, where F and m_F are the hyperfine quantum numbers. Next, the atoms are adiabatically loaded into the triangular lattice of

depth 9.7(6) E_r^{Tri}. Here, $E_r^{Tri} = \hbar^2\pi^2/(2ma_{latt}^2) = h \times 8.2$ kHz is the recoil energy where h is Planck's constant, m is the atomic mass, and $a_{latt} = 1003$ nm. The tunneling parameter is $t = h \times 436(40)$ Hz. The atom number and density in the lattice is adjustable by varying evaporation parameters. Once the atoms are in the lattice, we tune the scattering length to $525(4)a_0$, where a_0 is the Bohr radius, thereby adjusting the interaction to $U/t = 10(1)$. To detect the singles density ($n^s = n - n_\uparrow n_\downarrow$), the atom motion is frozen by linearly increasing the lattice depth up to 100 E_r^{Tri}. For imaging, we turn off all magnetic fields and switch to maximum lattice depth $\sim 10^4 E_r^{Tri}$. Images of MI for different interaction strengths are shown in Figs. 5.1(b,c). By varying the atom number loaded into the lattice, we observe MI and band insulators (BI) at $U/t = 10(1)$ (Fig. 5.2). The MI region (Fig. 5.2(b)) has nearly unit filling and atom number fluctuations are suppressed. When the chemical potential μ exceeds the value of $U/2$ (approximately half-filling), doubly-occupied sites are formed, therefore a BI region in the center of the trap forms as shown in Figs. 5.2(c,d). Doubly-occupied sites are detected as empty sites due to light-assisted collisions at the imaging stage [136].

5.3 Triangular-lattice Mott insulators

To access the singles density profile, we perform a deconvolution to determine the site occupation numbers and obtain singles density (n^s) and variance ($\sigma_{n^s}^2$) via azimuthal averaging (bottom panel of Fig. 5.2). We fit the experimental density profile using determinantal quantum Monte Carlo (DQMC) and Numerical Linked Cluster Expansion (NLCE) calculations. The temperature and chemical potential of the atoms in the trap are free parameters in the nonlinear least-squares fitting. We find good agreement with a global fit relying on a local density approximation using $\mu(\mathbf{r}) = \mu_0 - \frac{1}{2}m\omega^2 r^2$. The results of the fitting can be found in Fig. 5.2. We observe a small deviation at the center of the trap, which we attribute to the lower statistics and the uncertainty in the determination of the exact center of the system for azimuthal averaging. We observe an increased temperature for larger atom numbers as

a result of reduced evaporative cooling. Lifetime measurements in the lattice show no significant density-dependent heating.

5.4 Spin-spin correlations

Spin-spin correlations have proven to be essential observables for the understanding of the Hubbard model on square lattices [49, 52–54]. The spin-spin correlator is defined as $C^z_{\mathbf{a}}(\mathbf{r}) = 4\Big(\langle S^z_{\mathbf{r}} S^z_{\mathbf{r+a}} \rangle - \langle S^z_{\mathbf{r}} \rangle \langle S^z_{\mathbf{r+a}} \rangle \Big)$, where the spin operator is $S^z_{\mathbf{r}} = (n_{\mathbf{r},\uparrow} - n_{\mathbf{r},\downarrow})/2$. Here, the parameter $\mathbf{a}$ denotes the shift in the lattice site number between the two correlated positions, and $\mathbf{r}$ is the current lattice site. We access the observable $C^z_{\mathbf{a}}(\mathbf{r})$ via a linear combination of different correlators that can be measured directly in the experiment.

The fate of antiferromagnetic correlations on frustrated lattices is not obvious because the ordering is not compatible with the lattice structure. Despite the geometric frustration, we find significant antiferromagnetic correlations at nearest-neighbor sites although our temperatures are above the exchange energy scale $J = 4t^2/U \approx 0.4t$. The reduced antiferromagnetic correlation, compared to the maximal correlation of -1 can be interpreted as incomplete anti-alignment of the spins. At large interactions, the Hubbard model maps to the Heisenberg model, and 120° order is expected (Fig. 5.1) Negative nearest-neighbor correlations of $C^z_{\mathbf{b1}} = -0.078(22)$, $C^z_{\mathbf{b2}} = -0.053(23)$ and $C^z_{\mathbf{b1-b2}} = -0.071(28)$ are observed for three directions ($\mathbf{b1}$, $\mathbf{b2}$ and $\mathbf{b1} - \mathbf{b2}$) as depicted in Fig. 5.3(a). The correlations overlap within the error bars, indicating a symmetric triangular lattice. We compare the experimental data with a correlation map calculated by DQMC at $U/t = 10$ and $k_B T/t = 0.8$ (Fig. 5.3(b)). The calculated nearest-neighbor spin-spin correlations agree with the experimental data within error bars. The observed negative correlations among all nearest neighbors is consistent with 120° order. Next-nearest-neighbor spin-spin correlations in the experimental data are consistent with zero within the typical uncertainty of 0.02, which we believe is limited by the currently realized tempera-

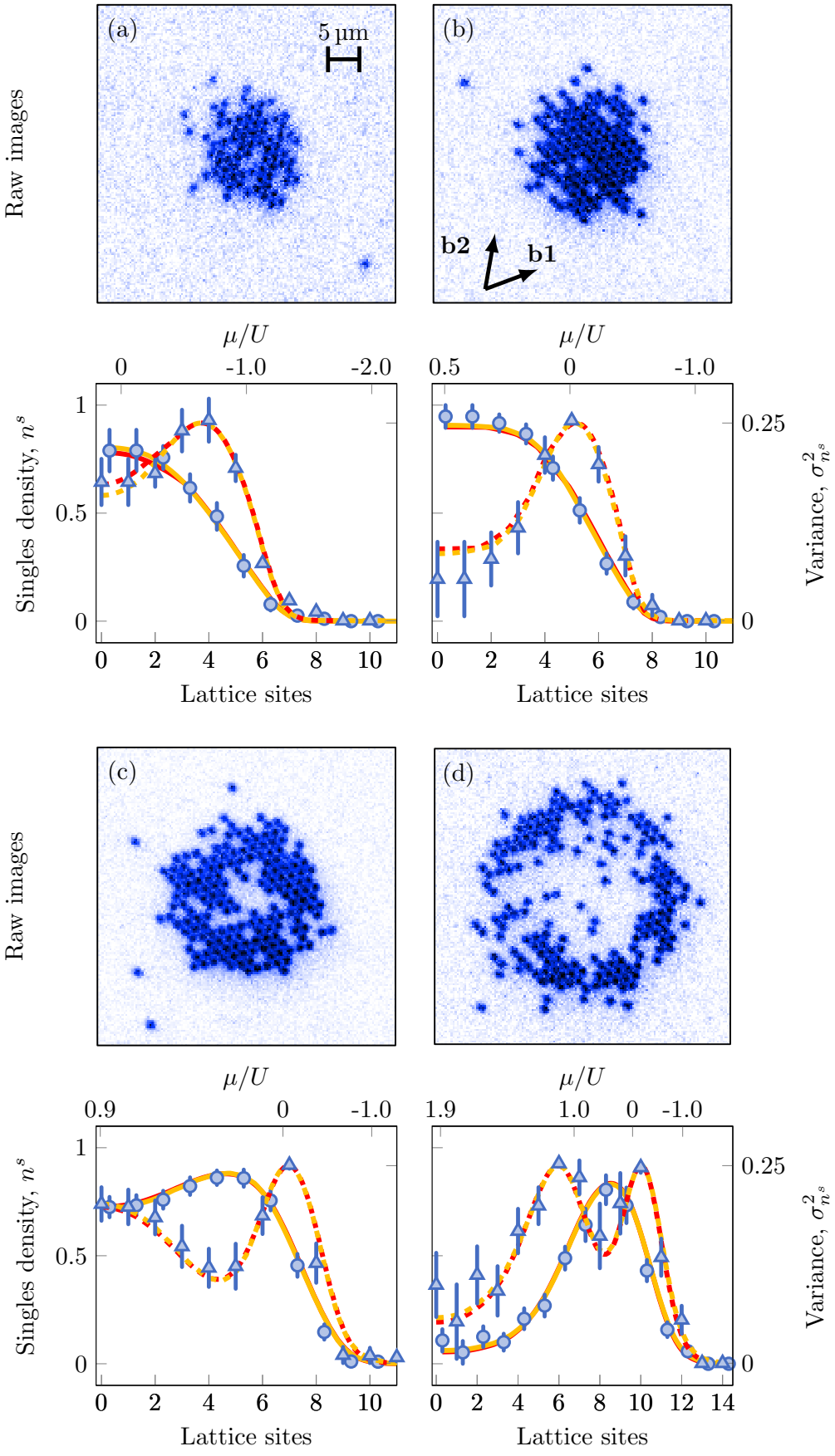
(a)
5 µm
(b)
b2
b1
Raw images
μ/U
0
-1.0
-2.0
0.5
0
-1.0
Singles density, n^s
Variance, $\sigma^2_{n^s}$
1
0.5
0
0.25
0
0 2 4 6 8 10
Lattice sites
(c)
(d)
0.9
0
-1.0
1.9
1.0
0
-1.0
0 2 4 6 8 10 12 14

Figure 5.2: **Triangular-lattice Mott insulators.** (a)-(d), top, Site-resolved fluorescence images of fermionic Mott insulators with increasing atom number integrated from fit, 77, 119, 175, and 183 at interaction $U/t = 10(1)$. (a)-(d), bottom, Comparison of azimuthally averaged singles density (dots) and variance (triangles) with theory calculations, QMC (red) and NLCE (orange). The data points of the variance are horizontally offset by 0.3 lattice sites for clarity. Both singles density n^s and variance $\sigma^2_{n^s}$ are fit with QMC and NLCE theory using the local density approximation. The detected variance is the square of the standard deviation of the sample within a radial bin. The fits yield temperatures $k_BT/t = 0.9(2),\ 0.9(1),\ 1.5(1)$, and $2.4(1)$ with chemical potentials $\mu_0/U = 0.24(10),\ 0.5(4),\ 0.91(3)$, and $1.94(1)$, respectively, at the trap center for increasing atom number in both QMC and NLCE calculations. Error bars on n^s are standard error of the mean and error bars on $\sigma^2_{n^s}$ are determined by error propagation from $\sigma^2_{n^s} = n^s - (n^s)^2$.

tures in our experiment. Compared with the square lattice, where nearest-neighbor spin-spin correlation alternate in sign, the spin-spin correlations in the triangular lattice are smaller in magnitude and negative for all nearest neighbors in the same parameter regimes, which we attribute to the geometrically frustrated triangular structure.

5.5 Thermometry

To extract the temperature, we perform azimuthal averaging of nearest-neighbor correlations as a function of the distance from the trap center along the equipotential of the lattice and fit to DQMC and NLCE calculations using temperature and chemical potential at the trap center as free parameters (Fig. 5.4(a)). We also average the correlations along the three lattice axes because they are equal within error bars. We show the result as a band in Fig. 5.4(b) and obtain a temperature of $k_BT/t \sim 0.8$ by comparing correlations between experiment and theory calcula-

tions at half-filling. The measured temperature is consistent with the radial singles density fit in Fig. 5.2 with half-filling at the center of the system.

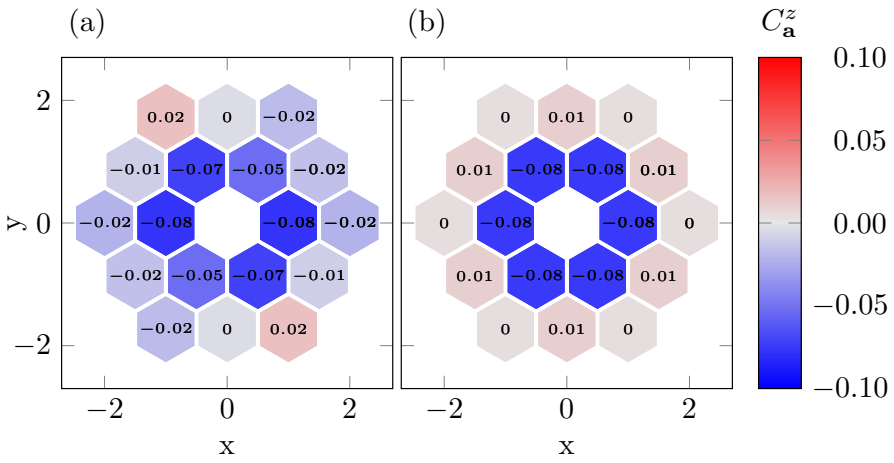

Figure 5.3: **Spin-spin correlations**. (a) Experimental correlations for $U/t = 10(1)$. The $C^z_{\mathbf{b1}}$, $C^z_{\mathbf{b2}}$ and $C^z_{\mathbf{b1-b2}}$ are observed as anti-correlated along $(1, 0)$, $(1/2, \sqrt{3}/2)$, and $(1/2, -\sqrt{3}/2)$. These values are the same within error bars suggesting tunneling isotropy of our triangular lattice. The correlations are extracted with post-selection from 400 experimental pictures. Typical values of experimental error bars are ~ 0.02 and evaluated by bootstrap. (b) Spin-spin correlations between nearest and next-nearest lattice sites calculated by DQMC at a temperature of $k_B T/t = 0.8$ near half-filling and C^z_0 is omitted for clarity. DQMC theory shows good agreement with experiment. The measured next-nearest-neighbor spin-spin correlations are consistent with zero within error bars.

This temperature is clearly below the interaction energy $U/t = 10(1)$, and lower than the tunneling energy scale and therefore quantum effects in the motion and interaction of the atoms can be observed. From comparisons to square lattice Mott insulators in our apparatus, we attribute the elevated temperature partially to the more complex lattice beam geometry which relies on the interference of three laser beams. Obtaining high contrast in three-beam interference is more sensitive to polarization purity and air-movement-induced beam pointing than for two-beam

interference. The resulting time-dependence of the lattice potential leads to heating. Heating and thermalization in triangular lattices, as well as the loading dynamics into the lattice, merit further theoretical and experimental study in the future.

In Fig. 5.4(c), we demonstrate our ability to tune interactions. The strongest nearest-neighbor spin-spin correlations in the triangular lattice are found for $U/t \sim 10$, whereas the strongest correlations in the square lattice occur near $U/t \sim 8$ ref. [54]. We observe atom loss when increasing the scattering length beyond a value of $\sim 650a_0$. Therefore, we change the lattice depth to reach larger U/t. We find good agreement with theory and note that the experimental temperature $k_BT/t \sim 0.9$ is almost independent of U/t.

Next-nearest-neighbor spin-spin correlations are challenging to measure as can be seen in Fig. 5.4(d). DQMC calculations show a suppression of spin-spin correlations for next-nearest neighbors by a factor of 8, compared to that for nearest neighbors, at a temperature $k_BT/t = 0.4$ and half-filling. As interactions are increased, the next-nearest-neighbor spin-spin correlations are expected to cross over from negative in a possible spin-liquid regime to positive in the 120° ordered phase in contrast to the situation in 2d square lattices at half-filling [52–54]. Experimental temperatures around $k_BT/t = 0.4$ or lower would therefore allow for the detection of next-nearest neighbor correlations and may make it possible to distinguish predictions for 120° order (the inset of Fig. 5.1(a)) and spin liquid correlations.

5.6 Conclusion and outlook

In conclusion, we prepared fermionic Mott insulators on a triangular optical lattice and performed single-site resolved imaging to detect spin-spin correlations which allow to infer the temperature of our systems. The radial density profiles of the observed Hubbard systems are in agreement with DQMC and NLCE calculations.

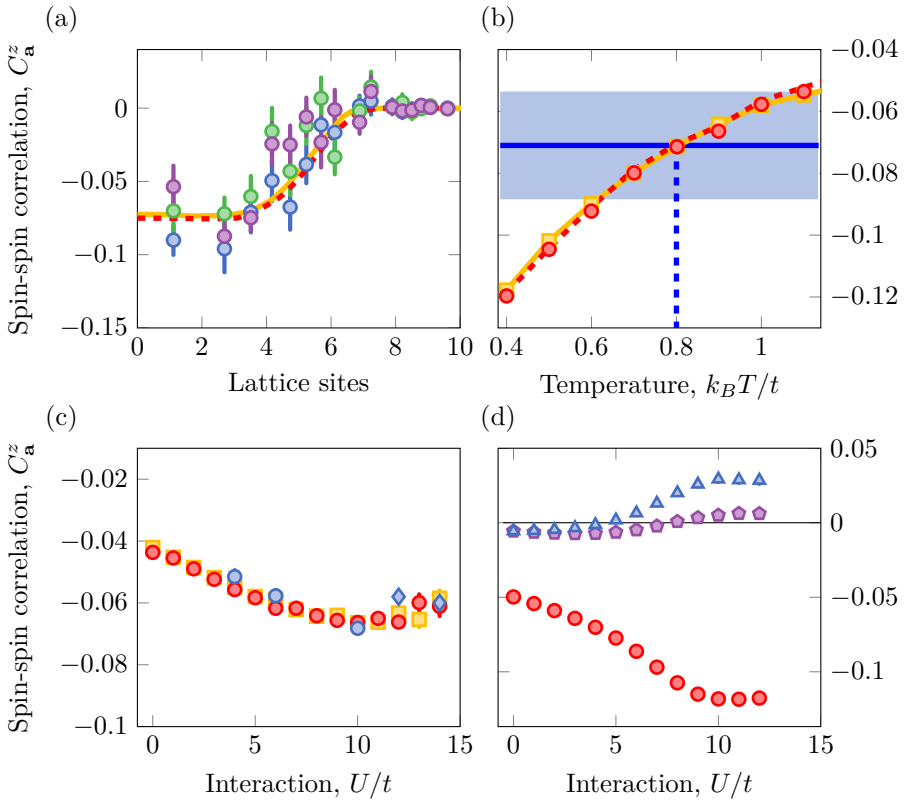

Figure 5.4: **Thermometry and interaction dependence of spin-spin correlations.** (a) Spatial variation of nearest-neighbor correlations. Blue, violet and green dots are measured correlations along $\mathbf{a} = \mathbf{b1}$, $\mathbf{b2}$ and $\mathbf{b1} - \mathbf{b2}$, respectively. We perform an azimuthal average along the equipotential of the lattice confinement. The experimental data is fit to DQMC (red dashed line) and NLCE (orange solid line) and we extract a temperature $k_BT/t = 0.80(10)$. Error bars are the standard error of the mean. (b) Nearest-neighbor spin-spin correlation as a function of temperature. The experimental correlations at the center of the trap are visualized by the light blue shaded band with average indicated by the blue line compared with calculations from DQMC (red dots) and NLCE (orange squares) at half-filling. Orange solid and red dashed lines are a guide to the eye. The width of the blue band indicates the error of nearest-neighbor spin-spin correlation evaluated by the error propagation of nearest-neighbor spin-spin correlations established in Fig. 5.3(b). We find $k_BT/t = 0.80(25)$ (blue dashed line). (c) Interaction dependence of nearest-neighbor spin-spin correlations. Measured correlations (blue dots)

are compared with DQMC (red dots) and NLCE (orange squares) theory for temperature $k_BT/t \sim 0.9$ at half-filling. Blue diamonds are measured using lattice depth of $12.0(7)\,\mathrm{E_r^{Tri}}$ to avoid losses at larges values of U. Error bars are the standard error of the mean evaluated by bootstrap. (d) DQMC calculation of spin-spin correlations at $k_BT/t = 0.4$ at half-filling for shifts $(1, 0)$, $(1.5, 0.9)$ and $(2, 0)$ (red dots, blue triangles and violet pentagons, respectively). The next-nearest-neighbor spin-spin correlations show a sign change versus U/t.

Reducing the temperatures in our system is an outstanding challenge. Possible ways to significantly reduce the temperature are a redesign of the trapping configuration during the final evaporation, the implementation of entropy redistribution techniques [126] or the addition of ^{7}Li to the system for sympathetic cooling [142]. Future experiments will access spin-density correlations to study kinetic magnetism [53, 74, 143], enabling the study of polarons with special properties caused by the frustrated nature of the triangular lattice [73, 144, 145]. Binding energies are expected to scale with the tunneling t and may be detectable at higher temperatures compared to square lattices [73]. Systems with increased binding energy are interesting because they may provide a path towards realizing repulsive pairing at higher temperatures and, therefore, higher-temperature superconductivity. Additional future directions where our experimental platform can challenge state-of-the-art numerical calculations include the study of transport properties [146] and the experimental search for chiral ordering predicted for triangular Hubbard systems [63, 129].

Chapter 6

Implementation of Spin-Resolved Imaging

This chapter discusses the setup of spin-resolved imaging that can expand the capabilities of quantum gas microscopy to measure more observable quantities such as spin-density correlations, which enables the detection of polarons. In general, quantum gas microscopy provides information only on single-component density and singles density, where holes and doubly-occupied sites are detected as empty sites, referred to as parity-projected density. The fundamental limitation is due to the light-assisted collisions. To prevent these collisions, a magnetic field gradient can be used to separate spin states into double-well potential or double light sheets. These approaches have been successfully demonstrated in previous studies [53, 104, 143, 147]. To overcome the limitations of our quantum gas microscope, spin-resolved imaging is implemented using Stern-Gerlach separation of the two-spin components into two light sheets, inspired by [104]. Both spin states are imaged in vertically separated light sheets.

The setup of the double light sheet is depicted in Fig. 6.1. We distribute the power of the main light sheet by a high-power 50:50 beamsplitter and then combine both light sheets with another beamsplitter. Note that we stabilize the light sheet in-

tensity before directing it to the first beamsplitter. This makes the relative powers between both beams stable. We add a 1:1 telescope to the longer path, thus ensuring the beams are identical and do not have relative focus shifts. During Fermi gas sequences, the second light sheet is not necessary, and we use a motorized shutter to block the beam. Assuming that atoms are frozen in deep lattices and are prepared for Stern-Gerlach separation, the atoms are captured by the two light sheets in the presence of a magnetic field gradient (the inset of Fig. 6.1). During the imaging process, we collect scattered light from atoms in both light sheets simultaneously through the high-resolution objectives and we split the fluorescence light of individual light sheet layers by a beamsplitter. The scattered light from both layers is focused onto a camera and we compensate for the focus shift of the reflected beam from the beamsplitter by a glass block. This configuration allows us not to move the camera to the other focus position, unlike previous studies [104, 143]. The light sheets can be individually controlled in the vertical direction by mirrors attached to galvanometers (GM1, GM2). Note that galvanometer GM2 controls the global position of both light sheets while GM1 controls only one light sheet. This setup enables the simultaneous control and adjustment of both light sheets. We demonstrate this controllability by simultaneously moving both light sheets in opposite directions and detecting the atoms using absorption imaging, as shown in Figs. 6.1(b,c).

An important key to performing the Stern-Gerlach separation is the magnetic field gradient. We form the anti-Helmholtz configuration of coils by reversing the current direction of one Feshbach coil using an H-bridge (see Fig. B.11 in the appendix). This allows us to access the maximum gradient strength of approximately 280 G/cm at a current of 200 A. The spin states that we choose to perform the separation are $|2\rangle$ and $|3\rangle$ because the state $|3\rangle$ has strong magnetic moments at almost zero fields and their magnetic moment signs are opposite. This means that they will move away from each other in the presence of a magnetic field gradient, making the capture process simpler and reducing the chance that the spins end up in the wrong layer.

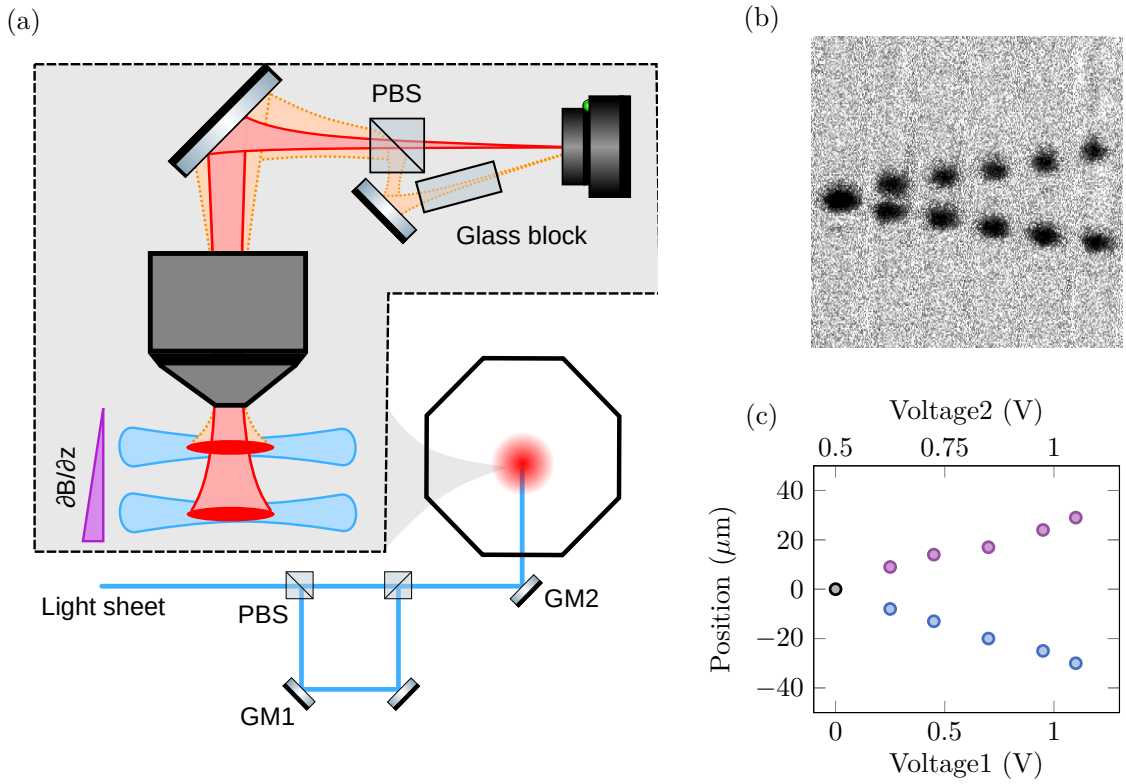

Figure 6.1: **Bilayer imaging using two light sheets.** (a) Schematic of light sheets. We split the total light sheet power into two beams called "LS1" (short path) and "LS2" (long path) using a polarizing beamsplitter (PBS). To prevent an expansion of the elliptical Gaussian beam, we add a 1:1 telescope (not shown) to the longer path, making the shape of LS2 identical to LS1. Both light sheets are combined by another PBS. To individually control the movement of the light sheets in the vertical direction, we attach mirrors to galvanometers (GM1, GM2). A glass block with a diameter of 1 inch and a length of 2.5 inches is used to compensate for the focus shift between the two layers. The relative angle between the two paths is approximately 12° at the camera. (b) Absorption images of light sheets. The two light sheets are initially overlapped at the same position (left, 0 V) and are then split by simultaneously increasing the voltages applied to the galvanometers. By varying galvanometers, both potentials can be individually controlled and here we move them away from each other. The separation between both light sheets can be greater than $50\,\mu\mathrm{m}$. The field of view is $200\,\mu\mathrm{m} \times 200\,\mu\mathrm{m}$. (c) Light sheet positions as a function of simultaneously applied voltages to galvanometers. Blue (violet) dots are light sheet potentials that capture spin states $|2\rangle$ ($|3\rangle$). The black dot represents the parameters in which two light sheets are located at the same position.

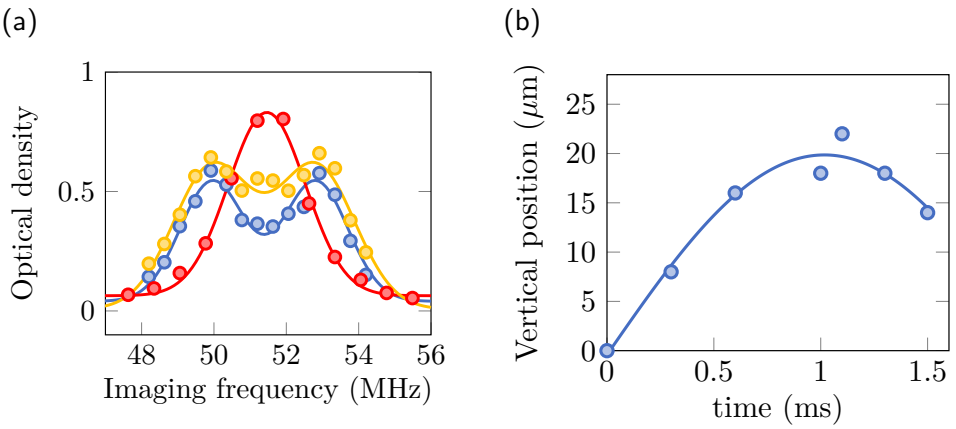

Figure 6.2: **Zero field measurement and oscillation of state $|3\rangle$.** (a) Optical density as a function of low-field imaging frequency in the presence of various magnetic fields. Background (red), anti-Helmholtz of Feshbach coils at $92\,\mathrm{A}$ (blue), Z-offset field at $10\,\mathrm{A}$ (orange). The two peaks correspond to the two hyperfine states, $|2\rangle$ and $|3\rangle$. The peak separations imply an offset magnetic field of 5.8 G. (b) A quarter period of simple harmonic motion. Here, we suddenly apply a magnetic field gradient of 35 G/cm to a lattice depth of $16\,\mathrm{E_r^{Sq}}$ and let the cloud evolve for a variable time. The oscillation occurs when the total forces on the atoms are not balanced, as the lattice acts as a restoring force to the center, and the force of the magnetic field gradient is proportional to the field gradient. By fitting the oscillation to a sinusoidal function, the oscillation frequency is extracted and yields approximately $(2\pi)\times$ 300 Hz. Note that this result is consistent with the measurement of a non-interacting Fermi gas, discussed in Section 4.5.

We ensure that the residual offset field of the magnetic gradient from Feshbach coils is either not completely zero or high by measuring the Zeeman splitting of the lowest hyperfine state at various field configurations (Fig. 6.2(a)). A large separation between spins can be achieved by maximizing the differential magnetic moment between the two spin states. We confirm the direction of separation of individual spins by holding a $|2\rangle - |3\rangle$ mixture in an optical lattice and suddenly turning on the magnetic field gradient for a variation of time. We then image a spin component using absorption imaging in a low-field regime. Here, we observe an oscillation as a

function of the hold time. This can be understood by considering simple harmonic motion around the trap center, with an initial velocity applied at the initial time, as depicted in Fig. 6.2(b).

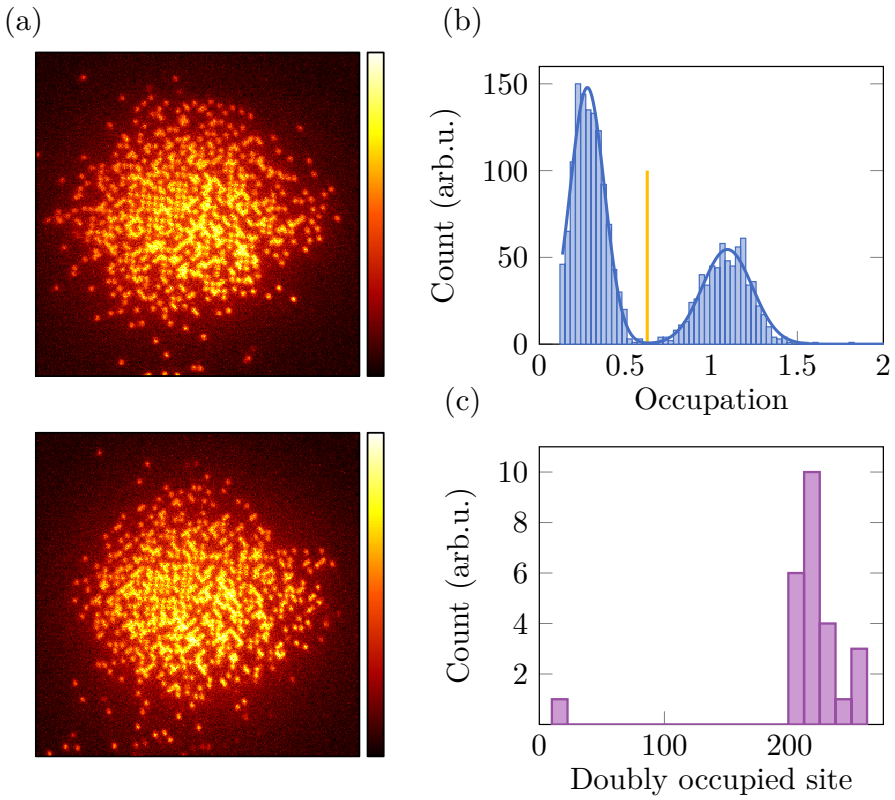

Figure 6.3: **Count histogram and reconstruction of spin-resolved imaging.** (a) Single-site resolution of $|1\rangle$ (top) and $|3\rangle$ (bottom). (b) Count histogram of reconstruction. Orange marks a threshold of occupation, allowing us to choose real single atoms from candidates. (c) Doubly-occupied sites of center overlap. By overlapping the center of $|1\rangle$ and $|3\rangle$, a certain configuration provides the lowest doubly-occupied sites and this is the correct overlapping of the two pictures.

With the capabilities of spin-resolved imaging, we study Fermi-Hubbard parameters as described in [58] using a balanced $|1\rangle - |3\rangle$ mixture. To obtain a $|2\rangle - |3\rangle$ mixture that is suitable for the Stern-Gerlach separation, we ramp the lattice to $50\,\mathrm{E_r^{Sq}}$ and apply a $|1\rangle - |2\rangle$ RF sweep centered at 595 G spanned by 50 kHz. This transfer has an efficiency greater than 99%. Next, we ramp up the lattice depth to $120\,\mathrm{E_r^{Sq}}$

and turn on a magnetic field gradient of approximately 170 G/cm. Two light sheets are simultaneously turned on and stay 8 µm apart from each other, capturing atoms occupying different states. We then move both light sheets further separated to 20 µm and perform fluorescence imaging. In Fig. 6.3(a), spin-resolved fluorescence images of spins show an antiferromagnetic patch as expected for a square lattice in a repulsive regime. We suppress the background noise from the other layer by increasing the exposure time to 2 s and the count histogram shows well-separated peaks between empty and occupied sites (Fig. 6.3(b)). The center position of both spins is sensitive to the overlapping procedure. For example, the accuracy of overlapping by the center of mass has an error of a few sites, typically less than 2 lattice sites. To overlap more precisely, we minimize doubly-occupied sites formed by two types of spin images, similar to [143], because we expect to see fewer doubly-occupied sites at half-filling which corresponds to a density of one. As a result, an impressive spin-resolved image is illustrated in Fig. 6.4, providing information on full density: spin up, spin down, doublon, and hole.

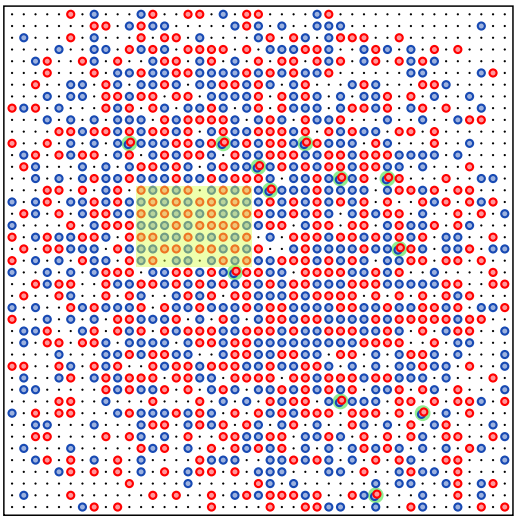

Figure 6.4: **Full density-resolved imaging.** Both spins (red, blue), shown in Fig. 6.3(a), are overlaid in the configuration where doubly-occupied sites are minimized, corresponding to the leftmost part of the histogram in Fig. 6.3(c). The green shading represents a doubly-occupied site and small dots are optical lattices. The lightly shaded yellow area illustrates an antiferromagnetic patch.

We check the fidelity of the Stern-Gerlach separation by preparing Mott insulators with the density of singles filling of 93.6(3)% and compare it to a spin-resolved image with a filling of 91.1(4)%. As a result, we obtain a separation fidelity of 97.8(4)%. The reduction of singles density in spin-resolved images indicates losses during the transport process illustrated in Fig. 6.5. We determine the imaging fidelity by taking a series of images similar to previous work [84]. In fact, the imaging fidelity is lower than the previous measurement because we increase the exposure time to suppress the background noise from the defocused layer. It is important to note that the splitting is very sensitive to the ratio of the single light sheet power to the lattice power. We find that the splitting does not separate well when the light sheet power is weaker than the lattice power. In addition, the imaging fidelity is also very sensitive to Raman parameters, especially the Raman repump detuning. This is because we use a stronger light sheet power, and the light shift plays an important role in fluorescence imaging.

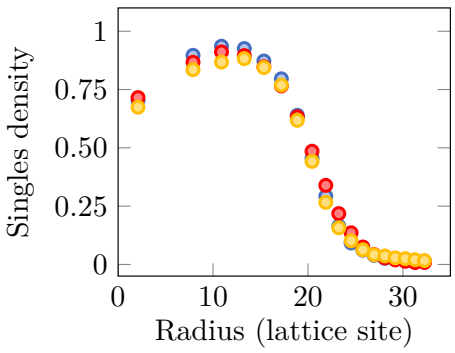

Figure 6.5: **Stern-Gerlach separation fidelity.** Singles densities without and with splitting are 93.6(3)% (blue), 91.1(4)% (red). The reverse process of the splitting is employed, yielding a lower singles density of 88.2(4)% (orange). This information allows us to obtain the separation fidelity of 97.8(4)%.

To verify our spin-resolved implementation, we measure the spin-spin correlation of a balanced $|1\rangle - |3\rangle$ mixture at a lattice depth of $7.4\,\mathrm{E_r^{Sq}}$ and a magnetic field of 603 G, resulting in $U/t \approx 7$. In Fig. 6.6(a), spin-spin correlations for nearest and next-nearest neighbors are measured and the correlations show a symmetry at density $n \approx 1$. The correlations beyond nearest neighbor sites are observed in Fig. 6.6(b). We note that this is the first time we have observed correlations beyond nearest neighbors in our quantum gas microscope. Unfortunately, this observation

is in a square lattice, not a triangular lattice. Temperature can be determined separately from correlations by the fluctuation-dissipation theorem, demonstrated in [147]. Here, we apply a similar approach to determine the temperature of a two-spin mixture. The density fluctuation-dissipation theorem is given by

$$\kappa n^2 = \frac{1}{T} \sum_{\delta} \Big(\langle \hat{n}_i \hat{n}_{i+\delta} \rangle - \langle \hat{n}_i \rangle \langle \hat{n}_{i+\delta} \rangle \Big), \tag{6.1}$$

where T is the temperature and δ is the correlated lattice site. κ is the compressibility which can be obtained as follows: By applying the local density approximation, the chemical potential can be written in terms of radial dependence. The compressibility, κ, is expressed as

$$\kappa n^2 = \left. \frac{\partial n}{\partial \mu} \right|_T = -\frac{1}{m\omega^2 r} \frac{\partial n}{\partial r}, \tag{6.2}$$

where n is the full density, m is the atomic mass, and ω is the confinement, which can be obtained from the measurement in Section 4.5. Therefore, we apply a linear fit to κn^2 and $\sum_\delta(\dots)$ and the system temperature is extracted from the slope. As can be seen in Figs 6.6(a,c), the temperatures are consistent between the two methods within error bars. Finally, we measure the spin-spin correlations dependence on interaction by varying magnetic fields at a fixed lattice depth. The correlations show the strongest value at $U/t \approx 7$, agreeing with numerical calculations (Fig. 6.6(d)).

Here, the second generation of our quantum gas microscope is prepared to study interesting phenomena described by the Fermi-Hubbard model beyond a two-spin component in the following chapter.

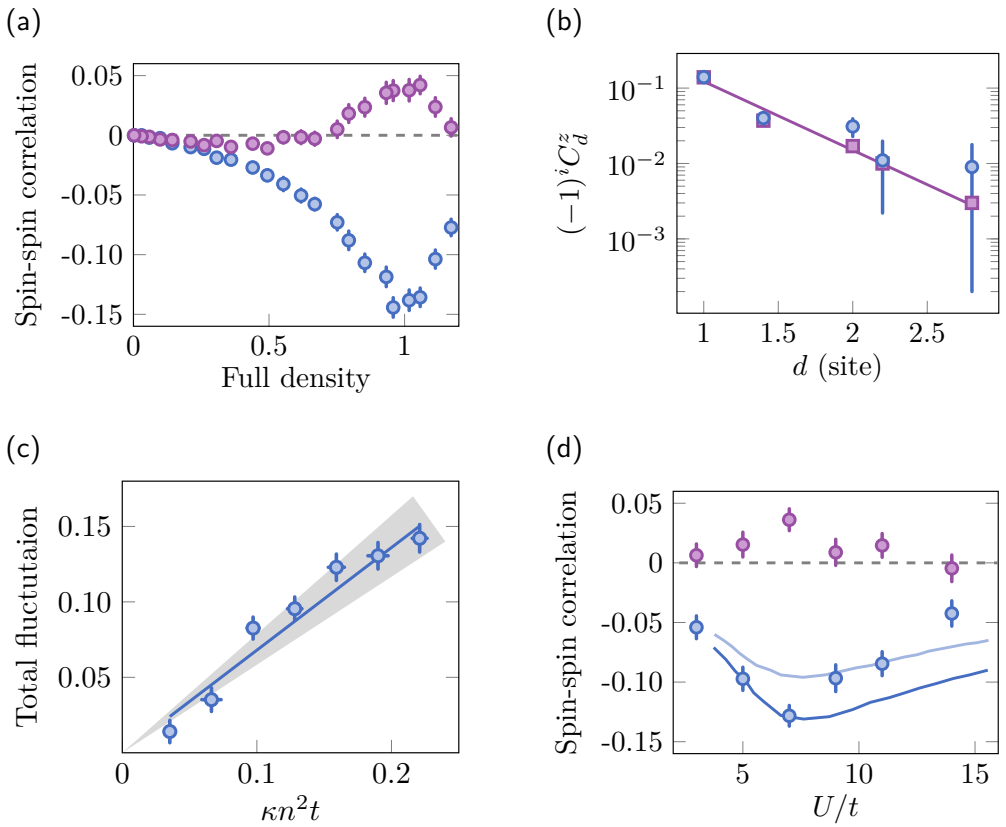

Figure 6.6: **Spin-spin correlations.** (a) Correlations at $U/t \approx 7$. Blue and violet dots are nearest and next-nearest neighbors. The correlations are symmetric about half-filling (full density is unity) due to particle-hole symmetry. (b). Spin-spin correlations as a function of correlated distance. Data are represented by blue dots, and the calculation of DQMC at $k_B T/t = 0.6$ and $U/t = 7$ is denoted by violet squares. The solid line is an exponential function as a guide to the eye. (c) Total density fluctuations as a function of compressibility. The slope of the linear regression yields the temperature of $k_B T/t = 0.68(8)$ indicated by gray shading. This is consistent with the observation from the spin-spin correlations. (d) Spin-spin correlations as a function of interaction at a density of one (half-filling). Note that the correlation of the rightmost point at $U/t = 14$ is selected at $n \approx 0.9$ due to the unavailability of density in the dataset. The blue dots represent nearest neighbors, while the violet dots represent next-nearest neighbors. The blue and light blue solid lines illustrate theoretical calculations at $k_B T/t = 0.88$ and $k_B T/t = 0.65$ at half-filling, taken from [52].

Chapter 7

Quantum Gas Microscopy of Three-Component Fermi-Hubbard Systems

A two-component Fermi gas is of interest for the understanding quantum phases, particularly the crossover from Bardeen–Cooper–Schrieffer (BCS) superfluidity, where fermions form pairs, to Bose-Einstein Condensates (BECs), characterized by composite bosons. The crossover is an exciting intersection for both high-temperature superconductivity and cold-atom superfluidity. Extending the number of spin components in systems leads to a wide variety of novel effects, for example, color superfluidity and aspects of quantum chromodynamics may become accessible to direct experimental study. In this chapter, I present our recent measurement of a balanced three-component Fermi gas in an optical lattice. First, I discuss how we apply our spin-resolved imaging to detect densities and pairing correlations in the three-component Fermi lattice systems. Finally, I present a simple picture for understanding the configurations of three-component fermions in an optical lattice for different interaction regimes. We note that this work is currently under discussion, and the interpretation of certain effects is awaiting a more detailed understanding

through comparison with theoretical calculations. We are currently collaborating with a theoretical group using Determinantal Quantum Monte Carlo (DQMC) and Numerical Linked-Cluster Expansion (NLCE) calculations.

In two-component Fermi gases, three-body phenomena are suppressed due to the Pauli exclusion principle. However, introducing an additional spin state makes three-body effects relevant, therefore leading to new physics phenomena such as Efimov physics. In Efimov physics, interactions are nearly resonant, and the competition between pairwise components supports the formation of three-body bound states, referred to as trimers, even at larger interparticle spacings. However, these trimers are highly unstable due to three-body recombination, which is a three-body collision in which two particles form a deeply bound dimer. The lifetimes of these trimers are predicted to be less than the typical timescale of quantum gas experiments [148].

The stability of a three-component fermionic ^{6}Li was studied in free space and the stability was determined by the three-body loss rate coefficient at various magnetic fields in both balanced [149, 150] and imbalanced three-component mixtures [151]. In addition, the direct measurement of binding energy by radio-frequency spectroscopy confirmed the existence of Efimov trimers [152]. The formation of a fermionic three-component bound state allows the subject of quark matter to be studied through ultracold atoms. For example, a quark color superconductor is predicted in one-dimensional (1d) attractive three-component systems [153]. A quantum phase transition between color superfluidity and baryons, referred to as trimers in this context, is predicted to occur in the SU(3) model with attractive interactions [154].

On the other hand, in optical lattices, two-component Fermi lattice gases can be effectively described by Hubbard models, which were introduced as model systems to understand the physics of strongly correlated electronic systems [118]. The SU(2) Hubbard model is believed to capture key aspects of high-temperature superconductivity [23]. Using pseudo-spin states via nuclear spins, SU(N) Hubbard systems were realized in ^{173}Yb. These systems are anticipated to manifest exotic physics beyond

classical models. For example, in SU(3), three-sublattice order is predicted in the Heisenberg model at zero temperature, or a mechanism known as "order by disorder" leads to two-sublattice order at temperatures comparable to the exchange energy [155, 156]. Examples of experimental studies include the SU(6) Mott insulator in a 3d cubic lattice [157, 158] and the equation of state of SU(3) and SU(6) systems [159]. Measurements of antiferromagnetic correlations have been conducted in the SU(6) Fermi-Hubbard model in 1d, 2d square, and 3d cubic lattice geometries [160]. However, in the presence of the coupling of nuclear and electronic angular momenta, the SU(N) symmetry is broken, as exemplified by ^{6}Li atoms. Three-component systems with unequal interaction strengths have been studied numerically, revealing a variety of quantum phases. In particular, different classes of Mott insulating states have been identified, depending on the interactions [161–163].

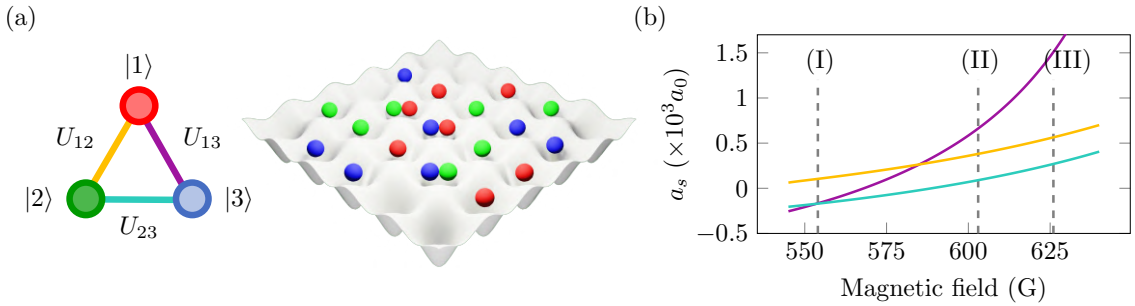

Figure 7.1: **Quantum gas microscopy of three-component Fermi gases.** (a) The definition of spin components and interactions between pairwise components (left) and three-component Fermi lattice gases (right). (b) Tunability of the three interactions for pairwise components, U_{13} (violet), U_{12} (orange), and U_{23} (cyan). (I)-(III) represent interaction regimes at magnetic fields of 555.9(1), 603.3(1), and 625.9(3) G chosen for measurements.

In this work, we study a balanced three-component Fermi gas in a square lattice with imbalanced interactions and investigate the competition among the pairwise components through pairing correlations. Here, we define the three lowest hyperfine states of ^{6}Li as $|1\rangle = |F = 1/2, M_F = 1/2\rangle$, $|2\rangle = |F = 1/2, M_F = -1/2\rangle$, and $|3\rangle =$

$|F = 3/2, M_F = -3/2\rangle$ where F and m_F are the hyperfine and magnetic quantum numbers. We label the three spin components as $|1\rangle$ (red), $|2\rangle$ (green), and $|3\rangle$ (blue). Their pairwise interactions are represented by U_{12} (orange), U_{23} (cyan), and U_{13} (violet), as illustrated in Fig. 7.1(a). The nature of Feshbach resonances enables us to tune the relative interaction strengths (Fig. 7.1(b)) from all repulsive interactions (II, III) to one repulsive and two attractive interactions (I). In addition, varying the lattice depth offers a variety of accessible absolute interactions.

7.1 Fermi-Hubbard model

Our system is well described by the three-component Fermi-Hubbard model in a two-dimensional square lattice, with the Hamiltonian given by

$$\begin{aligned}\hat{\mathcal{H}} = &- t \sum_{\langle \mathbf{r}\mathbf{r}' \rangle} \sum_{\alpha=1}^{3} (\hat{c}^{\dagger}_{\mathbf{r}\alpha} \hat{c}_{\mathbf{r}'\alpha} + \hat{c}^{\dagger}_{\mathbf{r}'\alpha} \hat{c}_{\mathbf{r}\alpha}) - \sum_{\mathbf{r}} \sum_{\alpha=1}^{3} \mu_{\alpha}(\mathbf{r}) \hat{n}_{\mathbf{r}\alpha} \\ &+ \sum_{\mathbf{r}} \sum_{\alpha \neq \beta} U_{\alpha\beta} \hat{n}_{\mathbf{r}\alpha} \hat{n}_{\mathbf{r}\beta},\end{aligned} \tag{7.1}$$

where $\alpha, \beta \in \{1, 2, 3\}$ represents the fermionic colors that correspond to the three lowest hyperfine states, t is the tunneling strength between nearest-neighbor lattice sites, $U_{\alpha\beta}$ is the on-site interaction between a pairwise component $\alpha\beta$, $\hat{c}_{i\alpha}(\hat{c}^{\dagger}_{j\alpha})$ is the annihilation (creation) operator for a fermion with color α on lattice site $\mathbf{r}$, $\hat{n}_{\mathbf{r},\alpha} = \hat{c}^{\dagger}_{\mathbf{r}\alpha} \hat{c}_{\mathbf{r}\alpha}$ is the number operator, and $\mu_{\alpha}(\mathbf{r})$ is the chemical potential of a fermion color α. We apply the local density approximation (LDA) to map the variation in atom density in the presence of a confinement potential to a homogeneous gas i.e., $\mu_{\alpha}(\mathbf{r}) = \mu_{0,\alpha} - (1/2)m\omega^2 r^2$ where ω is the confinement frequency, m is the atomic mass, and $\mu_{0,\alpha}$ is the chemical potential at the trap center for the fermionic color α. As can be seen, the Fermi-Hubbard model provides the theoretical foundation for our system. Subsequently, the Hubbard parameters are calibrated.

Tunneling calibration

The tunneling parameter is calibrated using a similar approach as discussed in section 4.3.1. Here, we prepare non-interacting Fermi gases of a $|1\rangle - |3\rangle$ mixture in a square lattice and perform amplitude modulation for 100 ms with an amplitude of 5% of the offset power over a certain range of modulation frequencies. Atom losses are observed near the transition from the $S-$band to the $D-$bands (Fig. 7.2). This observation allows us to extract the lattice depth for a certain lattice beam power, similar to previous work [58]. We now turn our focus to calibrating the interaction strengths in the system, a critical step in characterizing the Fermi-Hubbard model, as discussed in the following section.

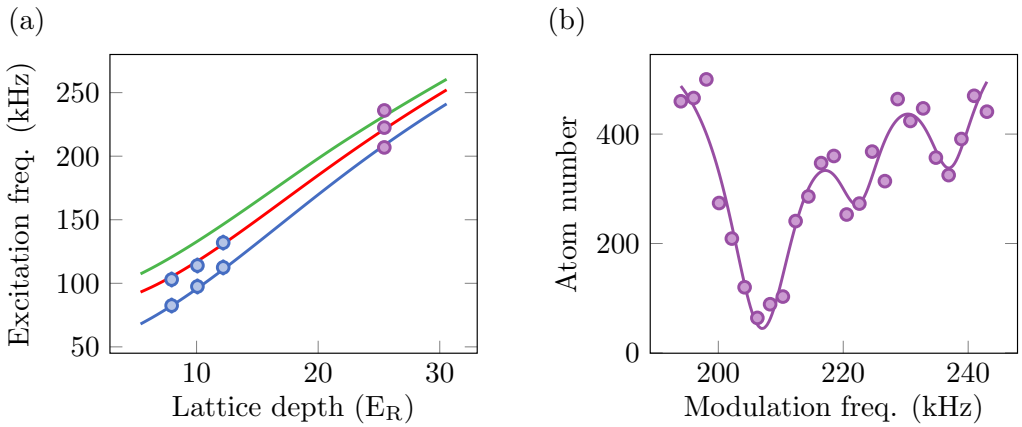

Figure 7.2: **Band excitation of a square lattice.** (a) Band excitation as a function of lattice depth. Dots represent the measurements and solid lines are the excitation frequencies calculated using the band structure in the tight-binding limit. The third resonance is not obvious for shallow lattice depths. (b) Lattice amplitude modulation of the violet dots in (a). Data (dots) are fit to a triple Gaussian function (solid line). Using the knowledge of excitation frequencies, we determine the experimental lattice depths.

Interaction calibration

To obtain the interaction between spin components, we prepare a $|1\rangle - |3\rangle$ band insulator at a target field and we use a lattice depth of $15.0(3)\,E_r^{Sq}$. We transfer

atoms from the state $|1\rangle$ to the state $|2\rangle$ using a pulse duration of 1 ms. By scanning the RF frequency, the state $|1\rangle$ of singles and doublons can be transferred to the state $|2\rangle$ (Fig. 7.3). The separation of the two peaks allows us to determine the interaction strength. A detailed discussion of this technique can be found in Section 4.3.1.

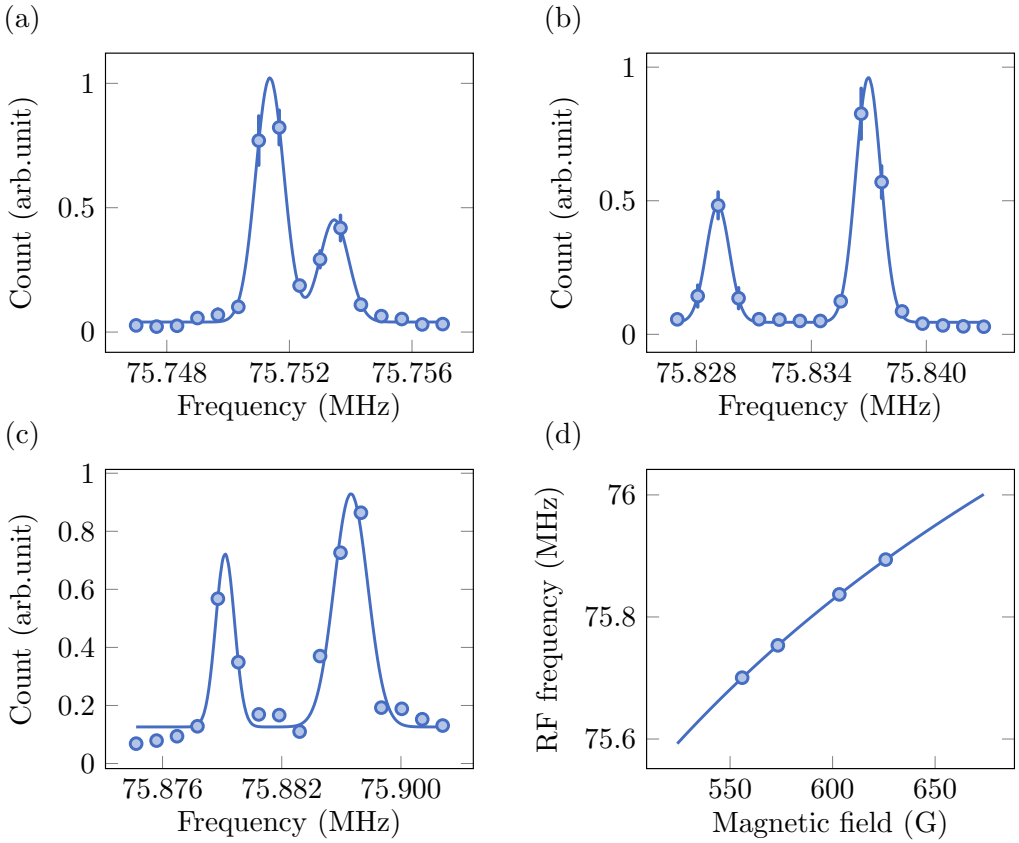

Figure 7.3: **Hubbard interaction calibration.** Magnetic offset fields of (a) 573.3(3) G, (b) 603.3(1) G, and (c) 625.9(3) G are used with a lattice depth of $15.0(3)\,\mathrm{E_r^{Sq}}$. The right peak corresponds to the transfer of the state $|1\rangle$ from the singles component, while the left peak is due to the transfer of the state $|1\rangle$ from a $|1\rangle - |3\rangle$ doubly-occupied site. The magnetic field can be inferred using the peak of singles transfer, and the peak separation is proportional to the interaction strength, similar to the approach in ref. [164]. The peak separations in (a)-(c) are 2.10(7), 7.85(8), and 14.8(16) kHz. (d) Energy separation of the singles transfer as a function of magnetic field. Dots represent the measurements obtained from (a)-(c). The RF spectroscopy of the leftmost dot is not shown. The solid line is calculated using the Breit-Rabi formula.

7.2 High-temperature series expansion

The Fermi-Hubbard model is expected to describe our three-component systems. However, due to the challenging nature of numerical calculations for three-component many-body systems, we roughly approximate the systems using the high-temperature series expansion (HTSE) in the atomic limit, where the tunneling strength is suppressed compared to the interaction strength. This concept was introduced in Section 4.4 for a two-component mixture. Here, we work with a three-component mixture. The partition function that represents this system is given by

$$Z = \sum_{n_1=0}^{1} \sum_{n_2=0}^{1} \sum_{n_3=0}^{1} z(n_1, n_2, n_3), \tag{7.2}$$

and

$$z(n_1, n_2, n_3) = \exp\left(\tilde{\beta}(\sum_{\alpha=1}^{3} \mu_\alpha n_\alpha - \sum_{\alpha\neq\gamma} U_{\alpha\gamma} n_\alpha n_\gamma) \right), \tag{7.3}$$

where $\tilde{\beta} = 1/(k_B T)$ and Z is the partition function. We note that in Eq 7.3, the chemical potentials, μ_α, are introduced for three spin components due to the symmetry breaking of SU(3) in our system. The pairwise interactions, $U_{\alpha\gamma}$, are imbalanced in the system. The summations in Eq. 7.2 are restricted between 0 and 1 for each spin component, representing the fermionic nature of the systems where two identical spins are not allowed to occupy the same site.

According to the partition function, we can calculate observable quantities, discussed as follows: The singles occupation is calculated as

$$n_s = \frac{1}{Z} \sum_{n_1=0}^{1} \sum_{n_2=0}^{1} \sum_{n_3=0}^{1} \mod (n_1 + n_2 + n_3, 2)\ z(n_1, n_2, n_3). \tag{7.4}$$

Here, the $\mod (n_1 + n_2 + n_3, 2)$ function projects the total density onto 0 or 1, reflecting the loss of doubly-occupied sites during imaging caused by light-assisted collisions.

The single-component densities of the three-component mixture are simultaneously determined as

$$[\bar{n}_1, \bar{n}_2, \bar{n}_3] = \frac{1}{Z} \sum_{n_1=0}^{1} \sum_{n_2=0}^{1} \sum_{n_3=0}^{1} [n_1, n_2, n_3]\ z(n_1, n_2, n_3). \tag{7.5}$$

Next, the mean squared single-component densities are calculated as

$$[\bar{n_1^2}, \bar{n_2^2}, \bar{n_3^2}] = \frac{1}{Z} \sum_{n_1=0}^{1} \sum_{n_2=0}^{1} \sum_{n_3=0}^{1} [n_1^2, n_2^2, n_3^2] \; z(n_1, n_2, n_3). \tag{7.6}$$

By combining Eq. 7.5 and 7.6, the variance of full density is expressed as

$$\begin{aligned} \sigma^2 &= \bar{n^2} - \bar{n}^2 \\ &= \sum_{\alpha=1} \bar{n_\alpha^2} - (\sum_{\alpha=1} \bar{n}_\alpha)^2. \end{aligned} \tag{7.7}$$

Finally, the doublon densities of each pairwise component are computed as

$$\begin{aligned} (\bar{n}_{d13}, \bar{n}_{d12}, \bar{n}_{d23}) = \frac{1}{Z} \sum_{n_1=0}^{1} \sum_{n_2=0}^{1} \sum_{n_3=0}^{1} [n_1 n_3, n_1 n_2, n_2 n_3] \\ z(n_1, n_2, n_3). \end{aligned} \tag{7.8}$$

7.3 Experimental setup

To realize a balanced three-component Fermi lattice gas, we prepare a spin-balanced Fermi gas using $|1\rangle - |3\rangle$ mixture of ^{6}Li atoms in a single layer of a one-dimensional accordion lattice, discussed in Section 3.9. We obtain a three-component mixture by applying radio-frequency (RF) pulses to drive the $|1\rangle - |2\rangle$ and $|2\rangle - |3\rangle$ transitions during final evaporation at a magnetic field of 594 G. The optimization of a balanced three-component mixture is accomplished by fine-tuning the pulse duration around the one-third period of Rabi oscillations shown in Fig 7.4. We note that collisions between atoms within the timescale of the experiment result in an incoherent mixture of spin states. We verify the spin population for each dataset by constructing a count histogram as demonstrated in Fig. 7.5.

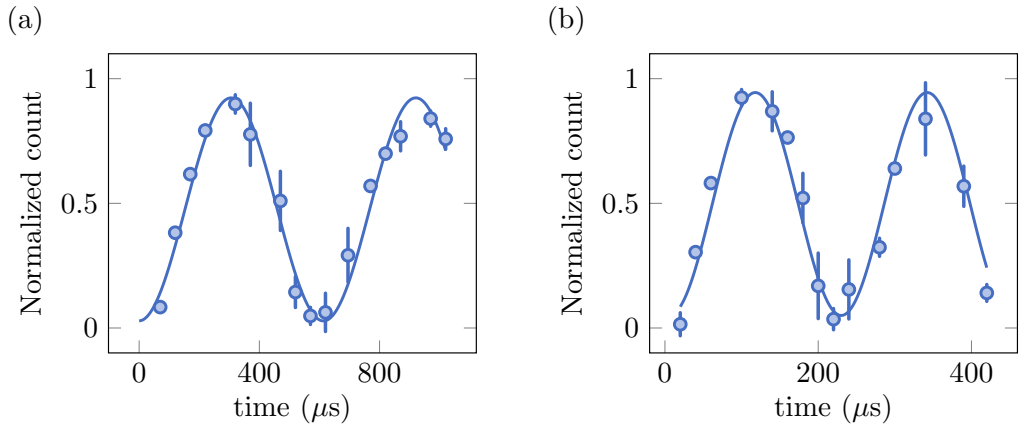

Figure 7.4: **Rabi oscillation of the three lowest hyperfine states.** (a) $|1\rangle - |2\rangle$ oscillation. We drive the $|1\rangle - |2\rangle$ transition with a Rabi frequency of $(2\pi) \times 1.63(8)$ kHz at a magnetic field of 594 G. (b) $|2\rangle - |3\rangle$ oscillation. The $|2\rangle - |3\rangle$ transition is driven and exhibits a Rabi frequency of $(2\pi) \times 4.46(21)$ at the same magnetic field as in (a). We note that the Rabi frequency depends on the power of the RF applied in the experiment. Error bars represent the standard error of the mean over three datasets.

Next, we tune the magnetic field to 625.9(3) G corresponding to scattering lengths of $564(3)a_0$, $1509(16)a_0$, and $269(3)a_0$ for a_{12}, a_{13} and a_{23}, where a_0 is the Bohr radius, for three pairs of spin mixtures. Atoms are loaded into a square lattice of a desired depth between $9.1(2)\,\mathrm{E_r^{Sq}}$ and $16.0(3)\,\mathrm{E_r^{Sq}}$ where $\mathrm{E_r^{Sq}} = \hbar\pi^2/(2ma_{\mathrm{latt}}^2) = h \times 14.6$ kHz is the recoil energy and h is Planck's constant, m is the atomic mass, and $a_{\mathrm{latt}} = 752$ nm. This configuration gives us $U_{13}/t = 87(10)$, $U_{12}/t = 33(4)$, and $U_{23}/t = 16(2)$. The atom number and density in the lattice are adjustable by varying evaporation parameters. The motion of atoms is frozen by rapidly ramping up the lattice to $50\,\mathrm{E_r^{Sq}}$ in 500 µs. Afterward, we prepare for the Stern-Gerlach experiment of two components by removing one component and transferring the remaining atoms to the $|2\rangle - |3\rangle$ mixture. We apply a similar procedure as discussed in Chapter 6 for spin-resolved imaging by splitting the components vertically and imaging both components simultaneously. As a result, we obtain the fluorescence imaging of two spin states simultaneously. By repeating the same procedure for each pair of

spin components, the full information of a three-component Fermi lattice system is revealed.

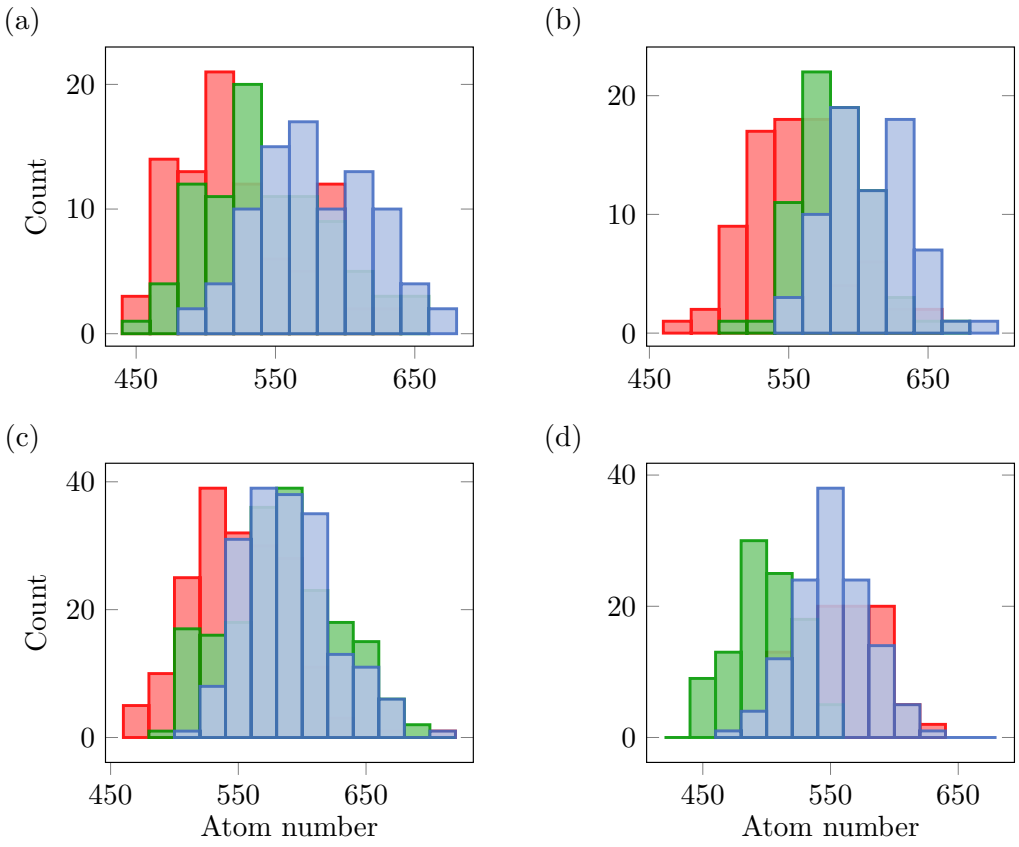

Figure 7.5: **Atom number histogram.** (a), (b), (c), and (d) correspond to Figs. 7.6, 7.7(a,c), 7.7(b,d), and 7.8, respectively. Red, green, and blue represent the states, $|1\rangle$, $|2\rangle$, and $|3\rangle$. The histogram bin width is 10 atoms. The fluctuations in the atom numbers for each spin component are within 10%.

7.4 Three-component Mott insulators

In the first measurement, we use the information from spin-resolved imaging to study the single-component density for each color, n_α, as a function of radius from the trap center. The summation of these single-component densities gives the total density, $n = n_1 + n_2 + n_3$, as depicted in Fig. 7.6(a). Hereafter, we will discuss observable quantities as a function of the total density. This allows us to compare the system

properties without considering their radial dependence. The doubly-occupied site density of the $\alpha\beta$ pairwise component, $n^d_{\alpha\beta}$, can be constructed by overlapping spin components, as discussed in Chapter 6. As can be seen in Fig. 7.6(b), n^d_{23} has a higher fraction than n^d_{13} and n^d_{12} due to the lower interaction U_{23}. The pairwise component with lower interaction is energetically favored and forms first at a lower energy cost. In this measurement, we observe a weak plateau at unity filling (Fig. 7.6(a)), indicating that the system behaves as a Mott insulator at high temperatures. We confirm the Mott insulating state by studying the variance of the total density, which is defined in Eq 7.7. In particular, we access the variance from the experiment by expanding σ^2 as follows:

$$\sigma^2 = \left\langle (n_1 + n_2 + n_3)^2 \right\rangle - \left\langle (n_1 + n_2 + n_3) \right\rangle^2 . \tag{7.9}$$

We define $\sigma^2_{\langle n_i n_j \rangle}$ as

$$\sigma^2_{\langle n_i n_j \rangle} = \langle n_i n_j \rangle - \langle n_i \rangle \langle n_j \rangle , \tag{7.10}$$

and the variance can be written in terms of observable quantities

$$\begin{aligned} \sigma^2 = {} & \sigma^2_{\langle n_1, n_1 \rangle} + \sigma^2_{\langle n_2, n_2 \rangle} + \sigma^2_{\langle n_3, n_3 \rangle} \\ & + 2(\sigma^2_{\langle n_1, n_2 \rangle} + \sigma^2_{\langle n_1, n_3 \rangle} + \sigma^2_{\langle n_2, n_3 \rangle}). \end{aligned} \tag{7.11}$$

Here, $\langle \ldots \rangle$ denotes the averaging over ensembles. We note that our spin-resolved imaging offers the detection of all terms in Eq. 7.11, whereas the first three terms can be obtained without the spin-resolved resolution. As a result, we observe a suppression of the variance at unity density (Fig. 7.6(c)), similar to a two-component Mott insulator. However, due to strong three-body losses at a magnetic field of approximately 626 G, accessing higher densities is challenging [149, 150]. Additionally, we confirm the signature of the Mott insulator by studying the compressibility, κ, defined in Eq. 6.2. We note that the full density, n, is extracted from single-component densities of three spin states, n_α, and ω is the confinement obtained from the measurement of a non-interacting Fermi gas, discussed in Section 4.5. In Fig. 7.6(d), we observe suppression of the compressibility in the region of unity filling, suggesting insulating behavior in the regime of an ordinary Mott insulator.

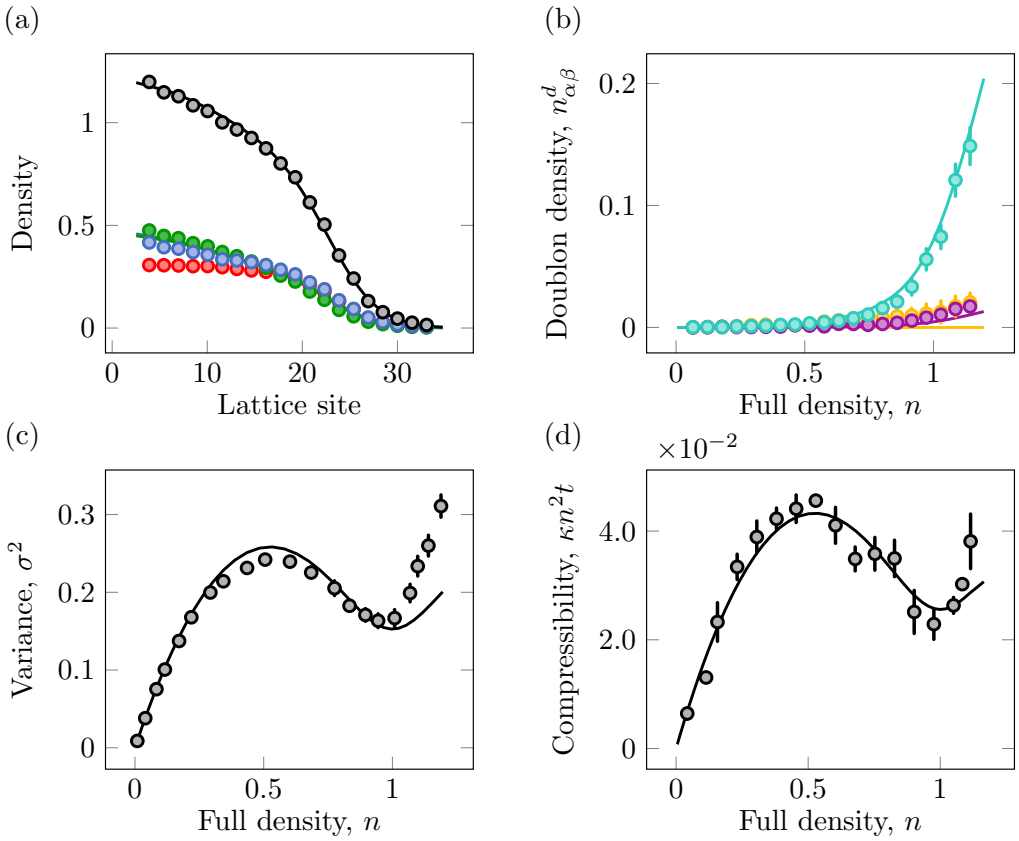

Figure 7.6: **Three-component Mott insulators.** (a) Density as a function of radius from the trap center for $|1\rangle$ (red), $|2\rangle$ (green), and $|3\rangle$ (blue) at $U_{13}/t = 87(10)$, $U_{12}/t = 33(4)$, and $U_{23}/t = 16(2)$, referring to regime III of Fig. 7.1(b). The full density (black) is obtained by summing up all individual spin component densities. The data is fitted to the high-temperature series expansion in the atomic limit by imposing global chemical potentials and temperature as free parameters. The fit results in $\mu_{0,1} = 15.4(7)$, $\mu_{0,2} = 15.0(9)$, $\mu_{0,3} = 15.2(9)$ and $k_B T/t = 5.7(4)$. (b) Doubly-occupied density as a function of full density for pairwise components, $|1\rangle - |3\rangle$ (violet), $|1\rangle - |2\rangle$ (orange), and $|2\rangle - |3\rangle$ (cyan). (c) On-site density variance. The suppression is observed at the density of one atom per lattice site, similar to the compressibility measurement shown in (d). Error bars are the standard error of the mean over 45 datasets. (b)-(d) use the same datasets as (a).

7.5 Competition between pairwise components

To study the interplay between two spin components, $\alpha\beta$, we define a pairing correlation, given by

$$C_{\mathbf{a}}^{\alpha\beta} = \langle n_{\alpha,\mathbf{r}} n_{\beta,\mathbf{r}+\mathbf{a}} \rangle - \langle n_{\alpha,\mathbf{r}} \rangle \langle n_{\beta,\mathbf{r}+\mathbf{a}} \rangle \tag{7.12}$$

where $\mathbf{a}$ denotes the shift in the lattice site number between the two correlated positions, and $\mathbf{r}$ is the current lattice site.

In Fig. 7.7(a), we enhance the center filling by 10% through a 14% increase in the lattice depth to $16.0(3)\,\mathrm{E_r^{Sq}}$, resulting in stronger confinement while atom numbers are fixed. However, the half-filling regime is still out of reach. We expect that an improvement in atom numbers and possibly stronger confinement could allow us to reach this regime eventually. By considering the on-site pairing correlation for $|2\rangle - |3\rangle$, denoted as C_0^{23}, we observe a negative correlation for densities less than unity. This indicates that atoms of spin $|2\rangle$ and $|3\rangle$ tend to avoid occupying the same site. We observe a turning point of C_0^{23} at unity filling, with a crossover to positive correlation at $n \approx 1.1$. These correlations indicate that the $|2\rangle - |3\rangle$ state is more likely to form a pair at higher densities than a density of one, while the remaining pairs still tend to avoid each other.

To further enhance the density to approximately half-filling, we explore the regime where three-body loss is close to a minimum [149, 150]. We ramp the magnetic field to the regime (II) as shown in Fig. 7.1(b), and the lattice is set to $9.1(2)\,\mathrm{E_r^{Sq}}$, therefore providing $U_{13}/t = 11.5(5)$, $U_{12}/t = 6.6(3)$, and $U_{23}/t = 1.6(1)$. We observe a positive on-site pairing correlation for C_0^{23} and negative on-site pairing correlations for C_0^{13} and C_0^{12} over a range of accessible densities. All on-site pairing correlations seem to exhibit a turning point for the three pairs close to half-filling. For both regimes represented in Figs. 7.7(a,c) and 7.7(b,d), the relative interactions are not significantly different, however, the absolute interactions are distinct.

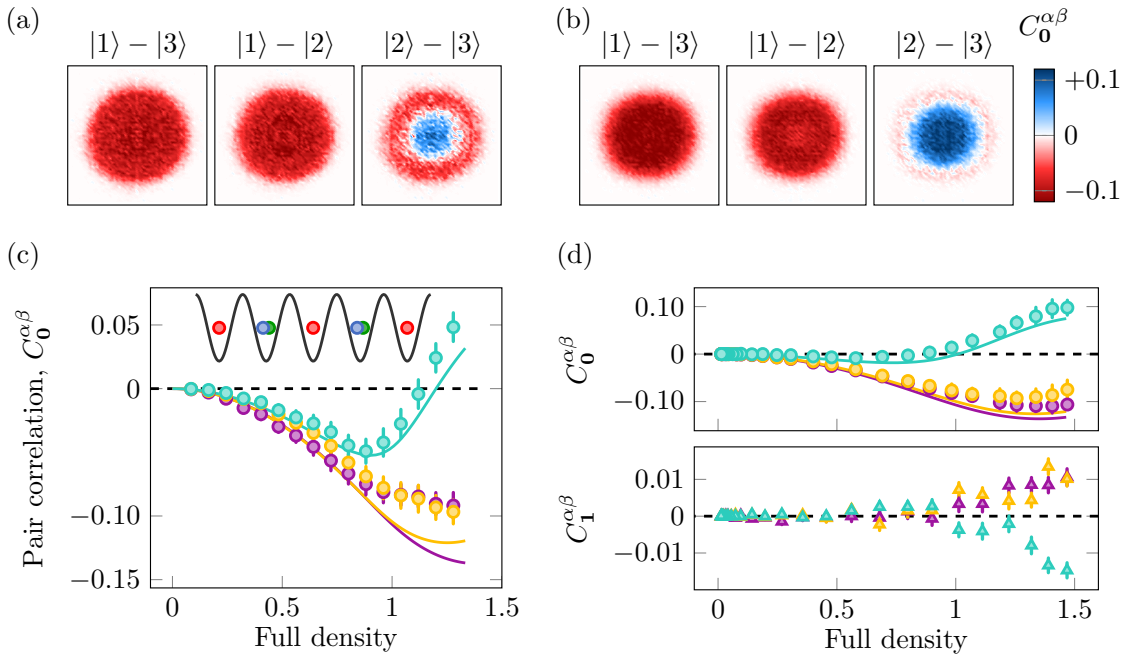

Figure 7.7: **Flavor-selective pairing.** (a,c) Direct measurement of on-site pairing correlations in a Fermi lattice gas with interactions, $U_{13}/t = 143(18)$, $U_{12}/t = 53(7)$, and $U_{23}/t = 26(3)$, referring to regime III of Fig. 7.1(b). The corresponding chemical potentials are $\mu_{0,1} = 32(1)$, $\mu_{0,2} = 31(3)$, $\mu_{0,3} = 30(2)$, and the temperature is $T/k_B t = 10(1)$ obtained from the HTSE fit. On-site pairing correlation maps for pairwise components are shown in (a). Each map has a field of view of 80×80 lattice sites. (c) Azimuthal averaging of the on-site correlations (dots) as a function of full density for $|1\rangle - |3\rangle$ (violet), $|1\rangle - |2\rangle$ (orange), and $|2\rangle - |3\rangle$ (cyan). (b,d) Measurement of the on-site and nearest-neighbor pairing correlations for interactions $U_{13}/t = 11.5(5)$, $U_{12}/t = 6.6(3)$, and $U_{23}/t = 1.6(1)$ (refer to regime II of Fig. 7.1(b)) with on-site pairing correlation maps (b). The corresponding chemical potentials are $\mu_{0,1} = 3.4(9)$, $\mu_{0,2} = 3.0(4)$, $\mu_{0,3} = 3.1(4)$, and the temperature is $T/k_B t = 1.3(4)$. (d) Azimuthal averaging of the on-site (dots) and nearest-neighbor (triangles) pairing correlations. Error bars indicate the standard error of the mean over 39 datasets and 97 datasets for (a,c) and (b,d). The inset in (c) presents a cartoon of the simplest configuration with such correlations in the lattice, constructed based on the pairing correlations.

We study the competition between pairwise components further by exploring the regime (III), demonstrated in Fig. 7.1(b) where we have two attractive and one repulsive interaction. Doubly-occupied density is measured as a function of full density depicted in Fig. 7.8(a), showing competition among $|1\rangle - |3\rangle$ and $|2\rangle - |3\rangle$ pairwise components with similar attractive interactions. Higher doubly-occupied density is expected for attractive pairs because they do not require paying energy costs to occupy the same lattice site, and we confirm our hypothesis from the on-site pairing correlation that the attractive pairs are most likely to occupy the same site while the repulsive pair prevents each other for a whole observable density range up to unity filling (Fig. 7.8(c)). Beyond this filling, the on-site pairing correlation of a $|1\rangle - |2\rangle$ pairwise component is stronger and approaches a zero-crossing at a full density of $n \approx 1.4$. This can be viewed as the competition of repulsive interaction to attractive interactions becomes relevant for the filling greater than a density of one.

We check the validity of temperature measurement by applying the total density fluctuation-dissipation theorem [147, 165] given by

$$\kappa n^2 = \frac{1}{T} \sum_{\mathbf{a}} \Big(\langle n_{\mathbf{r}} n_{\mathbf{r}+\mathbf{a}} \rangle - \langle n_{\mathbf{r}} \rangle \langle n_{\mathbf{r}+\mathbf{a}} \rangle \Big). \tag{7.13}$$

Here, we expand the full density similar to the approach, discussed in Eq 7.9. The theorem can be written in terms of observable quantities, expressed as

$$\kappa n^2 = \frac{1}{T} \sum_{\mathbf{a}} \left[C_{\mathbf{a}}^{11} + C_{\mathbf{a}}^{22} + C_{\mathbf{a}}^{23} + 2(C_{\mathbf{a}}^{13} + C_{\mathbf{a}}^{12} + C_{\mathbf{a}}^{23}) \right], \tag{7.14}$$

where T is the temperature and can be obtained by applying a linear fit to κn^2 and $\sum_{\mathbf{a}}(\dots)$. As a result, we confirm the consistency between methods within the same order of magnitude for Fig. 7.8(b) and these methods agree within the error bars with the other datasets presented in Figs. 7.6 and 7.7. It is important to note that the fit of the high-temperature series expansion to this regime I of Fig. 7.1(b) shows a huge discrepancy in the on-site pairing correlations. This is attributed to the failure of the simple model where the tunneling strength is no longer negligible.

In particular, the delocalization of spins and many-body effects are relevant and go beyond the simple model.

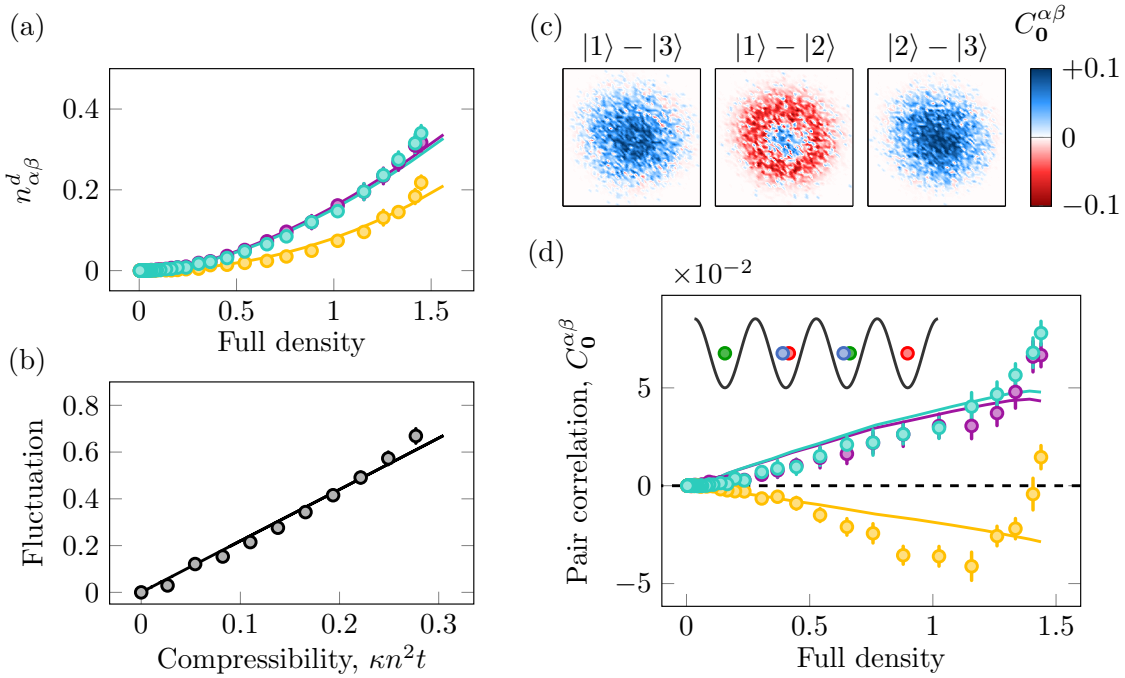

Figure 7.8: **Attractive pairing** (a) Doublon density of a Fermi lattice gas with interactions, $U_{13}/t = -2.4(1)$, $U_{12}/t = 1.8(1)$, and $U_{23}/t = -2.6(1)$. These interactions correspond to regime I of Fig. 7.1(b). (b) Total density fluctuation as a function of compressibility. The slope of the solid line represents the temperature of the system. Here, we obtain a temperature of $k_B T/t = 2.2(3)$. (c,d) Direct measurement of on-site pairing correlations. The corresponding chemical potentials are $\mu_{0,1} \approx -0.5$, $\mu_{0,2} \approx -0.9$, $\mu_{0,3} \approx -1.4$, and the temperature is $k_B T/t \approx 2.8$ using HTSE fit. (c) On-site pairing correlation maps with a field of view of 80×80 lattice sites. (d) The azimuthal averaging of on-site pairing correlations as a function of full density. Note that the HTSE fit has a large error and the reported fit and the corresponding results should be regarded as a guide to the eye. Error bars are the standard error of the mean over 40 datasets. The inset represents a simple configuration of three-component fermions occupying the lattice. (b)-(d) use the same datasets as (a).

In Fig. 7.9(a), we finally show the on-site pairing correlation at unity filling as a function of a magnetic field at a fixed lattice depth of $9.1(2)\,\mathrm{E_r^{Sq}}$. The correlation of the pairwise interaction, U_{23}, exhibits a crossover at a magnetic field of approximately 610 G, corresponding to $(U_{13}, U_{12}, U_{23})/t \simeq (13, 7, 2)$. This crossover represents the minimum interaction required to break down a correlated pair before reaching the Mott transition at unity filling.

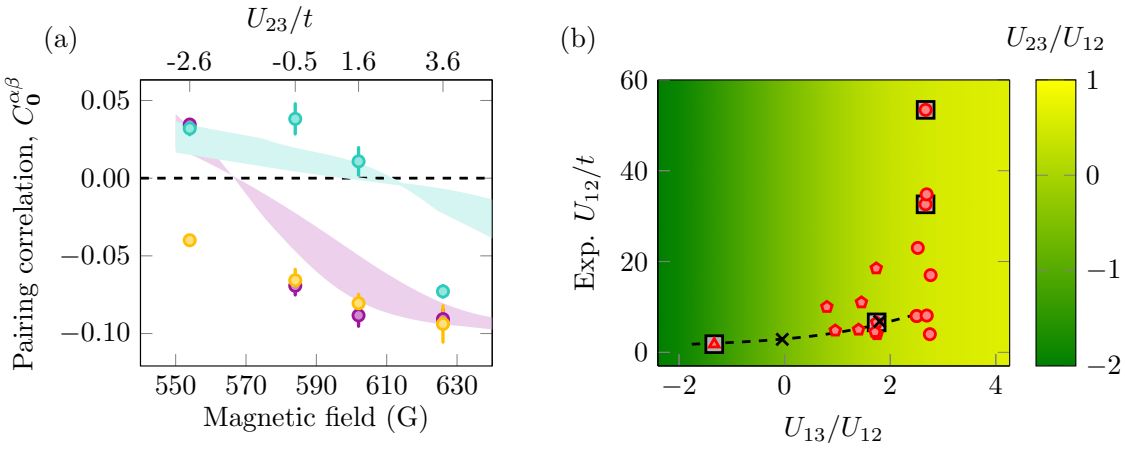

Figure 7.9: **Phase diagram of a three-component Fermi mixture.** (a) Magnetic field dependence of on-site pairing correlation at full density of $n = 1.0(1)$. The $|1\rangle - |3\rangle$ and $|2\rangle - |3\rangle$ pairing correlations show a crossover between pairing and anti-pairing over the accessible range. The shading areas illustrate calculations of on-site correlations using HTSE at unity filling with temperatures between $k_BT/t = 2$ and $k_BT/t = 5$, assuming the global chemical potentials for each spin are the same. (b) Projected 3d density plot of U_{13}/U_{12}, experimental U_{12}/t, and U_{23}/U_{12}. The ratio of interactions is calculated from the magnetic field between 550 G and 650 G. The y-axis is accessible interaction U_{12}/t from the experiment. Red symbols are all available data and black squares are data discussed in the text. The black dashed line represents the experimental trajectory in (a). Circles, pentagons, and triangles represent Mott insulating behavior, flavor-selective pairing, and attractive pairing, respectively. Criteria to characterize this behavior are discussed in the text. Black crosses mark zero-crossing points in (a)

In contrast, the pairing correlation of the $|1\rangle - |3\rangle$ pairwise component, C_0^{13}, shows a crossover at a magnetic field of approximately 568 G. This zero-crossing point corresponds to $(U_{13}, U_{12}, U_{23})/t \simeq (0, 2.8, -1.7)$ and represents the maximum interaction required to form a correlated pair of C_0^{13} before reaching to the attractive-pairing regime at unity filling. All available data are summarized in Fig. 7.9(b). We sort our data into three categories using on-site pairing correlations of the $|1\rangle - |3\rangle$ and $|2\rangle - |3\rangle$ pairwise components, C_0^{13} and C_0^{23}: Mott insulating (MI), flavor-selective pairing (FSP), and attractive-pairing (AP) states. The pairing correlation C_0^{23} tends towards stronger anti-pairing for densities up to unity filling in the MI state (Figs. 7.7(a,c)), whereas the FSP state tends towards correlated pairing at unity filling (Figs. 7.7(b,d)). The AP state represents the state in which the competition from a $|1\rangle - |3\rangle$ pair becomes relevant compared to a $|2\rangle - |3\rangle$ pair, and the pairing correlation C_0^{13} crosses over to correlated pairing (Fig. 7.8).

7.6 Conclusion and outlook

In conclusion, we demonstrate quantum gas microscopy of three-component Fermi lattice gases in the Hubbard regime. We observe three-component Mott insulators, flavor-selective localization, and selective pairing at temperatures down to the tunneling scale through the direct detections of spin densities and pairing correlations. Our measurements are compared with simulations using high-temperature series expansion at the atomic limit and agree well up to unity filling for stronger interactions. The discrepancy at higher filling may be resolved with simulations taking into account finite tunneling, such as DQMC and NLCE.

Limitations preventing us from achieving three-component Mott insulators at half-filling with temperatures lower than the tunneling scale are attributed to three-body losses at a measurement field of approximately 626 G. To avoid strong losses, increasing the confinement of the vertical 1d lattice, referred to as the accordion lattice in the text, is feasible while staying in the minimum three-body loss regime

at around 600 G for Hubbard physics. Overcoming these limitations may enable a further increase in phase-space density and the observation of a novel paired Mott phase at half-filling.

Our system opens up the ability to study three-component fermionic systems in various optical lattice geometries. In particular, the triangular and kagome lattices may show exotic phases such as chiral states that break time-reversal symmetry [166, 167]. In addition, a three-component system in ultracold atoms provides a pathway for studying color superfluidity and aspects of quantum chromodynamics [154].

Chapter 8

Conclusion and Outlook

In this dissertation, I have reported on the implementation of fermionic quantum gas microscopy in square and triangular lattice geometries. This setup enables us to explore strongly interacting fermionic systems. For the first time, we image fermionic lithium in a triangular lattice via a Raman sideband cooling technique with an imaging fidelity of 98%. The impressive setup of the triangular lattice is phase-stable and uses a recycled-beam approach. By propagating the lattice beam upward in three dimensions, we gain a larger lattice spacing which benefits our site-resolved imaging. In addition, our system has the tunability to switch between square and triangular lattices or superimpose between the lattices for future studies.

Our single-site imaging offers insights into unprecedented details of Hubbard physics in geometrically frustrated triangular optical lattices such as singles density and single-component density. With the measurement of singles occupation, we observe the suppression of singles density variance in the regime of strong interaction which indicates a Mott insulator state. By employing spin-removal and doublon hiding techniques, antiferromagnetic spin-spin correlations are realized up to nearest neighbors. The measurements reveal 120° correlations which are expected for the system. We demonstrate thermometry in the frustrated system through spin-spin correlations. Additionally, we inspire other researchers to overcome our limitations

in temperature by probing exotic states in frustrated systems.

The next generation of our quantum gas microscope allows us to perform spin-resolved imaging in a square lattice using two light sheets that simultaneously capture spins in the presence of a magnetic gradient. The spin-resolved imaging detects the full statistics of the Fermi-Hubbard model in the lowest band, in contrast to the first quantum gas microscope which can measure only the parity projected of the full density. We verify the accuracy of our spin-resolved imaging by measuring spin-spin correlations and observe correlations beyond nearest neighbors.

Three-component fermions have been first realized in our square-lattice quantum gas microscopy. The nature of Feshbach resonances breaks the interaction symmetry, resulting in a competition between pairwise components as can be observed through doubly-occupied site densities and pairing correlations. The correlations enable us to draw a simple picture of the configuration of three-component fermions in a square lattice at a temperature comparable with the tunneling energy, near half-filling density. We also demonstrate the validity of the density fluctuation-dissipation theorem in the three-component mixture, providing another way to extract the temperature of a three-component system.

In conclusion, these measurements have shown the capabilities of quantum gas microscopy to simulate condensed matter systems through ultracold-atom systems created in an optical lattice. Additionally, it has the potential to simulate nuclear physics phenomena, such as the formation of baryons and their superfluidity. In the future, we plan to apply our microscope to study challenging topics as discussed in the following.

Outlook

As can be seen in Chapter 5, our main limitation preventing us from observing frustrated systems in more detail is the temperature achieved in the experiment that has the same order of tunneling energy. We have strong evidence that the issue comes

from the lattice laser beams and it is challenging to suppress the noise at low intensity (less than 50 mW), however, this is the typical power used for shallow lattice (approximately $10\,E_r^{Sq}$). We plan to leverage the advantages of EOM to overcome the limitations of AOM at high frequencies by integrating them, thus achieving a higher bandwidth for intensity stabilization. In addition, the entropy redistribution technique can be applied, leading to a lower temperature in the Hubbard system [126]. The efforts to reduce noise are currently in progress.

Spin-resolved imaging of our triangular lattice is challenging because of the small optical lattice beam sizes. The separation of two light sheets requires approximately 20 µm and this distance is almost the half-width of the triangular beam, leading to dramatically reduced lattice depth, and it is difficult to efficiently perform Raman sideband cooling. Alternately, the triangular geometry can be generated by overlapping a 1d lattice on the square lattice, as successfully achieved in several experiments [71, 78, 168].

The Fermi-Hubbard model beyond short-range interactions can be accessible using the Rydberg dressing approach [169–171]. The study of nonlocal interactions in a 2d Fermi gas in an optical lattice poses a new possibility to introduce off-site interactions that make the model more realistic [172]. We plan to apply a similar approach to study nonlocal interactions in the triangular lattice.

The dynamical properties of the Hubbard model challenge numerical simulations [173] and the study of the Hubbard model under a periodic drive shows interesting features like correlations in fermionic many-body systems can be reduced, enhanced, or change their sign [174]. By utilizing the capabilities of digital mirror devices (DMD) and spatial light modulators (SLM), we anticipate delving into the realm of out-of-equilibrium Hubbard physics, opening new avenues for groundbreaking research.

Appendix A

Electronics

A.1 Acousto-optic modulator

An acoustic-optical modulator (AOM) is a device that uses an acoustic wave to tune the frequency of a laser beam by a few MHz. To control the AOM there are three main components to be considered, a piezo-electric transducer, a crystal, and an AOM driver. The transducer is attached to the crystal and the AOM driver provides a radio-frequency (RF) signal to the transducer. The RF creates longitudinal waves (sound waves) traveling through the crystal, which results in varying refractive indices of the crystal, therefore leading to the laser beam diffracted (Bragg diffraction). The diffraction of the laser beam can be analyzed by the Fresnel equations from a medium of refractive index, n, into a medium of refractive index, $n + \Delta n$, and derivation can be found in [175, 176].

When the laser beam propagates through the crystal, it interacts with phonons. The conservation of momentum indicates that

$$\hbar\mathbf{k}_f = \hbar\mathbf{k}_i \pm \hbar\mathbf{K}, \tag{A.1}$$

where $\mathbf{k}_f, \mathbf{k}_i$ are the wavevector of diffracted and incident beams, and $\hbar\mathbf{K}$ is the

phonon momentum. Also, the conservation of energy dictates

$$\hbar\omega_f = \hbar\omega_i \pm \hbar\omega_0, \tag{A.2}$$

where $\hbar\omega_i$ and $\hbar\omega_f$ are the incident and diffracted photon energies, and $\hbar\omega_0$ is the energy of the phonon.

The first-order intensity is given by

$$I_{\text{diffracted}} = I_{\text{incident}} \sin^2\left(\frac{\pi l}{\sqrt{2}\lambda}\sqrt{M I_{\text{acoustic}}}\right), \tag{A.3}$$

where l is the optical path in the acoustic beam, I_{acoustic} is the acoustic intensity in the diffraction medium, and M is the diffraction figure of merit defined by Eq. 12.3-20 in [176]. The condition for maximum intensity is given by the Bragg angle

$$\sin\theta_B = \frac{\lambda}{2\Lambda}, \tag{A.4}$$

where λ and Λ are the wavelengths of the laser beam and the sound wave in the diffraction medium.

AOM Controller

We built our AOM controller boxes by assembling the following parts:

1. Power supply (±15 V using HAD15-0.4-AG, 24 V using HN24-3.6-AG)
2. Voltage reference (LT1236)
3. Amplifier (Becker AMP590033H, Mini circuit ZHL-03-5WFX)
4. Local Oscillator (ZOS-75+, ZOS-100+, ZOS-150+, ZOS-300+)
5. Mixer (ZLW-1+, ZLW-3+)
6. RF Switch (ZASWA-2-50DRA+)

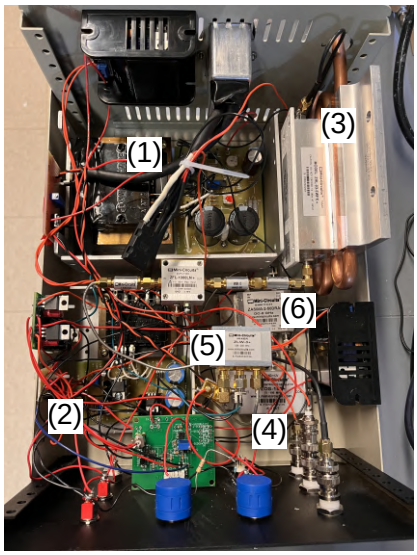

The power supply provides a DC voltage of 24 or ±15 V. The voltage is stepped down to ± 5 V and 12 V using circuit the circuit in Fig. A.1. To switch between

internal and external control, on-on switches are attached to the front panel. Two potentiometers are also attached for internal control of the local oscillator and RF amplitude. To provide a stable voltage for the potentiometers, we use a voltage reference (LT1236) that provides a constant voltage of 10 V to the first potentiometer while the second one provides a tunable voltage between 0 and 0.5 V. The first potentiometer is connected to a local oscillator and the second one is connected to a voltage follower before connecting to a mixer (ZLW-1+) at pin I. The RF signal generated by the local oscillator is attenuated before being connected to the mixer at pin L. The output signal from pin R is attenuated by a small DC from pin I. As a result, the mixer is used as an attenuator. Then the signal is connected to an RF switch (ZASWA-2-50DRA+). The switch can be controlled by an on-off mechanical switch or TTL. When the switch is on, it allows the signal to be amplified by a 2 W amplifier (AMP590033H) for low-power AOM or a 5 W amplifier (ZHL-03-5WFX) for high-power AOM. The typical output signal has a value of $32 - 36$ dBm. To prevent overheating in the high-power amplifier when the water-cooling is off, we apply a relay (IXYS CPC1718J) to control the DC power to the amplifier via an interlock.

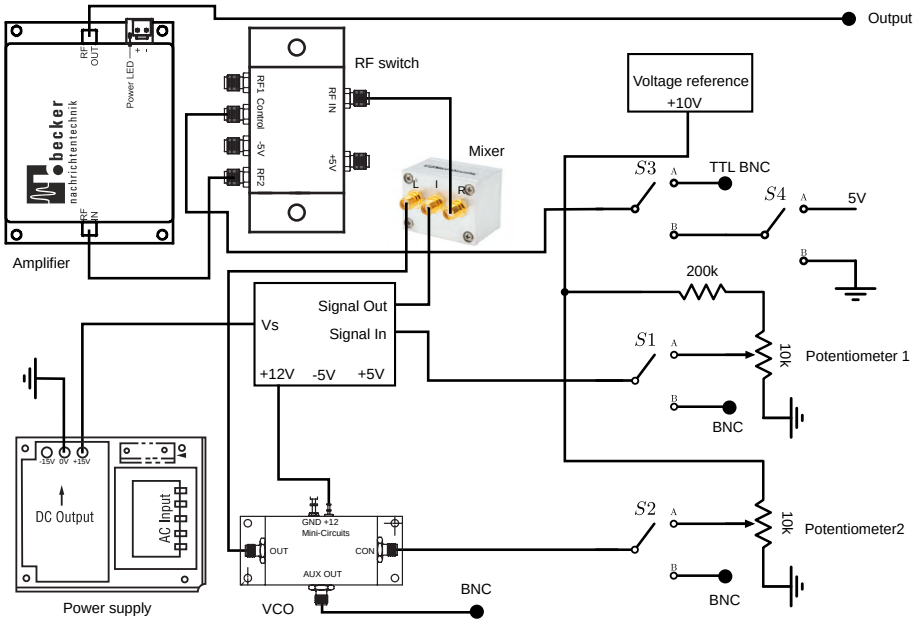

Figure A.1: **Low-power AOM driver setup.**

A.2 Electro-optic modulator

An electro-optic modulator (EOM) is an optical device that can modulate the phase, frequency, amplitude, and polarization of a beam relying on the Pockels effect [176]. The EOM consists of a non-linear crystal and an electrode attached to the crystal. The crystal changes its refractive index when an electric field from the local oscillator is applied. When a traveling beam, $A\exp(ikx - i\omega t)$, propagates through the crystal, the beam travels at the boundary from an index of refraction n to an index of refraction $n + \Delta n$ with different speeds, resulting in a phase change. Assuming the sinusoidal signal is applied, the phase of the traveling wave can be written as $\beta\sin(\Omega t)$. Here, the traveling wave in the medium is described by

$$\Psi(x,t) = Ae^{i(kx-\omega t-\beta\sin(\Omega t))}. \tag{A.5}$$

In practice, the amplitude of modulated phase β is much smaller and it can be expanded by Taylor's series and given by

$$\Psi(x,t) \simeq Ae^{i(kx-\omega t)}(1 - i\beta\sin(\Omega t)). \tag{A.6}$$

We simplify the expression in terms of exponential components

$$\begin{aligned}\Psi(x,t) &\simeq Ae^{-i\omega t}\left(1 - \frac{\beta}{2}\left(e^{i\Omega t} - e^{-i\Omega t}\right)\right)e^{ikx} \\ &= A\left(e^{-i\omega t} - \frac{\beta}{2}e^{i(-\omega+\Omega)t} + \frac{\beta}{2}e^{i(-\omega-\Omega)t}\right)e^{ikx}.\end{aligned} \tag{A.7}$$

Here, the first term is the incoming beam and the remaining terms are the sidebands with frequencies shifted by $\pm\Omega$. There is a series of sidebands when β is not small, and the expression leads to Bessel functions known as the Jacobi–Anger expansion,

$$\Psi(x,t) = Ae^{i(kx-\omega t)}\left(\sum_{k=0}^{\infty} J_k(\beta)e^{ik\Omega t} + \sum_{k=1}^{\infty}(-1)^k J_k(\beta)e^{-ik\Omega t}\right). \tag{A.8}$$

The fraction of optical power transferred into each of the first-order sidebands is determined by $[J_1(\beta)]^2$, and the fraction of optical power of the carrier is given by $[J_0(\beta)]^2$. To achieve the maximum amplitude of the first-order sideband, the Bessel

function argument β should be approximately 1.84 radians, resulting in a sideband amplitude of $[J_1(1.84)]^2 = 34\%$.

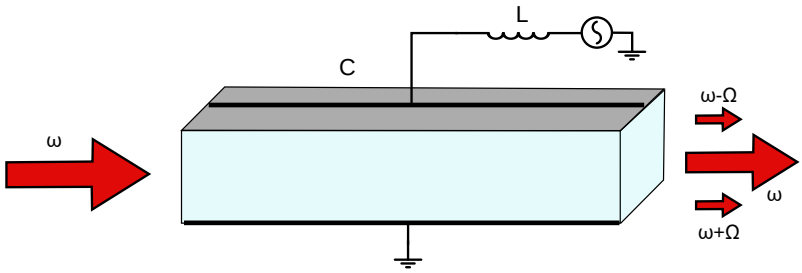

Figure A.2: **Schematic of EOM.** A phase modulation is imprinted on the traveling wave by an LC circuit. The EOM crystal is made of MgO: $LiTaO_3$ (5%) and sandwiched between Au and Cr electrodes coating on two z-planes. Both electrodes can be treated as a capacitor. The resonance frequency is determined by measuring the reflected power of a coupler (Mini-circuits ZFDC-10-2).

A.3 Intensity stabilization

In Fig. A.3, the laser intensity is controlled by a proportional–integral (PI) controller. Specifically, the reference voltage U is compared with the photodiode voltage Y and the controller uses the error signal, $U - Y$, to provide an output signal based on P and I gains to control the RF amplitude to the AOM via a mixer.

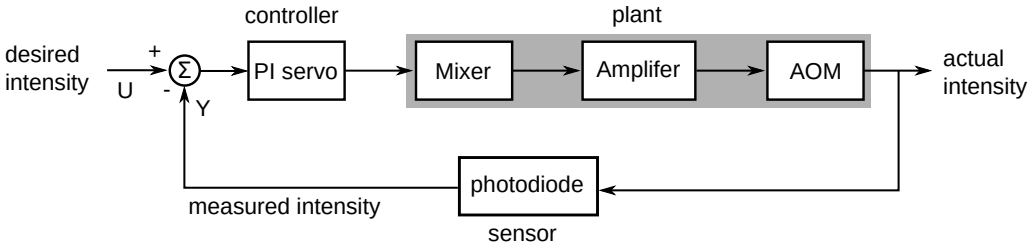

Figure A.3: **Feedback diagram of intensity stabilization.**

A.4 Two-step voltage controller oscillator

The frequency of the imaging laser is tuned by transmitting a reference signal from a Keysight 33600A to a phase lock circuit. However, we find that it requires at least 200 ms for the General Purpose Interface Bus (GPIB) command, and this time scale is crucial for experiments. It is important to note that the laser lock does not tolerate large frequency jumps of the reference. To reduce the transmission time and ensure a smooth frequency change, our voltage controller oscillator is implemented, referred to as VCO (Fig. A.4), which provides a frequency from 20 MHz to 80 MHz, thus allowing full control of the imaging frequency from low to high field. Note that a typical commercial VCO with bandwidth more than about twice the minimum to maximum frequency is essentially not available.

A.5 H-bridge driver

To enhance our ability to control the magnetic offset field, we integrate an H-bridge driver with the 4N-Channel MOSFET (APTM50HM65FT3G-ND). This setup enables us to globally reverse the direction of the offset field. Subsequently, we noticed that the magnetic field gradient of our MOT setup is counter to gravity, leading to inefficient evaporation. To address this, we implemented a home-built H-bridge by employing four high-current N-channel MOSFETs (IXFN420N10T) and its controller as shown in Figs. B.11 and A.5. This configuration, in conjunction with isolated power supplies for each MOSFET, allows us to flip the direction of the MOT field for higher-current operation. These isolated power supplies control the differential voltage between the gate and source channels in the case of an ungrounded source. To ensure safety while reversing the field direction during running current flow, we add a magnetic field sensor that converts the field strength that exceeds a set point to a logic value. By utilizing a D-latch, we can reverse the field using a TTL signal. It is important to note that the field direction cannot be reversed while the current is actively flowing. The system design can operate at a current of 200 A,

and potentially more depending on the MOSFETs employed.

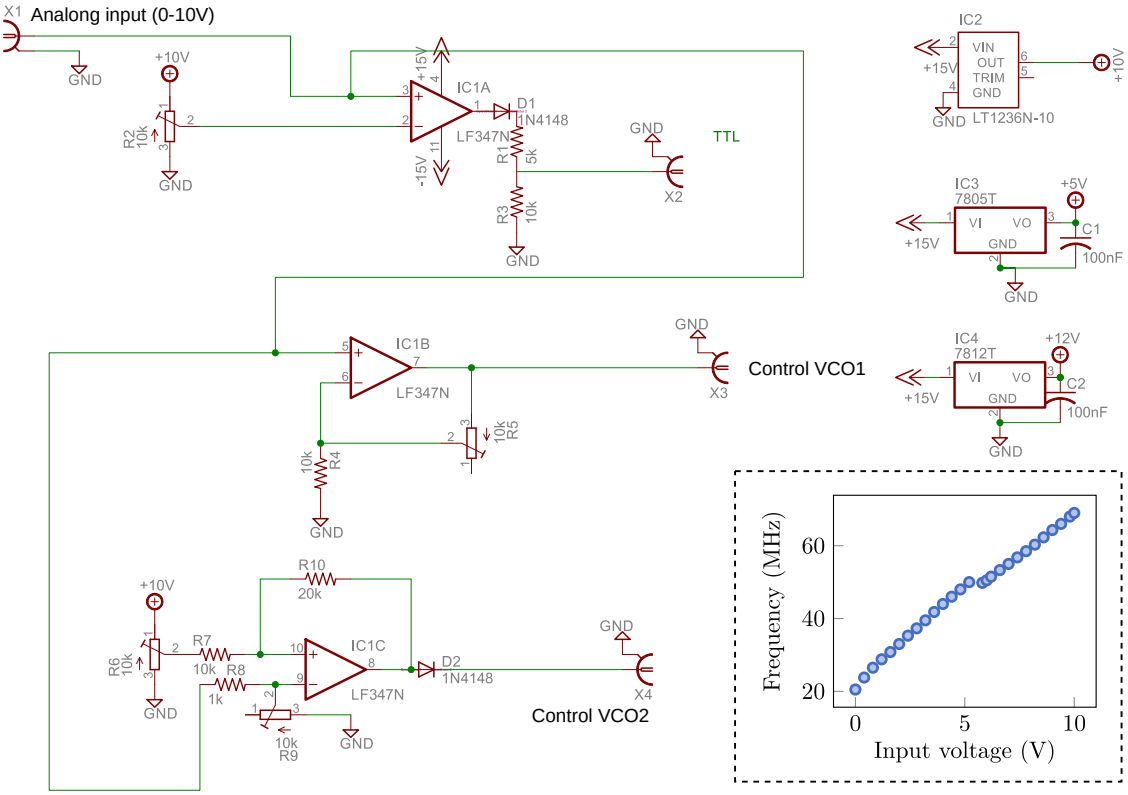

Figure A.4: **Two-step VCO.** This circuit enables the operation of two VCOs for an extended frequency range. The setup involves connecting two VCOs to an RF switch (ZASWA-2-50DRA+, not shown). IC1A acts as a comparator which provides a HIGH state of TTL to the RF switch when the analog input surpasses a specific threshold, denoted as A and determined by resistor R_2. Meanwhile, IC2A provides VCO1 with a voltage range of 0 to A, effectively covering a designated frequency range. On the other hand, IC3A imparts a voltage range spanning from B to C to the VCO2, encompassing yet another defined frequency range. The values of B and C can be linearly adjusted through resistors R_9 and R_6. Diode D_1 prevents a negative voltage to the TTL channel. The fine-tuning of trimmers facilitates a smooth transition between the two VCOs, ensuring a continuous frequency. The inset represents the output frequency of the VCOs as a function of an input voltage to the circuit. Here, we construct the device using ZOS-50+ and ZOS-75+.

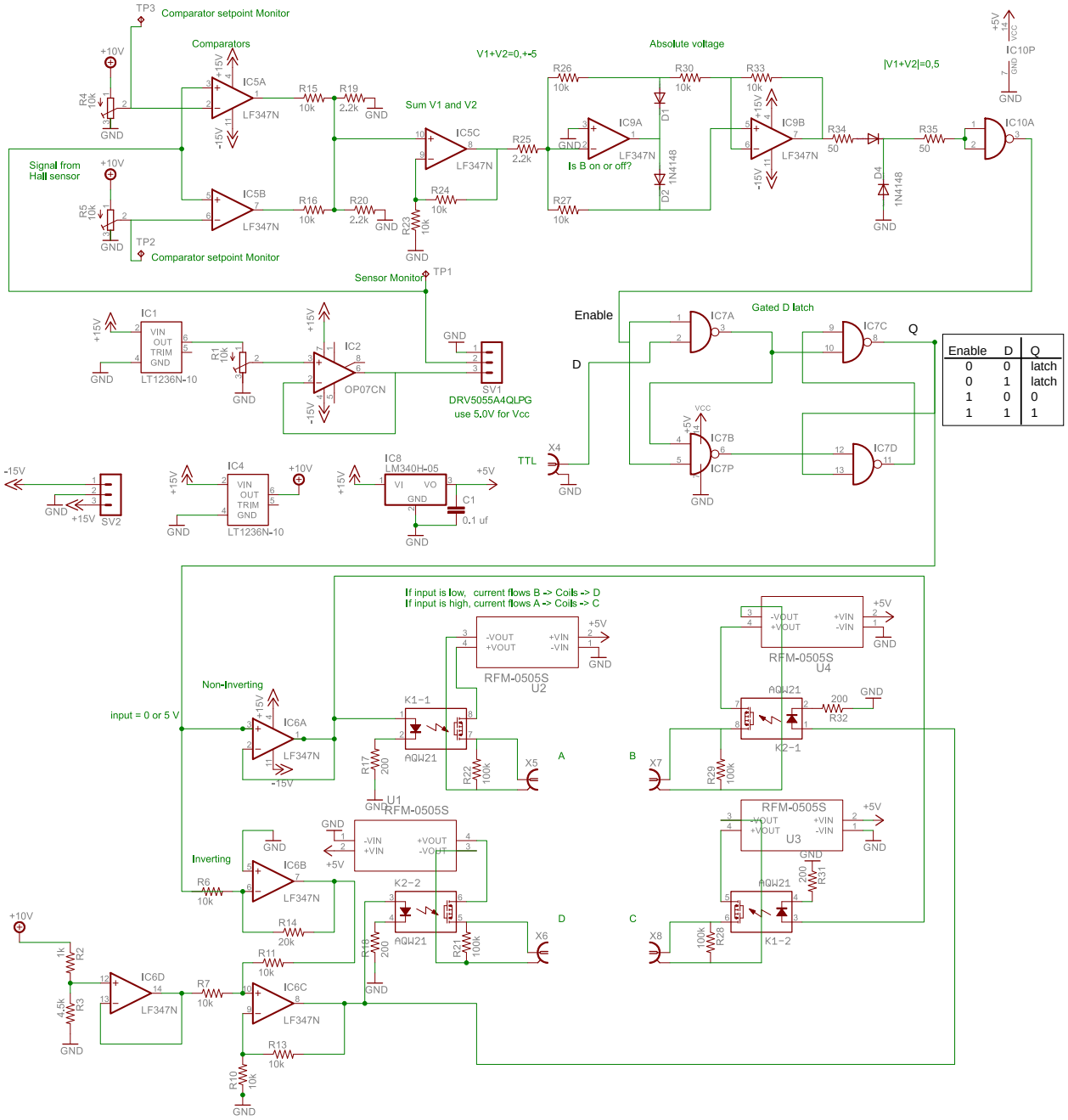

Figure A.5: **H-bridge driver.** This circuit facilitates the reversal of current direction through an H-bridge configuration when no current is actively flowing. The magnetic field surrounding a wire is detected by a hall sensor (DRV5055A4QLPG) and a series of op-amps are utilized to compare the field signal against set points that can be adjusted through resistors R_4 and R_5. This comparison process converts the magnetic field into a logical signal at IC10A. This signal is driven to a HIGH state when the magnetic field strength remains below the set point. Subsequently, a TTL signal is triggered to govern

the direction of the current. When a current is flowing, a D-latch prevents any attempt to reverse the current direction. Outputs A-D control the gates of the MOSFETs on the H-bridge. To ensure accurate referencing of TTL signals to the MOSFETs, every channel is driven independently and fully differential.

A.6 Rotational waveplate

The imaging of single atoms on a triangular lattice is still not completely understood. Asymmetric triangular lattices formed by linear polarizations show higher imaging fidelity, however, they cannot be used to study Hubbard physics in symmetric systems. To study physics on symmetric triangular lattices, we rely on imaging in an asymmetric triangular lattice. We adiabatically connect these lattices using a motorized rotatable waveplate (Thorlabs DDR25) shown in Fig. A.6. Later, we realized that sigma polarization can be used to study Hubbard physics in a symmetric triangular lattice and the site-resolved imaging can be obtained with the same configuration. Here, we use the rotational waveplate to adjust the symmetry of our triangular lattice instead.

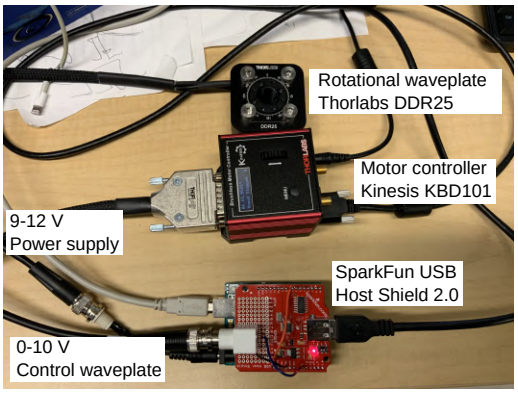

Figure A.6: **Rotational waveplate with Arduino.** We control the angle of a waveplate using 0-10 V which corresponds to a waveplate angle of 0-360°. The controlled voltage is connected to an Arduino, which communicates with a motor controller (Kinesis KBD101) via the USB Host Shield 2.0.

Appendix B

Existing Apparatus

B.1 Vacuum chamber setup

The components of our vacuum chamber include the oven tower, Zeeman slower, science chamber, and science tower, as illustrated in Fig. B.1. This design draws inspiration from the work of the Waseem group at Princeton University [177] and the Jochim group at the University of Heidelberg [178]. The oven is filled with 95% isotope of ^{6}Li provided by Sigma-Aldrich (340421-10G) demonstrated in Fig. B.2(a), and a thermal band wrapped around it can heat the oven to 350°C, resulting in the generation of lithium vapor. The oven tower serves as a connection between the lithium oven and the Zeeman slower. This tower is equipped with four Kodial glass viewports (Kurt J. Lesker VPZL-450Q), and its lower section links to an ion pump (VacIon Starcell Plus 75) controlled by an IPC Mini Pump Controller (75-55-40SC). A turbo pump (HiPace 80) can be attached through an all-metal angle valve (VAT 54132-GE02-0001) positioned near the top. To mount the titanium sublimation cartridge (Agilent Technologies 716-0050), a reducing flange (Kurt Lesker RF600X275) is employed, transitioning from CF100 to CF40. Additionally, a movable vacuum feedthrough which can be controlled by a servo motor as an atomic beam shutter, prevents the ^{6}Li coating at the gate valve. A metal gate valve (VAT 48124-CE01-

0001) is connected between the oven tower and the Zeeman slower tube to separate the lithium oven from the science chamber, while another metal gate valve (VAT 48132-CE01-0002) separates space between the science chamber and the in-vacuum mirror of the Zeeman slower. The science chamber is the spherical octagon from Kimball Physics (MCF600-SphOct-F2C8) consisting of eight viewports for optical access. These viewports are from Kurt J. Lesker VPZL-275Q. To facilitate optical access along the Zeeman slower coils, a T-flange housing a mounted gold mirror is implemented, similar to [179].

Vacuum parts cleaning

Cleaning vacuum parts for Ultra High Vacuum (UHV) applications is essential to maintain the purity and integrity of the vacuum environment. Contaminants can adversely affect experimental outcomes and equipment performance. To clean these parts, we follow these steps: Vacuum parts are initially sonicated in an acetone solution that is a strong solvent for removing a wide range of organic contaminations including grease, oils, and some adhesive residues using Sonicator (Quantrex 650). We then sonicate them in isopropyl alcohol to remove polar contaminants and inorganic residues. Custom-made vacuum parts require an additional step at the beginning. They are sonicated in Alconox mixed with tap water to remove contaminants. Vacuum viewports and windows are not sonicated to prevent damage to their coating. After cleaning, all parts are placed on UHV-grade aluminum foil to air dry and are subsequently wrapped in foil until assembly.

Assembly and baking

We achieved reliable seals for all flange connections by employing copper gaskets in combination with silver-plated hex bolts and nuts. To ensure a leak-tight seal, we follow a precise tightening procedure. Using a torque wrench set to the recommended torque pressure, we systematically tighten the bolts in a star pattern. This method ensures that our seals are secure and free from leaks.

(a) Rendered image

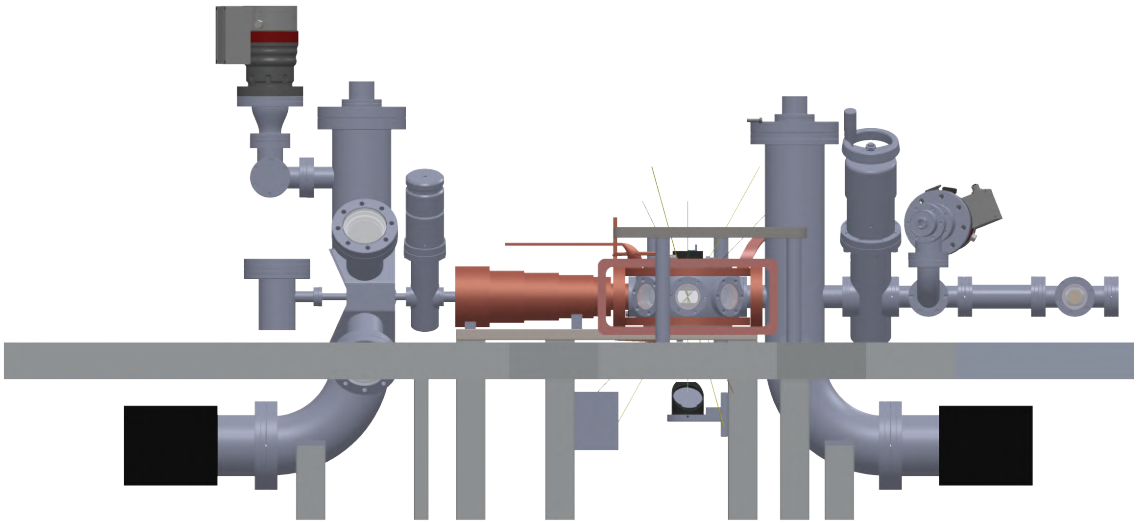

(b) Raw image

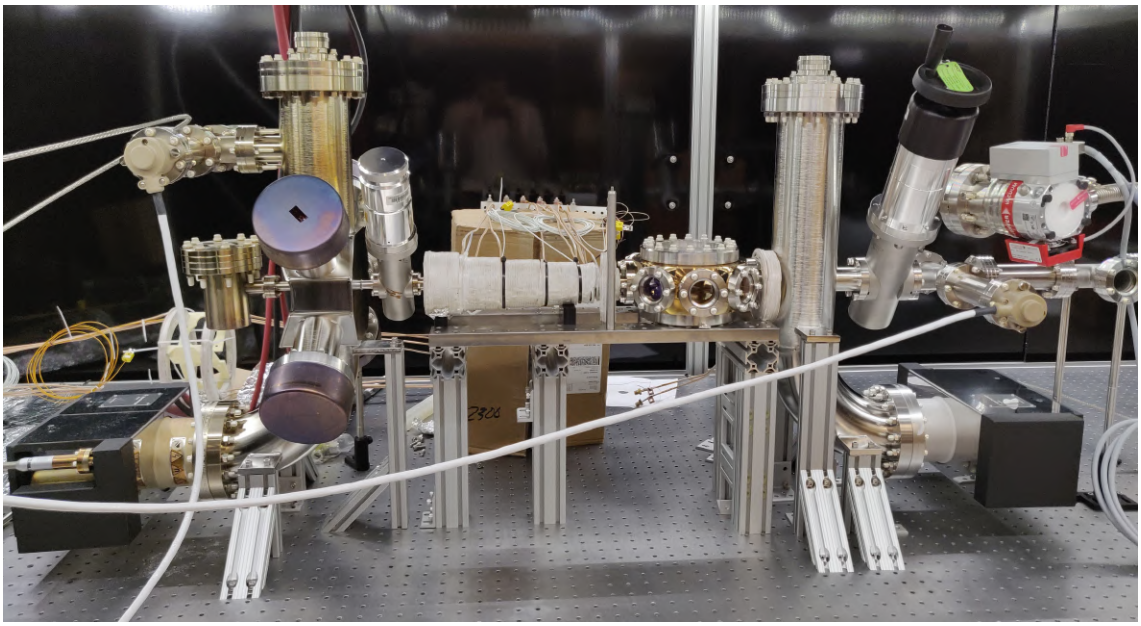

Figure B.1: **Vacuum chamber.** From left to right: ion pump, lithium oven, 6-way tower, Zeeman slower, science chamber, 4-way chamber, and turbo pump.

To evacuate our vacuum system, we connect a turbo pump to an angle valve, and the outlet port of the turbo pump is linked to a rough pump (Agilent Technologies IDP-7). The angle valve remains closed at this point. We begin the process by running only the rough pump until it reaches the ultimate pressure of 4×10^{-2} mbar. After

reaching this pressure, we switch on the turbo pump. The angle valve is opened only when the turbo pump runs at its maximum speed of 9×10^4 rpm. To ensure there are no leaks in the system, we employ a SmartTest Helium leak detector (HLT 550). Helium is sprayed around suspicious areas like flange connections, and leaks are detected by observing spikes in helium pressure. In the case of a leak, we seal it by applying a leak sealant (CELVA-2) to the specific location of the leak. The evacuation process continues until the pressure reaches the ultimate pressure of 10^{-7} mbar. Once this pressure is achieved, we proceed to the next step.

(a) (b)

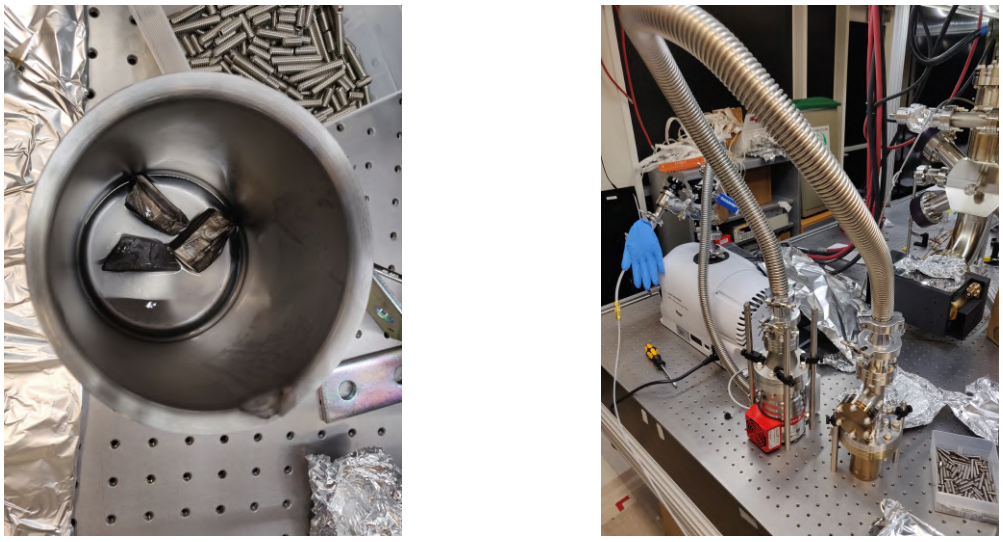

Figure B.2: **Lithium.** (a) 95% isotope of ^{6}Li chunk. (b) Image after baking ^{6}Li chunk in the oven section. To eliminate the mineral oil layer on the surface, a Pentane rinse is performed, followed by baking to remove any oxidized layers. Note that Acetone cannot be used due to its potential to oxidize ^{6}Li. To minimize oxidation when in contact with air, we flush argon during the process.

To bake the vacuum system, we initiate the process by wrapping the components with an initial layer of aluminum foil. Over this layer, we apply heating tape without overlapping to ensure the tape's integrity is maintained and to facilitate even heat distribution during baking. For delicate components like windows and viewports, we take extra precautions by covering them with metal caps to shield them from

direct contact with the heating tape. To monitor the temperature accurately, we attach thermocouples at various critical locations within the system (Table. B.1). An additional layer of aluminum foil is then wrapped over the heating tape, providing an effective heat barrier (Fig. B.3). In the case of the ion pump, we remove the magnets before applying the foil and heating tape to prevent any potential magnet degradation from the elevated temperatures. We gradually increase the temperature, maintaining a controlled rate of approximately 1°C per minute until we reach the designated target temperature shown in Table. B.1. The baking process continues over a week, allowing the pressure inside the system to stabilize and reach a steady state at a fixed temperature. We note that the lithium chunks are baked in the oven section separated from the main chamber shown in Fig. B.2(b).

(a) (b)

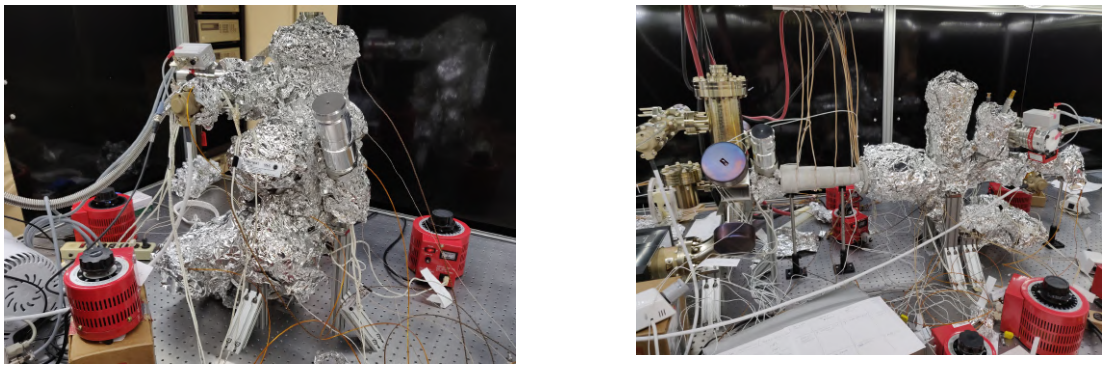

Figure B.3: **Baking of the vacuum system.** (a) Oven tower. (b) Main science chamber and science tower.

Next, we proceed by removing the heating tape from the ion pump section and restoring the magnets to their original configuration. The ion pump is activated once the pressure reaches 10^{-7} mbar. We activate the titanium-sublimation filaments multiple times with a short duration i.e., 2 minutes at 40 A until the pressure stabilizes. This process facilitates the sublimation of titanium, resulting in a thin and clean titanium film coating the inner surface of the vacuum system. This freshly deposited titanium is highly reactive. When residual gases within the chamber come into contact with the chamber walls, a chemical reaction occurs. The reaction leads

to the formation of stable compounds that adhere to the walls. This effectively reduces the gas pressure within the chamber.

Vacuum part	Max temperature (°C)	Target temperature (°C)
Zeeman slower	250	100
Angle valves	200	180
Gate valves	300	180
Tower	450	350
TSP	250	200
Top and bottom windows	200	180
Side windows	200	180
Ion gauges	450	350
Ion pumps	400	350

Table B.1: **Baking temperatures.**

B.2 Control system

The experiment is precisely controlled by the ADwin-Pro II system, which has a 64-bit floating-point unit (FPU) for math co-processing. This ensures robust computing capabilities as well as an Ethernet interface that facilitates efficient data transmission. Key features of the ADwin-Pro II system include:

1. ADwin-Pro II AOut-8/16 (×4): These modules offer 8 channels each, boasting 16-bit resolution and a voltage range of ±10 V (Table. B.2).

2. PRO-II-DIO-32-TICO (×2): With 32 TTL channels per module, these units provide built-in edge detection or edge output at a frequency of up to 100 MHz (Table: B.3).

3. PRO-CPU-T12-ENET (×1): This module integrates an Ethernet interface that supports high-speed data transmission at 1 Gbit/s. This enables seamless communication between the ADwin-Pro II system and the experiment computer.

Analog outputs can be directly connected to electronic devices. However, certain devices, such as intensity stabilization and power supply in the current control mode, require more attention due to ground loops. To address this, we connect them to an isolated amplifier before connecting to the devices. Labels of analog outputs are listed in Table B.2. All digital outputs are connected to optocouplers, which protect the computer from voltage spikes, possibly created at the experiment, before connecting to target devices. Lists of TTL are shown in Table B.3.

Channel	Used for
DAC00	Square lattice intensity
DAC01	-
DAC02	Triangular lattice waveplate
DAC03	MOT repump Intensity
DAC04	MOT cooling intensity
DAC05	Zeeman beam intensity
DAC06	CMOT detuning
DAC07	-
DAC08	Feshbach current
DAC09	ODT high intensity
DAC10	ODT low intensity
DAC11	-
DAC12	Light sheet intensity
DAC13	Triangular lattice intensity
DAC14	Light sheet AOM frequency
DAC15	Bottom beam intensity

Channel	Used for
DAC16	Raman cooling intensity
DAC17	Raman repump intensity
DAC18	Raman repump AOM freq.
DAC19	Raman cooling AOM freq.
DAC20	Green AOM frequency
DAC21	Green intensity
DAC22	Light sheet galvanometer
DAC23	DMD intensity
DAC24	RF frequency sweep
DAC25	Green PZT
DAC26	2^{nd} Light sheet galvanometer
DAC27	MOT current
DAC28	-
DAC29	-
DAC30	X-offset current
DAC31	Imaging frequency

Table B.2: **Analog outputs channels of ADWIN system.**

Channel	Used for
A0	MOT repump shutter
A1	MOT cooling shutter
A2	Imaging shutter
A3	Repump AOM
A4	Cooling AOM
A5	Zeeman AOM
A6	Andor Camera trigger
A7	High field TTL
B0	Square lattice override
B1	Final Zeeman field
B2	MOT field
B3	Feshbach field
B4	-
B5	Basler camera trigger
B6	IPG AOM
B7	Reverse X-offset field
C0	Reverse Y-offset field
C1	Reverse Z-offset field
C2	Offset field switch
C3	ODT servo override
C4	ODT integrator short
C5	Atomic beam shutter
C6	Oscillascope trigger
C7	RF switch
D0	RF generator trigger
D1	MOT top mirror shutter
D2	Light sheet AOM
D3	Light sheet integrator short
D4	Triangular AOM
D5	-
D6	Triangular integrator short
D7	Bottom beam integrator short

Channel	Used for
E0	Bottom beam AOM
E1	Raman cooling AOM
E2	Raman repump AOM
E3	Raman repump shutter
E4	Raman cooling shutter
E5	Vertical imaging shutter
E6	Horizontal imaging shutter
E7	-
F0	Square lattice pinning
F1	-
F2	Square lattice AOM
F3	Green shutter
F4	Green AOM
F5	Green integrator short
F6	Triangular lattice pinning
F7	Light sheet pinning
G0	Bottom beam shutter
G1	Dipole trap shutter
G2	Light sheet shutter
G3	MOT current flip
G4	Sq. lattice shutter
G5	$\|1\rangle - \|2\rangle$ antenna switch
G6	Square integrator short
G7	Triangular lattice AOM
H0	2^{nd} Light sheet switch
H1	Current flip for Feshbach coils
H2	Current flip for X-offset coils
H3	DMD AOM
H4	DMD shutter
H5	Zeeman first coil field
H6	2^{nd} Light sheet shutter
H7	-

Table B.3: **Digital outputs channels of ADWIN system.**

We control the ADwin Pro II using software implemented in C, developed by Stefan Kuhr and later further improved by Peter Schauss, as shown in Fig. B.4.

(a) Sequence control interface

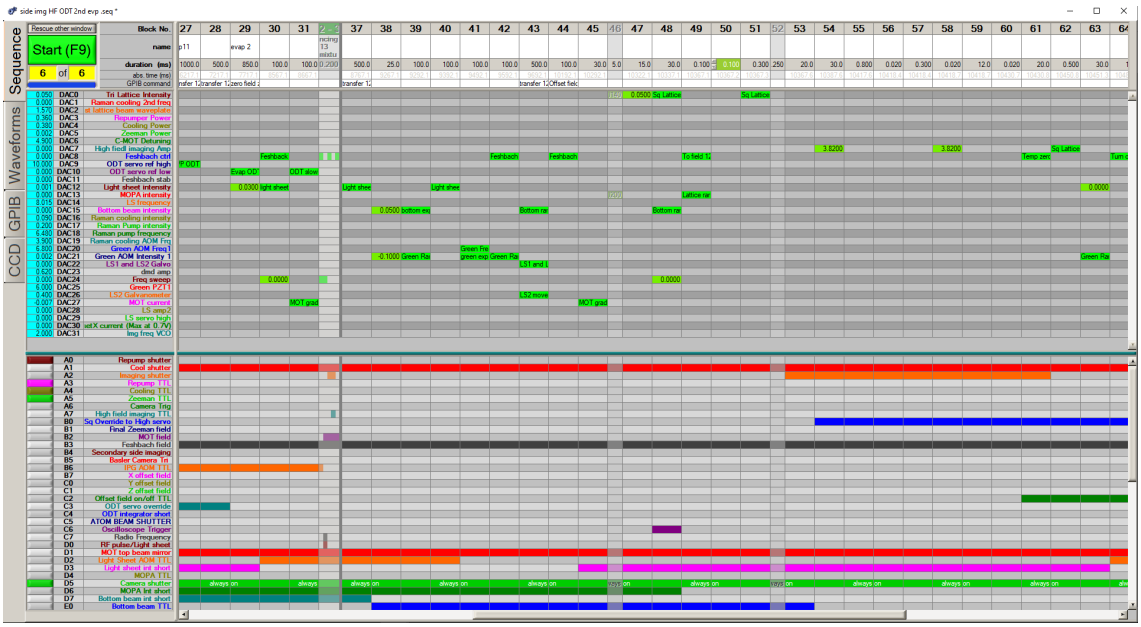

(b) Setting interface

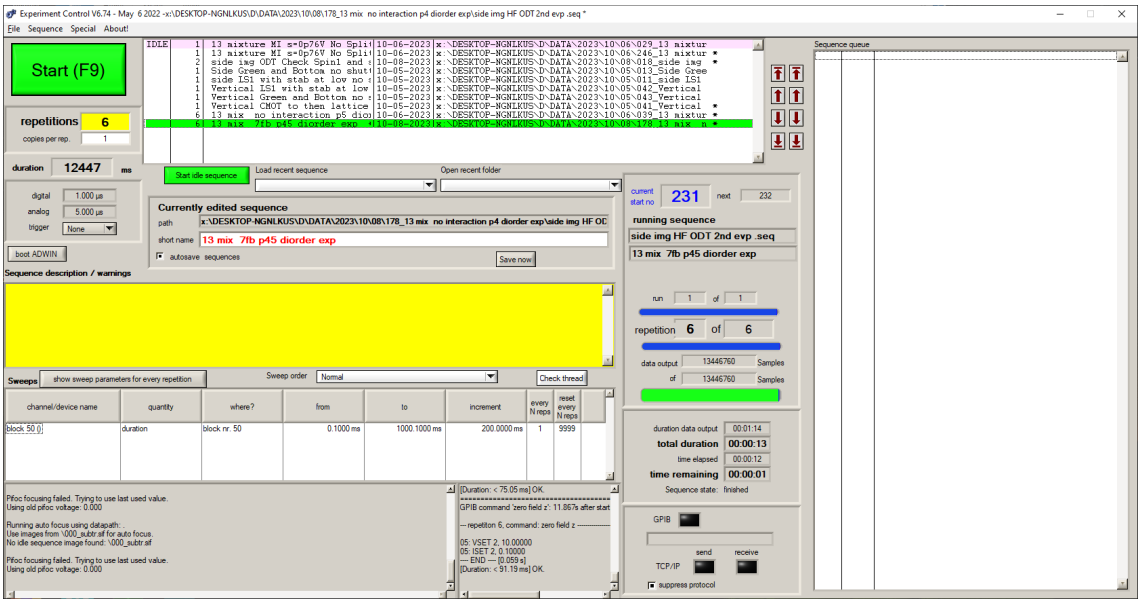

Figure B.4: **Experiment software.**

B.3 Sequences

Loading from MOT into ODT

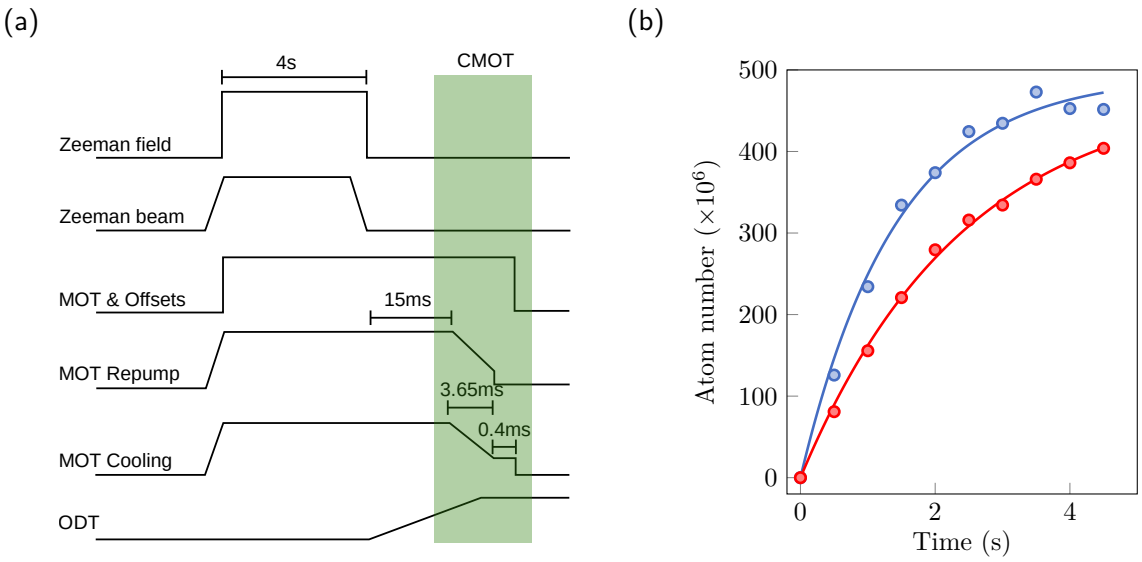

Figure B.5: **MOT to ODT sequence.** (a) Atoms are captured by the magneto-optical trap (MOT) within $4\,\mathrm{s}$. Subsequently, atoms are loaded into the optical dipole trap (ODT) using a compression technique shaded in green. Here, we gradually increase the power of the ODT beam while simultaneously reducing both the cooling and repump powers of the MOT. Additionally, during this process, the laser frequency is red-detuned from $30\,\mathrm{MHz}$ to $5\,\mathrm{MHz}$ with respect to the atomic transition. (b) MOT loading rate. Without magnetic extension (red) and after optimized placement of the extension (blue). Data are fit to $N_0(1-\exp(-t/\tau))$, where N_0 is the maximum atom number in the MOT and τ is the time constant. The loading rate is the slope of the exponential function at $t = 0$. The plot was taken from previous work [90].

Degenerate Fermi gases

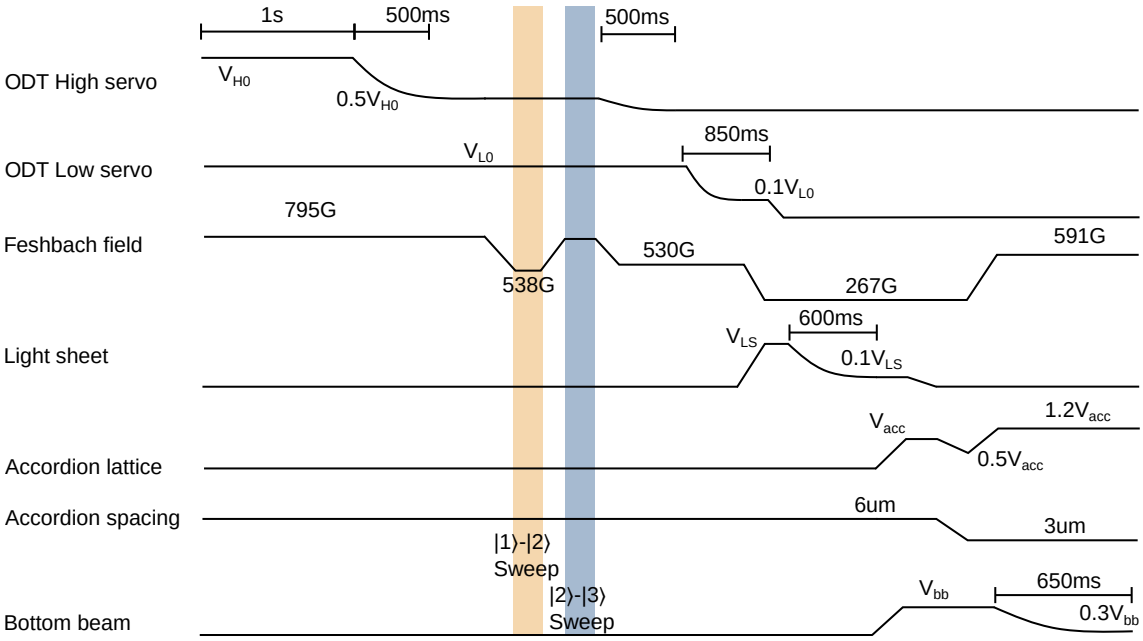

Figure B.6: **Sequence to prepare Fermi gases.** Atoms are evaporated in the ODT using three steps described in the main text. In the middle of the process, we apply a few consecutive RF sweep pulses with pulse duration of $10\,\mathrm{ms}$ between $|1\rangle$ and $|2\rangle$ states centered at $75.607\,\mathrm{MHz}$ and spanning $500\,\mathrm{kHz}$, leading to a balanced spin mixture as shaded in orange. We prepare a $|1\rangle - |3\rangle$ mixture by applying $|2\rangle - |3\rangle$ pulse centered at $81.930\,\mathrm{MHz}$ and spanning $500\,\mathrm{kHz}$ for $50\,\mathrm{ms}$ (blue shaded). Next, we adiabatically load atoms into the light sheet and perform evaporation at attractive interactions before loading them into the accordion lattice at the largest spacing. To reach degenerate 2d Fermi gases, we perform the last evaporation in the accordion lattice in combination with the bottom beam. Here, we use laser beam powers as follows: $V_{\mathrm{H0}} = 100\,\mathrm{W}$, $V_{\mathrm{L0}} = 10\,\mathrm{W}$, $V_{\mathrm{LS}} = 2\,\mathrm{W}$, $V_{\mathrm{acc}} = 1\,\mathrm{W}$, and $V_{\mathrm{bb}} = 1\,\mathrm{W}$.

Spin-resolved imaging

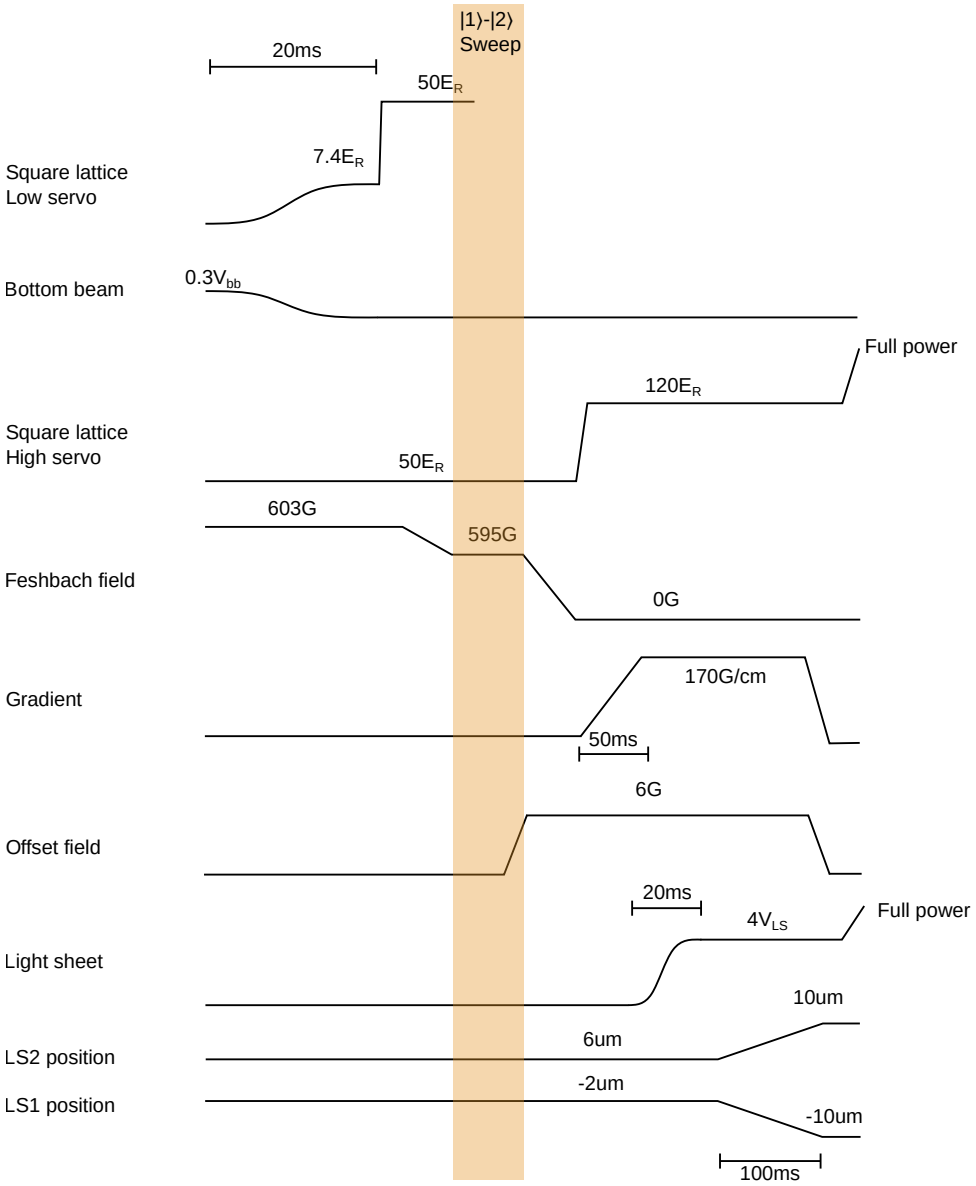

Figure B.7: **Spin-resolved imaging sequence.** Assuming the atoms are prepared in the final evaporation, we adiabatically ramp up the lattice to a target depth while simultaneously reducing the power of the bottom beam. Next, we freeze the motion of atoms by rapidly ramping up the lattice to $50\,\mathrm{E_r^{Sq}}$ in $500\,\mu\mathrm{s}$. We prepare a $|2\rangle - |3\rangle$ mixture by employing a $|1\rangle - |2\rangle$ transfer followed by turning off the magnetic field. To perform spin-resolved imaging, we increase the lattice depth to $120\,\mathrm{E_r^{Sq}}$ and increase the magnetic field gradient to $170\,\mathrm{G/cm}$. After that, two light sheets simultaneously capture both spin states and we perform fluorescence imaging.

B.4 Water-cooling system

Magnetic fields are important for controlling atoms. These fields are generated by running current through coils with a maximum current of 200 A. However, it is important to note that there is heating involved due to resistance. The issue becomes more pronounced during long-term experiments. To prevent significant heating, we use a water-cooling system consisting of an Optitemp M171 heat exchanger and an EF Cooling WKW175HE for low and high-pressure operations, as shown in Fig. B.8. Both heat exchangers are connected to the house water supply. An inline water filter (NSF LAKOS) is directly connected to the house water supply to directly remove sediment. For operational safety, motorized valves are integrated to shut off the water flow in case of leakage detected by the interlock system. The presence of the flow switches enables the monitoring of water flow through the system. To prevent potential clogs within the coils, a reusable 60 µm filter (Swagelok SS-8TF-60) is installed between the chilled water supply and the coils supply in the high-pressure path. The normal operation of temperature and pressure for the water-cooling system is shown in Table. B.4. We monitor the ambient temperature at important locations in the laboratory (Fig. B.9).

Location	Pressure (PSI)	Temperature (°C)
House supply	72	15
House return	20	18
Chilled water	400	20
Coils supply	250	-
Coils return	~ 0	20

Table B.4: **Temperature and pressure for the water-cooling system.** Flow rate is 3 gallons per minute (GPM) for the high-pressure cooling circuit.

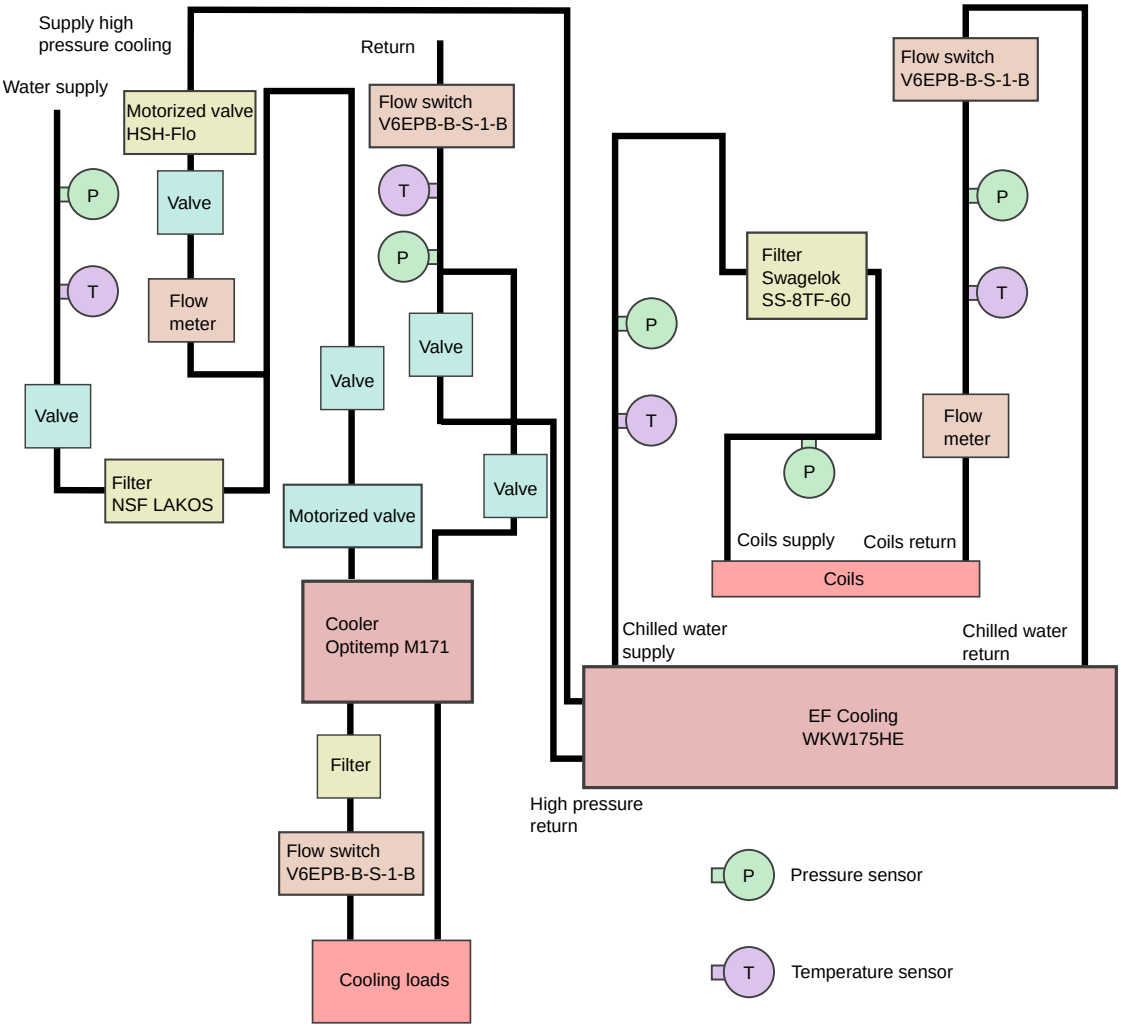

Figure B.8: **Water-cooling system.** Cooling loads for the low-pressure pump (Optitemp M171) consist of coil switches, IPG 1070 nm laser, beam dump, 100 W RF amplifier, offset field switch, H-bridge for the MOT, spatial light modulator, and the Verdi V10. The high-pressure pump (EF Cooling WKW175HE) is primarily used to dissipate heat from the coils. Heat exchanger Neslab RTE-111 or RTE-7 is used to cool the MOPA laser (not shown).

To mitigate potential risks stemming from water leaks, burns, and incorrect operations, an interlock system is implemented. In Fig. B.10, the main interlock controls the power of AOM drivers and DC power supplies. During standard operation, the relay state remains CLOSED (shorted). For enhanced safety, a water interlock is

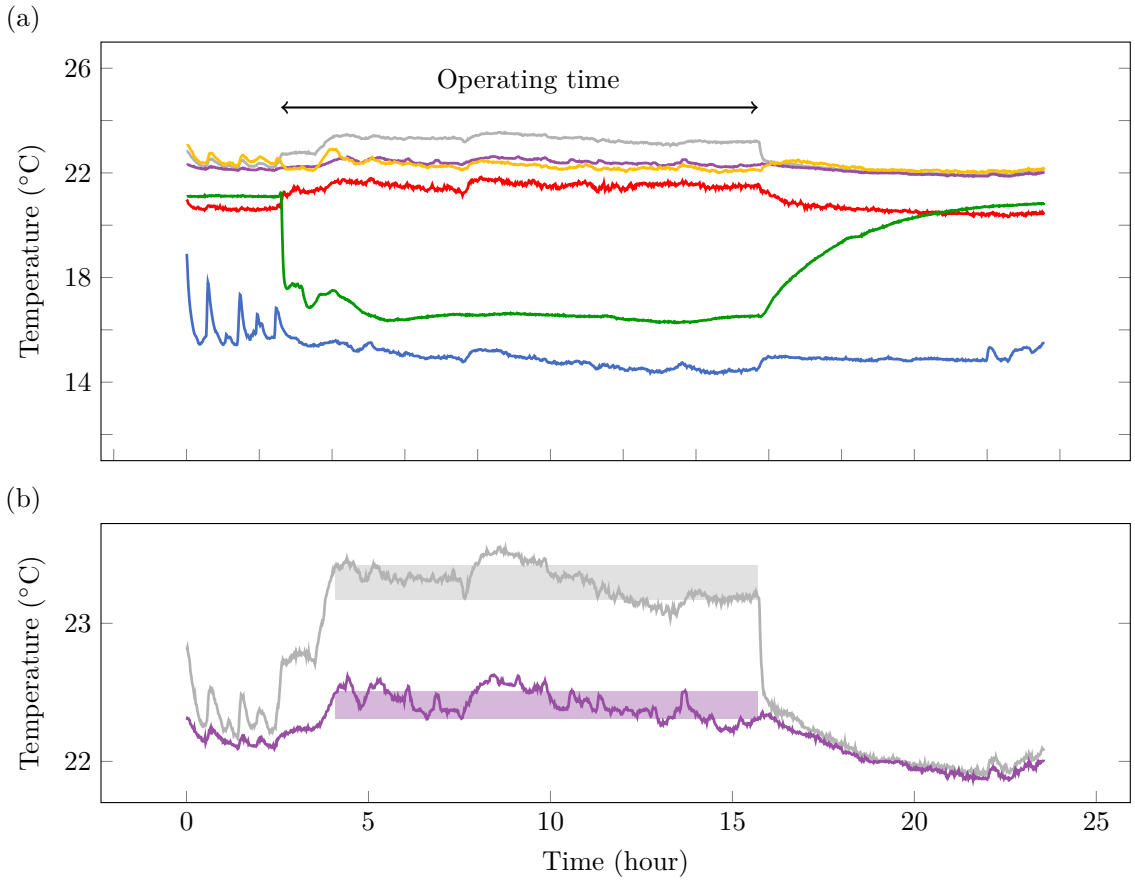

Figure B.9: **Ambient temperature for experiments.** (a) Measurements of all sensors in the laboratory: air outlet (blue), air return (red), house water supply (green), experimental table (gray), laser table (violet), and high-pressure water return (orange). (b) Zoom in on the essential parts of (a). Gray (23.3 ± 0.1°C) and violet (22.4 ± 0.1°C) shading represent temperature variation during stable operating times.

incorporated to monitor potential leaks through water sensors. In the event of a water leak, the interlock state is changed to "OPEN" which subsequently triggers the closure of motorized valves and signals the main interlock. To address situations where the high-pressure pump malfunctions, a temperature interlock is in place to monitor coil temperatures using a standard digital temperature switch (Dwyer Instruments 40T-10) connected to thermocouples on each coil. The normal operation of temperature on experimental parts is illustrated in Table. B.5.

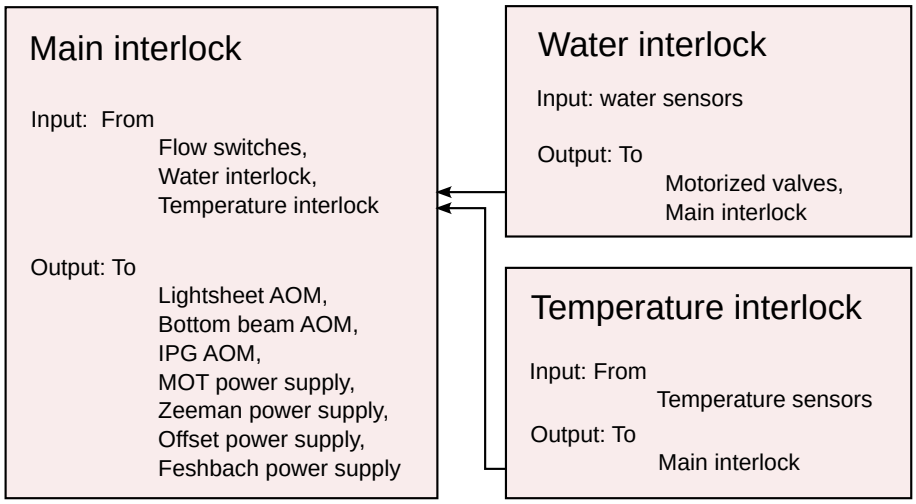

Figure B.10: **Interlock system.** The primary interlock operates as a safety switch for both AOM drivers and power supplies. This setup allows for the experiment to be paused in case of malfunction, reducing the potential for catastrophic consequences. The water interlock employs sensors to identify water leaks and subsequently manages motorized valves. Coil temperatures are continually monitored using sensors connected to the temperature interlock. To ensure safe operations in temperature, an acceptable operational range is established, with adjustments facilitated by a standard digital temperature switch.

Sensor	Temp. (°C)
Oven bottom side	311
Oven tube side	317
MOT top coil	$23.9 - 25.7$
Zeeman slower	23.2
Feshbach top coil	21.3
Feshbach bottom coil	22.5

Sensor	Temp. (°C)
MOT bottom coil	$21.9 - 24.6$
Y Offset	21.8
X Offset	20.1
MOT MOSFET	23.6
Feshbach MOSFET	23.4
Feshbach cooling plate	21.1

Table B.5: **Typical operating temperatures of experimental components.**

B.5 Power supplies

Various power supplies are used in the experiment, as detailed in Table B.6. The MOT power supply (ASTEX ECR) is consistently set at a fixed current of 150 A. The Zeeman slower operates with two distinct power supplies, with the final Zeeman segment adjacent to the science chamber necessitating higher operational current. For the offset field, current adjustments are made through GPIB. The offset along the x-direction can be adjusted up to 50 A, particularly when introducing a gradient via an H-bridge. To maintain low-current noise during atom interaction control, we employ a controllable voltage through an analog channel via the Delta Elektronika SM18-220.

	Power supply	Current (A)	Voltage (V)
MOT	ASTEX ECR	150	14.3
Zeeman 1st part	HP 6012B	40	9.7
Zeeman final part	Lambda EMS	55	2.1
Offset X	HP 6032A	$0-50$	
Offset Y and Z	HP 6621A	$0-10$	
Feshbach	Delta Elecktronika SM18-220	$0-220$	12

Table B.6: **Power supplies for coils.**

In Fig. B.11, the MOT coils are arranged in an anti-Helmholtz configuration, and the field direction can be reversed using an H-bridge. Unlike the Feshbach coils, which typically operate in a Helmholtz configuration to maintain a uniform field around the center. By reversing the polarity of the lower Feshbach coils, an anti-Helmholtz configuration can be achieved, resulting in an increased gradient suitable for the Stern-Gerlach separation.

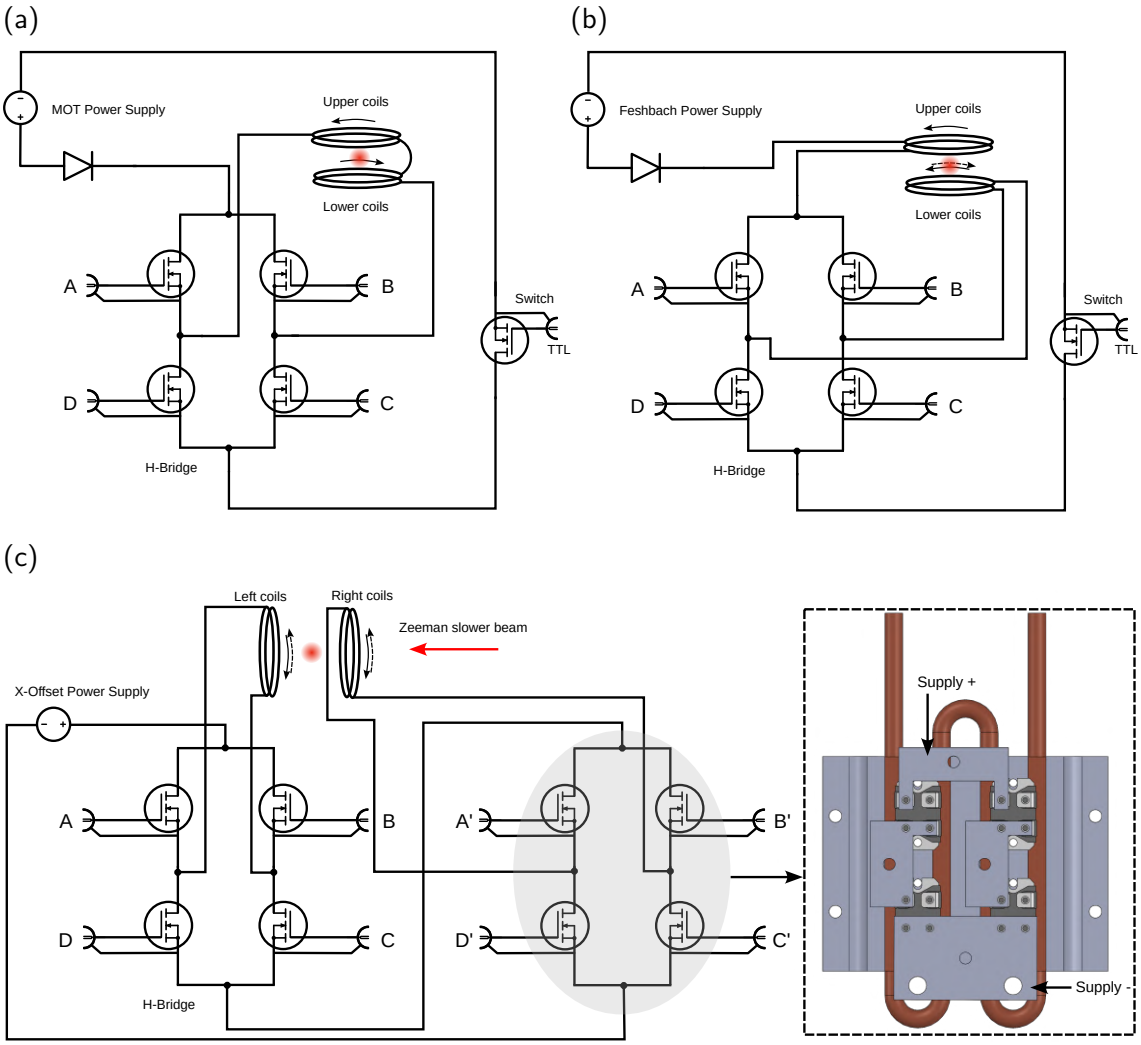

Figure B.11: **Connections of coils.** (a) MOT, (b) Feshbach, and (c) X-Offset coils. Here, N-channel MOSFETs (IXFN420N10T) are used as switches, and through the arrangement of four MOSFETs. This results in an H-bridge configuration, thus granting us the ability to reverse the polarity. The inset shows a rendered image of the H-bridge mounted on a cooling plate.

B.6 Magnetic coils

In this section, I describe the design of magnetic coils for various purposes and our coils winding process. As depicted in Fig. B.12, we used the lath to wind the coils

and we applied high-temperature epoxy over each coil layer and allowed it to dry for a day before repeating the process. This was repeated until we completed the final layer.

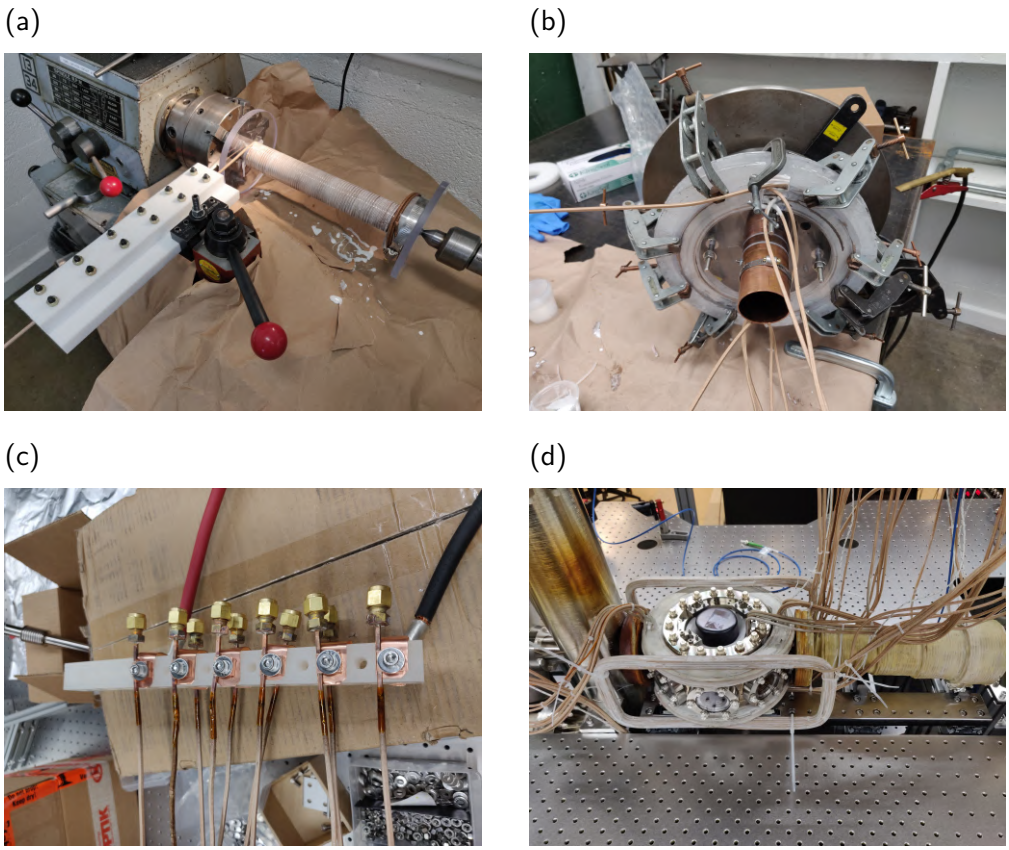

Figure B.12: **Coils winding.** (a) Zeeman slower coils were wounded using a lathe. A white wire guide is designed to prevent twisting of the hollow core during the winding process. (b) MOT coils winding. (c) Connections for electric wires and water-cooled pipes. Copper lugs are silver-soldered to the surface of the square cross-section coil while the brass Swagelok pieces connect the water pipe to the hollow core of the coils. Thin copper pieces are utilized to establish connections between coils. (d) Image capturing the impressive final assembly of all the coils.

Zeeman slower coils

Zeeman slower plays a crucial role in experiments involving cold atoms as described in Section 3.2 [180]. They provide a spatially varying magnetic field that benefits Doppler cooling, enhancing the loading efficiency and maximizing the achievable atom number within a MOT. The design of Zeeman slowers can be separated into two categories: those using wound coils and those utilizing permanent magnets.

In our experiment, we initially adopted the approach of using wound coils to construct the Zeeman slower. Subsequently, we optimized the loading rate by incorporating permanent magnets into the section adjacent to the ^{6}Li oven [90]. Employing wound coils requires considerable effort in terms of construction and the implementation of a water-cooling system. The field strength can be adjusted through current, nevertheless, it is constrained by heat dissipation limitations. It is important to note that the latter approach allows the magnetic field to be electronically switched, and no background fields are generated at the position of the MOT. We confirmed by simulating the magnetic field using the Radia package [89].

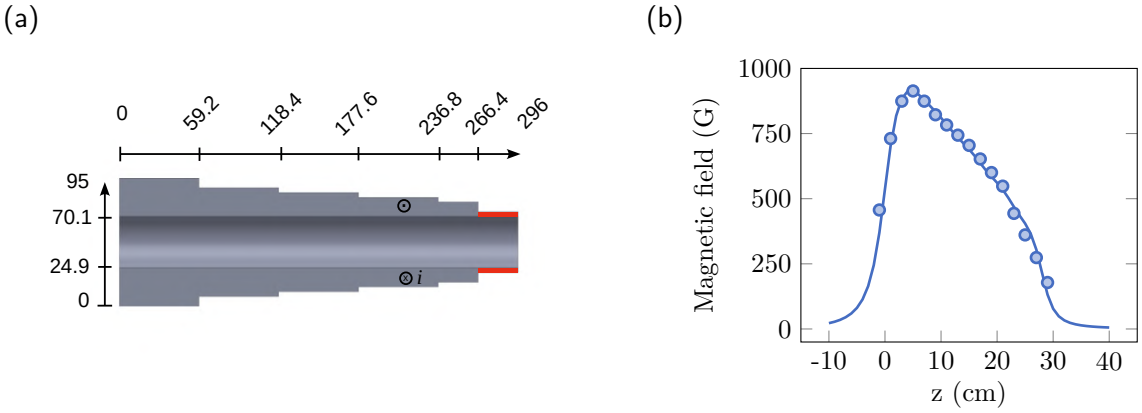

Figure B.13: **Zeeman slower coils.** (a) Cross-section of the Zeeman slower. The scale is measured in millimeters. The final Zeeman coils, highlighted in red, require higher current through other power supplies (refer to Table. B.6). The design was inspired by the Jochim group [178]. (b) Axial magnetic field as a function of position. Measurements are represented by dots, and the solid line is the result of a simulation.

MOT coils

The quadrupole field is essential for the magneto-optical trap (MOT) and is created using three pairs of coils organized in an anti-Helmholtz configuration depicted in Figs. B.14(a,b). The MOT coils generate magnetic field gradients of 20 G/cm along the x- and y-axes and 40 G/cm along the z-axis at the origin when a current of 140 A is applied (Fig. B.14(c)).

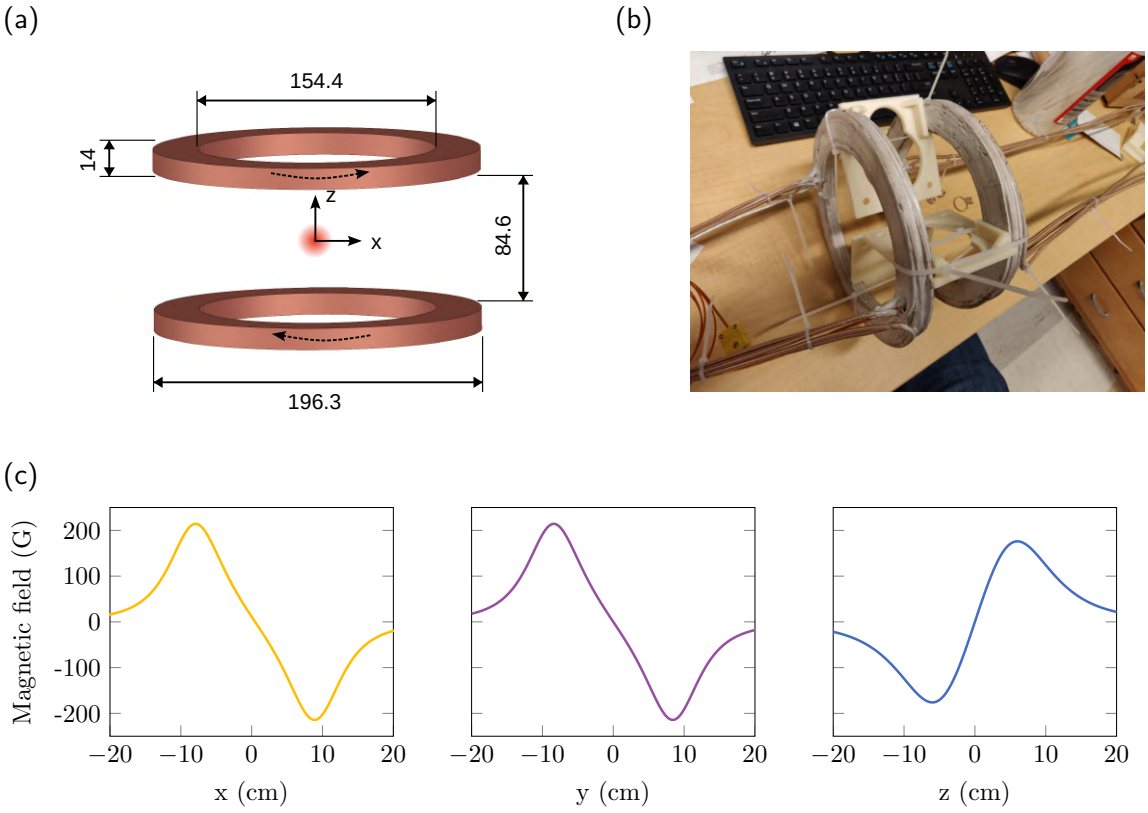

Figure B.14: **MOT coils.** (a) Schematic of the MOT coils. The inner and outer diameters are 154.4 mm and 196.3 mm. Dashed arrows represent the current flow direction. (b) Raw image of the assembled MOT coils. (c) The magnetic field along x- (left), y- (center), and z- (right) directions as a function of position at a current of 140 A. The magnetic field gradient is determined by the slope of the field at the origin.

Feshbach coils

Feshbach resonances enable the adjustment of atomic interactions through an external magnetic field. To create a uniform field at the atom position, a Helmholtz configuration is employed, where the upper and lower coils are separated by 54 mm. The inner diameter is 54.2 mm, while the outer diameter is 89.2 mm, resulting in a uniform field over a few millimeters (Fig. B.15). By positioning the Feshbach coils in proximity to the reentrant vacuum viewports, we can achieve a magnetic field strength of approximately 900 G for a current of 200 A.

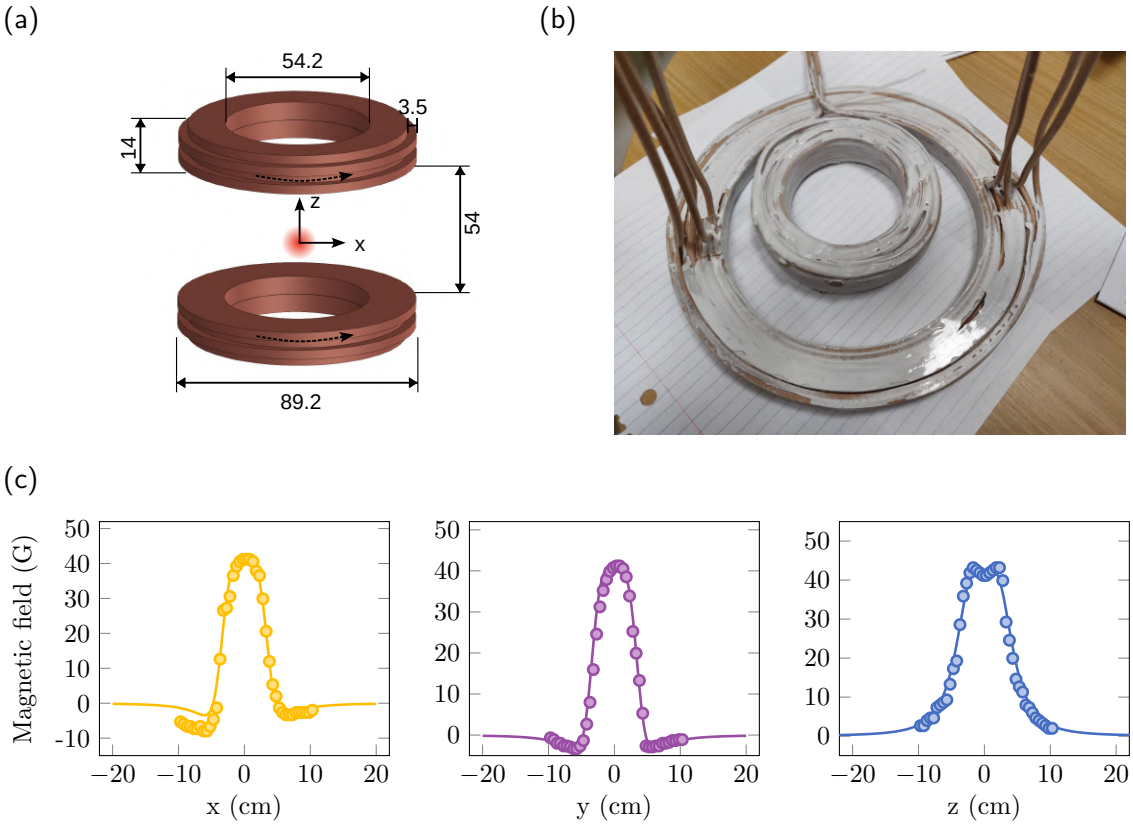

Figure B.15: **Feshbach coils.** (a) Schematic of the Feshbach coils. Dashed arrows represent the current flow direction. The scale is measured in millimeters. (b) Raw image of the Feshbach coils (small) and the MOT coils (large). (c) The magnetic field along the z-axis is a function of position. Here, a current of 10 A is applied for the measurements (dots). The solid lines are calculated by a simulation.

Offset coils

To extend the loading capacity from the MOT to the optical dipole trap, we apply offset fields during the compressed MOT. The fields are generated by a set of three pairs of Helmholtz coils (Fig. B.16). These magnetic fields provide an additional background field to control and manipulate the MOT position within a specific range (Fig. B.17), which is more limited than the scope designed for Feshbach coils.

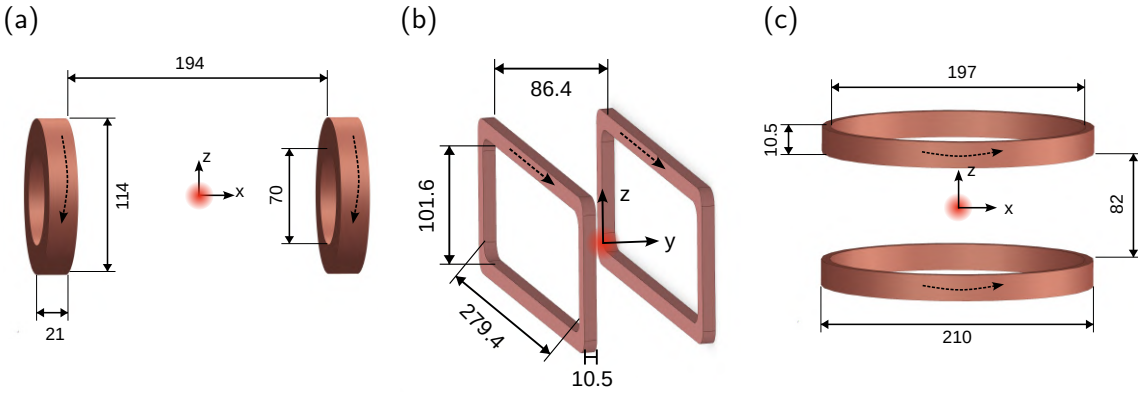

Figure B.16: **Magnetic offset coils.** Schematic of the (a) X-offset, (b) Y-offset, and (c) Z-offset coils. Dashed arrows represent the current flow direction. The scale is measured in millimeters. Note that the Z-offset coils were wound within the MOT coils to save space.

B.7 Cameras

Cameras offer several benefits to the observation, measurement, and analysis of ultracold-atomic systems. Table. B.7 summarizes a list of cameras used in the experiment for different purposes. For example, we use Andor Zyla 4.2 plus along with a magnification system of approximately 30× to collect fluorescence for site-resolved imaging.

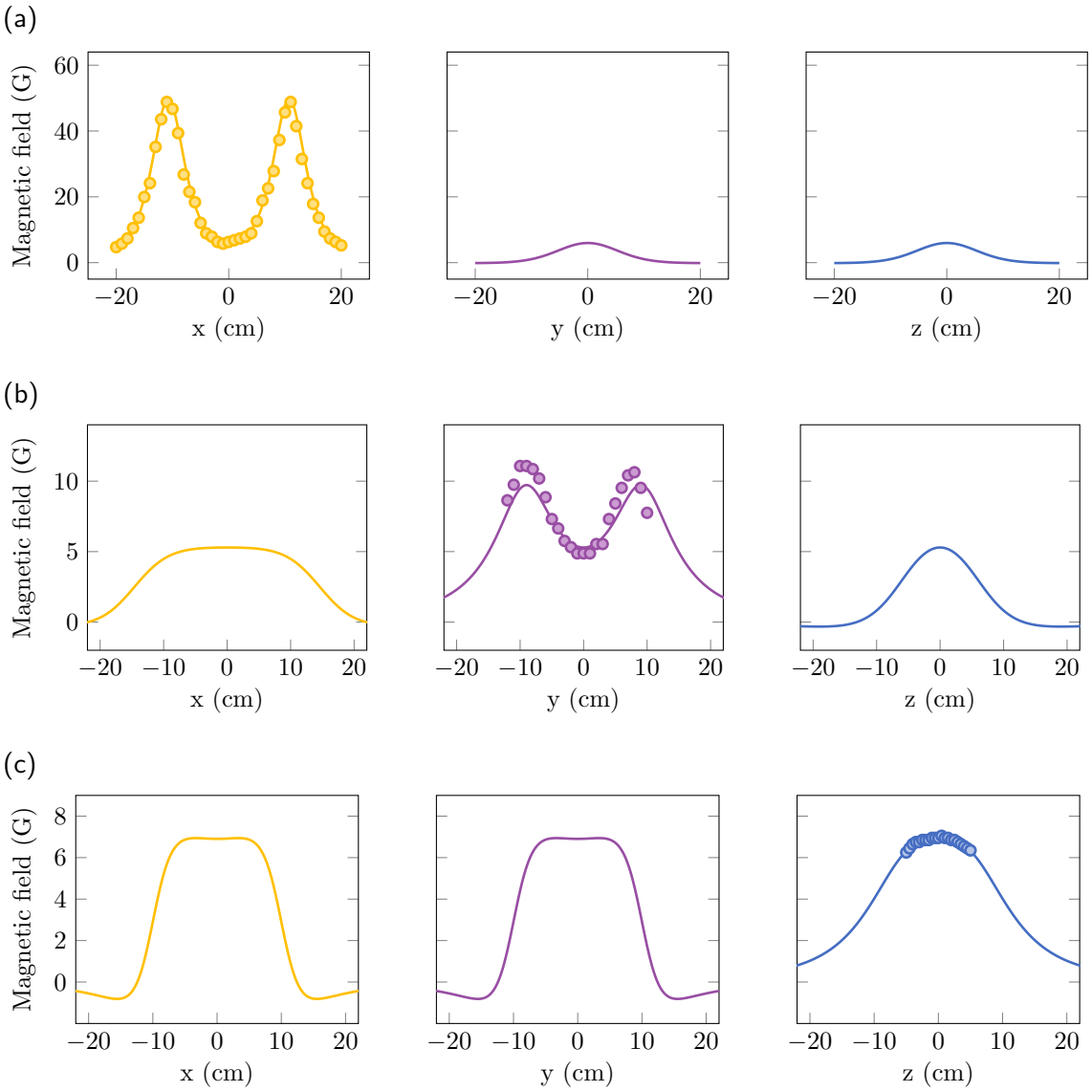

Figure B.17: **Magnetic field of offset coils.** Magnetic field profiles in the (a) X-offset, (b) Y-offset, and (c) Z-offset coils. The left, middle, and right panels show the magnetic field along the x-, y-, and z-directions, when a current of 10 A is applied.

Camera	Used for	Magnification
Andor Zyla 4.2 plus	Vertical absorption and fluorescence	30×
Basler a2A3840-45ucBAS	Horizontal absorption	1× or 5×
Basler acA720-520um	Absorption along accordion lattice	5×
Newport LBP2-HR-VIS2	-	-

Table B.7: **Cameras used in experiment.**

Appendix C

Cold Atoms

C.1 Dipole traps formed by Gaussian beams

A Gaussian beam has an electric field amplitude satisfied with the paraxial Helmholtz equation. Let us assume the polarization is along the x-direction and the propagation in the z-direction. The electric field is expressed as

$$\mathbf{E}(r,z) = E_0\hat{x}\frac{w_0}{w(z)}\exp\left(\frac{-r^2}{w(z)^2}\right)\exp\left[-i\left(kz + k\frac{r^2}{2R(z)} - \psi(z)\right)\right]. \tag{C.1}$$

The power carried by the field per unit area is referred to as the intensity of the beam, given by

$$\begin{aligned} I(r,z) &= \frac{1}{2}\left|\mathrm{Re}\left(\mathbf{E}\times\mathbf{H}^*\right)\right| \\ &= I_0\left(\frac{w_0}{w(z)}\right)^2\exp\left(\frac{-2r^2}{w^2(z)}\right), \end{aligned} \tag{C.2}$$

where I_0 is the maximum intensity related to the total power P_0 by $I_0 = 2P_0/\pi w_0^2$. According to the optical dipole trap potential formed by a Gaussian beam, the shape of the potential is a Gaussian function with a full width at half maximum (FWHM) equal to $\sqrt{2\ln 2}\, w_0$ at focus.

To evaluate the Gaussian beam trap frequency, assume that we are interested in the beam focus, where $w(z) = w_0$. However, for any propagation distance z, the beam waist $w(z)$ is position-dependent and is determined by $w_0\sqrt{1+(z/z_R)^2}$, where

$z_R = \pi w_0^2 n/\lambda$ is known as the Rayleigh range. The Gaussian potential is expanded in a series about $r = 0$ up to the second order at $z = 0$, and expressed as

$$I(r,0) = \frac{2P_0}{\pi w_0^2} + \frac{4P_0}{\pi w_0^4} r^2 + \mathcal{O}(r^3). \tag{C.3}$$

By equating the second-order coefficient to the harmonic oscillator i.e., $4P_0/\pi w_0^4 \simeq (1/2)m(2\pi f_\perp)^2$, the transverse trap frequency is given by

$$f_\perp = \frac{1}{\pi w_0^2}\sqrt{\frac{-2P_0\eta_{\text{dip}}}{m\pi}}, \tag{C.4}$$

where η_{dip} is the conversion coefficient or a constant that relates intensity to potential, which depends on the atomic properties. It can be obtained by taking a prefactor of Eq. 3.13.

C.2 Fluorescence imaging

Fluorescence imaging is the simplest technique used to extract information from an atomic cloud. On-resonant light is sent to the atomic cloud and the atoms emit scattered light, which is captured by a system of lenses and passes to the low-noise scientific CMOS camera (Andor Zyla 4.2 plus). The camera opens its shutter and we collect light for a certain exposure time. When using this technique, systematic errors have to be taken into account, such as CMOS sensitivity, quantum efficiency, and losses.

By estimating the number of emitted photons, we can determine the atom number in the cloud. Here, we assume that atoms scatter light in all directions and the first lens closest to the atoms has a diameter of D, and is placed at a distance L from the atomic cloud. This lens captures a fraction of the scattered light by

$$\text{Fraction} = \frac{\pi(D/2)^2}{4\pi L^2} = \frac{D^2}{16L^2}. \tag{C.5}$$

The camera has a conversion gain that converts electron signals to digital counts, known as analog-digital units (ADU). Here, we obtain the ADU by summing the

counts over all pixels. The total number of photons emitted by the atomic cloud within time interval Δt is given by

$$n = \frac{\text{ADU} \times \text{CMOS sensitivity}}{\text{QE} \times \text{Loss} \times \text{Fraction}}, \tag{C.6}$$

where the CMOS sensitivity provides the number of photoelectrons per ADU, and QE is quantum efficiency that indicates how many incident photons create electron-hole pairs for camera read-out. This QE is wavelength-dependent and the losses take into account some light scattered from the surface of the lens.

The total number of atoms emitting photons is obtained by

$$N = \frac{n}{\Gamma_{\text{sc}} \Delta t}, \tag{C.7}$$

where Δt is the exposure time and Γ_{sc} is the scattering rate of the atom-photon interaction given by [93]

$$\Gamma_{\text{sc}} = \left(\frac{\Gamma}{2}\right) \frac{I/I_{\text{sat}}}{1 + (I/I_{\text{sat}}) + 4(\Delta/\Gamma)^2}. \tag{C.8}$$

Here Δ is the detuning frequency from the transition, Γ is the natural linewidth, and I_{sat} is the saturated intensity for the transition. This technique is used to determine the atom number in the MOT, as discussed in Section 3.3 of the main text.

C.3 Absorption imaging

The idea of absorption imaging is that atomic density is encoded in the on-resonant probing beam because some parts of the beam are absorbed by the atoms, resulting in a shadow image [181]. The intensity of the probe beam after passing through the atomic cloud is governed by Beer's law,

$$I = I_0 e^{-\text{OD}}, \tag{C.9}$$

where I_0 and I are the beam intensities before and after passing the atomic cloud, and OD represents the optical density.

In the experiment, we typically take three pictures for one dataset as follows: The first picture shows the atom interaction with the light field, I_A. The second picture shows only the light field, I_F, because atoms disappear due to the on-resonant light in the first picture. The last picture is the background light where the light field is completely off, I_G. By combining all three pictures, the optical density is given by

$$\mathrm{OD}(x,y) = -\log_{10}\left[\frac{I_A(x,y) - I_G(x,y)}{I_F(x,y) - I_G(x,y)}\right]. \tag{C.10}$$

The optical density is related to atomic column density, $n(x,y)$, by

$$\mathrm{OD}(x,y) = n(x,y)\sigma, \tag{C.11}$$

where σ denotes the absorption cross-section, expressed as

$$\sigma = \frac{\sigma_0}{1 + (I/I_{\mathrm{sat}}) + 4(\Delta/\Gamma)^2}. \tag{C.12}$$

Here, $\sigma_0 = \hbar\omega\Gamma/(2I_{\mathrm{sat}})$ represents the on-resonance cross-section and ω is the angular frequency of the probe beam.

To extract the atom number, the column density is integrated over space

$$N = \int\int n(x,y)\ dxdy = \frac{1}{\sigma}\int\int \mathrm{OD}(x,y)\ dxdy. \tag{C.13}$$

C.4 Time of flight

To determine the temperature of the atoms, time of flight (TOF) is a useful technique. From a microscopic point of view, temperature is determined by the average velocity of atoms. The observation of atomic cloud expansion implies its temperature. Assuming a non-interacting cloud that obeys Boltzmann's statistics, the number of atoms occupying the energy state E_i is given by

$$n_i(x,y) \propto \exp\left(-\frac{E_i}{k_B T}\right), \tag{C.14}$$

by applying $E_i = (1/2)mv_i^2$ and $v = \Delta x/\Delta t$, the atomic density after an expansion time Δt is

$$n_i(x,y) \propto \exp\left(-\frac{m(\Delta x)^2}{2k_B T(\Delta t)^2}\right). \tag{C.15}$$

As can be seen, the atomic density is approximated by a Gaussian distribution i.e., $f(x) = (1/\sigma\sqrt{2\pi})\exp[-(\Delta x/\sigma)^2/2]$. When the cloud's size σ and Δt are known variables, the temperature can be extracted by measuring the size of the cloud as a function of time, expressed as

$$\sigma^2 = \sigma_0^2 + \frac{k_B T}{m}(\Delta t)^2, \tag{C.16}$$

where σ_0 is the size of the atomic cloud at the initial time. Note that Δx has to be converted to the real spatial coordinate by considering the pixel's size l and we take into account the magnification from a system of lenses M (e.g., $\Delta x = l\Delta x_{\text{pixel}}/M$). For the fit, we set σ_0 and T as free parameters. Our results are shown in Fig. C.1(a) after the free evaporation in the ODT and in Fig. C.1(b) after the second evaporation in the ODT. This technique only works for thermal clouds. For degenerate gases, the quantum nature has to be taken into account, see the following section.

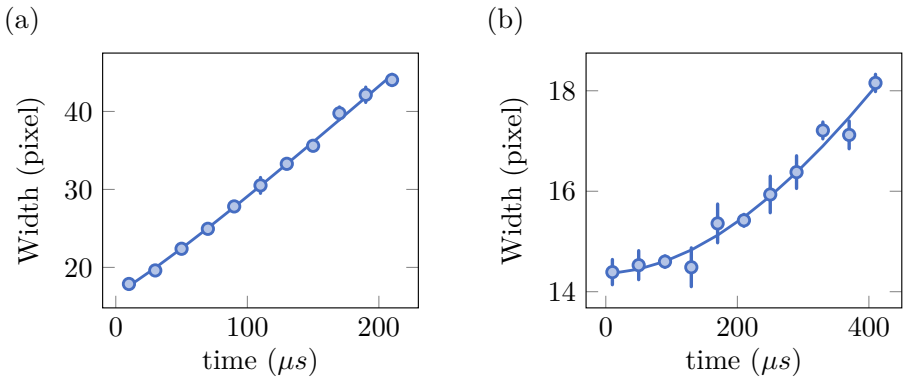

Figure C.1: **Time of flight measurement.** (a) Time-dependent cloud size after free evaporation in the ODT. Temperature extracted from the fit of Eq. C.16 is 35 µK. (b) Cloud size as a function of time for the second evaporation in the ODT, achieving a temperature of 300 nK. Here, 1 pixel = 1.5 µm.

C.5 Degenerate Fermi gases

The transition from the classical into the degenerate regime can be characterized by the phase-space density defined as the number of particles inside a cubic volume

formed by the thermal de Broglie wavelength (λ_{dB}), given by

$$\rho = n\lambda_{\mathrm{dB}}^3, \tag{C.17}$$

where n is the atomic density and the thermal de Broglie wavelength is defined as $\lambda_{\mathrm{dB}} = h/\sqrt{2\pi m k_B T}$.

The atom number is determined by absorption imaging, as discussed in Section C.3, and extracting the temperature of a degenerate Fermi gas is challenging through the time of flight. To address this challenge, we consider the unique density profiles of Fermi gases, which differ from those of thermal clouds.

When the temperature is colder, atoms enter the quantum regime, and the time of flight is limited by fitting the density distribution under the assumption of a Gaussian function. However, fermions at low temperatures cannot be described by a Gaussian function. It can be shown that the density profile of fermions is the polylogarithm function instead. One might extract the size of the atomic cloud for different times, as described in Section C.4 using the polylogarithm function, however, it requires a time-consuming process. Here, I present a faster and more precise procedure by taking a single absorption image of the atomic cloud and fitting it to the expected profile. The derivation below is adapted from [182, 183].

The non-interacting fermions are described as the Fermi-Dirac distribution, given by

$$f_{\mathrm{fermion}}(E) = \frac{1}{z^{-1}e^{\beta E} + 1} = \frac{1}{e^{\beta(E-\mu)} + 1}, \tag{C.18}$$

where the fugacity is defined as $z = e^{\beta\mu}$, μ is the chemical potential, E is the energy, and $\beta = 1/(k_B T)$.

Our potential in the accordion lattice combined with the bottom beam is approximated as a quasi 2d harmonic potential ($\omega_{x,y} \ll \omega_z$). The region around the trap center can be approximated by $V(\mathbf{r}) = (1/2)m(\omega_x^2 x^2 + \omega_y^2 y^2)$ with the density of state $g(\epsilon) = \epsilon/(\hbar^2\omega_x\omega_y)$. A fundamental quantity that governs the behavior of fermionic systems and provides insights into their thermal, electrical, and quantum properties

is known as Fermi energy, E_F. It is defined as the highest energy occupied by a system of fermions at absolute temperature $T = 0$. Assume that the system consists of N particles and by the definition, the last occupied state has an energy of E_F, the total atom number in the system is given by

$$N = \int_0^{E_F} g(\epsilon)\, d\epsilon = \int_0^{E_F} \frac{1}{\hbar^2 \omega_x \omega_y} \epsilon\, d\epsilon. \tag{C.19}$$

We rearrange Eq C.19 and solve for the Fermi energy, obtaining

$$E_F = \hbar \sqrt{2N\omega_x \omega_y}, \tag{C.20}$$

and the Fermi temperature, which is the temperature equivalent to the Fermi energy, is

$$T_F = \frac{\hbar}{k_B} \sqrt{2N\omega_x \omega_y}. \tag{C.21}$$

For finite temperatures, saying T, the total number of particles is given by

$$N = \int_0^{\infty} \frac{g(\epsilon)}{z^{-1} e^{\beta E} + 1}\, d\epsilon = -\left(\frac{k_B T}{\hbar \sqrt{\omega_x \omega_y}}\right)^2 \mathrm{Li}_2(-z), \tag{C.22}$$

and by combining Eq. C.21 with Eq. C.22, the system temperature in units of the Fermi temperature is written as

$$\frac{T}{T_F} = \left[-2\mathrm{Li}_2(-z)\right]^{-1/2} = \left[-2\mathrm{Li}_2(-e^{\beta\mu})\right]^{-1/2}. \tag{C.23}$$

As can be seen, with the knowledge of the fugacity, the temperature compared to the Fermi temperature is determined.

To map the Fermi-Dirac distribution to measurement quantities, the expression in Eq. C.18 can be converted into phase-space variables by replacing the single-particle energy with the Hamiltonian. Therefore, the mean occupation in terms of the phase-space variables is

$$f_{\text{fermi}}(\mathbf{r}, \mathbf{p}) = \frac{1}{e^{\beta(\mathbf{p}^2/2m + V(\mathbf{r}) - \mu))} + 1}. \tag{C.24}$$

To calculate the density of a 2d Fermi gas, we integrate over the momentum space. The density is given by

$$\rho_{\text{2d fermi}}(\mathbf{r}) = \int \frac{d^2\mathbf{p}}{(2\pi\hbar)^2} f_{\text{fermi}}(\mathbf{r}, \mathbf{p}) = -\frac{1}{\lambda_{dB}^2} \mathrm{Li}_1\left(-e^{\beta(\mu - V(\mathbf{r}))}\right). \tag{C.25}$$

In the experiment, we access the distribution through in-situ absorption imaging along the z-direction, obtaining the column density of a 2d Fermi gas, expressed as

$$n_{2D}^{\text{observe}}(x,y) = \frac{n_{2D,0}\text{Li}_1\left(-\exp\left[\beta\mu - \beta m\left(\omega_x^2 x^2 + \omega_y^2 y^2\right)/2\right]\right)}{\text{Li}_1\left(-e^{\beta\mu}\right)}. \tag{C.26}$$

For simplicity, we define the Gaussian width as $\sigma_i^2 \equiv (\beta m \omega_i^2)^{-1}$ where $i = x, y$. The above expression is simplified to

$$n_{2D}^{\text{observe}}(x,y) = \frac{n_{2D,0}\text{Li}_1\left(-\exp\left[\beta\mu - \left(\frac{x^2}{2\sigma_x^2} + \frac{y^2}{2\sigma_y^2}\right)\right]\right)}{\text{Li}_1\left(-e^{\beta\mu}\right)}. \tag{C.27}$$

For arbitrary expansion time, the width is time-dependent and can be written as

$$\sigma_i^2 = \sigma_{i,0}^2(1 + (\omega_i \Delta t)^2), \tag{C.28}$$

where Δt is the expansion time and $\sigma_{i,0}$ is the initial width along the i direction.

For the fit, we apply Eq. C.27 and set $n_{2D,0}$, $e^{\beta\mu}$ and σ_i as free parameters. The temperature of the system is determined using Eq. C.23 and T_F is extracted through the atom number provided in Eq. C.21, assuming $\omega_{x,y}$ are known parameters. The trap frequency can be measured by separate measurements, for example, amplitude modulation spectroscopy as described in the main text.

C.6 Feshbach resonances

In 1993, Tiesinga et al. studied a resonance in the scattering length at specific values of the magnetic field [184]. Based on this observation, the scattering length can be tuned via a magnetic field from repulsive to attractive interactions. The Feshbach resonances offer a wide range of applications in ultracold gases, such as controlling the interaction between atoms in the regime of interest. For example, the creation of mBECs formed by ^{6}Li atoms by sweeping magnetic field from high to low field centered in the vicinity of 810 G, as discussed in the main text.

Here, I discuss a simple model of the Feshbach resonances summarized from [38, 185] as follows: Two atoms are in scattering states, referred to as the open channel.

When the atoms collide with each other at a resonant energy, they couple to a molecular-bound state, referred to as the closed channel. The key point is that the magnetic dipole moments in both channels are different, allowing for an energy difference in both channels that can be controlled by a magnetic field.

From the mathematical perspective, Feshbach resonances can be described by a couple of two subspaces. Let $\mathcal{P}$ and $\mathcal{Q}$ be projection operators onto the open and closed channels. The two subspaces span the whole space and satisfy $\mathcal{P}+\mathcal{Q} = \mathbb{1}$. This implies that any state can be written as a superposition of wavefunctions projected onto the two subspaces i.e., $|\Psi\rangle = |\Psi_P\rangle + |\Psi_Q\rangle$. The Schrodinger equation for the system is split into two coupled equations:

$$(E - H_{PP})\,|\Psi_P\rangle = H_{PQ}\,|\Psi_Q\rangle\,, \tag{C.29}$$

$$(E - H_{QQ})\,|\Psi_Q\rangle = H_{QP}\,|\Psi_P\rangle\,, \tag{C.30}$$

where the projected Hamiltonians onto $\mathcal{P}$ and $\mathcal{Q}$ space are denoted as $H_{PP} = \mathcal{P}H\mathcal{P}$ and $H_{QQ} = \mathcal{Q}H\mathcal{Q}$. We note here that $H_{PQ} = \mathcal{P}H\mathcal{Q}$ and $H_{QP} = \mathcal{Q}H\mathcal{P}$ represents the coupled Hamiltonians between the two subspaces.

To solve the coupled equations, Eq. C.30 is rearranged to

$$|\Psi_Q\rangle = (E - H_{QQ} + i0)^{-1}\,H_{QP}\,|\Psi_P\rangle\,,$$

and plug to Eq. C.29. One can show that

$$(E - H_{PP} - H'_{PP})\,|\Psi_P\rangle = 0, \tag{C.31}$$

where we define $H'_{PP} = H_{PQ}\,(E - H_{QQ} + i0)^{-1}\,H_{QP}$ and $+i0$ represents a small positive imaginary part.

As can be seen, the term H'_{PP} describes the atom-atom interaction in the subspace of the open channel $\mathcal{P}$. In other words, a transition occurs from the $\mathcal{P}$ subspace to the $\mathcal{Q}$ subspace, propagating in the $\mathcal{Q}$ space and then transitioning back to the $\mathcal{P}$ subspace. The scattering length is related to the energy by a factor and first-order

perturbation theory is applied as follows:

$$\frac{4\pi\hbar^2}{m}a = \frac{4\pi\hbar^2}{m}a_{\mathrm{nr}} + \sum_n \frac{|\langle\psi_n|H_{QP}|\psi_0\rangle|^2}{E - E_n}, \tag{C.32}$$

where $4\pi\hbar^2 a/m$ has a unit of energy, a_{nr} is the scattering length when there is no coupling between open and closed channels, ψ_0 represents the scattering state, and ψ_n indicates the bound state with its corresponding energy E_n.

In the case of the energy $E \equiv E_{\mathrm{th}}$ close to a particular bound state energy, E_{res}, other terms contribute less. As a result, the scattering length is approximated by

$$\frac{4\pi\hbar^2}{m}a = \frac{4\pi\hbar^2}{m}a_{\mathrm{nr}} + \frac{|\langle\psi_{\mathrm{res}}|H_{QP}|\psi_0\rangle|^2}{E_{\mathrm{th}} - E_{\mathrm{res}}}. \tag{C.33}$$

In Eq. C.33, the difference in energy is determined by the hyperfine structure in the presence of a magnetic field,

$$E_{\mathrm{th}} - E_{\mathrm{res}} = (2\mu_s - \mu_b)(B - B_0),$$

where μ_s and μ_b are the single-atom magnetic moment and the magnetic moment of the bound state. The scattering is finally expressed in a simple form as

$$a(B) = a_{\mathrm{nr}}\left(1 - \frac{\Delta}{B - B_0}\right), \tag{C.34}$$

where Δ is the width of the resonance and B_0 represents the magnetic field that causes the scattering length to diverge to $\pm\infty$.

C.7 Kapitza-Dirac scattering

To derive the probability after the atomic cloud interacts with a pulse of a 1d periodic potential, we start with the Hamiltonian given by

$$\hat{H} = -\frac{\hbar^2}{2m}\frac{\partial^2}{\partial z^2} + V_0 \sin^2 kz.$$

In the Raman-Nath regime, the kinetic energy is neglected, $\beta\alpha \ll 1$, where β and α are defined in the main text (Section 3.10.1). The evolution of the wavefunction is given by

$$|\Psi\rangle = \exp\left(-\frac{i}{\hbar}\int dt' V(z,t')\right)|\psi_0\rangle = \exp\left(-\frac{i}{\hbar}V_0\tau\sin^2 kz\right)|\Psi_0\rangle\,.$$

Note that the product of V_0 and τ represents the pulse area, which we treat as an independent variable in the measurement instead of using either V_0 or τ. By applying the fact that the exponential of a complex sinusoidal function can be expanded in terms of Bessel functions of the first kind as follows:

$$e^{i\alpha\cos(\beta)} = \sum_{n=-\infty}^{\infty} i^n J_n(\alpha) e^{in\beta},$$

here, $e^{in\beta}$ can be viewed as a plane-wave basis. The wavefunction is finally expressed as

$$|\Psi\rangle = |\Psi_0\rangle\, e^{-\frac{i}{2\hbar}V_0\tau} \sum_{n=-\infty}^{\infty} i^n J_n\left(\frac{V_0\tau}{2\hbar}\right) e^{i2nkz} = \mathrm{e}^{-\frac{i}{2\hbar}V_0\tau} \sum_{n=-\infty}^{\infty} i^n J_n\left(\frac{V_0\tau}{2\hbar}\right) |g, 2n\hbar k\rangle,$$

where $|g, 2n\hbar k\rangle$ represents the ground state wavefunction with momentum $2n\hbar k$, here, the index, n, ranges over integers ($n = 0, \pm 1 \pm 2, \dots$). The result shows that the initial cloud at rest ($k = 0$) is separated into $2n + 1$ clouds with different momenta.

C.8 Hyperfine Zeeman splitting

Atoms in the presence of a magnetic field can be described by the Hamiltonian given by

$$H = H_0 + A\mathbf{I} \cdot \mathbf{J} + H_{\text{zeeman}}, \tag{C.35}$$

where H_0 is the bare Hamiltonian, A is the magnetic dipole constant that describes the coupling between nuclear spin and total angular momentum, and H_{zeeman} represents the Zeeman effect on the atoms [186, 187]. The Zeeman Hamiltonian takes the form

$$H_{\text{zeeman}} = -\mu \cdot \mathbf{B}, \tag{C.36}$$

where μ is the total magnetic moment due to fine structure and nuclear spin, expressed as

$$\mu = -\frac{\mu_B}{\hbar}\left(g_J\mathbf{J} + g_I\mathbf{I}\right), \tag{C.37}$$

here, g_J and g_I are the Lende g-factor for fine structure and nuclear spin. The g_J can be written in terms of the electron orbital g-factor g_L and electron spin g-factor g_S as follows:

$$g_J = g_L \frac{J(J+1) + L(L+1) - S(S+1)}{2J(J+1)} + g_S \frac{J(J+1) + L(L+1) - S(S+1)}{2J(J+1)}. \tag{C.38}$$

To simplify the Hamiltonian in Eq C.35, we assume the magnetic field is directed along the z-axis, i.e., $\mathbf{B} = B\hat{z}$ and we drop the offset energy from the bare Hamiltonian. The Hamiltonian becomes

$$H = A\mathbf{I}\cdot\mathbf{J} + \frac{\mu_B B}{\hbar}\big(g_J J_z + g_I I_z\big). \tag{C.39}$$

By applying $\mathbf{F} = \mathbf{J} + \mathbf{I}$ and squaring both sides, the product between angular momenta can be written as

$$\mathbf{I}\cdot\mathbf{J} = \frac{1}{2}\big(\hat{F}^2 - \hat{J}^2 - \hat{I}^2\big). \tag{C.40}$$

A good quantum number for the Zeeman Hamiltonian is J, m_j, I, m_I with an eigenbasis representation $|J, m_J; I, m_I\rangle$. The matrix elements of the Zeeman Hamiltonian are given by

$$\langle J, m'_J; I, m'_I|\frac{\mu_B B}{\hbar}\big(g_J J_z + g_I I_z\big)|J, m_J; I, m_I\rangle = \frac{\mu_B B}{\hbar}\big(g_J m_z + g_I m_I\big)\delta_{m'_I,m_I}\delta_{m'_J,m_J}, \tag{C.41}$$

whereas the matrix elements of the hyperfine structure are

$$\begin{aligned}\langle J, m'_J; I, m'_I|\frac{1}{2}\big(\hat{F}^2 - \hat{J}^2 - \hat{I}^2\big)|J, m_J; I, m_I\rangle = {}& \langle J, m'_J; I, m'_I|\frac{1}{2}\hat{F}^2|J, m_J; I, m_I\rangle \\ & -\frac{\hbar^2}{2}\big(J(J+1) + I(I+1)\big)\delta_{m'_I,m_I}\delta_{m'_J,m_J}.\end{aligned} \tag{C.42}$$

Next, we decouple this quantity, $\langle J, m'_J; I, m'_I|\hat{F}^2|J, m_J; I, m_I\rangle$, by applying the identity $\sum_{F,m_F} |F, m_F\rangle \langle F, mF| = \mathbb{1}$. This leads to

$$\begin{aligned}\langle J, m'_J; I, m'_I|\hat{F}^2|J, m_J; I, m_I\rangle = \sum_{F',m_{F'}} \sum_{F,m_F} & \langle J, m'_J; I, m'_I|F', m_{F'}\rangle \\ & \langle F', m_{F'}|\hat{F}^2|F, m_F\rangle \langle F, m_F|J, m_J; I, m_I\rangle .\end{aligned} \tag{C.43}$$

The above expression indicates finding the Clebsch-Gordon coefficients, which can be evaluated using Winger $3-j$ symbols

$$\langle J, m_J; I, m_I | F, m_F \rangle = \sqrt{2F+1}(-1)^{-m_F+I-J} \begin{pmatrix} J & I & F \\ m_J & m_I & -m_F \end{pmatrix}. \tag{C.44}$$

Finally, the eigenvalues of the Hamiltonian in Eq C.39 reveal the energy shifts due to the magnetic field.

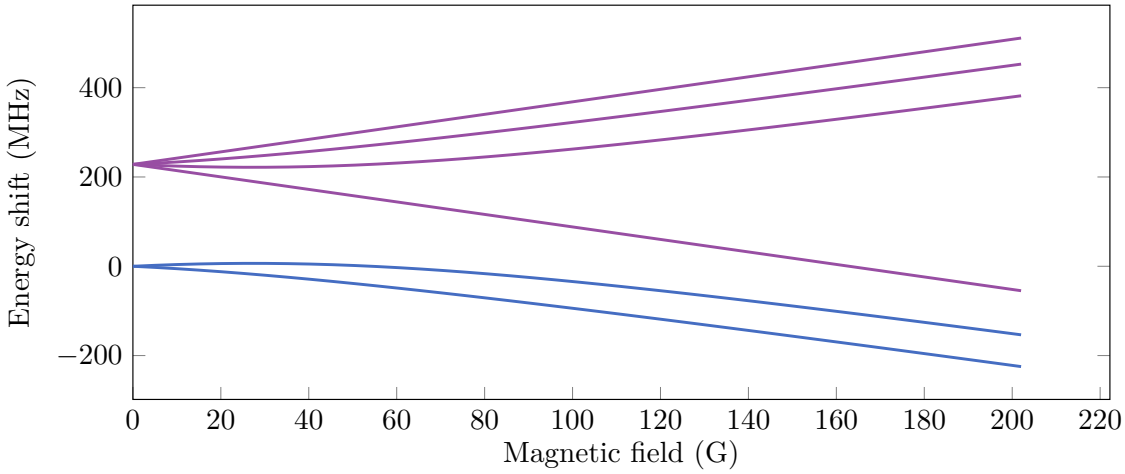

Figure C.2: **Zeeman shifts of the two lowest hyperfine states.** The $|S_{1/2}\ F=1/2\rangle$ state is represented by blue and the $|S_{1/2}\ F=3/2\rangle$ state is denoted as violet.

C.9 Light shift

The energy level of atoms can be shifted due to atom-light interaction. Here, I demonstrate the light shift in a two-level system. The time-dependent Schrodinger equation is given by

$$i\hbar\frac{\partial}{\partial t}|\Psi\rangle = \hat{H}\Psi, \tag{C.45}$$

and the Hamiltonian is $\hat{H} = \hat{H}_0 + \hat{V}$ where $\hat{H}_0$ is the Hamiltonian of the unperturbed atom and $\hat{V}$ is the perturbed Hamiltonian from the electromagnetic field. The wavefunction of the atoms governed by $\hat{H}$ can be written as

$$|\Psi\rangle = c_1(t)|0\rangle + c_2(t)e^{-i\omega_0 t}|1\rangle, \tag{C.46}$$

where $c_{1,2}$ are the time-dependent coefficients and ω_0 is the transition frequency. By taking a first derivative with respect to time, we have

$$\begin{aligned}\frac{\partial}{\partial t}|\Psi\rangle &= c_1(t)\frac{\partial}{\partial t}|0\rangle + c_2(t)e^{-i\omega_0 t}\frac{\partial}{\partial t}|1\rangle \\ &\quad + \dot{c_1}|0\rangle + \left(\dot{c_2}e^{-i\omega_0 t} - i\omega_0 c_2 e^{-i\omega_0 t}\right)|1\rangle ,\end{aligned} \tag{C.47}$$

Next, we plug Eqs. C.46 and C.47 to Eq. C.45

$$\begin{aligned}\hat{H}|\Psi\rangle &= \left(\hat{H}_0 + \hat{V}\right)|\Psi\rangle \\ &= 0 + c_2(t)\hbar\omega_0 e^{-i\omega_0 t}|1\rangle + c_1(t)\hat{V}|0\rangle + c_2(t)e^{-i\omega_0 t}\hat{V}|1\rangle .\end{aligned} \tag{C.48}$$

The above expression can be decomposed into two coupled equations,

$$i\hbar\dot{c_1} = c_2(t)\langle 0|\hat{V}|1\rangle e^{-i\omega_0 t}, \tag{C.49}$$

$$i\hbar\dot{c_2} = c_1(t)\langle 1|\hat{V}|0\rangle e^{i\omega_0 t}, \tag{C.50}$$

and we consider the matrix elements of the dipole moment interacting with the electric field $\mathbf{E} = E_0\hat{\epsilon}\cos\left(\omega t\right)$,

$$\langle 1|\hat{V}|0\rangle = E_0\langle 1|\mathbf{p}\cdot\hat{\epsilon}|0\rangle\cos\left(\omega t\right). \tag{C.51}$$

By applying the rotating wave approximation, which neglects the fast oscillation term, an approximation form is expressed as

$$e^{\pm i\omega_0 t}\cos\left(\omega t\right) \approx \frac{1}{2}e^{\mp i\Delta t}, \tag{C.52}$$

where $\Delta = \omega - \omega_0$ is the frequency detuning.

The two coupled equations are written as

$$i\hbar\dot{c_1} = \frac{\hbar\Omega^*}{2}c_2(t)e^{i\Delta t}, \tag{C.53}$$

$$i\hbar\dot{c_2} = \frac{\hbar\Omega}{2}c_1(t)e^{-i\Delta t}, \tag{C.54}$$

where the Rabi frequency $\Omega = (E_0/\hbar)\langle 1|\mathbf{p}\cdot\hat{\epsilon}|0\rangle$ describes the strength of the coupling between the atom and the electric field.

One can show that the coupled equations reduce to uncoupled second-order differential equations. However, we can remove the time dependence by introducing new coefficients $\tilde{c_1} = c_1$ and $\tilde{c_2} = c_2 e^{i\Delta t}$. Eqs. C.53 and C.54 are simplified to

$$i\hbar\dot{\tilde{c_1}} = \frac{\hbar\Omega^*}{2}\tilde{c_2}, \tag{C.55}$$

$$i\hbar\dot{\tilde{c_2}} = \frac{\hbar\Omega}{2}\tilde{c_1} - \hbar\Delta\tilde{c_2}, \tag{C.56}$$

or it can be written in matrix form as

$$i\hbar\frac{\partial}{\partial t}\begin{pmatrix}\tilde{c_1}\\ \\ \tilde{c_2}\end{pmatrix} = \frac{\hbar}{2}\begin{pmatrix}0 & \Omega^*\\ \\ \Omega & -2\Delta\end{pmatrix}\begin{pmatrix}\tilde{c_1}\\ \\ \tilde{c_2}\end{pmatrix}. \tag{C.57}$$

We diagonalize the matrix above and obtain the eigenvalues as follows:

$$E_g = \frac{\hbar}{2}\big(-\Delta - \sqrt{|\Omega|^2 + \Delta^2}\big), \tag{C.58}$$

$$E_e = \frac{\hbar}{2}\big(-\Delta + \sqrt{|\Omega|^2 + \Delta^2}\big). \tag{C.59}$$

By applying a very far-detuned light, i.e., $|\Delta| \gg \Omega$, the eigenvalues are approximated by

$$E_g = -\hbar\Delta - \frac{\Omega^2}{4\Delta}, \tag{C.60}$$

$$E_e = \frac{\Omega^2}{4\Delta}. \tag{C.61}$$

The light shift of the ground state and the excited state has opposite signs ($\pm\Omega^2/(4\Delta)$). For example, when a laser beam is red-detuned from the atomic transition, the ground state energy decreases while the excited state energy increases. This implies that the ground-state atoms experience an attractive force while the excited atoms experience a repulsive force from the red-detuned laser.

Appendix D

^{6}Li Atomic Properties

Scattering lengths

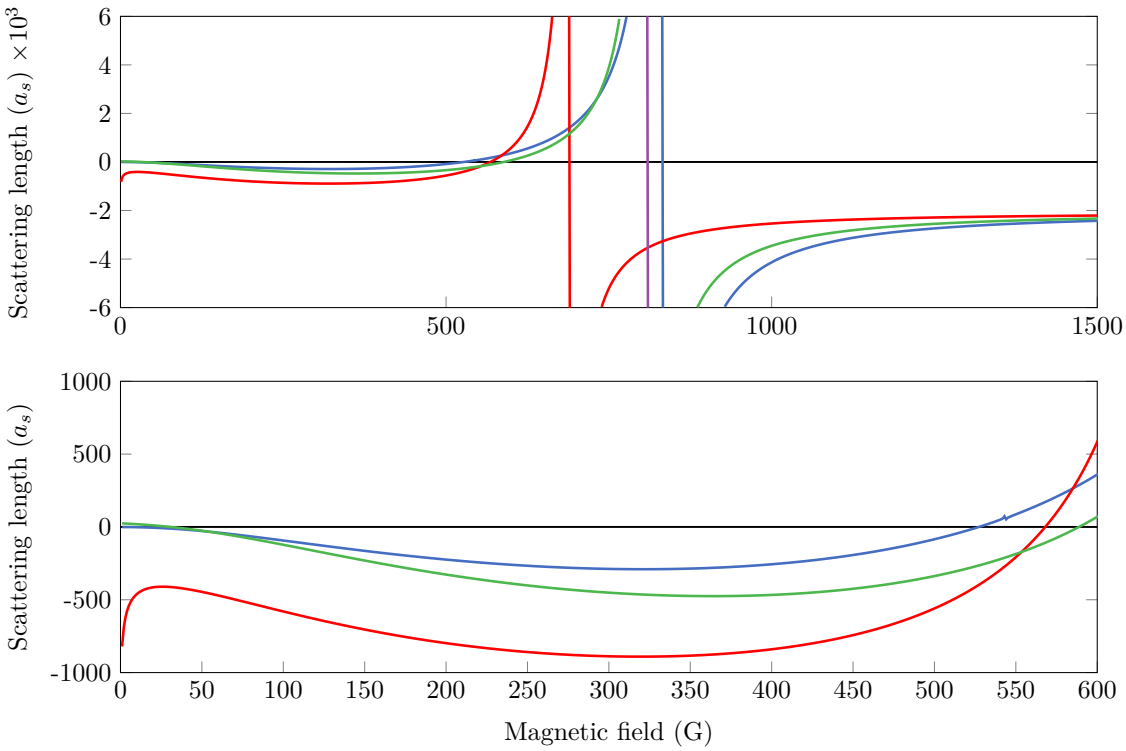

Figure D.1: **Scattering length of the three lowest hyperfine states of ^{6}Li.** Blue is $|1\rangle - |2\rangle$ mixture, red is $|1\rangle - |2\rangle$ mixture, and violet is $|2\rangle - |3\rangle$ mixture. The narrow Feshbach resonance for a $|1\rangle - |2\rangle$ mixture is observed in the measurement at a field of 543.3 G (Fig. 4.14(a)). Data for the figures is from ref. [96].

Atomic properties

Property	Symbol	Value	Unit
Atomic number	Z	3	
Nucleons	Z+N	6	
Natural abundance	η	7.6%	
Atomic mass	m	$9.9883414 \times 10^{-27}$	kg
Nuclear spin	I	1	
Electronic spin	S	1/2	
D1 transition	λ_{D1}	670.992421	nm
D2 transition	λ_{D2}	670.977338	nm
Natural Linewidth	Γ	5.8724	MHz
D1 Saturation Intensity	I_{sat}	7.59	mW/cm^2
D2 Saturation Intensity	I_{sat}	2.54	mW/cm^2
$2^2S_{1/2}$ Magnetic Dipole constant	A	152.13684	MHz
$2^2P_{1/2}$ Magnetic Dipole constant	A	17.386	MHz
$2^2P_{3/2}$ Magnetic Dipole constant	A	-1.155	MHz
$2^2P_{3/2}$ Electric Quadrupole constant	B	-0.10	MHz
Electron spin g-factor	g_S	2.0023	
Electron orbital g-factor	g_L	0.999996	
Total Nuclear g-factor	g_I	-0.000448	
Total Electronic g-factor ($2^2S_{1/2}$)	g_J	2.0023	
Total Electronic g-factor ($2^2P_{1/2}$)	g_J	0.6668	
Total Electronic g-factor ($2^2P_{3/2}$)	g_J	1.335	

Table D.1: **Fundamental physical properties of ^{6}Li.** The table is from ref. [188].

Appendix E

Timeline of the Experiment

2018

Fall: Peter Schauss joined the University of Virginia (UVA) and planned a ^{6}Li quantum gas microscope. Jirayu Mongkolkiattichai (J.M.) began his first year of Ph.D. at UVA.

2019

Spring and Summer: Liyu Liu (L.L.) and J.M. joined the team. Setting up lasers for ^{6}Li spectroscopy, imaging, Zeeman slower, MOT, and Raman cooling. Winding coils for Zeeman slower, MOT, Offsets, and Feshbach field.

Fall: Jin Yang (Postdoc) joined the team. First MOT of ^{6}Li

2020

Spring: Atoms were loaded into the optical dipole trap and observed first mBECs. The light sheet and bottom beam were set up.

Summer: MOPA laser was set up and observed Kapitza-Dirac diffraction from 1d and 2d optical lattices.

Fall: Implemented Raman sideband cooling in the triangular and square lattices. Imaged atoms in the lattices with single-site resolution.

2021

Spring: Submitted our manuscript on site-resolved imaging of ultracold fermions in the triangular lattice.

Summer: Paper published on PRX [84].

Fall: Observed Mott insulators in the square lattice and triangular lattice.

2022

Spring: Measurements of spin-spin correlations. Paper on extended Zeeman slower and NLCE submitted. The extended Zeeman slower paper published [90]. Davis Garwood and Jin Yang left the team.

Summer: NLCE paper published on PRA [124]. RF antennas were set up and observed the Rabi oscillations of $|1\rangle - |2\rangle$ and $|2\rangle - |3\rangle$ mixtures.

Fall: Submitted paper on fermionic triangular Mott insulators and spin-spin correlations.

2023

Spring: Switched back to the square lattice and tried to improve temperature. Set up spin-resolved imaging and DMD.

Fall: Obtained spin-resolved imaging and found that the temperature is high because of the lattice laser. The lowest temperature of $k_B T/t \simeq 0.5$ was obtained using the square lattice. J.M. was working on a three-component Mott insulator in the square lattice. L.L. was working on many-body localization in the square lattice disordered by the triangular lattice. The paper on fermionic triangular Mott insulators was finally published on PRA [58].

2024

Spring: J.M. prepared a manuscript for the three-component Mott insulators and also prepared for his Ph.D. defense. L.L. worked on two-component Mott insulators after changing the square-lattice AOM. Drew Wilkers started working on prelab tasks and prepared to take over J.M.'s position.

Bibliography

[1] D. Castelvecchi. The Stern–Gerlach experiment at 100. Nat. Rev. Phys. **4**, 140–142 (2022).

[2] A. Einstein. Über einen die Erzeugung und Verwandlung des Lichtes betreffenden heuristischen Gesichtspunkt. Ann. Phys. **322**, 132–148 (1905).

[3] A. B. Arons and M. B. Peppard. Einstein's Proposal of the Photon Concept—a Translation of the Annalen der Physik Paper of 1905. Am. J. Phys. **33**, 367–374 (1965).

[4] S. M. Bilenky and S. T. Petcov. Massive neutrinos and neutrino oscillations. Rev. Mod. Phys. **59**, 671–754 (1987).

[5] J. F. Clauser, M. A. Horne, A. Shimony, and R. A. Holt. Proposed Experiment to Test Local Hidden-Variable Theories. Phys. Rev. Lett. **23**, 880–884 (1969).

[6] A. Aspect, J. Dalibard, and G. Roger. Experimental Test of Bell's Inequalities Using Time-Varying Analyzers. Phys. Rev. Lett. **49**, 1804–1807 (1982).

[7] D. Bouwmeester, J.-W. Pan, K. Mattle, M. Eibl, H. Weinfurter, and A. Zeilinger. Experimental quantum teleportation. Nature **390**, 575–579 (1997).

[8] P. M. Paul, E. S. Toma, P. Breger, G. Mullot, F. Augé, P. Balcou, H. G. Muller, and P. Agostini. Observation of a Train of Attosecond Pulses from High Harmonic Generation. Science **292**, 1689–1692 (2001).

[9] F. Krausz and M. Ivanov. Attosecond physics. Rev. Mod. Phys. **81**, 163–234 (2009).

[10] M. Lewenstein, P. Balcou, M. Y. Ivanov, A. L'Huillier, and P. B. Corkum. Theory of high-harmonic generation by low-frequency laser fields. Phys. Rev. A **49**, 2117–2132 (1994).

[11] M. H. Anderson, J. R. Ensher, M. R. Matthews, C. E. Wieman, and E. A. Cornell. Observation of Bose-Einstein Condensation in a Dilute Atomic Vapor. Science **269**, 198–201 (1995).

[12] K. B. Davis, M.-O. Mewes, M. R. Andrews, N. J. van Druten, D. S. Durfee, D. M. Kurn, and W. Ketterle. Bose-Einstein Condensation in a Gas of Sodium Atoms. Phys. Rev. Lett. **75**, 3969–3973 (1995).

[13] C. C. Bradley, C. A. Sackett, J. J. Tollett, and R. G. Hulet. Evidence of Bose-Einstein Condensation in an Atomic Gas with Attractive Interactions. Phys. Rev. Lett. **75**, 1687–1690 (1995).

[14] B. DeMarco and D. S. Jin. Onset of Fermi Degeneracy in a Trapped Atomic Gas. Science **285**, 1703–1706 (1999).

[15] E. A. L. Henn, J. A. Seman, E. R. F. Ramos, A. H. Iavaronni, T. Amthor, and V. S. Bagnato. Evaporation in atomic traps: A simple approach. Am. J. Phys. **75**, 907–910 (2007).

[16] C. Pfleiderer, G. McMullan, and G. Lonzarich. Pressure induced crossover of the magnetic transition from second to first order near the quantum critical point in MnSi. Physica B Condens. Matter **206-207**, 847–849 (1995).

[17] Y. Zhou, J. Guo, S. Cai, J. Zhao, G. Gu, C. Lin, H. Yan, C. Huang, C. Yang, S. Long, et al. Quantum phase transition from superconducting to insulating-like state in a pressurized cuprate superconductor. Nat. Phys. **18**, 406–410 (2022).

[18] M. Greiner, O. Mandel, T. Esslinger, T. W. Hänsch, and I. Bloch. Quantum phase transition from a superfluid to a Mott insulator in a gas of ultracold atoms. Nature **415**, 39–44 (2002).

[19] D. Jaksch, C. Bruder, J. I. Cirac, C. W. Gardiner, and P. Zoller. Cold Bosonic Atoms in Optical Lattices. Phys. Rev. Lett. **81**, 3108–3111 (1998).

[20] I. Bloch. Ultracold quantum gases in optical lattices. Nat. Phys. **1**, 23–30 (2005).

[21] M. Lewenstein, A. Sanpera, V. Ahufinger, B. Damski, A. Sen(De), and U. Sen. Ultracold atomic gases in optical lattices: mimicking condensed matter physics and beyond. Adv. Phys. **56**, 243–379 (2007).

[22] I. Bloch, J. Dalibard, and W. Zwerger. Many-body physics with ultracold gases. Rev. Mod. Phys. **80**, 885–964 (2008).

[23] T. Esslinger. Fermi-Hubbard Physics with Atoms in an Optical Lattice. Annu. Rev. Condens. Matter Phys. **1**, 129–152 (2010).

[24] W. Hofstetter, J. I. Cirac, P. Zoller, E. Demler, and M. D. Lukin. High-Temperature Superfluidity of Fermionic Atoms in Optical Lattices. Phys. Rev. Lett. **89**, 220407 (2002).

[25] R. Jördens, N. Strohmaier, K. Günter, H. Moritz, and T. Esslinger. A Mott insulator of fermionic atoms in an optical lattice. Nature **455**, 204–207 (2008).

[26] U. Schneider, L. Hackermüller, S. Will, T. Best, I. Bloch, T. A. Costi, R. W. Helmes, D. Rasch, and A. Rosch. Metallic and Insulating Phases of Repulsively Interacting Fermions in a 3D Optical Lattice. Science **322**, 1520–1525 (2008).

[27] J. Bednorz and K. Mueller. Possible high temperature superconductivity. Z. Phys. **64**, 189–193 (1986).

[28] M. Imada, A. Fujimori, and Y. Tokura. Metal-insulator transitions. Rev. Mod. Phys. **70**, 1039–1263 (1998).

[29] J. Orenstein and A. J. Millis. Advances in the Physics of High-Temperature Superconductivity. Science **288**, 468–474 (2000).

[30] P. A. Lee, N. Nagaosa, and X.-G. Wen. Doping a Mott insulator: Physics of high-temperature superconductivity. Rev. Mod. Phys. **78**, 17–85 (2006).

[31] E. H. Lieb and F. Y. Wu. Absence of Mott Transition in an Exact Solution of the Short-Range, One-Band Model in One Dimension. Phys. Rev. Lett. **20**, 1445–1448 (1968).

[32] J. E. Hirsch. Two-dimensional Hubbard model: Numerical simulation study. Phys. Rev. B **31**, 4403–4419 (1985).

[33] M. Troyer and U.-J. Wiese. Computational Complexity and Fundamental Limitations to Fermionic Quantum Monte Carlo Simulations. Phys. Rev. Lett. **94**, 170201 (2005).

[34] M. Rigol, T. Bryant, and R. R. P. Singh. Numerical Linked-Cluster Approach to Quantum Lattice Models. Phys. Rev. Lett. **97**, 187202 (2006).

[35] R. P. Feynman. Simulating physics with computers. Int. J. Theor. Phys. **21**, 467–488 (1982).

[36] S. Lloyd. Universal Quantum Simulators. Science **273**, 1073–1078 (1996).

[37] S. Inouye, M. Andrews, J. Stenger, H.-J. Miesner, D. M. Stamper-Kurn, and W. Ketterle. Observation of Feshbach resonances in a Bose–Einstein condensate. Nature **392**, 151–154 (1998).

[38] C. Chin, R. Grimm, P. Julienne, and E. Tiesinga. Feshbach resonances in ultracold gases. Rev. Mod. Phys. **82**, 1225–1286 (2010).

[39] W. S. Bakr, J. I. Gillen, A. Peng, S. Fölling, and M. Greiner. A quantum gas microscope for detecting single atoms in a Hubbard-regime optical lattice. Nature **462**, 74–77 (2009).

[40] J. F. Sherson, C. Weitenberg, M. Endres, M. Cheneau, I. Bloch, and S. Kuhr. Single-atom-resolved fluorescence imaging of an atomic Mott insulator. Nature **467**, 68–72 (2010).

[41] M. Miranda, R. Inoue, Y. Okuyama, A. Nakamoto, and M. Kozuma. Site-resolved imaging of ytterbium atoms in a two-dimensional optical lattice. Phys. Rev. A **91**, 063414 (2015).

[42] R. Yamamoto, J. Kobayashi, T. Kuno, K. Kato, and Y. Takahashi. An ytterbium quantum gas microscope with narrow-line laser cooling. New J. Phys. **18**, 023016 (2016).

[43] K. Kwon, K. Kim, J. Hur, S. Huh, and J.-y. Choi. Site-resolved imaging of a bosonic Mott insulator of ^{7}Li atoms. Phys. Rev. A **105**, 033323 (2022).

[44] L. W. Cheuk, M. A. Nichols, M. Okan, T. Gersdorf, V. V. Ramasesh, W. S. Bakr, T. Lompe, and M. W. Zwierlein. Quantum-Gas Microscope for Fermionic Atoms. Phys. Rev. Lett. **114**, 193001 (2015).

[45] E. Haller, J. Hudson, A. Kelly, D. A. Cotta, B. Peaudecerf, G. D. Bruce, and S. Kuhr. Single-atom imaging of fermions in a quantum-gas microscope. Nat. Phys. **11**, 738–742 (2015).

[46] G. J. A. Edge, R. Anderson, D. Jervis, D. C. McKay, R. Day, S. Trotzky, and J. H. Thywissen. Imaging and addressing of individual fermionic atoms in an optical lattice. Phys. Rev. A **92**, 063406 (2015).

[47] A. Omran, M. Boll, T. A. Hilker, K. Kleinlein, G. Salomon, I. Bloch, and C. Gross. Microscopic Observation of Pauli Blocking in Degenerate Fermionic Lattice Gases. Phys. Rev. Lett. **115**, 263001 (2015).

[48] D. Greif, G. Jotzu, M. Messer, R. Desbuquois, and T. Esslinger. Formation and Dynamics of Antiferromagnetic Correlations in Tunable Optical Lattices. Phys. Rev. Lett. **115**, 260401 (2015).

[49] P. T. Brown, D. Mitra, E. Guardado-Sanchez, P. Schauß, S. S. Kondov, E. Khatami, T. Paiva, N. Trivedi, D. A. Huse, and W. S. Bakr. Spin-imbalance in a 2D Fermi-Hubbard system. Science **357**, 1385–1388 (2017).

[50] D. Greif, T. Uehlinger, G. Jotzu, L. Tarruell, and T. Esslinger. Short-Range Quantum Magnetism of Ultracold Fermions in an Optical Lattice. Science **340**, 1307–1310 (2013).

[51] R. A. Hart, P. M. Duarte, T.-L. Yang, X. Liu, T. Paiva, E. Khatami, R. T. Scalettar, N. Trivedi, D. A. Huse, and R. G. Hulet. Observation of antiferromagnetic correlations in the Hubbard model with ultracold atoms. Nature **519**, 211–214 (2015).

[52] M. F. Parsons, A. Mazurenko, C. S. Chiu, G. Ji, D. Greif, and M. Greiner. Site-resolved measurement of the spin-correlation function in the Fermi-Hubbard model. Science **353**, 1253–1256 (2016).

[53] M. Boll, T. A. Hilker, G. Salomon, A. Omran, J. Nespolo, L. Pollet, I. Bloch, and C. Gross. Spin- and density-resolved microscopy of antiferromagnetic correlations in Fermi-Hubbard chains. Science **353**, 1257–1260 (2016).

[54] L. W. Cheuk, M. A. Nichols, K. R. Lawrence, M. Okan, H. Zhang, E. Khatami, N. Trivedi, T. Paiva, M. Rigol, and M. W. Zwierlein. Observation of spatial charge and spin correlations in the 2D Fermi-Hubbard model. Science **353**, 1260–1264 (2016).

[55] J. H. Drewes, L. A. Miller, E. Cocchi, C. F. Chan, N. Wurz, M. Gall, D. Pertot, F. Brennecke, and M. Köhl. Antiferromagnetic Correlations in Two-Dimensional Fermionic Mott-Insulating and Metallic Phases. Phys. Rev. Lett. **118**, 170401 (2017).

[56] M. Gall, N. Wurz, J. Samland, C. F. Chan, and M. Köhl. Competing magnetic orders in a bilayer Hubbard model with ultracold atoms. Nature **589**, 40–43 (2021).

[57] J.-y. Choi, S. Hild, J. Zeiher, P. Schauß, A. Rubio-Abadal, T. Yefsah, V. Khemani, D. A. Huse, I. Bloch, and C. Gross. Exploring the many-body localization transition in two dimensions. Science **352**, 1547–1552 (2016).

[58] J. Mongkolkiattichai, L. Liu, D. Garwood, J. Yang, and P. Schauss. Quantum gas microscopy of fermionic triangular-lattice Mott insulators. Phys. Rev. A **108**, L061301 (2023).

[59] P. Anderson. Resonating valence bonds: A new kind of insulator? Mater. Res. Bull. **8**, 153–160 (1973).

[60] P. A. Lee. An End to the Drought of Quantum Spin Liquids. Science **321**, 1306–1307 (2008).

[61] L. Balents. Spin liquids in frustrated magnets. Nature **464**, 199–208 (2010).

[62] L. Savary and L. Balents. Quantum spin liquids: a review. Rep. Prog. Phys. **80**, 016502 (2016).

[63] A. Szasz, J. Motruk, M. P. Zaletel, and J. E. Moore. Chiral Spin Liquid Phase of the Triangular Lattice Hubbard Model: A Density Matrix Renormalization Group Study. Phys. Rev. X **10**, 021042 (2020).

[64] X.-Y. Song, A. Vishwanath, and Y.-H. Zhang. Doping the chiral spin liquid: Topological superconductor or chiral metal. Phys. Rev. B **103**, 165138 (2021).

[65] J. Struck, C. Ölschläger, R. L. Targat, P. Soltan-Panahi, A. Eckardt, M. Lewenstein, P. Windpassinger, and K. Sengstock. Quantum Simulation of Frustrated Classical Magnetism in Triangular Optical Lattices. Science **333**, 996–999 (2011).

[66] J. E. Hirsch and S. Tang. Antiferromagnetism in the Two-Dimensional Hubbard Model. Phys. Rev. Lett. **62**, 591–594 (1989).

[67] D. A. Huse and V. Elser. Simple Variational Wave Functions for Two-Dimensional Heisenberg Spin-1/2 Antiferromagnets. Phys. Rev. Lett. **60**, 2531–2534 (1988).

[68] T. Jolicoeur and J. C. Le Guillou. Spin-wave results for the triangular Heisenberg antiferromagnet. Phys. Rev. B **40**, 2727–2729 (1989).

[69] R. R. P. Singh and D. A. Huse. Three-sublattice order in triangular- and Kagomé-lattice spin-half antiferromagnets. Phys. Rev. Lett. **68**, 1766–1769 (1992).

[70] L. Capriotti, A. E. Trumper, and S. Sorella. Long-Range Néel Order in the Triangular Heisenberg Model. Phys. Rev. Lett. **82**, 3899–3902 (1999).

[71] M. Xu, L. H. Kendrick, A. Kale, Y. Gang, G. Ji, R. T. Scalettar, M. Lebrat, and M. Greiner. Frustration-and doping-induced magnetism in a fermi–hubbard simulator. Nature **620**, 971–976 (2023).

[72] Y. Nagaoka. Ferromagnetism in a Narrow, Almost Half-Filled *s* Band. Phys. Rev. **147**, 392–405 (1966).

[73] S.-S. Zhang, W. Zhu, and C. D. Batista. Pairing from strong repulsion in triangular lattice Hubbard model. Phys. Rev. B **97**, 140507 (2018).

[74] I. Morera, M. Kanász-Nagy, T. Smolenski, L. Ciorciaro, A. ç. Imamo ğlu, and E. Demler. High-temperature kinetic magnetism in triangular lattices. Phys. Rev. Res. **5**, L022048 (2023).

[75] R. Samajdar and R. N. Bhatt. Nagaoka ferromagnetism in doped Hubbard models in optical lattices. arXiv:2305.05683 (2023).

[76] K. Lee, P. Sharma, O. Vafek, and H. J. Changlani. Triangular lattice Hubbard model physics at intermediate temperatures. Phys. Rev. B **107**, 235105 (2023).

[77] M. Lebrat, M. Xu, L. H. Kendrick, A. Kale, Y. Gang, P. Seetharaman, I. Morera, E. Khatami, E. Demler, and M. Greiner. Observation of Nagaoka Polarons in a Fermi-Hubbard Quantum Simulator. arXiv:2308.12269 (2023).

[78] M. L. Prichard, B. M. Spar, I. Morera, E. Demler, Z. Z. Yan, and W. S. Bakr. Directly imaging spin polarons in a kinetically frustrated Hubbard system. arXiv:2308.12951 (2023).

[79] Y. Tang, L. Li, T. Li, Y. Xu, S. Liu, K. Barmak, K. Watanabe, T. Taniguchi, A. H. MacDonald, J. Shan, et al. Simulation of Hubbard model physics in WSe2/WS2 moiré superlattices. Nature **579**, 353–358 (2020).

[80] L. Ciorciaro, T. Smolenski, I. Morera, N. Kiper, S. Hiestand, M. Kroner, Y. Zhang, K. Watanabe, T. Taniguchi, E. Demler, et al. Kinetic magnetism in triangular moiré materials. Nature **623**, 509–513 (2023).

[81] S. M. Girvin and K. Yang. Modern condensed matter physics. Cambridge University Press, 2019.

[82] N. Ashcroft and N. Mermin. Solid State Physics. Saunders College Publishing, 1976.

[83] A. Fuhrmanek, R. Bourgain, Y. R. P. Sortais, and A. Browaeys. Light-assisted collisions between a few cold atoms in a microscopic dipole trap. Phys. Rev. A **85**, 062708 (2012).

[84] J. Yang, L. Liu, J. Mongkolkiattichai, and P. Schauss. Site-Resolved Imaging of Ultracold Fermions in a Triangular-Lattice Quantum Gas Microscope. PRX Quantum **2**, 020344 (2021).

[85] P. Schauss. High-resolution imaging of ordering in Rydberg many-body systems. PhD thesis. Ludwig-Maximilians-Universität München, 2015.

[86] D. J. McCarron, S. A. King, and S. L. Cornish. Modulation transfer spectroscopy in atomic rubidium. Meas. Sci. Technol. **19**, 105601 (2008).

[87] R. K. Raj, D. Bloch, J. J. Snyder, G. Camy, and M. Ducloy. High-Frequency Optically Heterodyned Saturation Spectroscopy Via Resonant Degenerate Four-Wave Mixing. Phys. Rev. Lett. **44**, 1251–1254 (1980).

[88] W. D. Phillips and H. Metcalf. Laser Deceleration of an Atomic Beam. Phys. Rev. Lett. **48**, 596–599 (1982).

[89] P. Elleaume, O. Chubar, and J. Chavanne. Computing 3D magnetic fields from insertion devices. Proceedings of the 1997 Particle Accelerator Conference **3**, 3509–3511 (1997).

[90] D. Garwood, L. Liu, J. Mongkolkiattichai, J. Yang, and P. Schauss. A hybrid Zeeman slower for lithium. Rev. Sci. Instrum. **93**, 033202 (2022).

[91] C. J. Foot. Atomic physics. Oxford University Press, 2004.

[92] T. A. Hilker. Spin-resolved microscopy of strongly correlated fermionic many-body states. PhD thesis. Ludwig Maximilians Universität München, 2017.

[93] H. J. Metcalf and P. Van der Straten. Laser cooling and trapping. Springer Science & Business Media, 1999.

[94] R. Grimm, M. Weidemüller, and Y. B. Ovchinnikov. Optical Dipole Traps for Neutral Atoms. Adv. At. Mol. Opt. Phys. **42**, 95–170 (2000).

[95] M. Bartenstein, A. Altmeyer, S. Riedl, R. Geursen, S. Jochim, C. Chin, J. H. Denschlag, R. Grimm, A. Simoni, E. Tiesinga, C. J. Williams, and P. S. Julienne. Precise determination of ^{6}Li cold collision parameters by radio-frequency spectroscopy on weakly bound molecules. Phys. Rev. Lett. **94**, 103201 (2005).

[96] G. Zürn, T. Lompe, A. N. Wenz, S. Jochim, P. S. Julienne, and J. M. Hutson. Precise Characterization of ^{6}Li Feshbach Resonances Using Trap-Sideband-Resolved RF Spectroscopy of Weakly Bound Molecules. Phys. Rev. Lett. **110**, 135301 (2013).

[97] C. Zener and R. H. Fowler. Non-adiabatic crossing of energy levels. Proc. R. soc. Lond. Ser. A-Contain. Pap. Math. Phys. Character **137**, 696–702 (1932).

[98] A. C. Vutha. A simple approach to the Landau–Zener formula. Eur. J. Phys. **31**, 389 (2010).

[99] S. Friebel, C. D'Andrea, J. Walz, M. Weitz, and T. W. Hänsch. CO_2-laser optical lattice with cold rubidium atoms. Phys. Rev. A **57**, R20–R23 (1998).

[100] D. Mitra, P. T. Brown, P. Schauss, S. S. Kondov, and W. S. Bakr. Phase Separation and Pair Condensation in a Spin-Imbalanced 2D Fermi Gas. Phys. Rev. Lett. **117**, 093601 (2016).

[101] M. F. Parsons, F. Huber, A. Mazurenko, C. S. Chiu, W. Setiawan, K. Wooley-Brown, S. Blatt, and M. Greiner. Site-Resolved Imaging of Fermionic ^{6}Li in an Optical Lattice. Phys. Rev. Lett. **114**, 213002 (2015).

[102] S. Al-Assam, R. A. Williams, and C. J. Foot. Ultracold atoms in an optical lattice with dynamically variable periodicity. Phys. Rev. A **82**, 021604 (2010).

[103] OXIDE Corporation. QPM Mount with TEC. 2021. URL: `https://www.opt-oxide.com/en/products/mount-with-tec/`.

[104] Z. Z. Yan, B. M. Spar, M. L. Prichard, S. Chi, H.-T. Wei, E. Ibarra-García-Padilla, K. R. A. Hazzard, and W. S. Bakr. Two-Dimensional Programmable Tweezer Arrays of Fermions. Phys. Rev. Lett. **129**, 123201 (2022).

[105] S. Gupta, A. E. Leanhardt, A. D. Cronin, and D. E. Pritchard. Coherent manipulation of atoms with standing light waves. Comptes Rendus de l'Académie des Sciences - Series IV - Physics **2**, 479–495 (2001).

[106] P. J. Martin, B. G. Oldaker, A. H. Miklich, and D. E. Pritchard. Bragg scattering of atoms from a standing light wave. Phys. Rev. Lett. **60**, 515–518 (1988).

[107] G. Birkl, M. Gatzke, I. H. Deutsch, S. L. Rolston, and W. D. Phillips. Bragg Scattering from Atoms in Optical Lattices. Phys. Rev. Lett. **75**, 2823–2826 (1995).

[108] B. Gadway, D. Pertot, R. Reimann, M. G. Cohen, and D. Schneble. Analysis of Kapitza-Dirac diffraction patterns beyond the Raman-Nath regime. Opt. Express **17**, 19173–19180 (2009).

[109] M. N. Kosch, L. Asteria, H. P. Zahn, K. Sengstock, and C. Weitenberg. Multifrequency optical lattice for dynamic lattice-geometry control. Phys. Rev. Res. **4**, 043083 (2022).

[110] S. Jin, K. Dai, J. Verstraten, M. Dixmerias, R. Alhyder, C. Salomon, B. Peaudecerf, T. de Jongh, and T. Yefsah. Multipurpose platform for analog quantum simulation. Phys. Rev. Res. **6**, 013158 (2024).

[111] J. Sebby-Strabley, M. Anderlini, P. S. Jessen, and J. V. Porto. Lattice of double wells for manipulating pairs of cold atoms. Phys. Rev. A **73**, 033605 (2006).

[112] M. Sbroscia, K. Viebahn, E. Carter, J.-C. Yu, A. Gaunt, and U. Schneider. Observing Localization in a 2D Quasicrystalline Optical Lattice. Phys. Rev. Lett. **125**, 200604 (2020).

[113] F. Gerbier. Quantum gases in optical lattices. Phys. World (2015).

[114] N. Fläschner, B. S. Rem, M. Tarnowski, D. Vogel, D.-S. Lühmann, K. Sengstock, and C. Weitenberg. Experimental reconstruction of the Berry curvature in a Floquet Bloch band. Science **352**, 1091–1094 (2016).

[115] W. Kohn. Analytic Properties of Bloch Waves and Wannier Functions. Phys. Rev. **115**, 809–821 (1959).

[116] A. Bunse-Gerstner, R. Byers, and V. Mehrmann. Numerical methods for simultaneous diagonalization. SIAM J. Matrix Anal. Appl. **14**, 927–949 (1993).

[117] S. Kivelson. Wannier functions in one-dimensional disordered systems: Application to fractionally charged solitons. Phys. Rev. B **26**, 4269–4277 (1982).

[118] J. Hubbard. Electron Correlations in Narrow Energy Bands. Proc. Roy. Soc. A **276**, 238–257 (1963).

[119] P. B. Blakie and C. W. Clark. Wannier states and Bose–Hubbard parameters for 2D optical lattices. J. Phys. B At. Mol. Opt. Phys. **37**, 1391–1404 (2004).

[120] L. W. Cheuk, M. A. Nichols, K. R. Lawrence, M. Okan, H. Zhang, and M. W. Zwierlein. Observation of 2D Fermionic Mott Insulators of ^{40}K with Single-Site Resolution. Phys. Rev. Lett. **116**, 235301 (2016).

[121] M. T. DePue, C. McCormick, S. L. Winoto, S. Oliver, and D. S. Weiss. Unity Occupation of Sites in a 3D Optical Lattice. Phys. Rev. Lett. **82**, 2262–2265 (1999).

[122] C. N. Varney, C.-R. Lee, Z. J. Bai, S. Chiesa, M. Jarrell, and R. T. Scalettar. Quantum Monte Carlo study of the two-dimensional fermion Hubbard model. Phys. Rev. B **80**, 075116 (2009).

[123] V. I. Iglovikov, E. Khatami, and R. T. Scalettar. Geometry dependence of the sign problem in quantum Monte Carlo simulations. Phys. Rev. B **92**, 045110 (2015).

[124] D. Garwood, J. Mongkolkiattichai, L. Liu, J. Yang, and P. Schauss. Site-resolved observables in the doped spin-imbalanced triangular Hubbard model. Phys. Rev. A **106**, 013310 (2022).

[125] A. Kale, J. H. Huhn, M. Xu, L. H. Kendrick, M. Lebrat, C. Chiu, G. Ji, F. Grusdt, A. Bohrdt, and M. Greiner. Schrieffer-Wolff transformations for experiments: Dynamically suppressing virtual doublon-hole excitations in a Fermi-Hubbard simulator. Phys. Rev. A **106**, 012428 (2022).

[126] A. Mazurenko, C. S. Chiu, G. Ji, M. F. Parsons, M. Kanász-Nagy, R. Schmidt, F. Grusdt, E. Demler, D. Greif, and M. Greiner. A cold-atom Fermi–Hubbard antiferromagnet. Nature **545**, 462–466 (2017).

[127] G. H. Wannier. Antiferromagnetism. The Triangular Ising Net. Phys. Rev. **79**, 357–364 (1950).

[128] P. W. Anderson. The Resonating Valence Bond State in La_2CuO_4 and Superconductivity. Science **235**, 1196–1198 (1987).

[129] X. G. Wen, F. Wilczek, and A. Zee. Chiral spin states and superconductivity. Phys. Rev. B **39**, 11413–11423 (1989).

[130] C. D. Batista, S.-Z. Lin, S. Hayami, and Y. Kamiya. Frustration and chiral orderings in correlated electron systems. Rep. Prog. Phys. **79**, 084504 (2016).

[131] Y. Zhou, K. Kanoda, and T.-K. Ng. Quantum spin liquid states. Rev. Mod. Phys. **89**, 025003 (2017).

[132] T. Yoshioka, A. Koga, and N. Kawakami. Quantum Phase Transitions in the Hubbard Model on a Triangular Lattice. Phys. Rev. Lett. **103**, 036401 (2009).

[133] T. Shirakawa, T. Tohyama, J. Kokalj, S. Sota, and S. Yunoki. Ground state phase diagram of the triangular lattice Hubbard model by density matrix renormalization group method. Phys. Rev. B **96**, 205130 (2017).

[134] I. Bloch, J. Dalibard, and W. Zwerger. Many-body physics with ultracold gases. Rev. Mod. Phys. **80**, 885–964 (2008).

[135] C. Gross and I. Bloch. Quantum simulations with ultracold atoms in optical lattices. Science **357**, 995–1001 (2017).

[136] D. Greif, M. F. Parsons, A. Mazurenko, C. S. Chiu, S. Blatt, F. Huber, G. Ji, and M. Greiner. Site-resolved imaging of a fermionic Mott insulator. Science **351**, 953–957 (2016).

[137] J. H. Drewes, L. A. Miller, E. Cocchi, C. F. Chan, N. Wurz, M. Gall, D. Pertot, F. Brennecke, and M. Köhl. Antiferromagnetic Correlations in Two-Dimensional Fermionic Mott-Insulating and Metallic Phases. Phys. Rev. Lett. **118**, 170401 (2017).

[138] J. Struck, M. Weinberg, C. Ölschläger, P. Windpassinger, J. Simonet, K. Sengstock, R. Höppner, P. Hauke, A. Eckardt, M. Lewenstein, and L. Mathey. Engineering Ising-XY spin-models in a triangular lattice using tunable artificial gauge fields. Nat. Phys. **9**, 738–743 (2013).

[139] P. Scholl, M. Schuler, H. J. Williams, A. A. Eberharter, D. Barredo, K.-N. Schymik, V. Lienhard, L.-P. Henry, T. C. Lang, T. Lahaye, A. M. Läuchli, and A. Browaeys. Quantum simulation of 2D antiferromagnets with hundreds of Rydberg atoms. Nature **595**, 233–238 (2021).

[140] G. Semeghini, H. Levine, A. Keesling, S. Ebadi, T. T. Wang, D. Bluvstein, R. Verresen, H. Pichler, M. Kalinowski, R. Samajdar, A. Omran, S. Sachdev, A. Vishwanath, M. Greiner, V. Vuletić, and M. D. Lukin. Probing topological spin liquids on a programmable quantum simulator. Science **374**, 1242–1247 (2021).

[141] A. Auerbach. Interacting Electrons and Quantum Magnetism. Springer, New York, 1990.

[142] I. Ferrier-Barbut, M. Delehaye, S. Laurent, A. T. Grier, M. Pierce, B. S. Rem, F. Chevy, and C. Salomon. A mixture of Bose and Fermi superfluids. Science **345**, 1035–1038 (2014).

[143] J. Koepsell, S. Hirthe, D. Bourgund, P. Sompet, J. Vijayan, G. Salomon, C. Gross, and I. Bloch. Robust Bilayer Charge Pumping for Spin- and Density-Resolved Quantum Gas Microscopy. Phys. Rev. Lett. **125**, 010403 (2020).

[144] M. Vojta. Spin polarons in triangular antiferromagnets. Phys. Rev. B **59**, 6027–6030 (1999).

[145] J. van de Kraats, K. K. Nielsen, and G. M. Bruun. Holes and magnetic polarons in a triangular lattice antiferromagnet. Phys. Rev. B **106**, 235143 (2022).

[146] A. Vrani ć, J. Vu či čevi ć, J. Kokalj, J. Skolimowski, R. Žitko, J. Mravlje, and D. Tanaskovi ć. Charge transport in the Hubbard model at high temperatures: Triangular versus square lattice. Phys. Rev. B **102**, 115142 (2020).

[147] T. Hartke, B. Oreg, N. Jia, and M. Zwierlein. Doublon-Hole Correlations and Fluctuation Thermometry in a Fermi-Hubbard Gas. Phys. Rev. Lett. **125**, 113601 (2020).

[148] E. Braaten, H. .-. Hammer, D. Kang, and L. Platter. Efimov physics in ^{6}Li atoms. Phys. Rev. A **81**, 013605 (2010).

[149] T. B. Ottenstein, T. Lompe, M. Kohnen, A. N. Wenz, and S. Jochim. Collisional Stability of a Three-Component Degenerate Fermi Gas. Phys. Rev. Lett. **101**, 203202 (2008).

[150] J. H. Huckans, J. R. Williams, E. L. Hazlett, R. W. Stites, and K. M. O'Hara. Three-Body Recombination in a Three-State Fermi Gas with Widely Tunable Interactions. Phys. Rev. Lett. **102**, 165302 (2009).

[151] G. L. Schumacher, J. T. Mäkinen, Y. Ji, G. G. T. Assumpção, J. Chen, S. Huang, F. J. Vivanco, and N. Navon. Observation of Anomalous Decay of a Polarized Three-Component Fermi Gas. arXiv:2301.02237 (2023).

[152] T. Lompe, T. B. Ottenstein, F. Serwane, A. N. Wenz, G. Zürn, and S. Jochim. Radio-Frequency Association of Efimov Trimers. Science **330**, 940–944 (2010).

[153] X.-J. Liu, H. Hu, and P. D. Drummond. Multicomponent strongly attractive Fermi gas: A color superconductor in a one-dimensional harmonic trap. Phys. Rev. A **77**, 013622 (2008).

[154] Á. Rapp, G. Zaránd, C. Honerkamp, and W. Hofstetter. Color Superfluidity and "Baryon" Formation in Ultracold Fermions. Phys. Rev. Lett. **98**, 160405 (2007).

[155] T. A. Tóth, A. M. Läuchli, F. Mila, and K. Penc. Three-Sublattice Ordering of the SU(3) Heisenberg Model of Three-Flavor Fermions on the Square and Cubic Lattices. Phys. Rev. Lett. **105**, 265301 (2010).

[156] E. Ibarra-García-Padilla, C. Feng, G. Pasqualetti, S. Fölling, R. T. Scalettar, E. Khatami, and K. R. A. Hazzard. Metal-insulator transition and magnetism of SU(3) fermions in the square lattice. Phys. Rev. A **108**, 053312 (2023).

[157] S. Taie, R. Yamazki, S. Sugawa, and Y. Takahashi. An SU(6) Mott insulator of an atomic Fermi gas realized by large-spin Pomeranchuk cooling. Nat. Phys. (2012).

[158] D. Tusi, L. Franchi, L. Livi, K. Baumann, D. Benedicto Orenes, L. Del Re, R. Barfknecht, T.-W. Zhou, M. Inguscio, G. Cappellini, et al. Flavour-selective localization in interacting lattice fermions. Nat. Phys. **18**, 1201–1205 (2022).

[159] C. Hofrichter, L. Riegger, F. Scazza, M. Höfer, D. R. Fernandes, I. Bloch, and S. Fölling. Direct Probing of the Mott Crossover in the SU(N) Fermi-Hubbard Model. Phys. Rev. X **6**, 021030 (2016).

[160] S. Taie, E. Ibarra-García-Padilla, N. Nishizawa, Y. Takasu, Y. Kuno, H.-T. Wei, R. T. Scalettar, K. R. Hazzard, and Y. Takahashi. Observation of antiferromagnetic correlations in an ultracold SU(N) Hubbard model. Nat. Phys. **18**, 1356–1361 (2022).

[161] S.-y. Miyatake, K. Inaba, and S.-i. Suga. Three-component fermionic atoms with repulsive interaction in optical lattices. Phys. Rev. A **81**, 021603 (2010).

[162] K. Inaba, S.-y. Miyatake, and S.-i. Suga. Mott transitions of three-component fermionic atoms with repulsive interaction in optical lattices. Phys. Rev. A **82**, 051602 (2010).

[163] K. Inaba and S.-I. Suga. Superfluid, staggered state, and mott insulator of repulsively interacting three-component fermionic atoms in optical lattices. Mod. Phys. Lett. B **27**, 1330008 (2013).

[164] D. Mitra, P. T. Brown, E. Guardado-Sanchez, S. S. Kondov, T. Devakul, D. A. Huse, P. Schauß, and W. S. Bakr. Quantum gas microscopy of an attractive Fermi–Hubbard system. Nat. Phys. **14**, 173–177 (2018).

[165] H. B. Callen and T. A. Welton. Irreversibility and Generalized Noise. Phys. Rev. **83**, 34–40 (1951).

[166] C. Boos, C. J. Ganahl, M. Lajkó, P. Nataf, A. M. Läuchli, K. Penc, K. P. Schmidt, and F. Mila. Time-reversal symmetry breaking Abelian chiral spin liquid in Mott phases of three-component fermions on the triangular lattice. Phys. Rev. Res. **2**, 023098 (2020).

[167] Y. Xu, S. Capponi, J.-Y. Chen, L. Vanderstraeten, J. Hasik, A. H. Nevidomskyy, M. Mambrini, K. Penc, and D. Poilblanc. Phase diagram of the chiral SU(3) antiferromagnet on the kagome lattice. Phys. Rev. B **108**, 195153 (2023).

[168] D. Wei, D. Adler, K. Srakaew, S. Agrawal, P. Weckesser, I. Bloch, and J. Zeiher. Observation of Brane Parity Order in Programmable Optical Lattices. Phys. Rev. X **13**, 021042 (2023).

[169] G. Pupillo, A. Micheli, M. Boninsegni, I. Lesanovsky, and P. Zoller. Strongly Correlated Gases of Rydberg-Dressed Atoms: Quantum and Classical Dynamics. Phys. Rev. Lett. **104**, 223002 (2010).

[170] N. Henkel, R. Nath, and T. Pohl. Three-Dimensional Roton Excitations and Supersolid Formation in Rydberg-Excited Bose-Einstein Condensates. Phys. Rev. Lett. **104**, 195302 (2010).

[171] J. E. Johnson and S. L. Rolston. Interactions between Rydberg-dressed atoms. Phys. Rev. A **82**, 033412 (2010).

[172] E. Guardado-Sanchez, B. M. Spar, P. Schauss, R. Belyansky, J. T. Young, P. Bienias, A. V. Gorshkov, T. Iadecola, and W. S. Bakr. Quench Dynamics of a Fermi Gas with Strong Nonlocal Interactions. Phys. Rev. X **11**, 021036 (2021).

[173] E. Perepelitsky, A. Galatas, J. Mravlje, R. Žitko, E. Khatami, B. S. Shastry, and A. Georges. Transport and optical conductivity in the Hubbard model: A high-temperature expansion perspective. Phys. Rev. B **94**, 235115 (2016).

[174] F. Görg, M. Messer, K. Sandholzer, G. Jotzu, R. Desbuquois, and T. Esslinger. Enhancement and sign change of magnetic correlations in a driven quantum many-body system. Nature **553**, 481–485 (2018).

[175] W. B. Leigh. Devices for optoelectronics. CRC Press, 1996.

[176] A. Yariv. Optical Electronics. 1991.

[177] D. Mitra. Exploring attractively interacting fermions in 2D using a quantum gas microscope. PhD thesis. Princeton University, 2018.

[178] F. Serwane. The setup of a Magneto Optical Trap for the preparation of a mesoscopic degenerate. Master thesis. University of Heidelberg, 2007.

[179] G. E. Marti, R. Olf, E. Vogt, A. Öttl, and D. M. Stamper-Kurn. Two-element Zeeman slower for rubidium and lithium. Phys. Rev. A **81**, 043424 (2010).

[180] W. D. Phillips. Nobel Lecture: Laser cooling and trapping of neutral atoms. Rev. Mod. Phys. **70**, 721–741 (1998).

[181] T. Pyragius. Developing and building an absorption imaging system for Ultracold Atoms. arXiv:1209.3408 (2012).

[182] B. Frohlich. A strongly interacting two-dimensional Fermi gas. PhD thesis. University of Cambridge, 2011.

[183] W. Ketterle and M. W. Zwierlein. Making, probing and understanding ultracold Fermi gases. Riv Nuovo Cimento **31**, 247–422 (2008).

[184] E. Tiesinga, B. J. Verhaar, and H. T. C. Stoof. Threshold and resonance phenomena in ultracold ground-state collisions. Phys. Rev. A **47**, 4114–4122 (1993).

[185] A. J. Moerdijk, B. J. Verhaar, and A. Axelsson. Resonances in ultracold collisions of ^{6}Li, ^{7}Li, and ^{23}Na. Phys. Rev. A **51**, 4852–4861 (1995).

[186] E. Arimondo, M. Inguscio, and P. Violino. Experimental determinations of the hyperfine structure in the alkali atoms. Rev. Mod. Phys. **49**, 31–75 (1977).

[187] J. Walls, R. A. Ashby, J. Clarke, B. Lu, and W. A. van Wijngaarden. Measurement of isotope shifts, fine and hyperfine structure splittings of the lithium D lines. Eur. Phys. J. D **22**, 159–162 (2003).

[188] M. E. Gehm. Properties of ^{6}Li. Jetlab, (2003).